GL00597

LBL-24661

Lawrence Berkeley Laboratory
UNIVERSITY OF CALIFORNIA

EARTH SCIENCES DIVISION

Analysis of P- and S-Wave VSP Data from the Salton Sea Geothermal Field

T.M. Daley
(M.S. Thesis)

September 1987

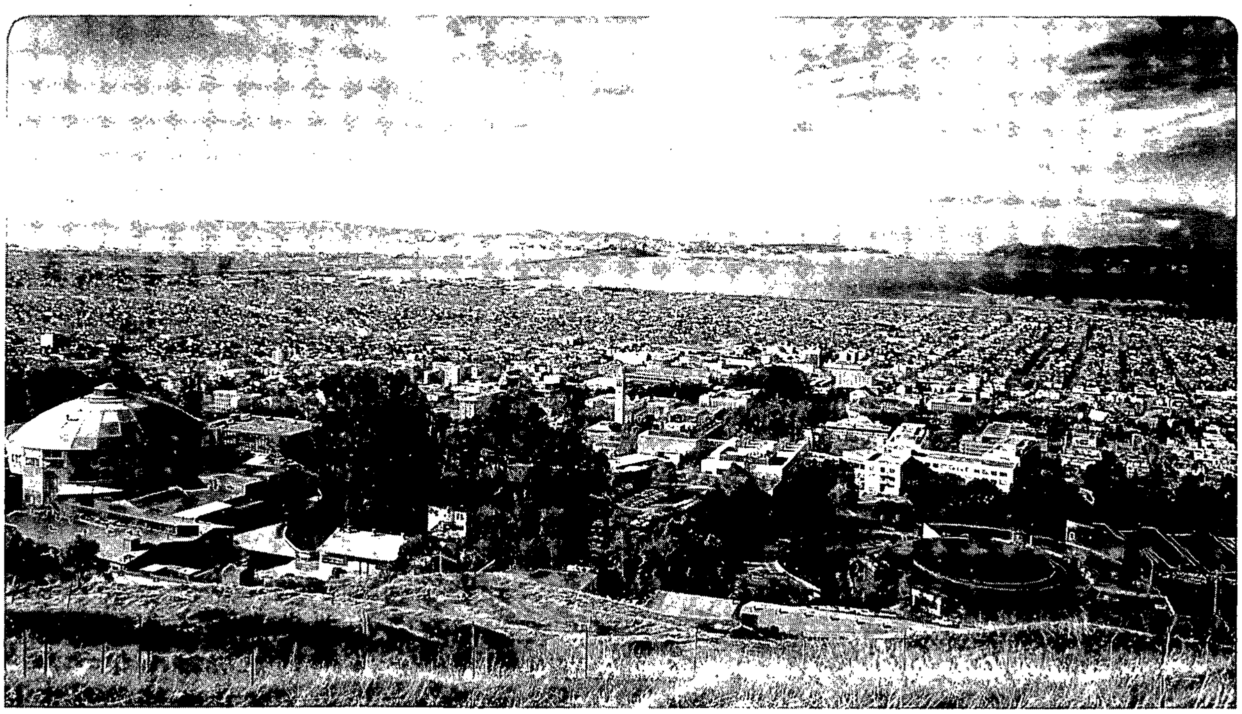

Prepared for the U.S. Department of Energy under Contract DE-AC03-76SF00098

Analysis of P- and S-Wave VSP Data from the Salton Sea Geothermal Field

Thomas Michael Daley

M.S. Thesis

Lawrence Berkeley Laboratory
University of California
Berkeley, California 94720

September 1987

ACKNOWLEDGEMENTS

First the formalities;

This work was supported through U. S. Department of Energy Contract No. DE-AC03-76SF00098 by the Assistant Secretary for Energy Research, Office of Basic Energy Sciences, Division of Engineering and Geosciences. The facilities for this research were provided by the Center for Computational Seismology at the Lawrence Berkeley Laboratory Earth Science Division, University of California.

And now the pleasantries;

It is doubtful my schooling would have reached its current level without the early encouragement of my parents, Roy and Anntoinette Daley, and the later years of education would have been much less enjoyable without the companionship and support of my wife, Lydia Palmin Daley.

The research included in this thesis was mostly developed during talks with my advisor, Dr. Thomas V. McEvilly, who fortunately found the time and energy for another student. Other productive and enlightening discussions were held with Drs. Frank Morrison, Shimon Coen and Ernest Majer. Among the students who added greatly to my graduate work in the Engineering Geoscience group are Cliff Schenkel (and Callie), Lupe Severson, Mike Wilt, Ted Asch, Ed Nichols, Dave Bartel and Dave Kennedy. Thanks to Dr. Alex Becker for providing support and crossover knowledge via a separate research project in electromagnetic geophysics.

Thanks to my friends Steve Lund and Jim Phelps for providing the breaks in my studies which were necessary to my sense of perspective (and my mental health). Thanks to Larry Blake's, La Val's/La Burrita, Henry's Pub, Triple Rock and the Starry Plough for food and drink. And thanks to Berkeley for the carnival.

Table of Contents

LIST OF FIGURES

LIST OF TABLES

CHAPTER 1

INTRODUCTION

In March of 1986 the Salton Sea Scientific Drilling Project (SSSDP) completed drilling California State Well 2-14 to a depth of 10,500 feet. This deep well was drilled by the Department Of Energy (DOE) as part of the Geothermal Technology Development program with scientific studies in the well funded by the Basic Energy Sciences office of DOE, the National Science Foundation and the U.S. Geological Survey. The well is located near the Salton Sea Geothermal Field in southern California. As part of the SSSDP, a vertical seismic profile (VSP) was conducted by the Lawrence Berkeley Laboratory's Earth Science Division. The processing and analysis of the Salton Sea VSP data is the basis of this thesis.

The objective of acquiring the VSP was to study the seismic wave propagation properties of the area near the well. There are several goals within this objective. The first goal is to use standard VSP analysis to obtain velocity models and search for reflective horizons within, and possibly beneath, the Salton Sea well. Another goal is the seismic detection of fracture zones surrounding the well including any indications of geothermal reservoirs. Also designed into the VSP is use of the shear wave sources to detect and analyze in-situ seismic anisotropy, if any, in rock surrounding the SSSDP. Finally, the SSSDP VSP data are used to test new particle motion analysis and display techniques for detecting fracturing and estimating the orientation of the fractures.

The usefulness of the VSP surveys has been well documented in the last decade; at least four books on VSP have been published and a number of new articles appear in the literature every year. It is assumed that the reader is somewhat familiar with VSP data, including the presence of upgoing and downgoing waves, tube waves, and the identification of reflector depth. For reference on these points any of several good review articles are available including Oristaglio, 1985 and Kennett, 1980. The application of VSP to anisotropy studies and fracture detection is more recent and is gaining in use. A 1987 meeting of the SEG included such titles as "Seismic Detection of Subsurface Fractures" (Becker and Perelberg, 1987) and "Estimate of Shear Wave Anisotropy Using Multicomponent

Seismic Data" (Corrigan, et.al., 1987). Both of these papers, among others published in recent months, are looking at the use of VSP to study fracture-induced anisotropy. The VSP performed at the SSSDP provides a fairly complete data set taken in an area whose seismic propagation properties and fracture properties are not well understood. This paper is an attempt to apply current analysis techniques to understand an unusual geologic setting, rather than a proof of the techniques in an area whose seismic properties are known.

In order to understand any geophysical data, geologic information is necessary. For this reason, the thesis will begin with a summary of the geology of the Salton Trough region and the Salton Sea Geothermal Field (SSGF). The information available from the SSSDP will also be summarized, although much has not yet been published. After the geologic summary, the design of the VSP will be discussed, including acquisition equipment and procedures. The data processing procedures and software used will be discussed as a separate section. Processing procedures will also be described at various times in the thesis where more specialized procedures are used. Data analysis makes up the bulk of the thesis and it is divided into a number of sections detailing the basic VSP interpretation, the anisotropy analysis and the fracture detection and orientation analysis. A combined interpretation of the results, with probable geologic causes for observed events, is presented as a separate section from the data analysis. Finally, a summary of results for each of the goals stated above will be given. The reader should note that a large volume of data were collected and various display methods were used (from the standard wiggle-trace to three-component hodographs). Much of these data are left in the appendices with important or representative figures given in the body of the thesis. Also given in the appendices are listings of FORTRAN programs developed in conjunction with the thesis work.

CHAPTER 2
GEOLOGY

1. REGIONAL SETTING

The regional setting of the Salton Sea Geothermal Field (SSGF) is one of complex tectonic interactions. Figure 1 shows the location of the Salton Trough, a long, narrow depression extending northwest from the Gulf of California in Northern Mexico to the Coachella Valley region in Southern California. The Salton Trough is a transitional zone on the boundary between the North American plate and the Pacific plate. The transition is from the transform faulting of the San Andreas fault system to the rifting associated with the East Pacific Rise. Both of these tectonic forces are currently active within the Salton Trough, but it is small spreading centers with their associated upwellings of mantle material which appear to be providing the geothermal heat source. The strike-slip faulting of the San Andreas system interacts with the rifting to create a complicated geologic province.

As an actively growing rift valley, the Salton Trough is subject to high rates of subsidence and sedimentation. The process of sedimentation has been ongoing since the Salton Trough first began developing in late Miocene or early Pliocene time (Crowell and Sylvester, 1979). Gravity and seismic refraction studies indicate the Trough contains over 6 km of sediments (Frith 1978, Randal 1974). This sedimentation has been dominated by the Colorado River, which enters in the center of the trough near Yuma, California. The Colorado River forms a delta which developed westward in mid-Pleistocene time (Younker, et al, 1982). The delta has alternated flow northward and southward, separating the Imperial Valley to the north and the Mexicali Valley to the south. Southern flow, which is the current direction, discharges into the Gulf of California while northern flow discharges into the Imperial Valley and can only escape by evaporation. The current Salton Sea is one of many historic inland seas within the northern end of the Salton Trough.

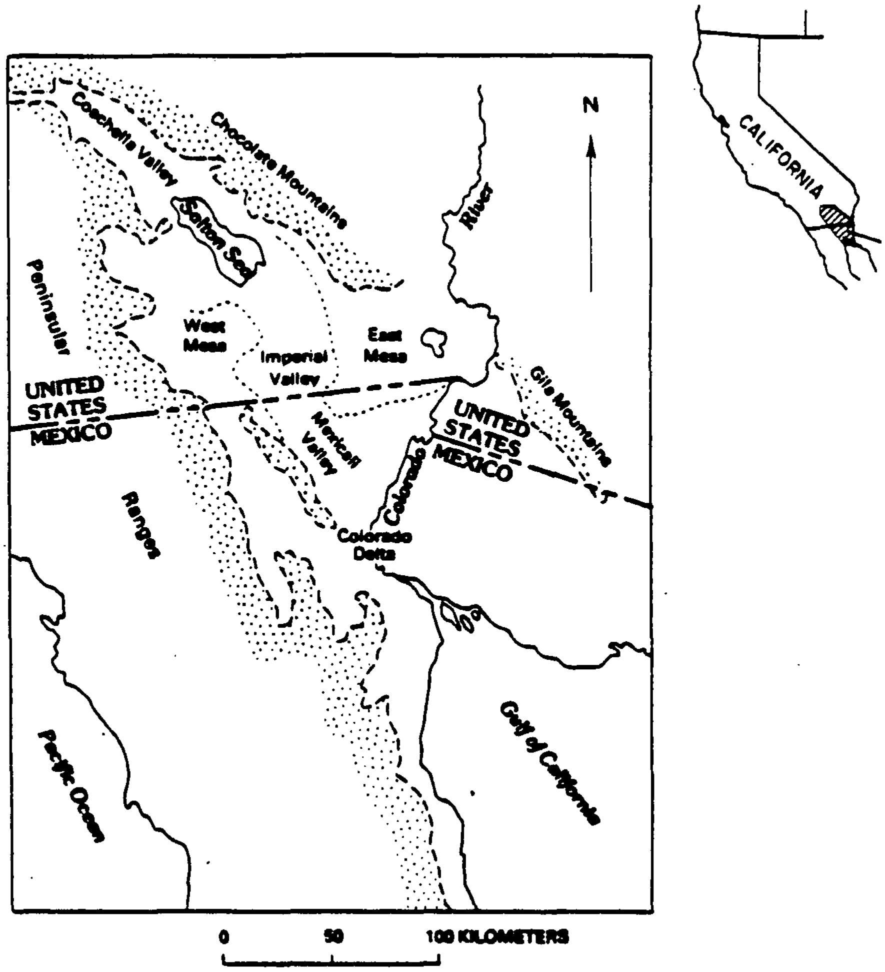

Figure 1. Location of Salton Trough. Surrounding crystalline mountain ranges are stippled. Dotted lines denote approximate boundaries of East and West Mesas of Imperial Valley. From Sharp, 1982.

2. SALTON SEA GEOTHERMAL FIELD

The Salton Sea geothermal field is situated south of the Salton Sea in one of the young pull-apart zones within the Salton Trough. The Salton Sea was formed between 1905 and 1907 when the Colorado River overflowed controlling levees and flowed north into the Salton Basin. The Salton Sea maintains its level because irrigation runoff from the Imperial Valley approximately matches the evaporation losses. Figure 2 shows the location of the SSGF as well as other geothermal fields within the Salton Trough. As an active rifting zone, the trough is an area of high regional heat flow. More than a dozen geothermal anomalies have been found in the Salton Trough, with the SSGF being one of the hottest. The SSGF is also one of the few geothermal areas of the trough showing surface manifestations of heat flow such as hot springs and fumaroles.

Drilling in the area of the SSGF began in 1927 when three wells were drilled to a maximum depth of 1473 feet (Lande and Elders, ed., 1979). These wells produced carbon dioxide commercially from shallow sands as part of the Imperial Carbon Dioxide field until production ended in 1954. The first geothermal production was from the Sinclair #1 well drilled as an oil prospect to 4725 feet in 1957. By 1964, ten more geothermal wells were drilled in the immediate vicinity, beginning with the Sportsman #1 (see Figure 3). All these well produced from hot water reservoirs with steam and brine mixed at the wellhead. The brine is highly mineralized with some wells having 300,000 ppm total dissolved solids.

The sediments of the SSGF are considered a complete sequence dating from early Pliocene. While most of the sediments are detritus from the Colorado river, some erosional runoff is seen from the Chocolate Mountains on the east and the Peninsular ranges to the west. The deltaic deposits are interbedded sands, clays, silts and pebble conglomerates (Elders, ed 1979). These deposits are intermixed with lake sediments. The sedimentary section at the SSGF has been extensively altered by the hydrothermal process associated with the geothermal resource. Thermal springs at the surface provide evidence that, in certain locations, hot brines have penetrated the entire sedimentary column (Younker, et al, 1982). Temperatures up to 365 degrees centigrade have been recorded in the geothermal wells of the SSGF.

The lateral structure of the SSGF is controlled by en echelon faulting with associated earthquake swarms (see Figure 3 for major fault locations). Studies of well information have defined three general depth zones, shown in Figure 4, which characterize the geothermal field (Randal, 1974, Younker, et. al., 1982). At shallow depths there is a low permeability cap rock of variable thickness (750 to 2000 feet). The cap rock is composed of evaporite deposits with anhydrite and carbonate grains dominating. This surface zone serves as an impermeable layer to fluids and as an insulator against heat flow. Below the cap rock is the reservoir rock section. Younker et. al., describe the transition from cap rock to reservoir rock as a "boundary between marine sediments (reservoir rock) deposited in the Gulf of California and lacustrine sediments (cap rock) deposited in the Salton Trough after it was isolated from the southern portion of the basin in the mid-Pleistocene". The porosity and permeability of the reservoir rock is generally assumed to include secondary and fracture induced components (Younker et. al. 1982, Muffler and White 1969). The porosity measured in five geothermal wells within the field was seen to decrease with depth from 25% to 5% over the 2000' to 6000' range (Younker et. al. 1982).

Below the reservoir rock is a zone of major hydrothermal alteration, the altered reservoir rock. Within this zone the porosity and permeability decrease with depth. The transition from reservoir rock to altered reservoir rock is marked by a gradual loss of calcite and a corresponding increase of pore-filling epidote as an alteration product which can evolve into large crystals. These transitions mark the general structure of the SSGF. The structure is fairly well defined by well information within the center of the field. Near the edges of the field, the transitions between cap rock, reservoir rock and altered reservoir rock become more vague. Since the SSSDP is outside of previous drilling on the fringe of the field, a close correlation with these transitions was not expected. Figure 3 shows the location of the SSSDP with respect to other wells in the field.

Geophysical studies have been performed in the SSGF dating back to an early magnetic survey by Kelley and Soske in 1936. The results of these geophysical studies are well summarized by

Younker et al, 1982, who state the following:

(1) The field is associated with a local gravity high, probably resulting from intrusion of dike material, or of hydrothermal alteration of sediment, or both (Biehler et al., 1964).

(2) The field is associated with a magnetic anomaly that probably reflects the presence of igneous material near the surface (Griscom and Muffler, 1971; Kelley and Soske, 1936).

(3) A resistivity anomaly probably reflects the boundary of the saline brine. The conductance of the sedimentary sequence is greatest in the area of the drilled field, but a broad area of high conductance extends along the axis of the valley (Meidav et al., 1976; Kasameyer, 1976).

(4) Seismic refraction data reveal the presence of high-velocity material within 1 km of the surface (Frith, 1978).

(5) Numerous earthquakes indicate that the area is tectonically active (Schnapp and Fuis, 1977).

(6) Interpretations of resistivity surveys, seismic refraction data, earthquake locations, and ground magnetic surveys are suggestive of the existence of several steeply dipping faults within the field (Muffler and White, 1968: Babcock, 1971; Meidav and Furgerson, 1972; Towse, 1975; Gilpin and Lee, 1978; Frith, 1978).

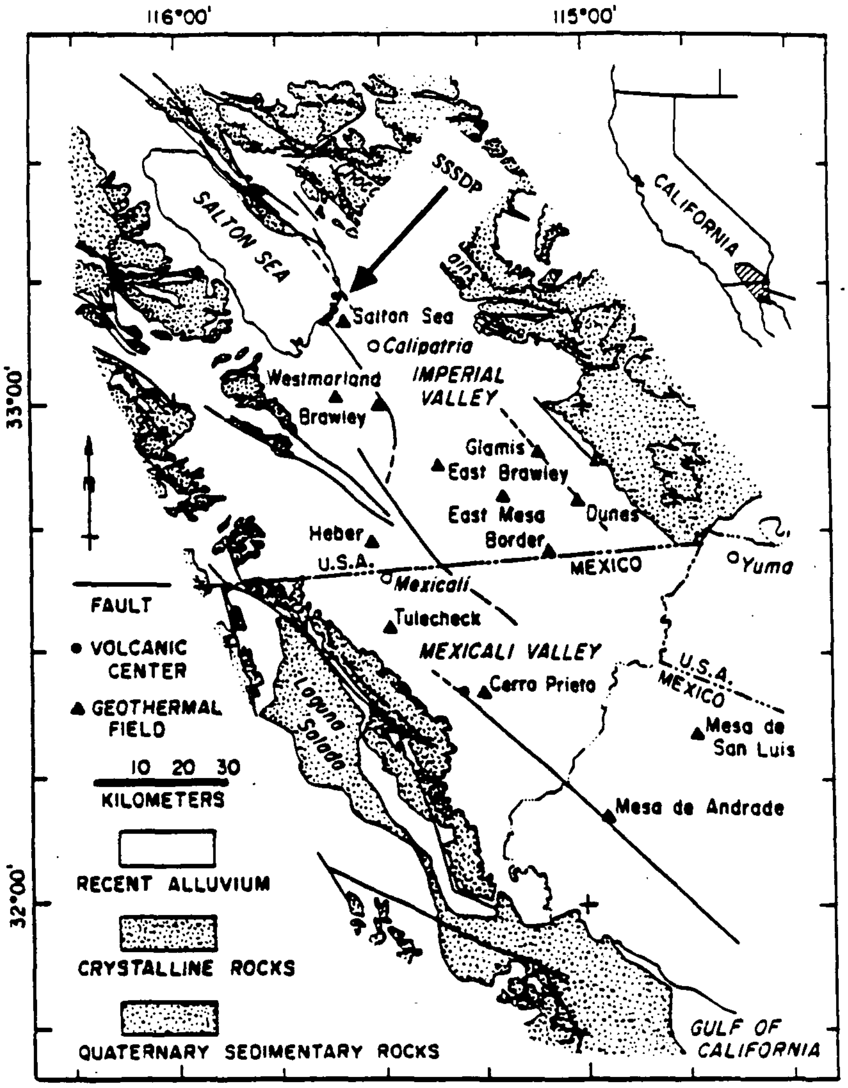

XBL 845-1692

Figure 2. Geothermal fields of the Salton Trough. Arrow indicates approximate location of Salton Sea Scientific Drilling Project. Adapted from Elders and Cohen, 1983.

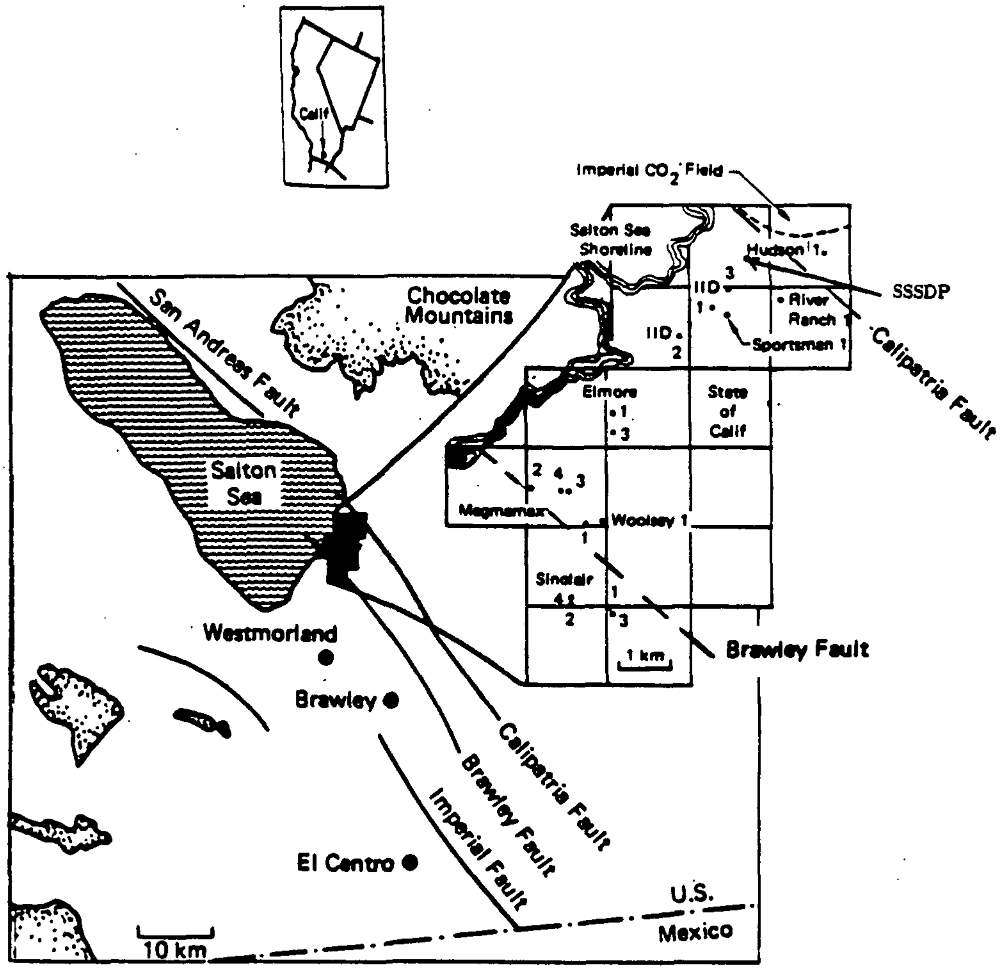

Figure 3. Location of wells and major faults within the Salton Sea Geothermal Field. Adapted from Younker, et al, 1980.

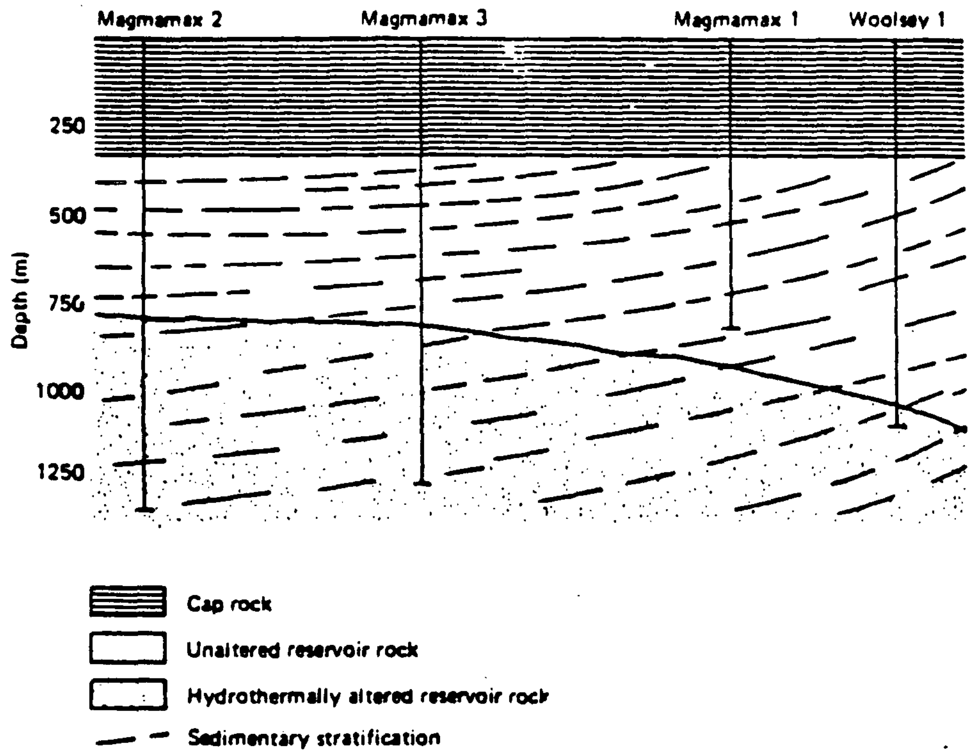

Figure 4. Stratigraphic zones of the Salton Sea Geothermal Field along an East-West cross section. The orientation of strata in the reservoir rock is shown by dashed lines. From Younker, et al, 1980.

3. SSSDP CORES AND GEOPHYSICAL WELL LOGS

The SSSDP VSP was performed after the well had been drilled to total depth. The preliminary results of mud logging, core analysis and well logs are therefore available for consultation. Figure 5 shows the stratigraphic column as interpreted from mud logging and core analysis. As expected, the well penetrated 10,500 feet of sediments consisting of sandstones, claystones, siltstones and some conglomerates. Igneous intrusives were first identified at 9500 feet. Figure 5 also shows where cores were taken and what hydrothermal alteration was noticed. Indications of alteration were actually observed in all the core sections taken, with the shallowest core (1553 feet) being described as "indurated mudstone". Major epidote alteration begins around 4500 feet. Zones of high porosity and permeability were easily identified by loss of drilling fluid circulation while drilling. These zones are identified in Table 1 (from Paillet ed, 1986).

The geophysical well logging included dual induction, natural gamma, spectral gamma, compensated neutron formation density, caliper, sonic, full waveform sonic and temperature. The quality of the logs obtained was generally poor with a number of logs being severly compromised by various problems including temperatures up to 300 degrees C, numerous zones of fluid loss, hole damage from cement plugs and mud coagulation and repeated trips in and out of the well. The sonic logs, which would normally be used in conjunction with the VSP velocity information, had serious problems with repeatability and cycle skipping and are therefore not incorporated with the VSP data. Recent studies comparing velocities derived from the full waveform sonic log with VSP derived velocities for 1500' of the well do show good agreement (Cheng, C.H., 1987 personal communication). Further analysis and processing of the sonic logs may lead to useful results if a detailed velocity profile is required. For reflection seismology, the velocity information provided by the VSP should be sufficient. Use of density logs with velocity information can provide measures of the elastic constants of the material surrounding the well.

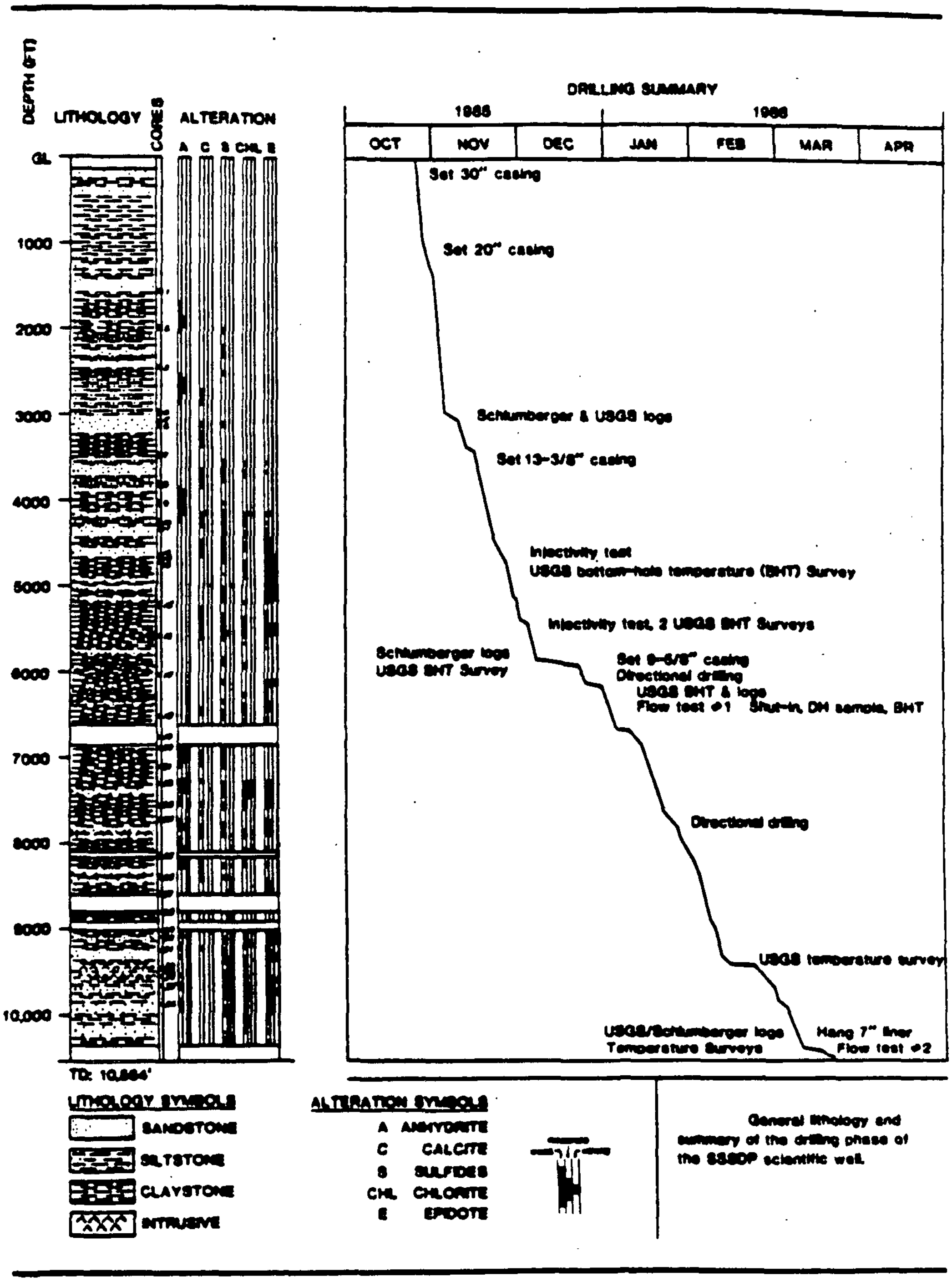

Figure 5. General Lithology and summary of the drilling phase of the SSSDP well. From Elders 1986.

TABLE 1 – LOST CIRCULATION ZONES (FROM PAILLET, 1986)

[ft, feet; bbl/h, barrels per hour; bbl, barrels]

Date	Depth (ft)	Fluid-loss (bbl/h)	Remarks
11/11-12/85	3,107-3,200	-15	Only zone of fluid loss above 6,100 ft
12/22/85	6,119-6,133	-30 to -100	Mineralized zone with epidote fracture fill
12/28-30-85	6,227		Conducted first flow test
1/5-15/86	6,637-6,889	Total	6,637 ft: added additives to drilling mud 6,771 ft: set cement plug 6,850 ft: set second cement plug 6,889 ft: injected cement under pressure, regained circulation
1/16/86	7,030-7,090	-85	Added additives to drilling mud
1/27-29/86	8,095-8,160	Total	Well flowing at depth of 8,126 ft; added combination of drilling-mud additives and cement; regained circulation
2/1-3/86	8,580-8,800	Total	Well flowing at depth of 8,580 ft; plugged with combination of drilling-mud additives and cement
2/4-5/86	8,800-8,920	-100	Losing fluid, yet drilling with returns; well flowed while tripping
2/5/86	8,948-9,020	Total	Plugged with combination of drilling-mud additives and cement
2/7/86	9,098	Total	Plugged with combination of drilling-mud additives and cement
2/10/86	9,254	Total	Well flowing, gained 400 bbl
2/11/86	9,450	Total	Plugged with combination of drilling-mud additives and cement
2/19-21/86	9,450		Cemented hole up to depth of 6,000 ft in four stages
3/9/86	10,450-10,460	-200	Plugged with combination of drilling-mud additives and cement by private contractor
3/9/86	10,475		Drilled without returns to total depth of 10,564 ft
3/17/86	10,564		Conducted second flow test

CHAPTER 3

SURVEY DESIGN AND DATA ACQUISITION

The design of the Salton Sea VSP was based on the objective of studying the seismic wave propagation properties at the well site. The limiting factors were, as usual, time and money. A well is not under control when a VSP is being conducted and any open hole is in danger of being lost until circulation of drilling fluid resumes. The VSP survey can be stopped to allow circulation to be restored, but this is time consuming and therefore expensive. It was decided to limit the VSP to about 40 hours of data acquisition. This time limitation allowed two source locations, a near offset at 300' and a far offset at 2300'. The VSP was also limited by high temperatures and unstable open hole conditions. These factors led to the decision to restrict the survey to the cased section of the well above 5750 feet. To obtain complete seismic information, both a P-wave source and a shear-wave source were used. The P-wave and shear-wave sources were Vibroseis (a trademark of CONOCO Inc.).

The goal of obtaining information about anisotropy and fracturing inferred from anisotropy led to the use of two orthogonal polarizations of shear waves. Two polarizations of shear waves were obtained with one vibrator by rotating it 90 degrees. The sources are labeled differently at the two offsets because of the nature of their expected particle motion (see Figure 6).

The sources labeled SH_r and SV are both generated by having the shear vibrator pad move radially toward and away from the well. The term SH_r is used at the near offset and the term SV is used at the far offset. This terminology is derived from the geometry of the transverse particle motion expected for the first arrival in an isotropic media. The source labeled SV at the far-offset gives an SV type of particle motion (i.e. transverse to the ray path in a vertical plane) because the raypath is not vertical. In other words, since the wave propagation vector of the SV source has a horizontal component, there is a vertical component of particle motion for the propagating shear wave. The source labeled SH_r at the near-offset has a vertical raypath (and vertical wave propagation vector), which means the particle motion is in the horizontal plane. The two near-offset shear sources then are *SH* sources polarized 90 degrees apart, labeled SH_t and SH_r.

The term SH_t is used at both offsets for the source generated by having the shear vibrator pad move transverse to the radial direction. This source motion, in an isotropic material, gives a wave with particle motion transverse to the raypath in the horizontal plane. Figure 6 shows the direction of particle motion expected for each source in an isotropic medium.

The SH_t and SH_r source motions are the same as those labeled *SH* and *SV*, respectively, in surface reflection work. It should be noted that this standard terminology of SH and SV shear waves is strictly valid only for transversely isotropic material with horizontal layering, otherwise the two wave types are not separable. Since the VSP data shows the surrounding material is not transversely isotropic, the simple model of separate SV and SH propagation does not hold. The actual shear-wave first arrivals will be seen to have a complex three-dimensional particle motion. The terms SH and SV will be taken to mean that part of the shear-wave particle motion in the horizontal plane or out of the plane, respectively.

The desire to study the three dimensional nature of the seismic wave field required the use of a three-component borehole geophone. A hydraulic wall-locking mechanism was used for maximum coupling with the well and the surrounding formations. The borehole tool was provided by Seismograph Service Corporation.

The vibrator source sweep was an 8 to 55 Hz upsweep, sixteen seconds long. The choice of sweep was governed by time limitations, the desire to have as broad a sweep as possible while putting maximum energy in the more easily transmitted lower frequencies, and a desire to avoid 60 Hz noise. This 8-55 Hz sweep is also a standard surface seismic sweep which allows the VSP to be integrated with future reflection studies. The P-wave vibrator used for this survey was a Failing Y600 BD with 7.5 tons of output force and the Shear wave vibrator was a Mertz model 13 with 15 tons of output force. The vibrators were provided by Lawrence Berkeley Laboratory and the wireline service was provided by the USGS. The data were recorded on a Texas Instruments DFS-IV 24-channel seismic data acquisition system. Only four channels were actually used, one for the source sweep and three for the borehole geophone's three components. The data were recorded uncorrelated at a two millisecond sample rate with a four second listening time following the 16 sec. sweep.

The choice of offsets was limited by the time available. A near-offset source was necessary to obtain accurate velocity information from vertical wave propagation. The near-offset data are in 50 foot depth intervals. While multiple far offsets were hoped for, only one far-offset data set was acquired because of time limitations and tool failure. 75-foot depth intervals were used at the far-offset, giving less spatial sampling, but using less time. The near offset location was 300 feet from the well, and the far offset was 2300 feet from the well, both on approximately the same azimuth of S45E. Figure 7 shows a schematic of the offsets and a list of the depths surveyed. The offsets' azimuths correspond with the trend of the Salton Trough meaning the shear wave polarizations were approximately parallel and perpendicular to the axis of the trough.

The acquisition procedure was designed for the most efficient use of the available time. The survey was begun at the bottom of the interval to be logged. This is done because the depth measurement is more accurate when the wireline is pulling a tool up the well instead of lowering it down. Starting at depth also reduces the impact of high temperatures since the tool is in the hottest part of the well first and as the well, which was cooled for the survey, begins to heat up, the tool is raised to cooler depths. After the tool is locked in place at a given depth, the wireline is slacked to prevent the resonance of a taught wireline. The downhole amplifier, which gives about 60dB of gain, is then turned on, providing amplification for the analog geophone output before the signal is sent over the wireline. The sources are alternated with one polarization of shear first, then the P source, then the other polarization of the shear source. By alternating the sources, the shear wave vibrator could be turned while the P wave vibrator is running its sweeps or while the tool is being moved up to the next level. Each source had three to ten sweeps stacked per level, depending on signal-to-noise ratio and on the time available.

The VSP was hampered by severe noise problems at the near-offset. The noise problem was worst between 2500' and 4000' and was worse on the horizontal components of the geophone than on the vertical. Possible causes of the noise will be discused in the velocity analysis section. High temperatures in the well stopped an effort to extend the survey to 7100' for the far offset when the tool failed after two levels (7100' and 7000') were recorded with the P source.

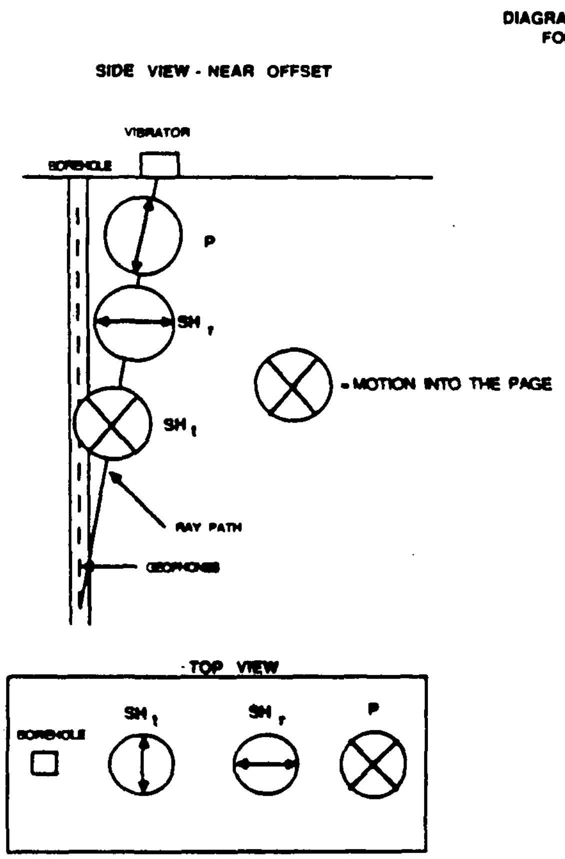

Figure 6. Diagram of expected particle motion for borehole geometry.

VSP SOURCE LOCATIONS

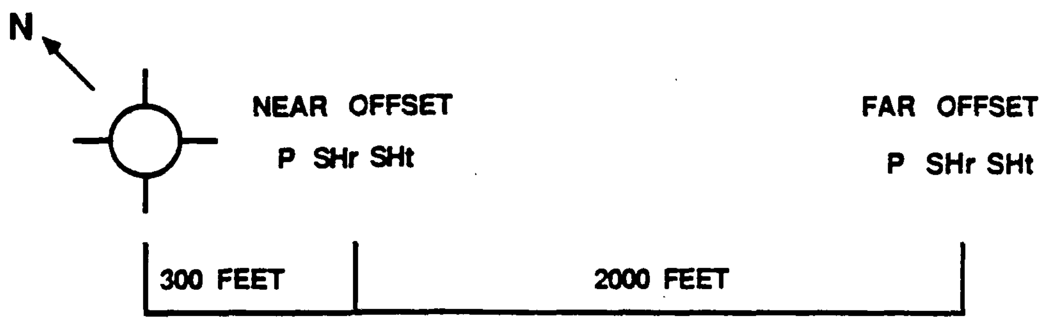

VSP GEOPHONE DEPTHS

NEAR OFFSET		FAR OFFSET	
P	500', 1000', 1500' 1900' - 5650'	P	1500', 1900' 1975' - 5650' 7000', 7100'
SHr	3050' - 5650' 1975' - 5650'	SV	1500', 1900'
SHt	500', 1000', 1500' 1900' - 5650'	SHt	1500', 1900' 1975' - 5650'

Figure 7. VSP source locations and geophone recording depths.

CHAPTER 4

DATA PROCESSING

1. EDITING AND SORTING OF DATA

The goal of the editing and sorting process is to produce sections of each geophone component from each of the sources with the best signal to noise ratio possible. The editing and sorting was performed with Digicon's Interactive Seismic COmputer (DISCO) software. This software package is organized into subroutine modules which can be used in any order. Some further processing and display was performed with specially written FORTRAN routines which will be identified when they are discussed. All processing was done on a VAX 11/780 computer at the Center for Computational Seismology at the Lawrence Berkeley Laboratory.

The first step of processing was to demultiplex the data and extract the four desired channels from the 24 channels of data and 4 auxiliary channels which were recorded. This was done with DISCO's 'DEMUX' routine. The next step was to edit noise out of the uncorrelated recordings. A major noise problem was spikes caused by movement of the borehole geophone while recording. If spikes are left in the data, the correlation process will produce noise at the correlation frequencies across the entire correlated output trace. Ideally, these spikes would be manually edited out with the minimum amount of trace removed. However, the large number of traces to be edited (over 2400 16-second traces) encouraged the development of an automated editing process from various subroutines available in the DISCO package. After experimenting with various arrangements, final editing was done with the following software:

(1) An eight pole Butterworth bandpass filter (DISCO's 'FILTER' module) with 3 dB points at 8 and 55 Hz to match the sweep. This removed any noise outside the spectrum of interest.

(2) DISCO's 'SPIKEDT' routine which looks for noise bursts or spikes in the following manner: Two consecutive windows of user specified length are passed through the data, if the ratio of signal level in the leading window to signal level in the trailing window exceeds a user

specified value, then the leading window is zeroed. The windows are moved one sample at a time for the whole trace. This routine was used with 300 millisecond windows and a detection ratio of four.

(3) A second run of the 8 to 55 Hz Butterworth filter to remove discontinuities caused by the zeroed section of data, and prevent the associated correlation noise.

After this automatic editing, each trace was correlated with a source sweep recorded with every shot. Each correlated trace was visually inspected and either chosen for use in the stacked records or removed from further processing. At this point a few levels were found to have no usable data.

The sorting of the data was done by giving each trace a separate header value for source type and depth. The geophone components were automatically assigned a channel number by the demultiplexing software. The data were then sorted into groups with the same source and geophone component, in order of increasing depth. Once the data traces were sorted in this manner they could be stacked, with all traces having the same source, geophone component, and depth stacked together. At this point the final stacked sections of the original data were available, but full interpretation could not yet begin. A remaining obstacle was the random orientation of the geophone components.

2. ROTATION OF BOREHOLE GEOPHONE COMPONENTS

The data, as recorded in the field, consist of three components of ground motion recorded at each level in the well. These components are oriented orthogonally with one aligned on the tool's axis. When set vertically in a well, the tool has one vertical component and two horizontal components. The orientation of the horizontal components relative to an arbitrary frame of reference is, unfortunately, not known. There are three main reasons for the lack of orientation. The primary problem is the fact that a borehole geophone rotates around its axis on the wireline cable which supports it. This rotation, which occurs while the geophone is moved between levels, causes the horizontal phones to be randomly oriented at each level. A second cause of variation in geophone orientation is the deviation of the well itself, which rarely is vertical. Well deviation can cause a systematic variation in the orientation of all three components as the tool is moved up the well. For wells with significant deviation, a deviation survey is usually run. This survey, if available, can be used to correct the geophone tilt. Thirdly, orientation error is caused by local variations in an uncased well. A severe washout can cause a tilt up to 10 or 15 degrees, depending on how the phone is locked to the wall. This survey was performed in an essentially undeviated, cased section of the well. However, until all borehole geophones are equipped with an orientation device, such as a gyroscope, the lack of known orientation will remain a source of uncertainty in interpretation.

There are various mathematical methods of determining the orientation of a three component geophone at each depth. In general, these methods depend on the assumption that the first arrival is a P-wave, which exhibits linear particle motion. The orientation of the three geophone components with respect to this particle motion can, in theory, be precisely determined. New data can be generated by projecting the particle motion onto any orthogonal coordinate system. This projection or 'rotation' of coordinates can be defined by two angles termed phi (ϕ) and theta (θ), and shown in Figure 8. Phi is the angle down from vertical and theta is the angle counter-clockwise around the vertical axis which is positive upwards. Once these two angles are known, the recorded data can be mathematically 'rotated' to recreate the signal which would have been recorded by geophones at any given orientation.

The 'wavefront' coordinate system which is most often used here is shown in Figure 9. This system has coordinates oriented in the directions that the P-wave, SH-wave and SV-wave first arrival's particle motion would occur for an isotropic material. Since the rotation is based on the angle at which the P-wave wavefront impinges on the geophone, and the curvature of the raypath is not known exactly, this wavefront coordinate system is not accurately defined with respect to the surface. If an assumption can be made that the vertical geophone component is truly vertical, and that the rays stay in one plane, then the wavefront rotation will give an absolute orientation with respect to the surface. For the Salton Sea well, which was cased and had deviation less than 10 degrees over the VSP intervals, the assumption of a true vertical component seems valid.

The method used to rotate the SSSDP data is eigenvalue analysis of the covariance matrix as described by Kanasewich (1981). The first step in this procedure is to pick the first P-wave arrival wavelet at each level. This is actually a non-trivial step since the wavelet may be distorted by signal-to-noise problems, and the particle motion is spread on 3 geophone components. As can be seen in Figures 10a and 10b, the vertical component gives good first arrivals for the near-offset data, but varying wavelet character for the far-offset data. The first arrival window for each level was picked manually with knowledge of the source wavelet and consistent decision making. Tests with varying windows show the method only varied five to ten degrees for any reasonable window.

Once the first arrival window has been picked, the next step is computing the covariance matrix. The covariance matrix is formed from N samples of the three components of data within the first-arrival window. The covariance matrix for three components, call them Z, X and Y, is

$$\begin{bmatrix} \Phi_{Z,Z} & \Phi_{Z,X} & \Phi_{Z,Y} \\ \Phi_{X,Z} & \Phi_{X,X} & \Phi_{X,Y} \\ \Phi_{Y,Z} & \Phi_{Y,X} & \Phi_{Y,Y} \end{bmatrix}$$

where

$$\Phi_{x_1,x_2}=\frac{1}{N}\sum_{i=1}^{N}(x_{1,i}-\mu_1)\,(x_{2,i}-\mu_2)$$

and

$$\mu_1=\frac{1}{N}\sum_{i=1}^{N}x_{1,i}= mean\ of\ component\ x_1$$

for

N observations of component $x_{1,i}$ $i=1,2,3,...N$.

Once this matrix is computed, the eigenvalues and their associated eigenvectors can be found. The eigenvector of the largest eigenvalue is a vector which defines the best fit of linear particle motion within the coordinate system of the geophone components. A coordinate rotation is then defined by using this vector as one new coordinate (called 'Radial') and constraining one new coordinate (called 'SH') to be perpendicular and made up of only the horizontal geophone components. This horizontal constraint assumes the tool is vertical and the 'horizontal' components are truly horizontal. Since the SSSDP well has little deviation, and the VSP was inside casing, this assumption should be quite good. If the well was deviated, a separate deviation survey would be required to properly orient the components. The third new coordinate axis (called 'SV') is simply orthogonal to the first two. The terms SH and SV are used because in an isotropic medium, the SH and SV sources would give first arrivals on these components only.

This eigenvector analysis gives the two rotation angles, ϕ and θ , shown in Figure 8. The new data traces in the rotated coordinate system are computed by the following matrix operation.

$$\begin{bmatrix} R \\ SV \\ SH \end{bmatrix} = \begin{bmatrix} \cos\phi & \cos\theta \sin\phi & \sin\phi \sin\theta \\ -\sin\phi & \cos\theta \cos\phi & \sin\theta \cos\phi \\ 0 & -\sin\theta & \cos\theta \end{bmatrix} \begin{bmatrix} Z \\ X \\ Y \end{bmatrix}$$

The accuracy of the rotation is dependent on the quality of the P-wave first arrival. At some levels the signal-to-noise ratio was not good enough to allow a very accurate determination of the particle motion direction. A measure of the particle motion linearity, which is then also a measure of the accuracy of rotation, is the ratio of the largest eigenvalue λ_1 to the second largest eigenvalue λ_2. Kanasewich suggested forming the rectilinearity function

$$F(\lambda_1, \lambda_2) = 1 - \left(\frac{\lambda_2}{\lambda_1}\right)$$

which will be close to one when the particle motion is linear. This function served as a guide to which levels had noise problems. For some levels with severe noise or dead traces it became necessary to use a θ angle which was an interpolation of nearby levels. In most cases the error of rotation is probably between 5 and 10 degrees. The rotation angles computed for the near-offset P-wave source are given in Table 2, while the far-offset P-wave rotation angles are in Table 3.

For the near-offset data, the P-wave rotation was applied to all three sources. This used the assumption that the shear waves had essentially the same near vertical raypath as the P-waves. For the far-offset data rotation there was a problem. The raypaths were different for P and S waves. The difference is clear because the shear-wave arrival does not show a continuous increase in travel time with increasing depth while the P-wave travel time does increase continuously with depth. This means that the shear-wave rays, particularly for the far-offset SH_t source, turned up at some point and arrived from below the geophone. To accurately rotate the far-offset shear wave data, another rotation method was necessary.

A solution to this dilemma was suggested by the detection of very linear particle motion from the SV source. The particle motion for the first arrival from the SV source was analyzed after the rotation was applied, and it showed linear motion which was rotated off the new 'SV' component by an angle which varied with depth in a consistent manner (see Figure 11). The linear motion implied isotropic propagation, but in that case the first arrival motion should be aligned on the SV component. The angle between the SV component and the axis of the particle motion is interpreted as the error between the P-wave raypath and the shear wave raypath. This 'error' angle delta (δ), is shown in Figure 12. Delta can be found with a two dimensional application of the covariance matrix algorithm to the R and SV components, finding the eigen vector of the larger eigen value of the matrix

$$\begin{bmatrix} \Phi_{R,R} & \Phi_{R,SV} \\ \Phi_{SV,R} & \Phi_{SV,SV} \end{bmatrix}$$

Again, the accuracy of the analysis can be inferred from a rectilinearity function. Delta is then added to phi from the P-wave rotation and the shear wave data are rotated with this new phi angle. The horizontal 'SH' component is not changed since the raypath error is assumed to be in the Radial - SV plane. The error angles and rectilinearity function values for the far-offset are shown in Table 4.

Analysis of arrivals from SH_t and SV sources showed a difference in their raypaths, but no method was known to recover this error angle. The SH_t source was therefore rotated with the same angles as the SV source and these angles are given in Table 5. Fortunately, the error between SH_t and SV raypaths should be much less than the error between P and SV sources since the error comes from differences in the waves' velocity gradients. The effect of the rotation is seen by comparing the plots in Figures 13a, 13b and 13c with those in Figures 33a, 33b and 33c. These figures show the unrotated and rotated data, respectively, from the far-offset SV source. Note especially the difference between vertical and radial components.

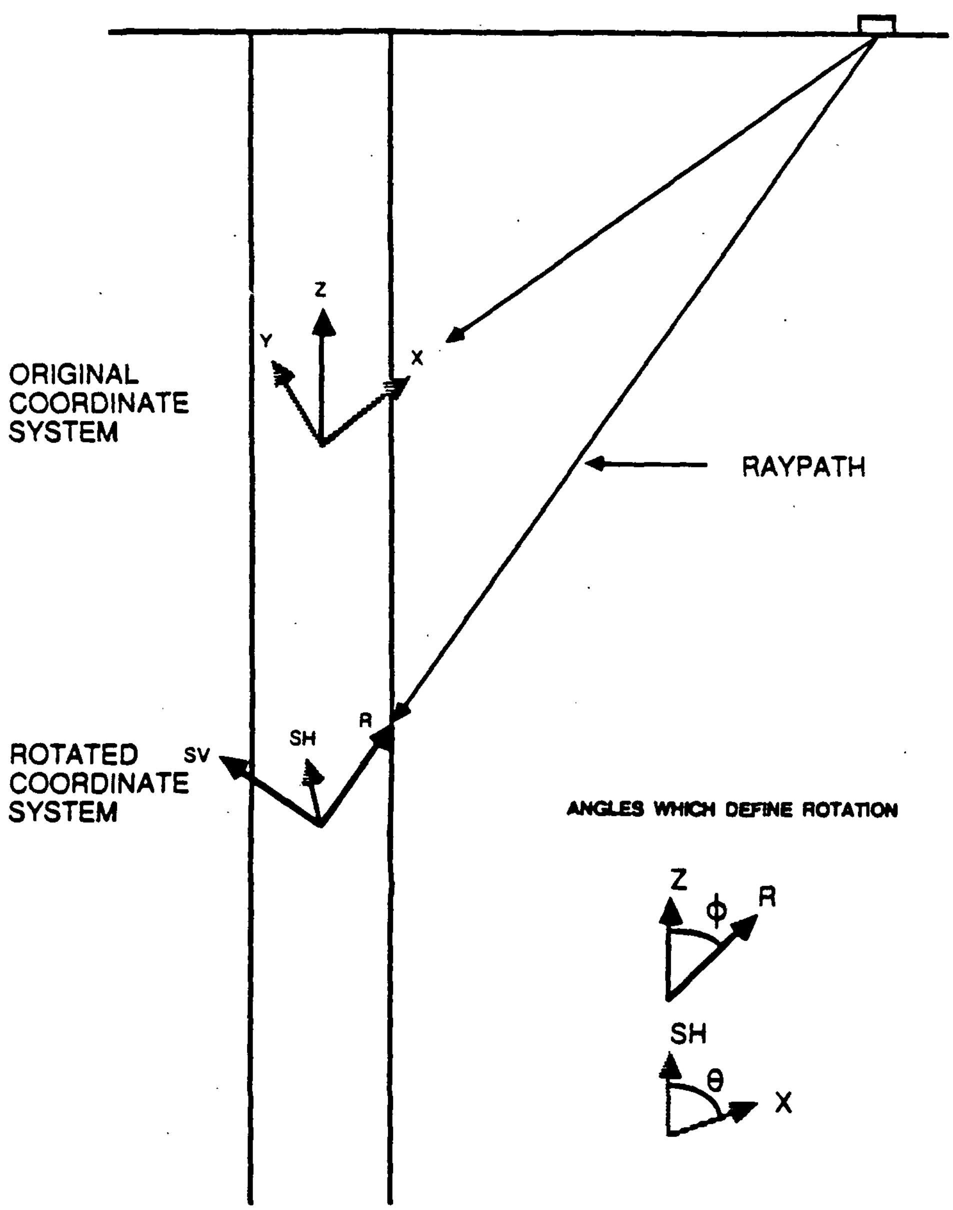

Figure 8. Diagram of coordinate change for 3-component borehole geophone.

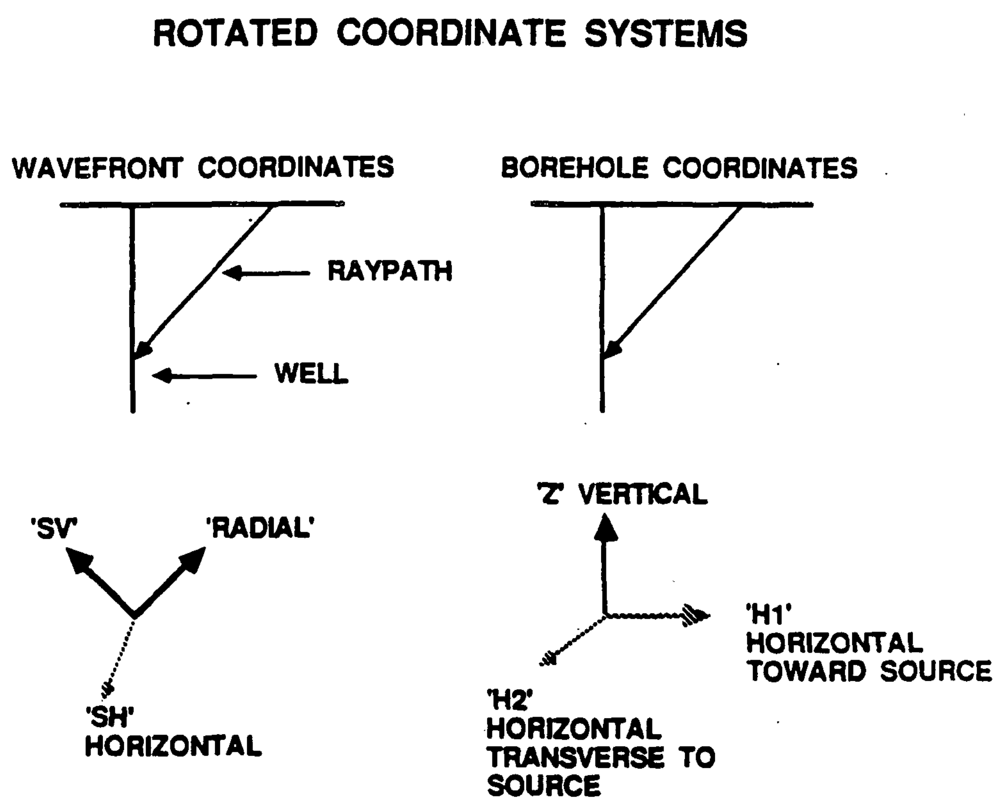

Figure 9. Rotated coordinate systems.

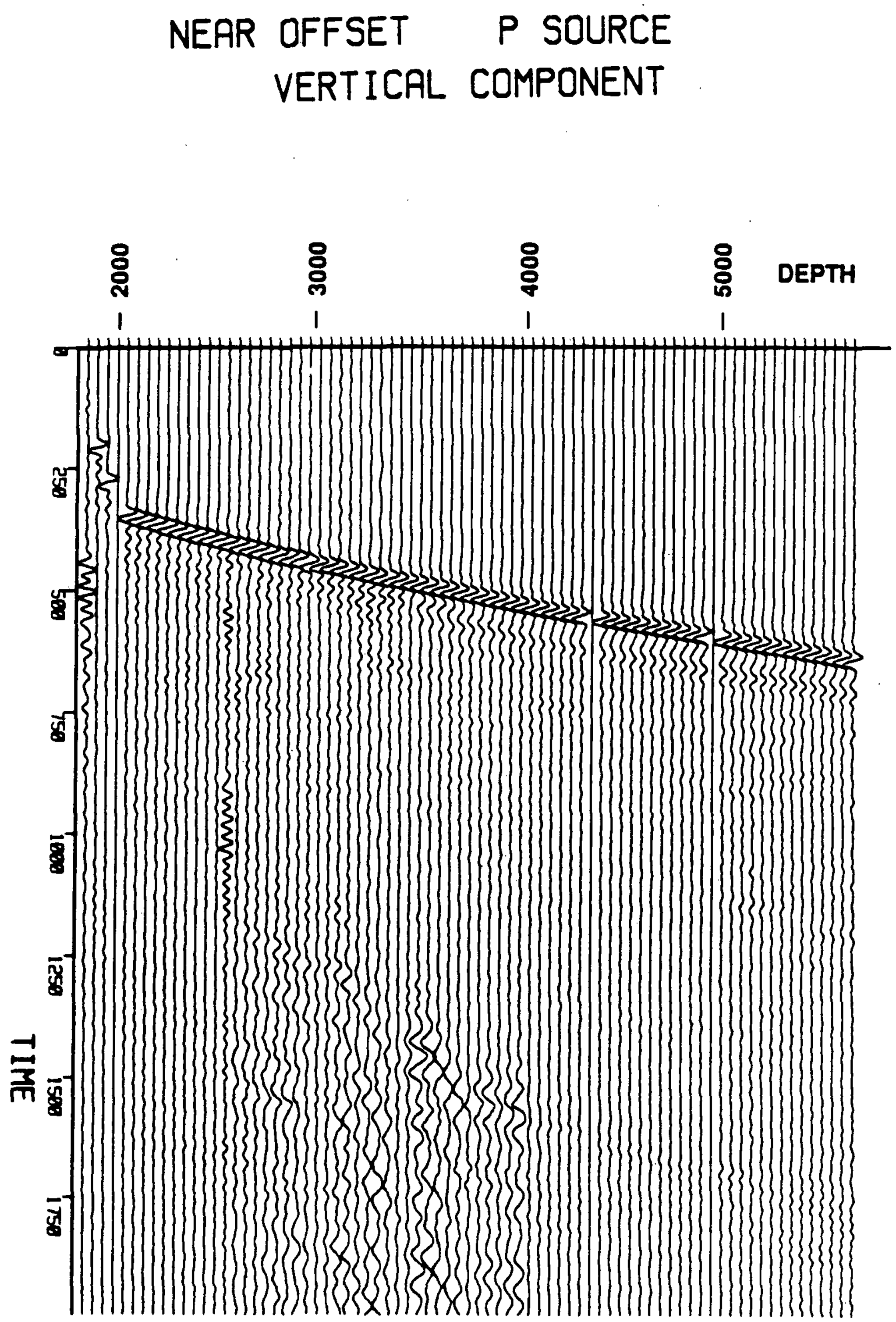

Figure 10a. Near-offset P-source, vertical component data.

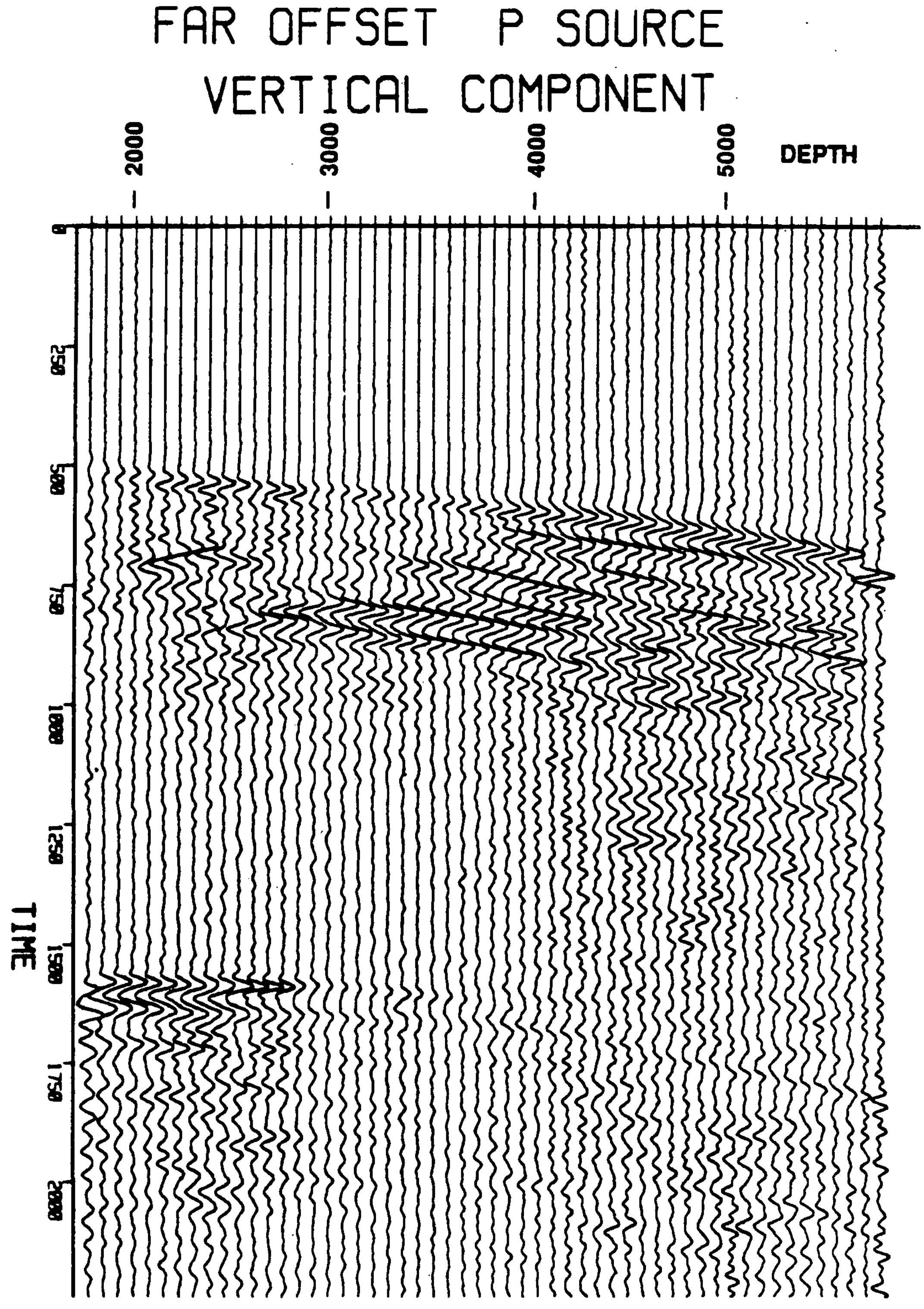

Figure 10b. Far-offset P-source, vertical component data.

TABLE 2 -- NEAR-OFFSET P-WAVE ROTATION ANGLES

DEPTH (FEET)	PHI	THETA	F
500	60.579	147.279	0.908
1000	7.132	-19.796	0.993
1500	11.104	64.536	0.961
2000	0.000	000.000	0.000
2050	4.038	-65.656	0.994
2100	6.193	-91.585	0.995
2150	5.720	-82.885	0.997
2200	4.828	-82.876	0.997
2250	5.245	-80.691	0.998
2300	3.239	-53.519	0.998
2350	4.363	-24.881	0.975
2400	5.755	-92.158	0.993
2450	3.954	54.110	0.997
2500	3.725	51.288	0.997
2550	2.339	115.934	0.999
2600	5.373	-139.374	0.936
2650	5.633	15.498	0.739
2700	2.248	6.415	0.746
2750	7.623	-134.746	0.960
2800	8.633	-23.407	0.964
2850	1.060	-78.807	0.788
2900	7.651	-89.164	0.721
2950	9.361	130.676	0.910
3000	7.700	134.489	0.940
3050	9.553	44.519	0.972
3100	3.763	-99.973	0.658
3150	4.630	68.409	0.987
3200	7.440	-32.903	0.824
3250	9.186	40.631	0.601
3300	1.000	-92.805	0.857
3350	5.256	-82.402	0.757
3400	4.590	100.155	0.810
3450	2.759	131.092	0.989
3500	1.250	151.168	0.999
3550	0.447	79.846	0.995
3600	2.111	146.112	0.959
3650	0.063	90.000	0.994
3700	0.000	0.000	0.000
3750	1.583	0.000	0.999
3800	0.904	46.791	0.995
3850	0.299	24.277	0.999
3900	7.254	-178.143	0.969
3950	0.535	157.853	0.997
4000	2.323	177.621	0.942
4050	5.381	21.630	0.928
4100	4.234	-7.285	0.989
4150	6.525	14.805	0.980
4200	9.714	-107.210	0.594
4250	11.493	-10.757	0.985
4300	14.364	3.000	0.981
4350	0.000	0.000	0.000
4400	13.562	7.044	0.966
4450	13.532	-9.140	0.971
4500	17.004	6.318	0.949
4550	14.600	-5.694	0.952
4600	19.387	-34.096	0.974
4650	18.761	-28.391	0.972
4700	16.382	-24.860	0.964
4750	22.597	-29.523	0.968
4800	20.301	-9.132	0.961
4850	25.567	35.616	0.894
4900	17.533	-6.851	0.931
4950	0.000	00.000	0.000
5000	19.903	-5.031	0.898
5050	15.563	12.542	0.781
5100	11.113	33.339	0.942
5150	7.975	-90.000	0.793
5200	10.394	64.233	0.598
5250	14.594	83.094	0.875
5300	7.543	134.879	0.933
5350	13.110	56.041	0.894
5400	7.206	20.488	0.968
5450	10.110	47.862	0.940
5500	12.575	-62.128	0.292
5550	13.911	95.207	0.700
5600	10.032	92.452	0.925
5650	5.706	105.426	0.901

TABLE 3 – FAR-OFFSET P-WAVE ROTATION ANGLES

DEPTH (FEET)	PHI	THETA	F
1500	77.088	-84.003	0.971
1900	70.276	-77.235	0.982
1975	69.205	-101.205	0.972
2050	71.454	-122.580	0.982
2125	76.687	-47.499	0.931
2200	70.627	-41.886	0.916
2275	74.773	-149.349	0.837
2350	69.564	-145.779	0.886
2425	68.096	-156.307	0.933
2500	68.895	-118.900	0.974
2575	77.160	-140.168	0.976
2650	77.490	-138.849	0.946
2725	69.418	-33.774	0.882
2800	65.892	-165.177	0.769
2875	65.453	-100.951	0.770
2950	75.975	-152.222	0.989
3025	78.982	-168.935	0.983
3100	76.566	-175.589	0.983
3175	66.226	-18.439	0.967
3250	64.517	-6.165	0.889
3325	74.117	-4.679	0.867
3400	72.433	-9.740	0.946
3475	67.130	-8.939	0.973
3550	62.494	-10.725	0.969
3625	59.161	-12.732	0.977
3700	61.511	-15.914	0.977
3775	54.916	-9.147	0.974
3850	56.336	-9.631	0.976
3925	52.965	-12.871	0.939
4000	52.730	-16.583	0.935
4075	48.530	-29.680	0.964
4150	48.307	-27.724	0.860
4225	46.692	-19.999	0.877
4300	49.731	-31.431	0.932
4375	40.992	-19.544	0.841
4450	41.891	-22.343	0.977
4525	45.404	-29.440	0.975
4600	44.565	-29.695	0.993
4675	37.396	-31.343	0.938
4750	44.970	-19.141	0.953
4825	53.079	-23.094	0.795
4900	41.781	-14.542	0.976
4975	3.288	-90.000	0.638
5050	43.262	-10.219	0.899
5125	40.532	-5.561	0.973
5200	24.916	-32.841	0.808
5275	32.724	7.285	0.962
5350	30.775	2.109	0.946
5425	14.342	28.346	0.930
5500	29.084	4.289	0.972
5575	16.568	22.269	0.997
5650	0.000	0.000	0.000

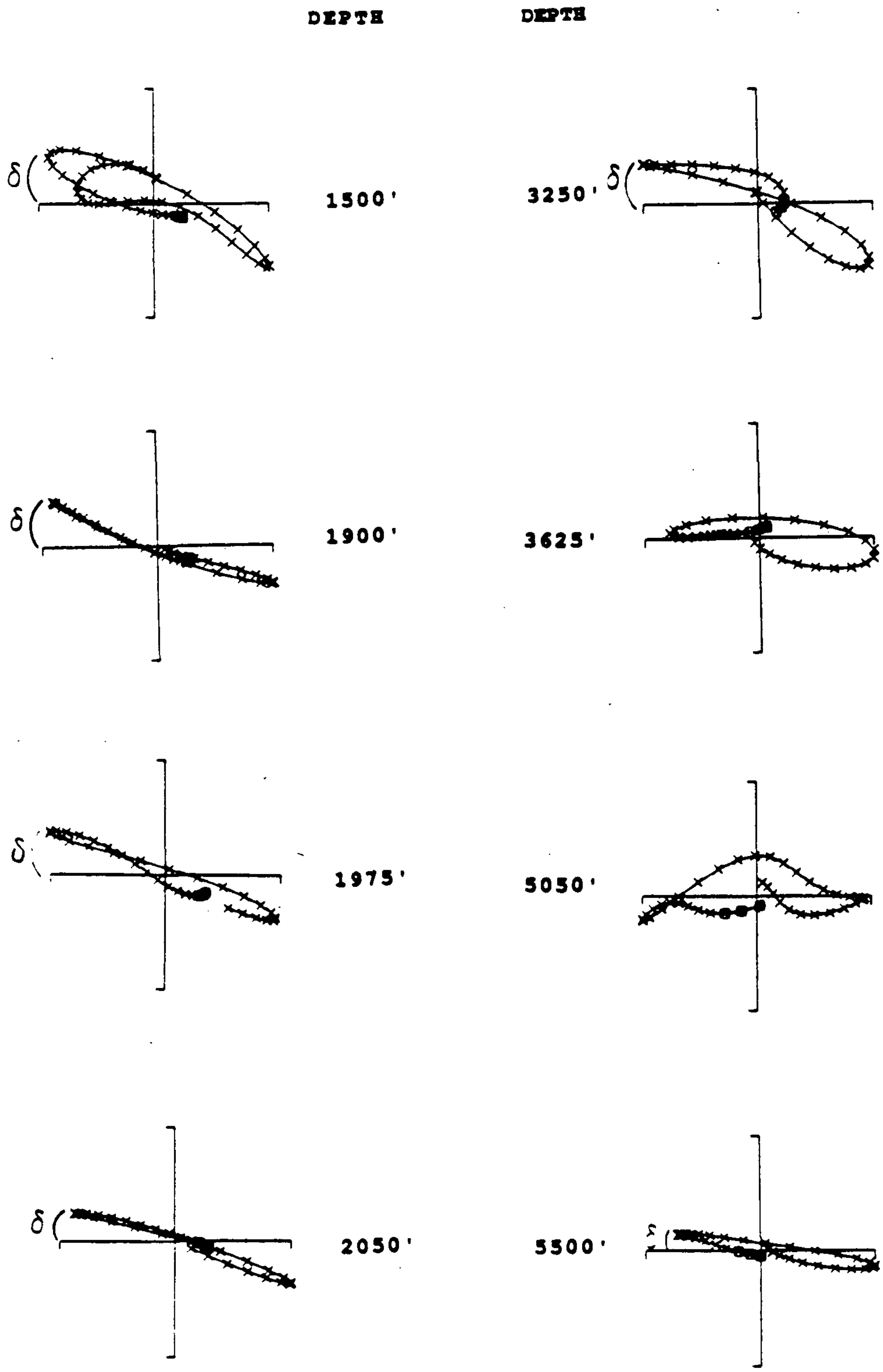

Figure 11. Particle Motion of far-offset *SV* source data. Radial component is on vertical axis and SV component is on horizontal axis.

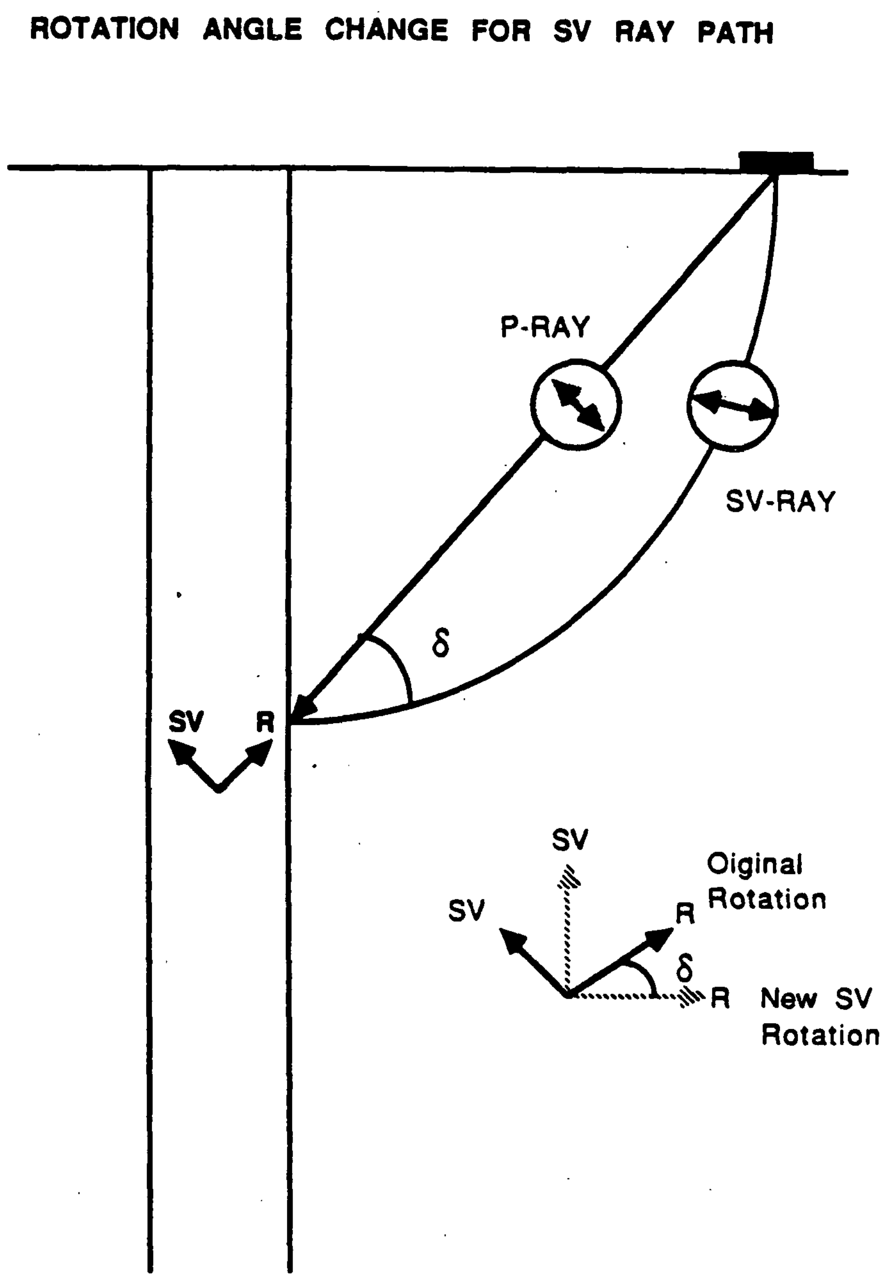

Figure 12. Rotation error angle δ seen between P raypath and SV raypath.

TABLE 4 – ERROR ANGLES FOR FAR-OFFSET ROTATION

DEPTH (FEET)	DELTA	F
1500	-24.271	0.9569
1900	-22.461	0.9759
1975	-22.223	0.9813
2050	-21.592	0.9833
2125	-20.719	0.9764
2200	-19.378	0.9674
2275	-19.062	0.9666
2350	-19.023	0.9652
2425	-19.239	0.9639
2500	-19.933	0.9563
2575	-20.025	0.9441
2650	-20.129	0.9314
2725	-20.138	0.9268
2800	-19.454	0.9259
2875	-19.461	0.9258
2950	-19.263	0.9218
3025	-19.021	0.9186
3100	-18.831	0.9176
3175	-19.028	0.9176
3250	-19.108	0.9178
3325	-19.059	0.9181
3400	-19.050	0.9181
3475	-18.951	0.9175
3550	-18.842	0.9171
3625	-18.700	0.9167
3700	-18.580	0.9168
3775	-18.452	0.9166
3850	-18.320	0.9164
3925	-18.224	0.9163
4000	-18.126	0.9162
4075	-18.043	0.9158
4150	-17.959	0.9154
4225	-17.866	0.9149
4300	-17.777	0.9144
4375	-17.691	0.9139
4450	-17.603	0.9134
4525	-17.506	0.9129
4600	-17.416	0.9124
4675	-17.332	0.9120
4750	-17.238	0.9115
4825	-17.145	0.9108
4900	-17.041	0.9101
4975	-16.973	0.9093
5050	-16.886	0.9087
5125	-16.806	0.9081
5200	-16.741	0.9076
5275	-16.659	0.9070
5350	-16.581	0.9065
5425	-16.518	0.9060
5500	-16.445	0.9054

TABLE 5 – FAR-OFFSET SHEAR-WAVE ROTATION ANGLES

DEPTH (FEET)	PHI	THETA
1500	101.08	-84.003
1900	92.276	-77.235
1975	91.205	-101.205
2050	93.454	-122.580
2125	96.687	-47.499
2200	89.627	-41.886
2275	93.773	-149.349
2350	89.564	-146.779
2425	87.096	-156.307
2500	88.895	-118.900
2575	97.160	-140.168
2650	97.490	-138.849
2725	89.418	-33.774
2800	85.892	-165.177
2875	85.463	-100.951
2950	95.975	-152.222
3025	96.982	-166.935
3100	95.566	-175.689
3175	85.226	-18.439
3250	83.517	-6.165
3325	93.117	-4.679
3400	91.433	-9.740
3475	86.130	-8.939
3550	80.494	-10.725
3625	78.161	-12.732
3700	80.511	-15.914
3775	73.916	-9.147
3850	74.336	-9.631
3925	71.965	-12.871
4000	71.730	-16.583
4075	67.530	-29.680
4150	66.307	-27.724
4225	64.692	-19.999
4300	67.731	-31.431
4375	59.992	-19.544
4450	59.891	-22.343
4525	63.404	-29.440
4600	62.565	-29.695
4675	54.396	-31.343
4750	62.970	-19.141
4825	70.079	-23.094
4900	58.781	-14.542
4975	59.288	-90.000
5050	60.262	-10.219
5125	57.532	-5.561
5200	41.916	-32.841
5275	48.724	7.285
5350	47.775	2.109
5425	31.342	28.346
5500	45.084	4.289

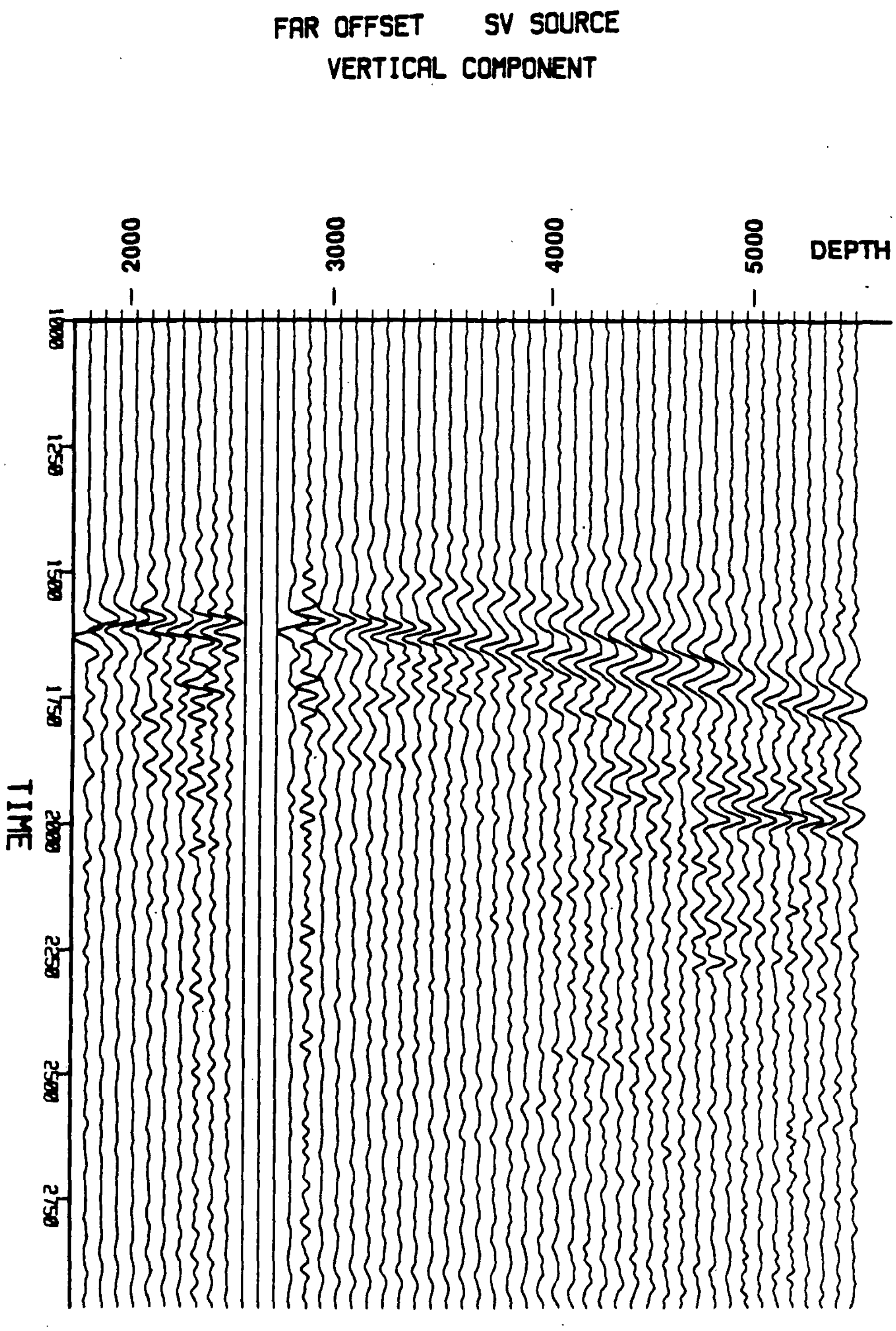

Figure 13a. Far-offset *SV* source, vertical component data.

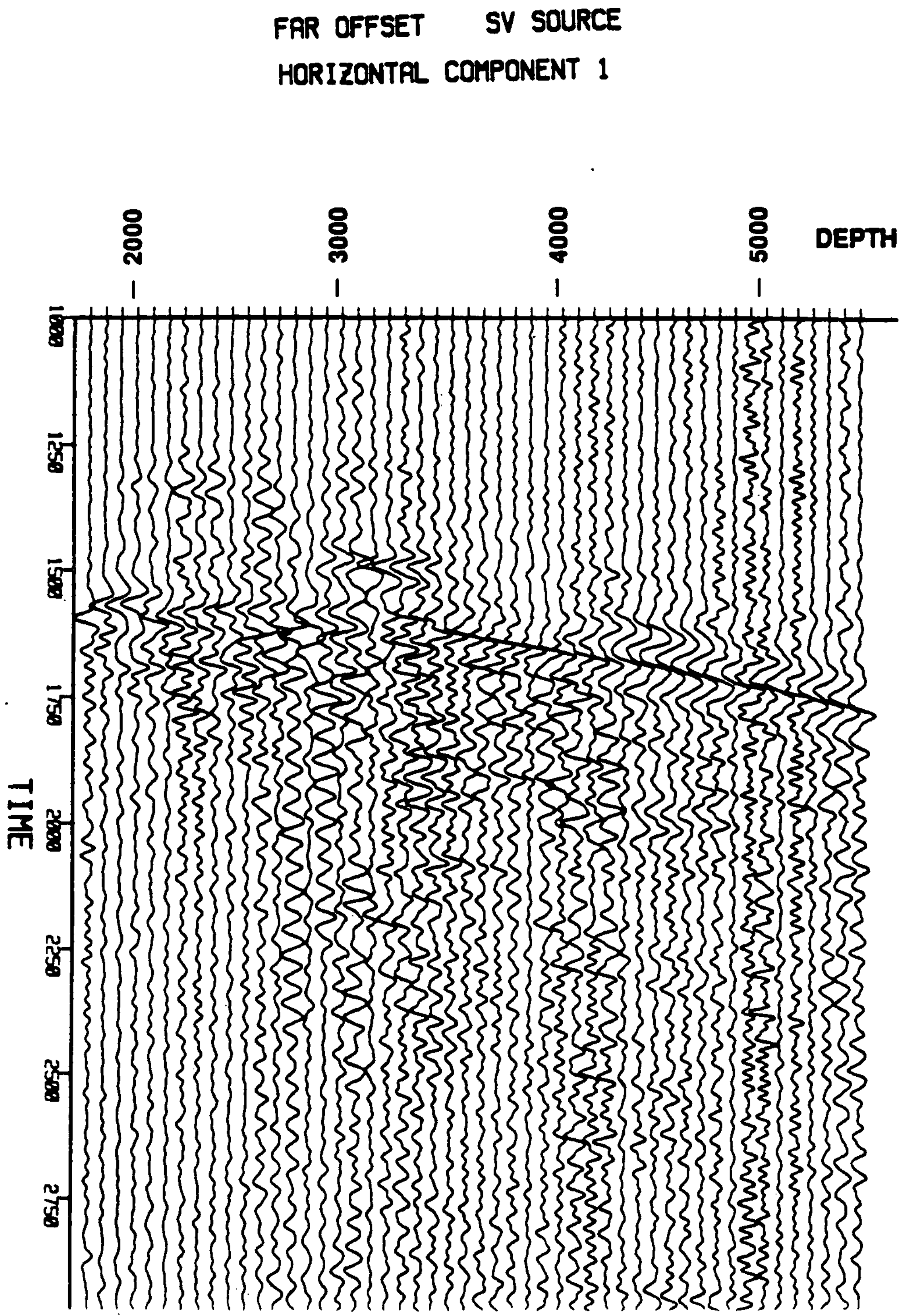

Figure 13b. Far -offset *SV* source, horizontal component 1.

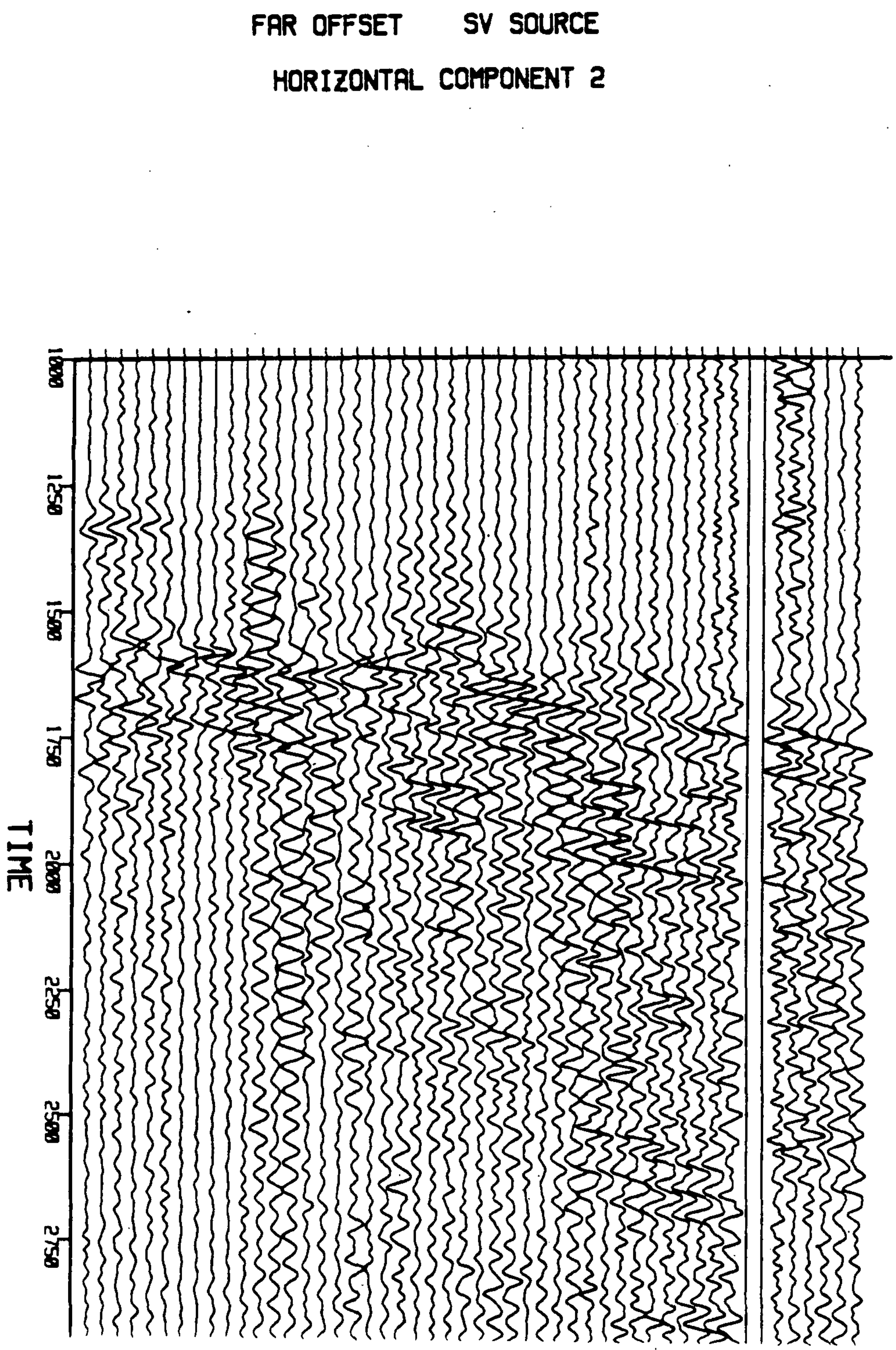

Figure 13c. **Far-offset** *SV* **source, horizontal component 2.**

3. OTHER PROCESSING PACKAGES USED

After the three components were rotated into a consistent coordinate system, more standard processing packages could be used to aid interpretation. One important tool for VSP interpretation is separation of upgoing and downgoing waves. This separation is possible because the vertical receiver geometry gives upgoing waves and downgoing waves opposite apparent velocities across the section. Apparent velocity is seen as moveout or 'dip' of an arrival on the VSP section, and events with differing velocities such as P-waves, shear waves and tube waves will exhibit different dips. A useful tool is some type of dip filter which will attenuate energy with a given dip anywhere on the section. A number of different methods have been proposed and studied for dipfiltering of VSP sections. Two DISCO modules were available for use. One was a user-written module 'DIPFIL', which is a time-distance domain filter. The other is DISCO'S 'COHERE' module which is a frequency-wavenumber domain filter. Tests of these two filters on the same data led to use of the DIPFIL module because of noise generated by COHERE. The filter was applied with a 4ms per trace slope and used a 25 Hz center frequency. The procedure used for dipfiltering included aligning the first arrivals by time shifting all the traces so their first arrival was at the same time. This means the downgoing energy would have zero dip across the section. This improved the filtering process since it was found that the filter works best on events with zero dip. The traces could be shifted back after filtering to preserve the correct time relations. The traces are left aligned when estimating the depth of reflections below the deepest level.

Other processing used standard seismic techniques such as automatic gain control (AGC), bandpass filters (the previously described Butterworth filter with adjustable bandwidth and rolloff), and trace equalization for plotting. Unless stated otherwise, all plots have individual trace normalization using the maximum amplitude on the trace. The particle motion analysis plotting routines used in the anisotropy studies were from specially written FORTRAN codes (HODOS.FOR in Appendix 4) used on the VAX 11/780 with a laser writer for output plots.

CHAPTER 5

DATA ANALYSIS

1. VELOCITY CALCULATION, NOISE PROBLEMS AND ACCURACY

The first step in analyzing the VSP data was calculation of the vertical velocity structure from the travel time of the near-offset first arrivals. The first arrival time was picked on the first peak of the P-wave wavelet and the first trough of the shear-wave wavelet. The shear-wave arrival was picked differently because its trough had consistently better signal-to-noise ratio than its peak. The signal-to-noise ratio of the first arrivals determine the accuracy of the velocity measurements. The quality of near-offset data ranges from excellent for the P-wave source to very poor for sections of both shear sources. Many of the shear-wave arrivals were not coherent enough to pick travel times (see Figure 14). A first arrival pick was only made at those depths where the first arrival wavelet had a consistent character.

The P-wave travel time was picked from the rotated radial component, the SH_t travel time was picked from the rotated SH component, and the SH_r travel time was picked from the rotated SV component. These components were used to measure the velocity of those arrivals having particle motion oriented the same as the source with respect to the raypath. Because of the near vertical raypath, the SV component of near-offset recordings is virtually in the horizontal plane, rotated 90 degrees from the SH component. When calculating velocities, a straight raypath assumption is used to correct the measured depth for the extra propagation distance due to the 300' source offset. The travel time information and average velocity calculations for P, SH_t and SH_r sources are shown in Tables 1-1 and 1-2 of Appendix 1.

Interval velocities were calculated from travel times between depth levels. If the level at the top of the interval was not pickable, the next shallowest level with a pickable first arrival was used. Therefore, at levels where signals were too noisy to pick, the interval velocity is averaged over a larger interval. The interval depth listed is the center of the interval regardless of interval distance. The interval velocities are listed for 100' and 500' intervals in Tables 1-3 and 1-4 of Appendix 1.

Using velocities for P and S-waves, the P/S ratio and Poisson's ratio (σ) could be computed. Poisson's ratio is calculated using the relation

$$\sigma = \frac{1}{2}\frac{\alpha^2-2\beta^2}{\alpha^2-\beta^2}$$

where α is the P-wave velocity and β is the shear-wave velocity. Computations were made using both SH_t and SH_r sources, although the SH_r source has fewer measurements. Interval ratios were computed with the same algorithm as the interval velocities. Table 1-5 and 1-6 in Appendix 1 give, respectively, the average and interval calculations for the P/S ratios and Poisson's ratio. The interval P/S ratios and Poisson's ratio calculations are given for 500-foot intervals. Figure 1-1 of Appendix 1 shows the interval Poisson's ratios for the SH_t source data. The FORTRAN program written to perform velocity and Poisson's ratio calculations, VEL.FOR, is listed in Appendix 4.

Analysis of the velocity data should include consideration of the data quality and the dependability of measurements. Since the P-wave arrivals have uniformly excellent signal-to-noise ratios, the P-wave interval velocities can be considered very precise. The error of the first break pick should be within ±2 ms. The shear-wave data quality is variable (see Figure 14). The SH_t arrivals are good from surface to 2550'; from 2550' to 4000' they are very poor and only a few arrivals were picked. The SH_r first arrivals are poor from 3050', the shallowest level, to 4200'; from 4250' to 5650' the first arrivals are good, with only a few unpickable levels in this zone. Because of the lower frequency content of the shear waves, the first arrival pick is less precise than P-wave arrivals with the same signal-to-noise ratio. The estimated shear-wave travel time error is ±5 ms.

The zone of noisy shear-wave arrivals is caused by large amplitude noise on the borehole tool's horizontal components. In general, the horizontal geophones within a borehole tool are more susceptible to noise vibrations than the vertical component because the weight of the tool tends to wedge it vertically in the well. Also, if the locking-arm is not fully set, the tool may allow horizontal vibrations; if vertical motion is allowed, the tool will tend to slide down the well. The horizontal components of the near-offset P-wave data, which were recorded without relocking the tool, have the same noisy zone.

There does appear to be other noise problems in the SSSDP well. The cement bond log shows a deterioration in the cement bond below 2500'. A poor bond will reduce the signal-to-noise ratio for all the data. A different cause of the noise zone is indicated by the difference in data quality between near-offset and far-offset data. The far-offset shear-wave first arrivals have better data quality at the same depths (see Figure 15). A possible factor is a lower number of sweeps run at each depth for the near-offset sources. There are also indications that a tube wave created low frequency noise coincident with the near-offset shear-wave first arrivals. Figure 16 shows how an event with tube wave velocity (T4), arrives at the same time as the noise begins. Whatever its cause, the poor signal-to-noise ratio of the near-offset shear-wave arrivals reduces the scope and accuracy of data analysis.

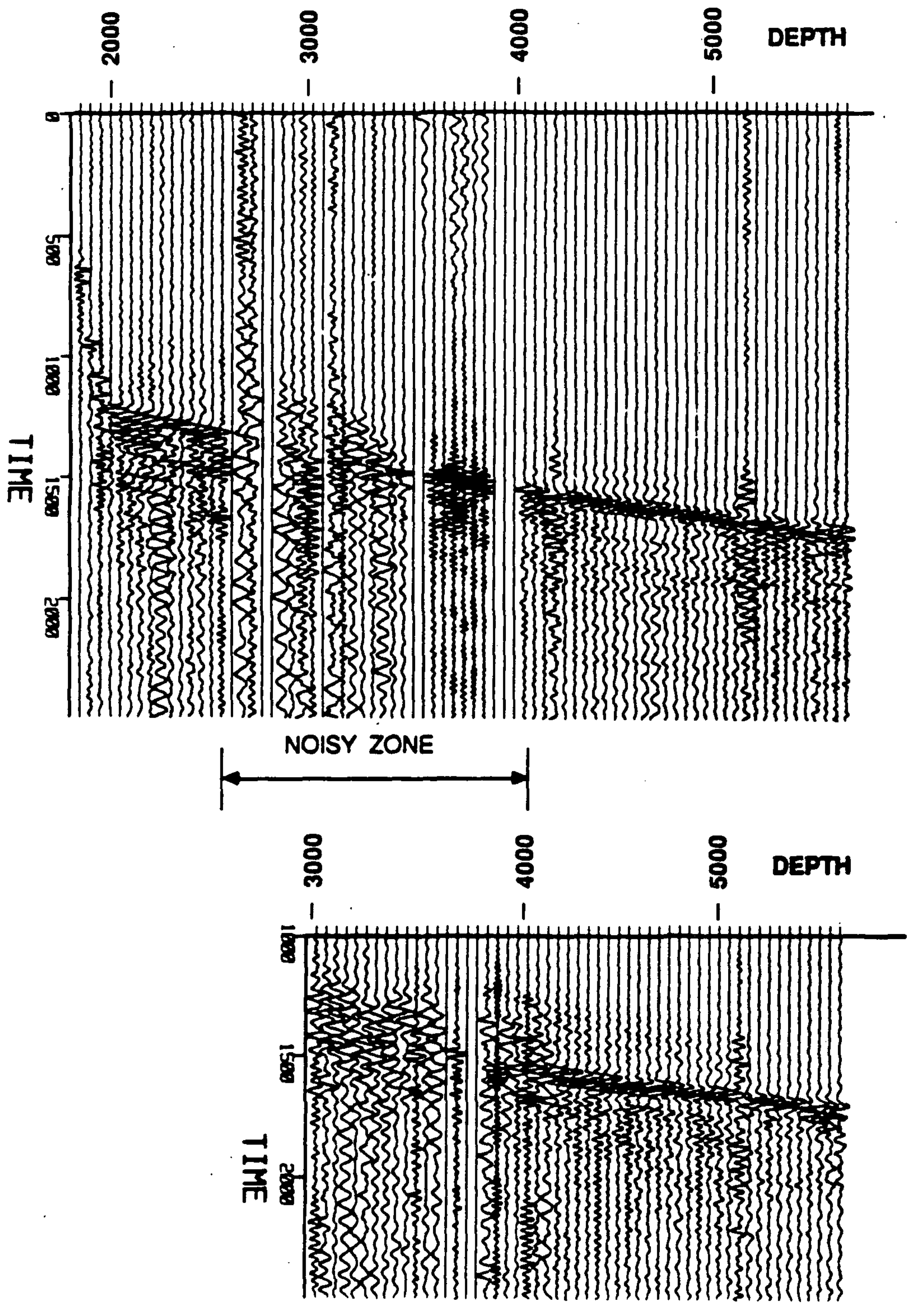

Figure 14. Comparison of near-offset *SH_t* source, SH component data (top) with near-offset *SH_r* source, SV component data (bottom).

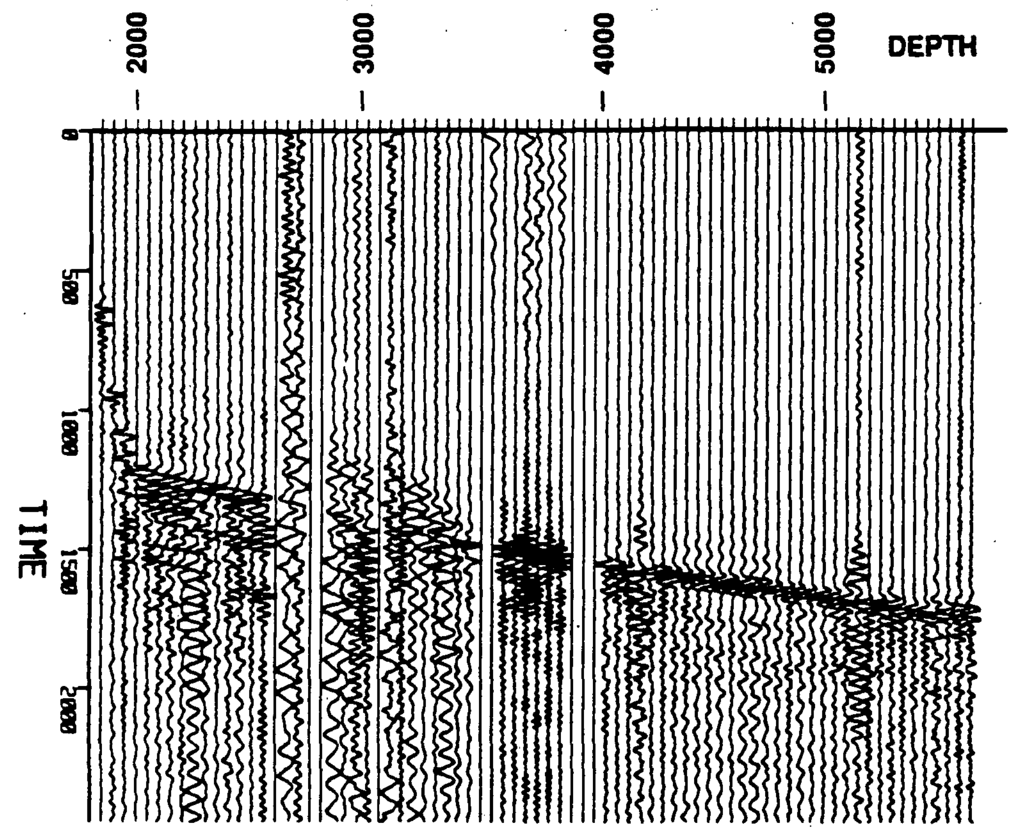

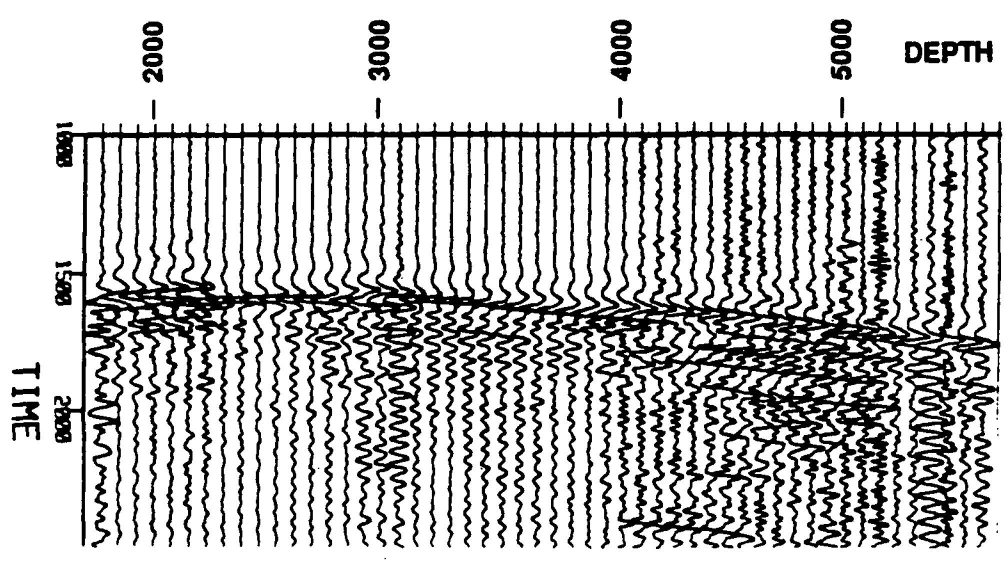

Figure 15. Comparison of near-offset SH_t source, SH component data (top) with far-offset SH_t source, SH component data (bottom).

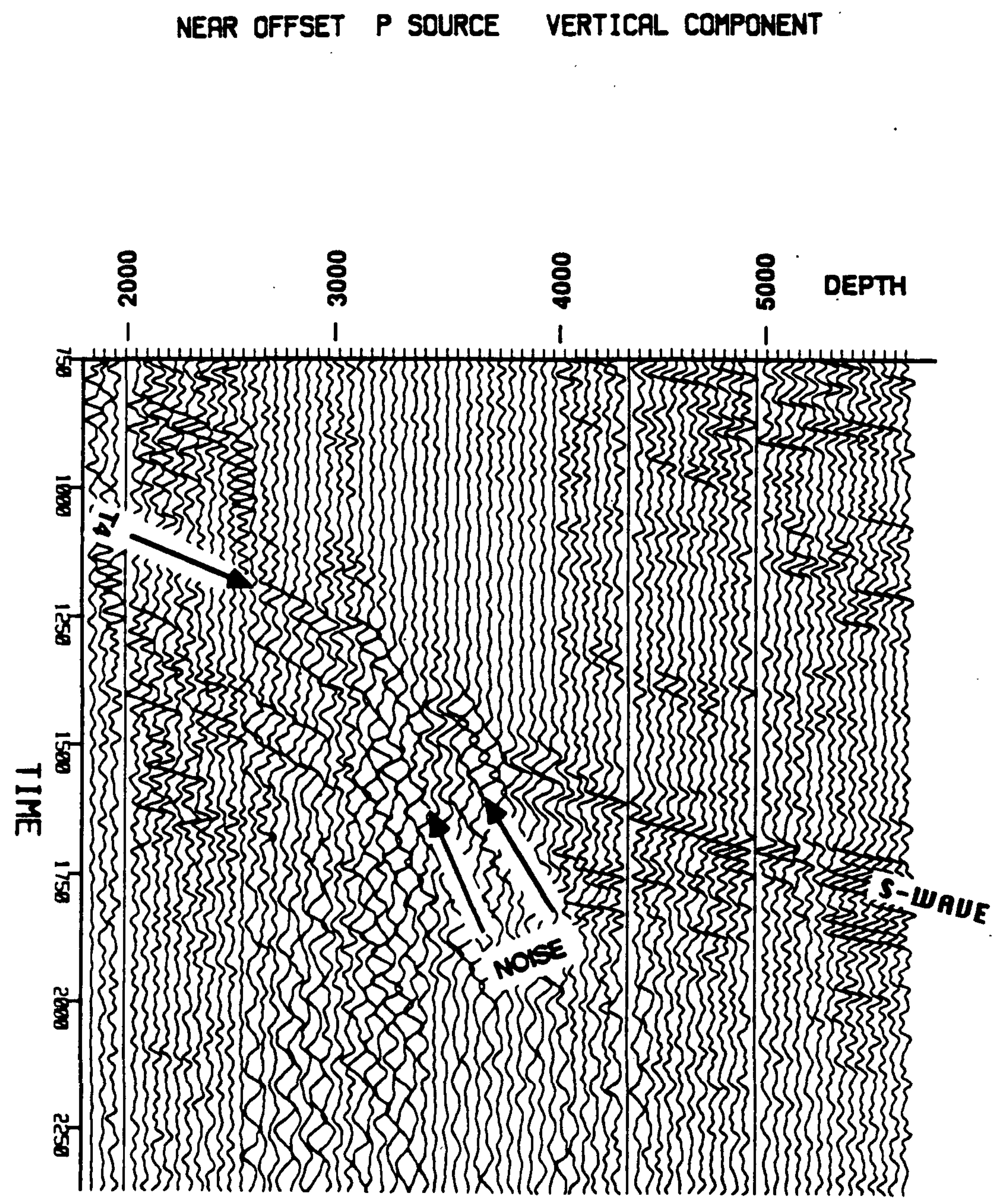

Figure 16. Near-offset P source, vertical component data showing possible generation of noise from a tube wave.

2. VELOCITY MODELING AND RAY TRACING

After computing the interval velocities for both P and S waves, a model could be developed for use in ray tracing. It was desirable to smooth the calculated interval velocities in order to reduce the number of velocity layers used for computation by the ray tracing software. Using the velocities from 100' intervals, zones where the velocity did not show sharp discontinuities were averaged, and models for P and S waves were developed. The S-wave model came from the SH_t velocities. Figure 17a shows the computed interval velocities at 100' intervals and Figure 17b shows the velocity models.

The simplified velocity models were used in ray tracing software to help understand the propagation of the observed arrivals. The ray tracing, shown in Figures 18a and 18b, used an algorithm which propagated straight-rays within each constant velocity layer. The first observation is that the near-offset data do represent vertical propagation for all but the shallowest levels. The far-offset data, however, have strongly bent raypaths caused by the velocity variation with depth. The ray tracing for the far-offset shear waves (Figure 18b) shows discrete changes in ray path for the shallow velocity layers. A change in ray path is the most likely explanation of the change in wavelet character seen at 2275' for the far-offset SH_t source. The far-offset shear waves actually have a turning point and arrive at some depths from below the geophone. This effect is seen on the rotated first arrivals for far-offset SH_t source in Figure 31a which have their earliest arrival at approximately 2800'.

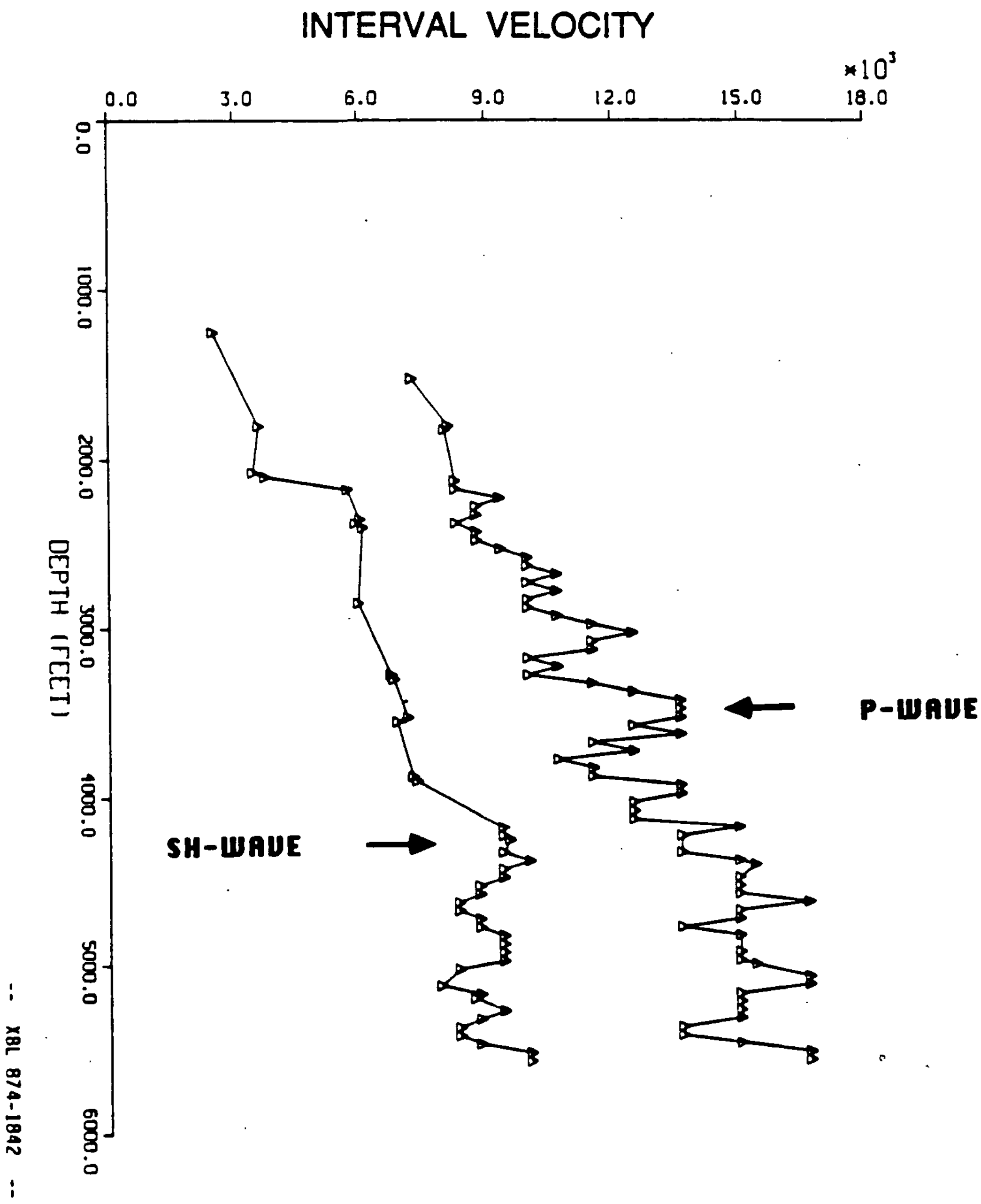

Figure 17a. Interval velocity measurements for P and SH waves.

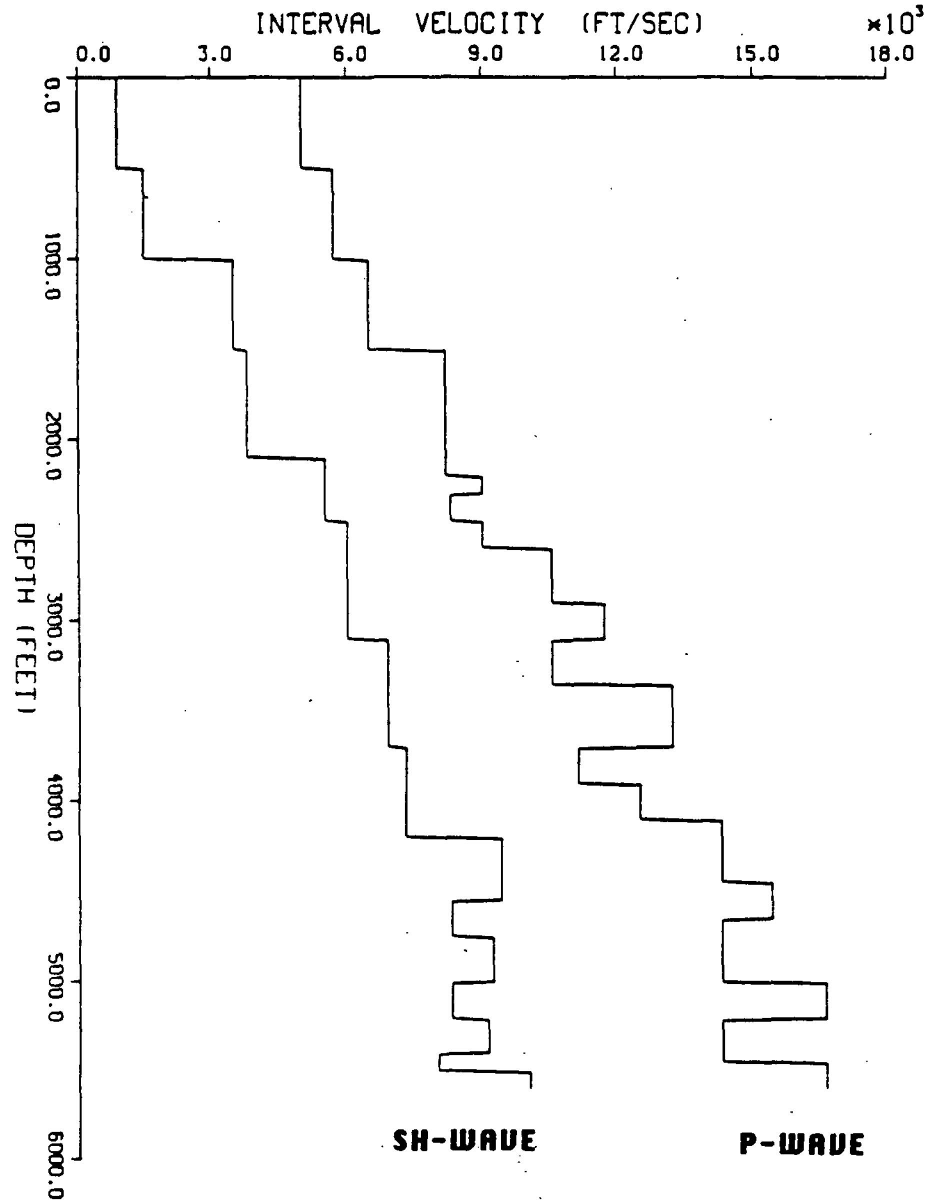

Figure 17b. Velocity models used for ray tracing.

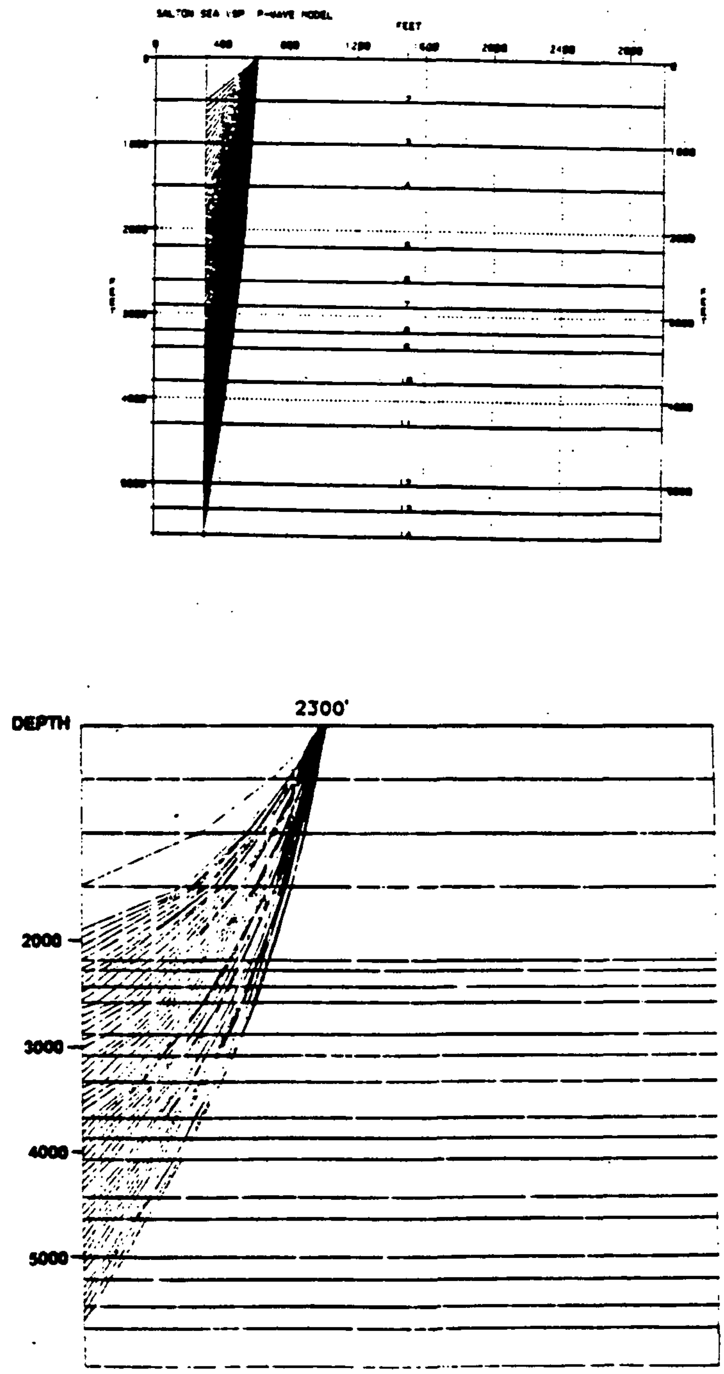

Figure 18a. P-wave ray tracing for near-offset source (top) and far-offset source (bottom).

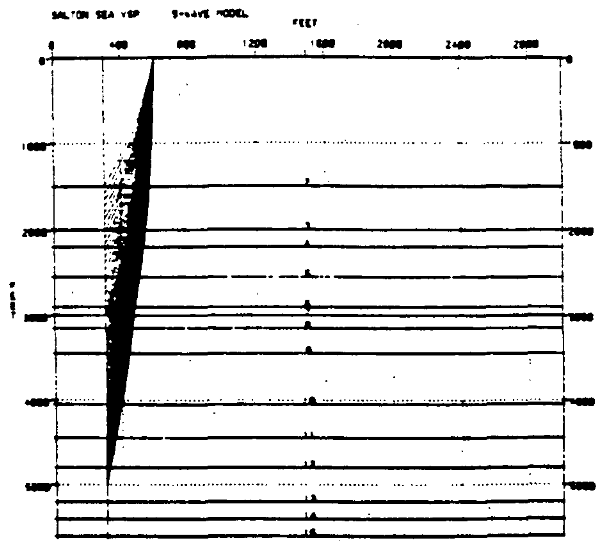

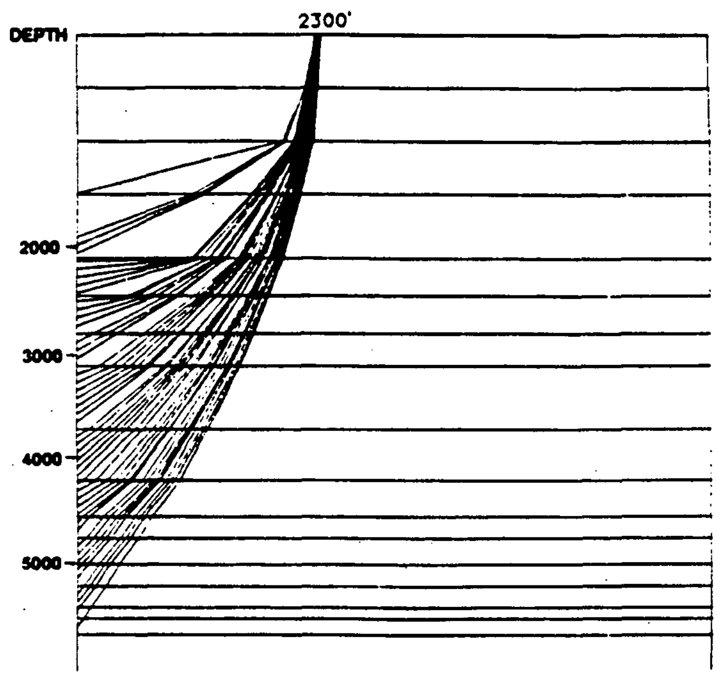

Figure 18b. Shear-wave ray tracing for near-offset source (top) and far-offset source (bottom).

3. EVENT IDENTIFICATION - REFLECTED AND TRANSMITTED ENERGY

3.1. NEAR-OFFSET P-SOURCE DATA

The first data traces to be analyzed for reflected energy were from the near-offset P-wave survey. Figures 19a, 19b and 19c shows the 3 rotated components. The SH and SV components show shear arrivals between 1 and 2 seconds and some P energy between .25 and .75 seconds. The radial component shows the P-wave first arrivals, but their large amplitude has left the rest of the trace uninterpretable because of the trace normalization used. Figure 20a shows a plot of the vertical component of the near-offset P source with AGC. An AGC was applied to enhance the later events and the vertical component was used because P reflections should be traveling nearly vertically. The first arrival is clearly visible as are the numerous downgoing multiples. With horizontal layering, the downgoing multiples will parallel the first arrivals (Balch and Lee 1984, Hardage 1985).

Also identifiable on this section are two tube waves (labeled T1 and T2), the second of which may be a multiple of the first. A tube wave is a low frequency, dispersive, Stoneley wave which propagates in the borehole fluid and decays exponentially away from the well (Toksoz and Stewart, 1984). The tube wave's average velocity was computed to be 4800 ft/sec, slower than P or shear waves. The zero frequency velocity of the tube wave (V_T) is related to the fluid velocity (α_1) and fluid density (ρ_1), and the surrounding rock's shear velocity (β_2) and density (ρ_2) by the following relation (Hardage, 1985):

$$V_T = \left[\frac{1}{\alpha_1^2} + \frac{\rho_1}{\rho_2 \beta_2^2} \right]^{-1/2}$$

Tube waves can be analyzed for the information they provide through velocity, attenuation and particle motion as well as depth of generation (Toksoz and Stewart 1984, Biot 1952, Cheng and Toksoz 1981, Hardage 1985, Huang and Hunter 1981). The strength of the tube waves observed in the SSSDP VSP indicates further analysis could be profitable, however a thorough study of the tube waves is outside the limits of this paper.

Other identifiable events on Figure 20a include a shear-wave arrival which seems to have an associated reflection. There are suggestions of P-wave reflections, but they are mostly obscured by the downgoing energy. The enhancement of upgoing reflected energy is the next step.

To emphasize the reflected energy, a dipfilter was applied which attenuated downgoing events and therefore enhanced the upgoing events. The dipfiltered vertical component section is shown in Figure 20b. Here the previously identified events stand out, but also seen clearly is reflected energy, labeled event E, from below the deepest level at 5650. Event E is clearly the strongest reflection and it is impossible to say if the later events are multiples or separate events, but a strong reflection is likely to have associated multiples. As can be seen, the central section of the data, from 3000' to 4000', is apparently blank. This effect is caused by the high amplitude noise associated with the shear arrival between 1250ms and 1500ms. The traces are normalized to the highest amplitude so the earlier, lower amplitude arrivals are not clearly visible. Fortunately, the noise is dominantly low frequency, so a high pass filter will reduce the noise. The highpass filtered section is shown in Figure 20c.

An estimate can be made of the depth at which a reflection is being generated. The procedure is to project the event down the section until it intersects a first arrival (the first arrivals can be aligned at one time, or not aligned, but the analysis is easier if they are aligned). The depth at which the projected reflection event intersects the first arrivals is the depth of generation (Hardage, 1985). If the reflection is from below the deepest level, this procedure assumes a constant velocity between the deepest level and the depth of reflection generation. Figure 21 shows the results of this interpretation. Event E has an estimated depth of generation of 7000', the later event F is estimated at 7600'. Event D is not a very coherent reflection because it only appears strongly on four traces, however it does have the moveout of a reflection and its depth of generation is estimated at 6650'.

The depth of generation of the tube wave can be identified in the same manner, except it is projected up the well. The estimated depth of tube wave T1 generation is 1800'. The second tube wave, T2, is estimated to be generated 500' above the surface, meaning the estimate is wrong by 500' and it then may be generated by surface waves incident on the borehole, or it is a multiple of the first tube wave. Another tube wave, T3, is apparently being generated by the shear wave at about 3000' although this may be a simple tube wave multiple.

Other identifiable events include a shear reflection, event G, being generated at approximately 4100'. This reflection appears to be a mode-converted P-wave. The evidence for this interpretation is the apparent velocity of the reflection. The estimated velocity of the reflection between 2000' and 3000' is 10,500 ft/sec while the measured P-wave velocity in this zone is 9,700 ft/sec and the shear wave velocity is 6000 ft/sec. Allowing for error in estimating the reflection velocity, event G appears to be P-wave energy. Also seen on this section are P reflections generated at approximately 2900', 4400', and 5450', labeled R2, R3 and R4 respectively.

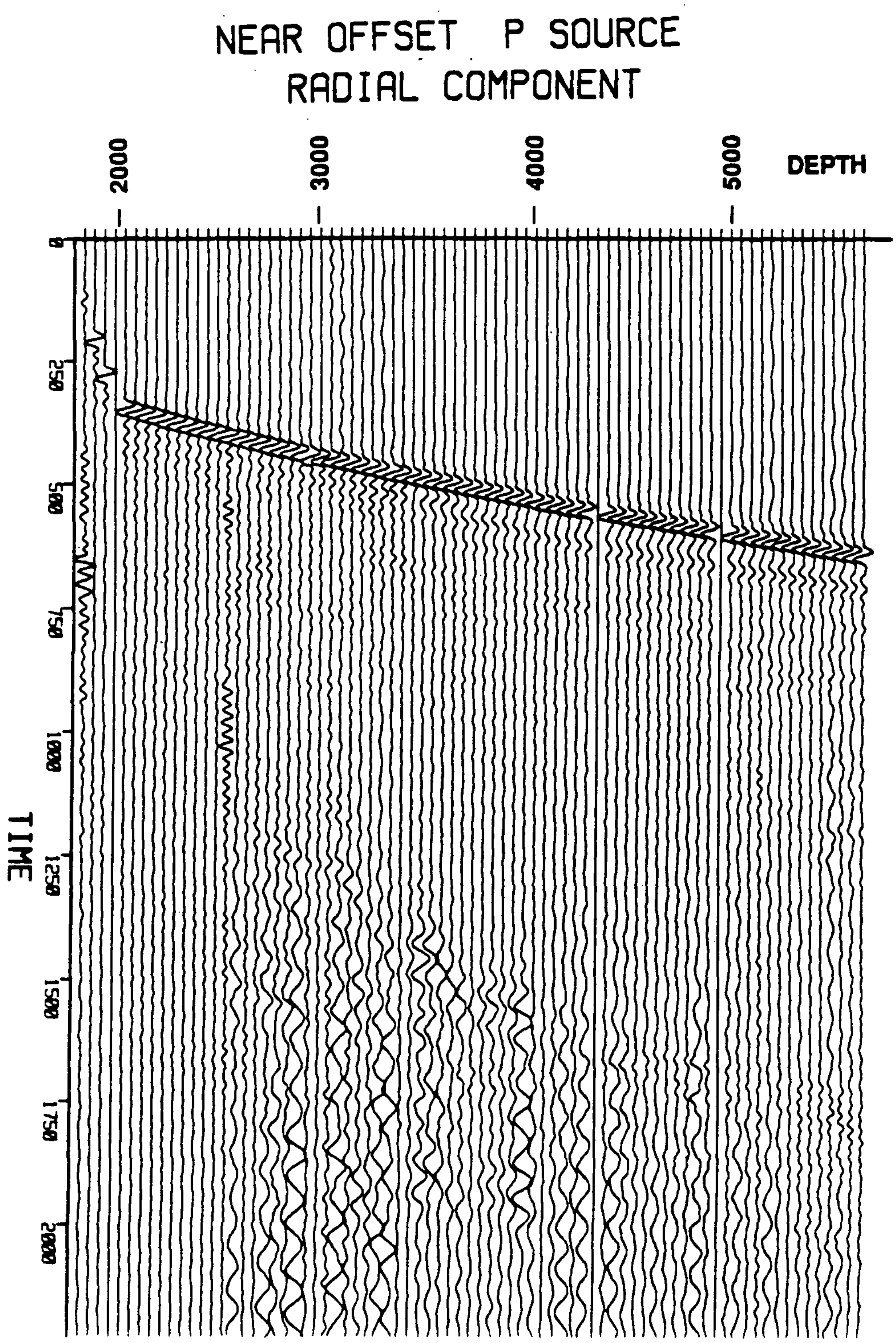

Figure 19a. Near-offset P source, radial component data.

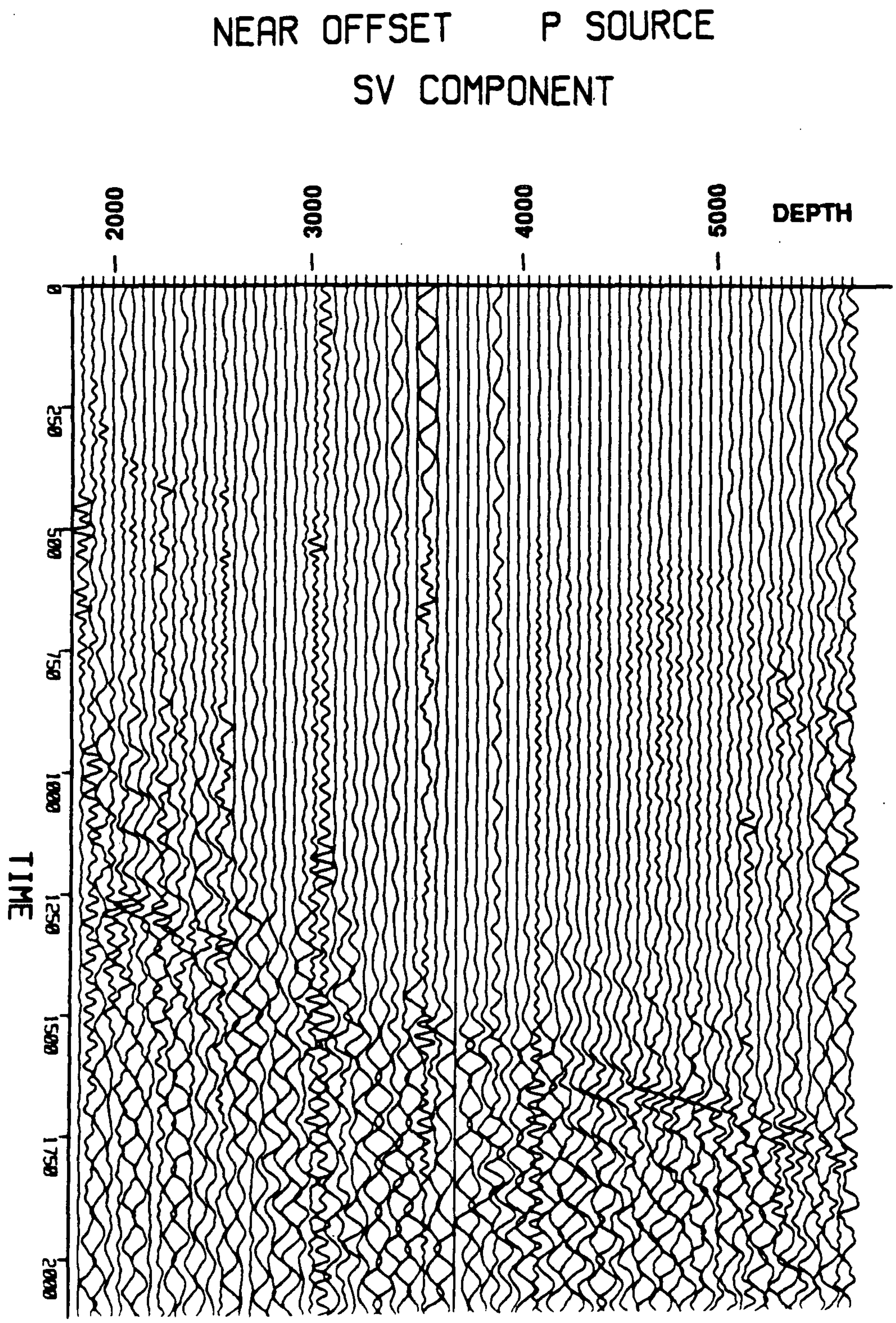

Figure 19b. Near-offset P source, SV component data.

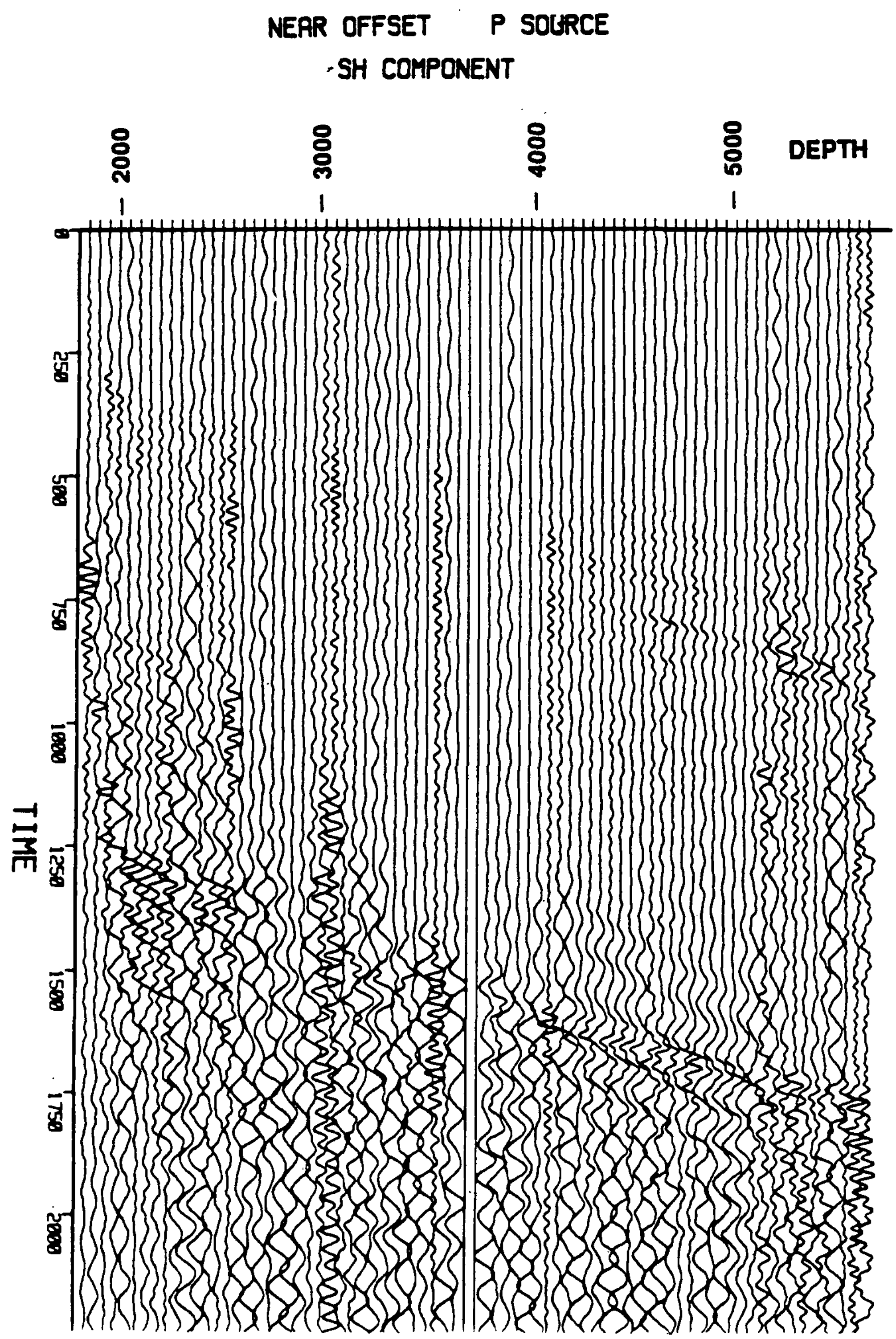

Figure 19c. Near-offset P source, SH component data.

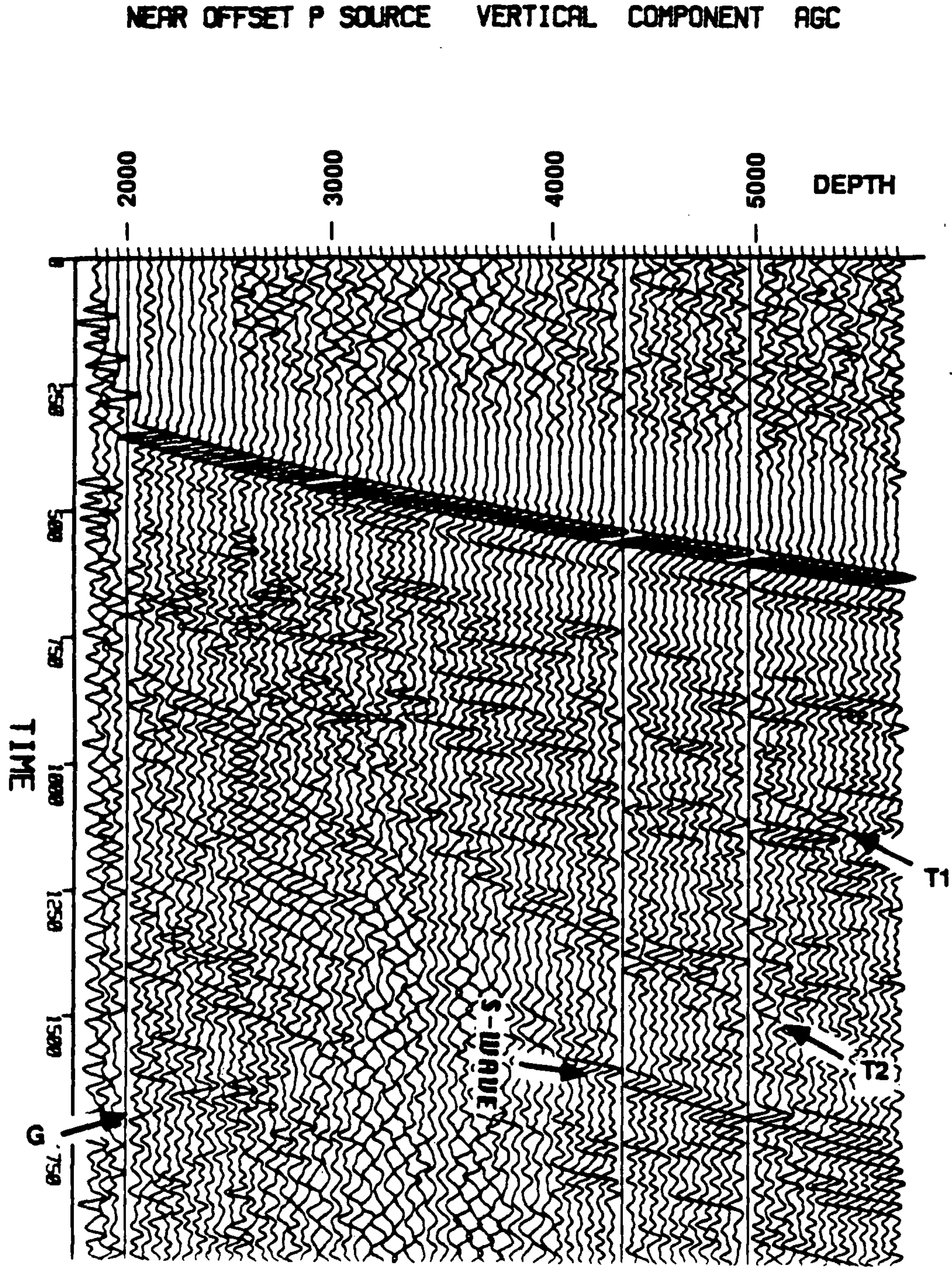

Figure 20a. Near-offset P source, vertical component data with AGC.

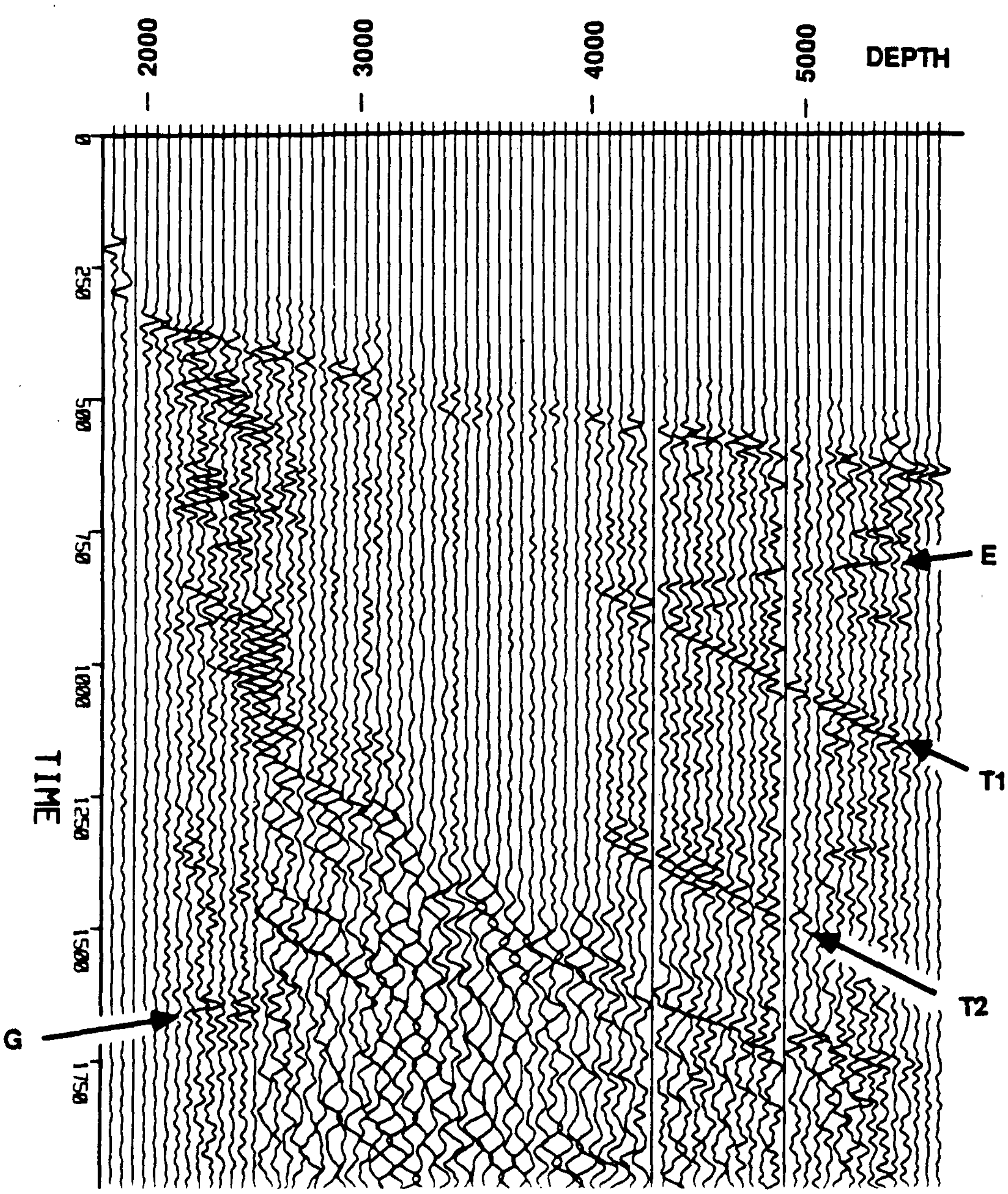

Figure 20b. Near-offset P source, vertical component data, dipfiltered.

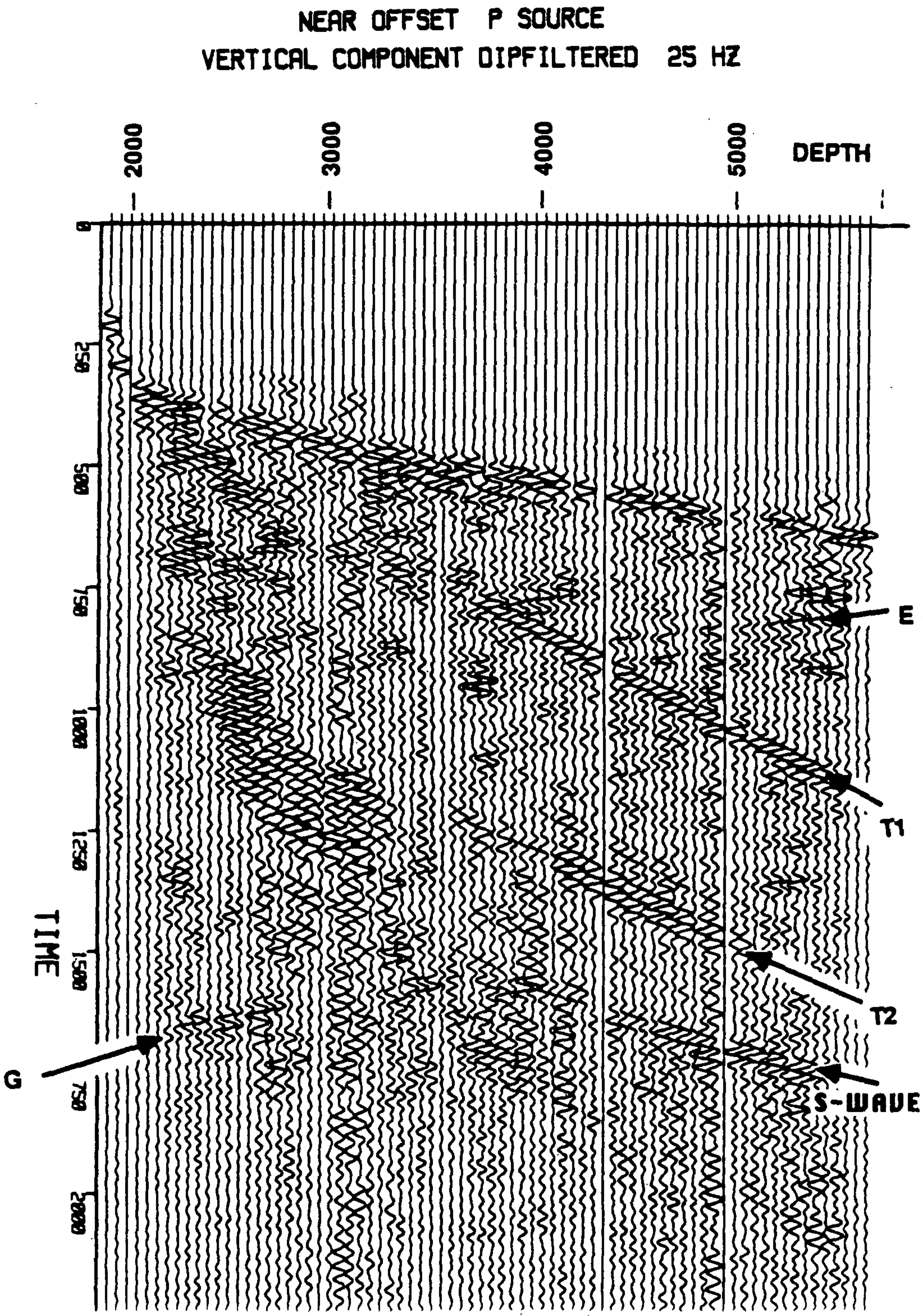

Figure 20c. Near-offset P source, vertical component data, dipfiltered with 25 Hz high pass filter.

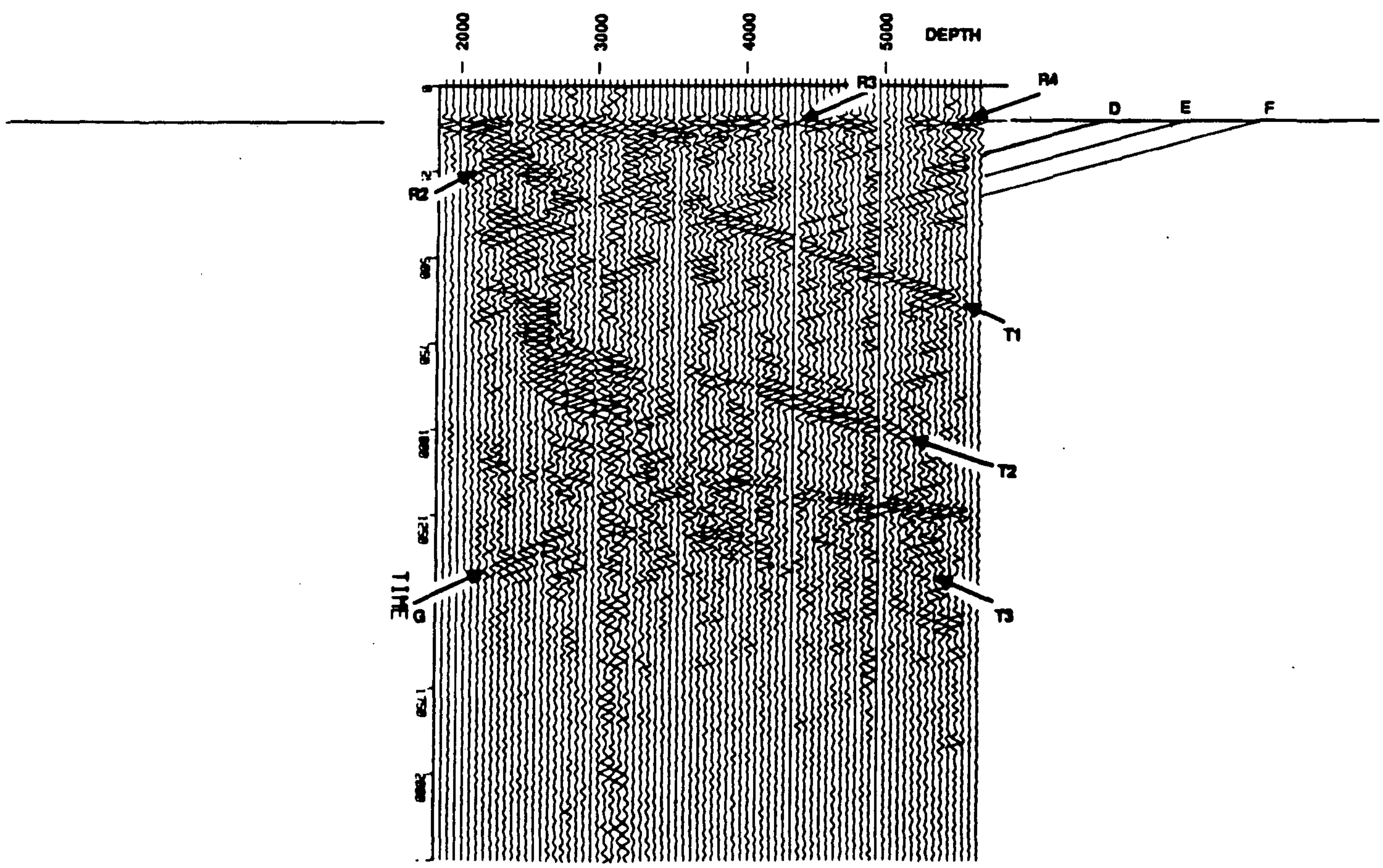

Figure 21. Identification of events on near-offset P source, vertical component data with dipfilter, high pass and aligned first arrivals.

3.2. NEAR-OFFSET SH_t SOURCE DATA

The near-offset shear surveys were, as discussed, hampered by severe noise problems. The traces between 2500' and 4000' are essentially useless. This gap in the data made the dipfiltering process noisy. The best sections to interpret were simply high pass filtered at 25 Hz with an AGC applied. This processing is shown for all three components in Figures 22a, 22b and 22c. The SH component data (Fig. 22a) shows two strong multiples, labeled M1 and M2 following the primary shear event. Since these multiples are not evenly spaced in time, they are probably being generated at different depths, but the data are not complete enough or quiet enough to identify their source depth. The SV component data (Fig. 22b) shows strong shear-wave arrivals and some multiples as well as indications of tube wave energy, event T2. The implications of strong first arrivals on the SV component will be discussed in conjunction with anisotropy detection. The radial component data (Fig. 22c) show a P-wave event, probably generated at the surface by the vibrator. Also seen is the tube wave event (T2) identified from the P-wave source. Weak indications of a reflector, labeled R1, can be seen on the radial component. The depth of generation of R1 is estimated at 4100', but accurate determination is not possible.

3.3. NEAR-OFFSET SH_r SOURCE DATA

The SH_r source suffered from the same poor signal- to-noise ratio as the SH_t source as can be seen in Figures 23a, 23b and 23c which show the three components of the SH_r survey. Again, the dipfiltering process was not found to provide interpretable events, so the sections shown are high pass filtered at 25 Hz (with a 6 pole Butterworth filter) and displayed with AGC applied. The first shear arrival is good from 4150' to 5650' on the SV and SH components (Figs. 23a and 23b). The radial and SV components (Figs. 23c and 23a) show tube wave energy (event T2), probably generated by surface waves at the top of the well's fluid column. The radial component also has converted P-wave arrivals with associated multiples. Shear-wave multiples can be seen on the SV and radial components, although they are not as strong as those from the SH_t source.

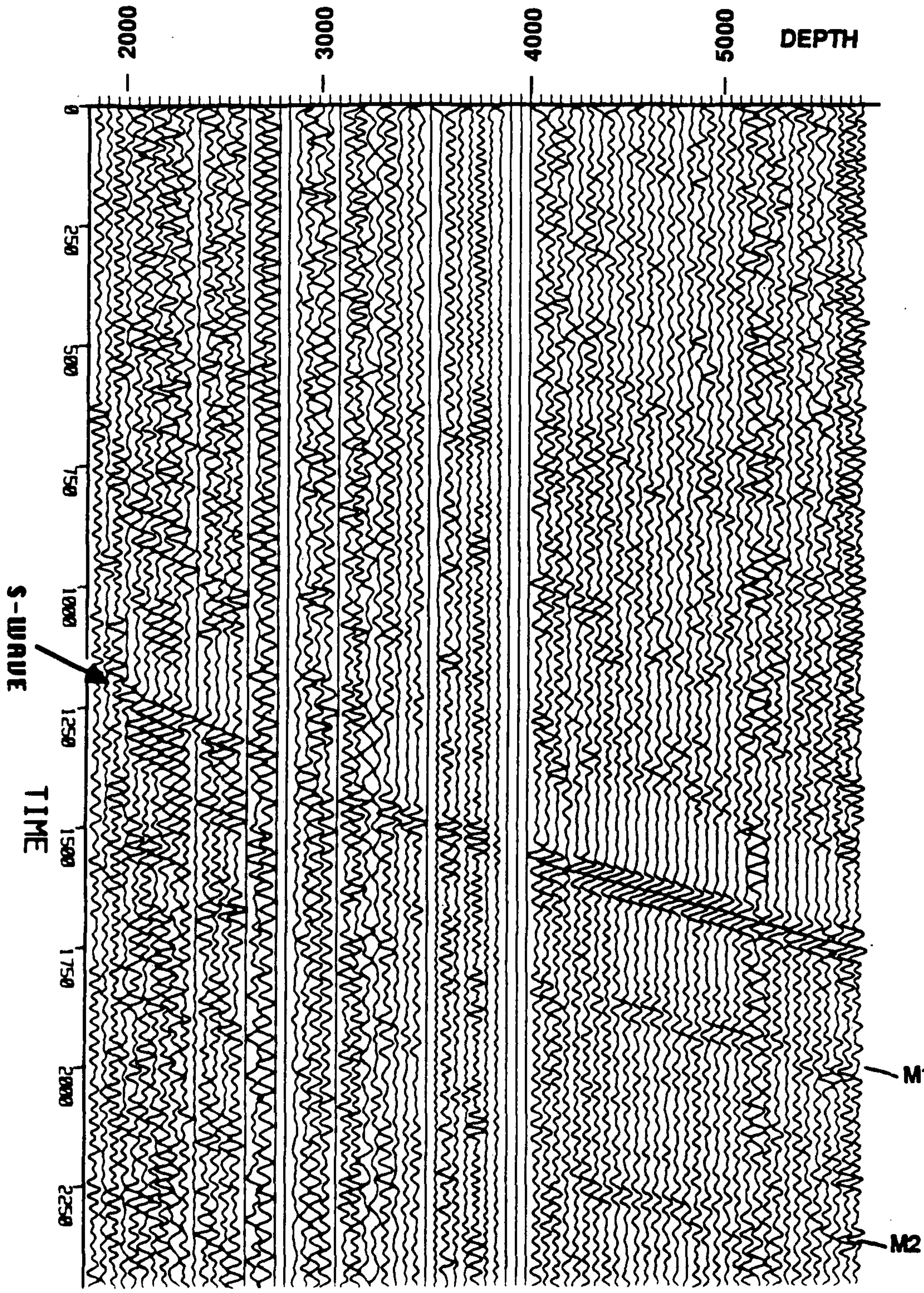

Figure 22a. Near-offset SH_t source data, SH component.

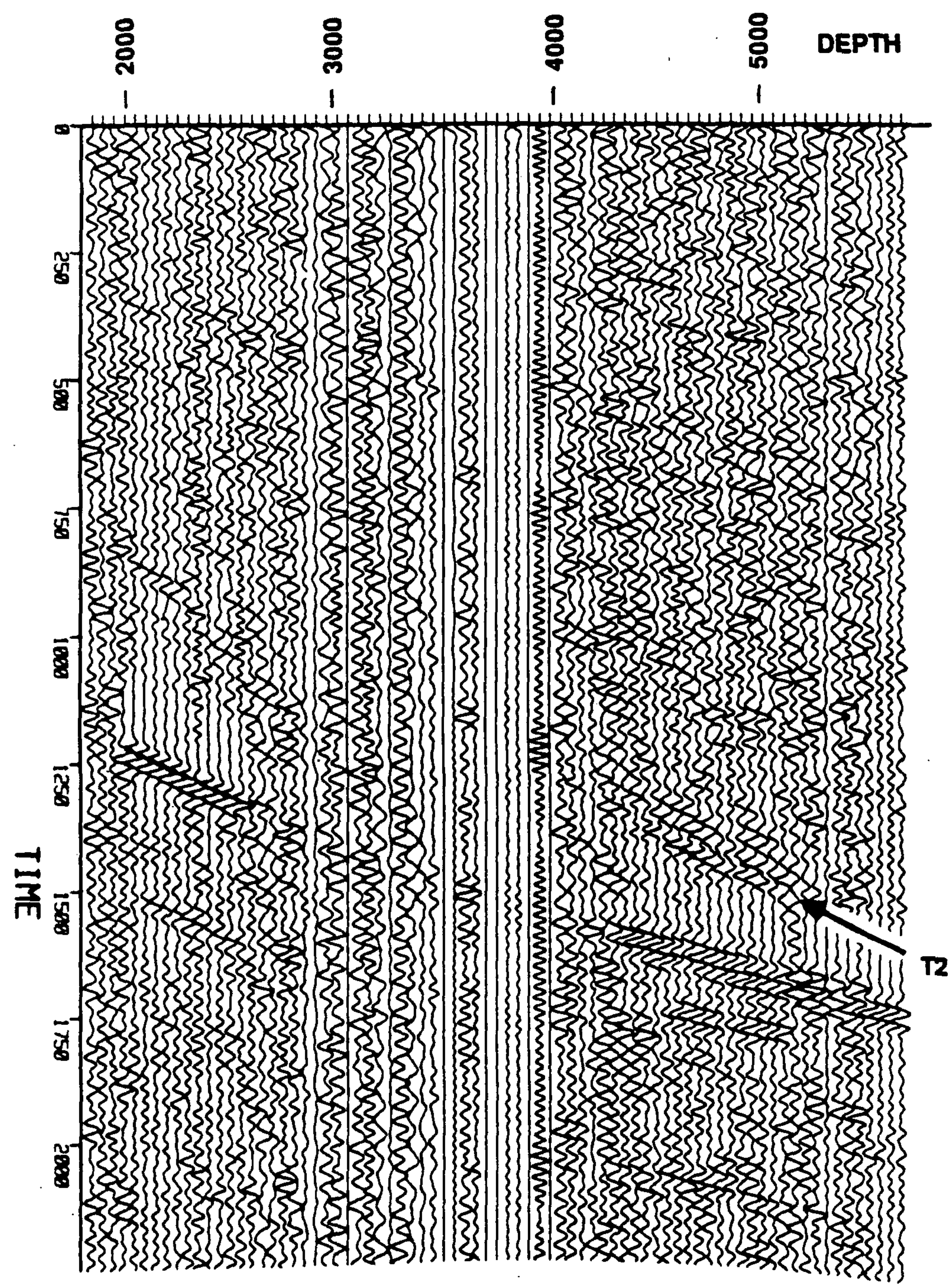

Figure 22b. Near-offset SH_t source data, SV component.

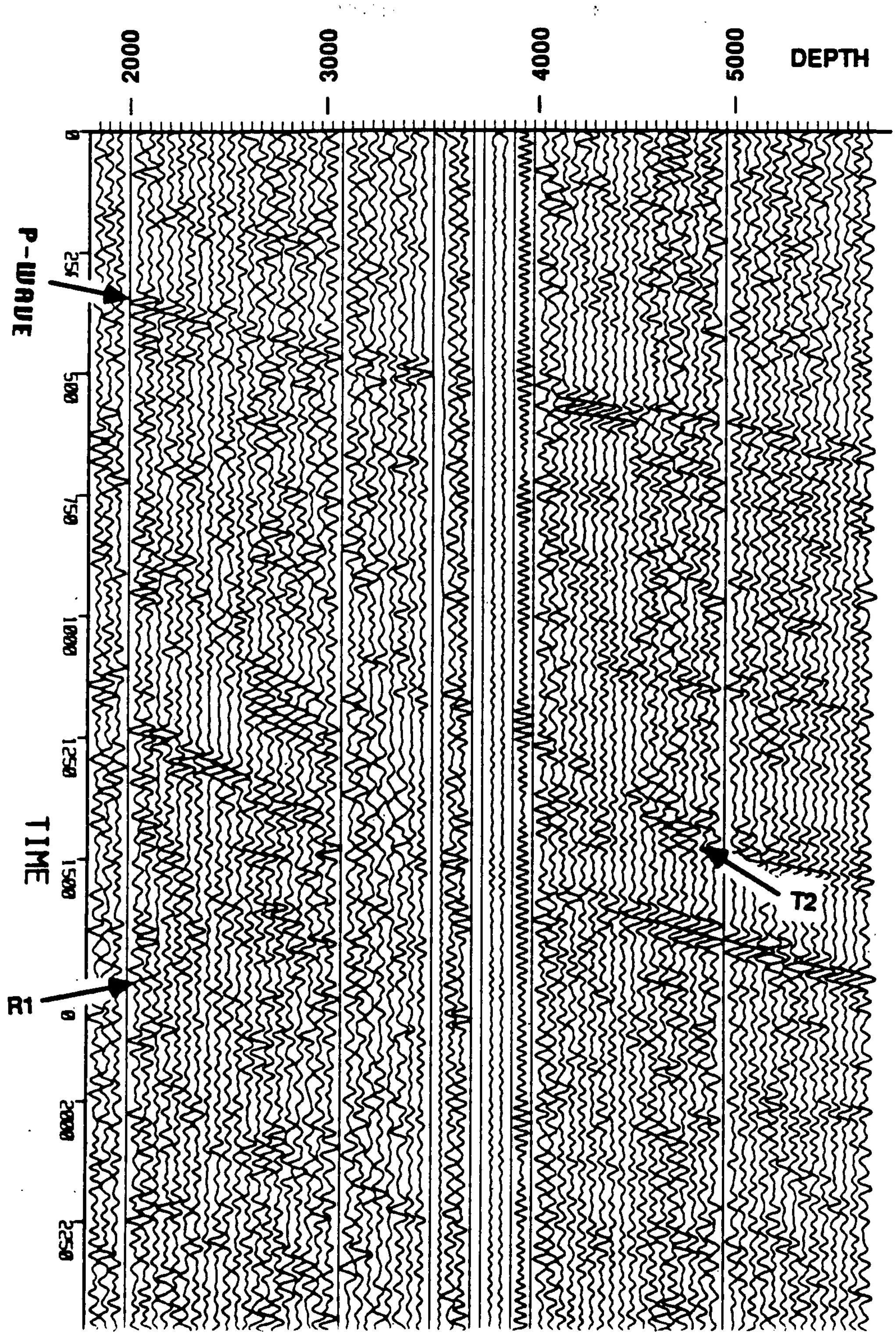

Figure 22c. Near-offset SH_t source data, radial component.

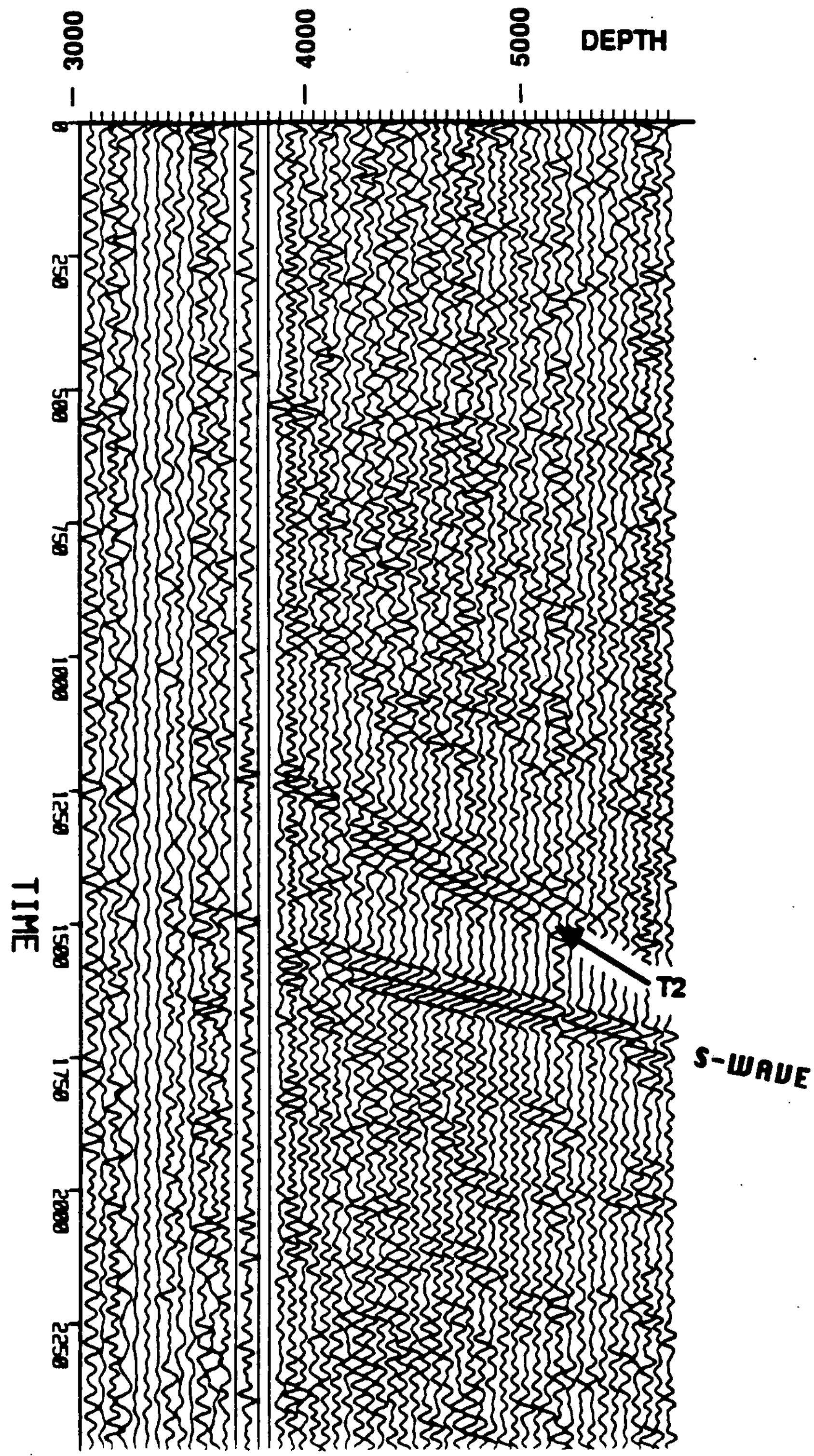

Figure 23a. Near-offset SH_r source data, SV component.

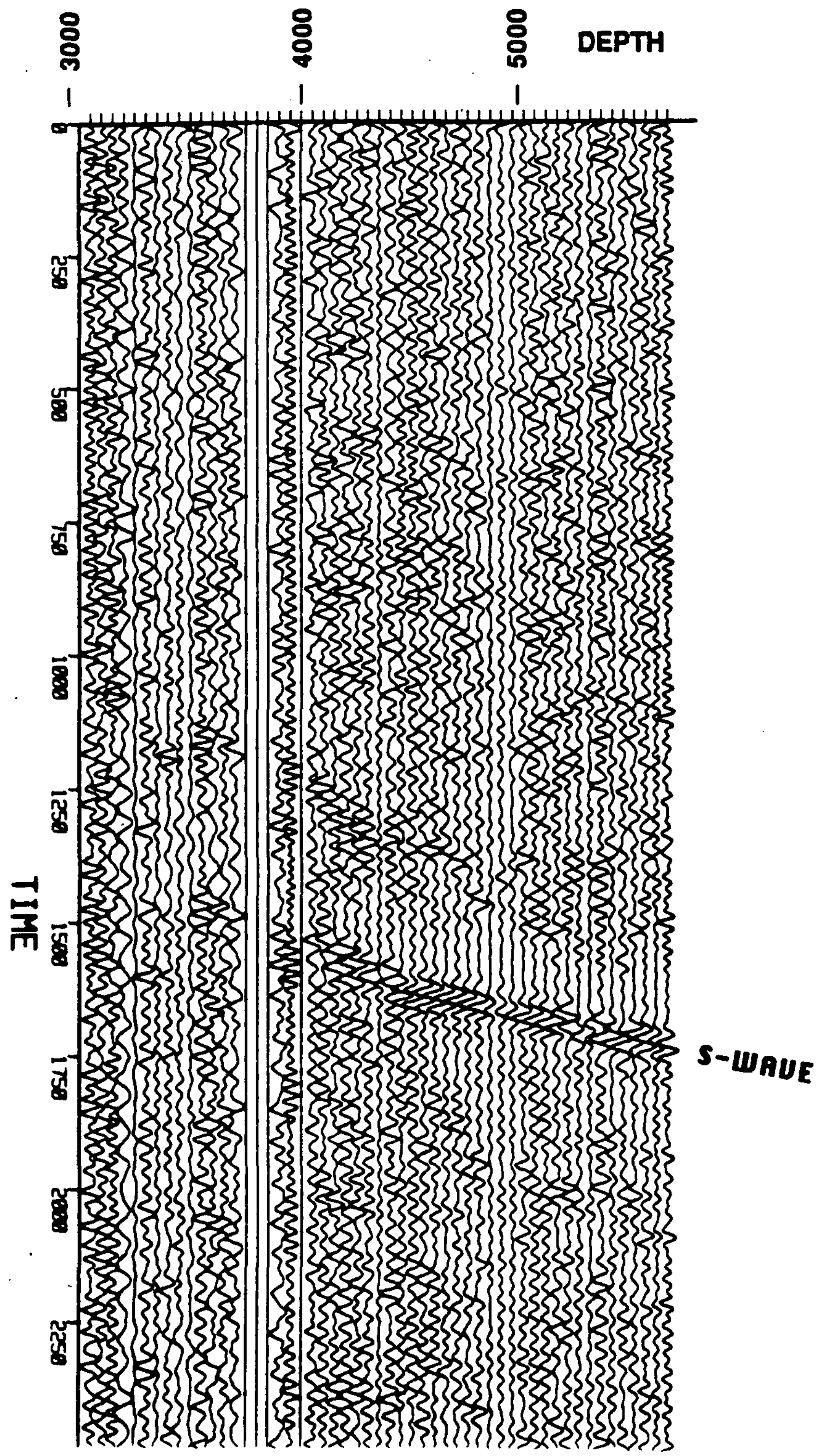

Figure 23b. Near-offset *SH*, source data, SH component.

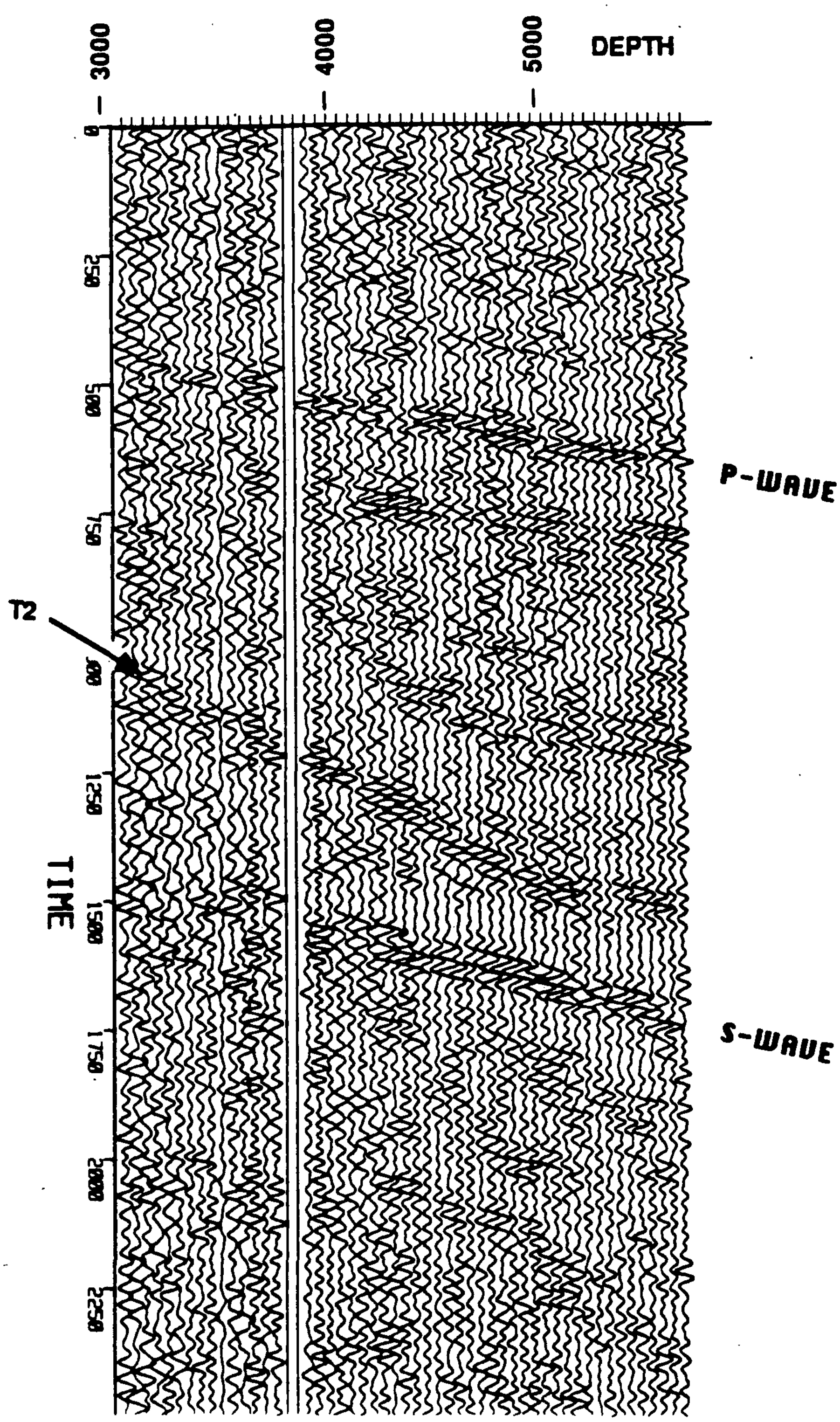

Figure 23c. Near-offset *SH*, source data, radial component.

3.4. FAR-OFFSET P SOURCE DATA

The data traces recorded by the far-offset P source are probably the most interesting and unusual in the survey. Figures 24a, 24b and 24c show the data from the rotated components. While the radial component shows good P-wave first arrivals, it is the SV component which is quite anomalous. A number of unexpected downgoing events, including the two labeled A and B, and one strong reflection event labeled C, dominate the first second of data on the SV component. If these events were reflections or multiples from horizontal layers they would have appeared on the near-offset data sets. Keeping in mind the near-offset P-wave survey, which did not show such strong events on any component, it is clear that a simple horizontal layer model could not explain these events. Also identifiable is a source-generated shear arrival at 1.6 seconds, identified because the far-offset shear sources' first arrivals have the same travel time.

The downgoing events seen on the SV component are not simple downgoing multiples of the P-wave since they do not parallel the downgoing first arrivals. Their apparent velocity, or moveout across the section, would be the same as the first arrivals if they were generated by a horizontal bed. If they were generated by a dipping bed, they would show a different moveout but they would still be observed on the near-offset survey. It was the analysis of the apparent velocity of these events which provided a key to understanding their generation.

The downgoing events A and B and the reflection, C, have the same moveout as the near-offset P-wave first arrivals. This observation implies these events are vertically travelling P-waves. The reason they are seen strongest on the SV component is explained by looking at Table 3 which has the rotation angle ϕ for the far-offset P source. For the first 30 levels, where these events are seen, phi is between 50 and 85 degrees. This means the radial component is close to true horizontal and the SV component is seeing most of the vertical particle motion. If these events are vertically travelling P-waves, whether upgoing or downgoing, they would have a vertical particle motion. In order to best see a vertically polarized wave, the original unrotated vertical geophone component should be used.

Figure 25 shows the original vertical component. Events A, B and C are still coherent even though the direct P ray has oblique incidence and the first arrival is weak on many traces. The event labeled F is more coherent here than on the SV component (Fig. 24b). Given the observations, the best interpretation of the events labeled A, B, C, and F is that they are caused by P-wave energy which has been scattered near the well. The depth of generation can be estimated by looking at events B and C which appear to be upgoing and downgoing waves from the same source. They have opposite polarity and can be traced back to a common point in time at the 3000' depth where they no longer are seen on the section. The time at which they appear is after the first arrival, implying they were generated at some distance from the well, causing a delay before they arrived above and below the depth of generation. These events are then explained as being generated at a depth of approximately 3000', and at some offset from the well. Figure 26 shows a schematic of this proposed scattering.

A likely cause of P-wave scattering, given the known geologic environment, is a localized zone of fracturing or perhaps a vertical boundary between open fractured rock and impermeable sealed rock. This explanation is suggested by studies of cores taken between 3012' and 3020'. These were found to have fractures which are "presently open and permeable" in a matrix of "chloritized and epidotized crossbedded sandstone and shales" (McKibben and Andes, 1986). This depth is also the only zone above 6000' which had fluid loss during drilling and was considered a possible flow zone. In fact, it was thought that a reservoir might be found near this depth because of projections made from wells in the SSGF, but the low rate of fluid loss and low permeability led to a decision to not test this zone (Sass, 1987, personal communication).

In order to look for other reflections, the vertical component section was dipfiltered to enhance upgoing energy. Figure 27 shows the dipfiltered vertical component. Notice that while the first arrivals are attenuated, the downgoing scattered energy (events A and B) is still apparent. Since the dipfiltering process removes any downgoing energy caused by interbed multiples from horizontal reflectors - these events have the same apparent dip as the first arrivals - the indication is again that the downgoing energy associated with events A and B is scattered and not reflected. A reflection from below the data set can also be seen on the dipfiltered section. In fact three reflections can be identified. Figure 28 shows the estimated depth of these reflections at 6100', 6900', and 7900'. Again these are estimates which assume a constant velocity below the deepest level and the later events may be multiples. The later upgoing events (after 1.1 seconds) actually appear to be primary reflections of the scattered energy as well as multiple reflections. There is also an indication of a reflection from approximately 2800' labeled event D. The different moveout between events D and C illustrates the difference between scattered and reflected energy.

In order to improve the resolution and separation of events, the dipfiltered vertical section was filtered with a 25 Hz high pass Butterworth filter. This filtered section, shown in Figure 29, shows the pairs of upgoing and downgoing events centered about 2950'. Events A and A' are the first pair which appear to be generated very near the well. In fact, the first wavelets for 2875' and 2950' show a reversal in polarity. The other labeled events, B, B', F and F', all appear to be generated between 2800' and 3100'. There are also events following the shear wave arrival which appear to be scattered from the same depth zone.

To confirm the scattering model, the apparent moveout of events A and A' was computed for comparison with the vertical velocity. Event A has an apparent velocity of 13,000 ft/sec between 3025' and 3925' while the vertical velocity is 11,800 ft/sec and the far-offset first arrival's moveout is 19,200 ft/sec. These velocities show that event A is related to the vertical velocity; its faster moveout velocity can be explained by allowing for some horizontal offset of the scattering source. Event A' has an apparent velocity of 9600 ft/sec between 2050' and 2950', while the vertical velocity is 9000 ft/sec and the far-offset first arrival's moveout is 29,000 ft/sec. Event A' is apparently vertical propagation and not an interbed multiple which would have a moveout close to the first arrivals.

The radial component in Figure 30a, shows good first arrivals which have an unexpected double peak character. The expected wavelet is the same as the near-offset P source (Figure 19a). The two deepest traces, which are check shots from 7000' and 7100', show the expected wavelet without the double peak. The double peak wavelet seen on the radial component is probably caused by a vertically traveling P-wave following the direct arrival close enough that their wavelets merge. At the 7000' depth the two events have either separated enough so that there is no interference, or the secondary event has attenuated enough to reduce its effect. A more complete data set is necessary to understand the change between 5650' and 7000'. A 25 Hz high pass filter was applied to the radial component to increase the resolution and see if a second event was interfering with the direct arrival. This section, Figure 30b, does indeed show a second event following the first arrival between 3175' and 4675'. It is the low frequency components of these two events which are overlapping and causing the double peak character seen in Figure 30a.

The SH component (Figure 24c) shows some of the characteristics of the SV component but it is more noisy. The downgoing scattered events can be seen, implying they have a horizontal component of motion. The shear arrival at 1600ms shows a reflection, event H, whose depth of generation is estimated at 2875', possibly the same zone which is generating the scattered energy.

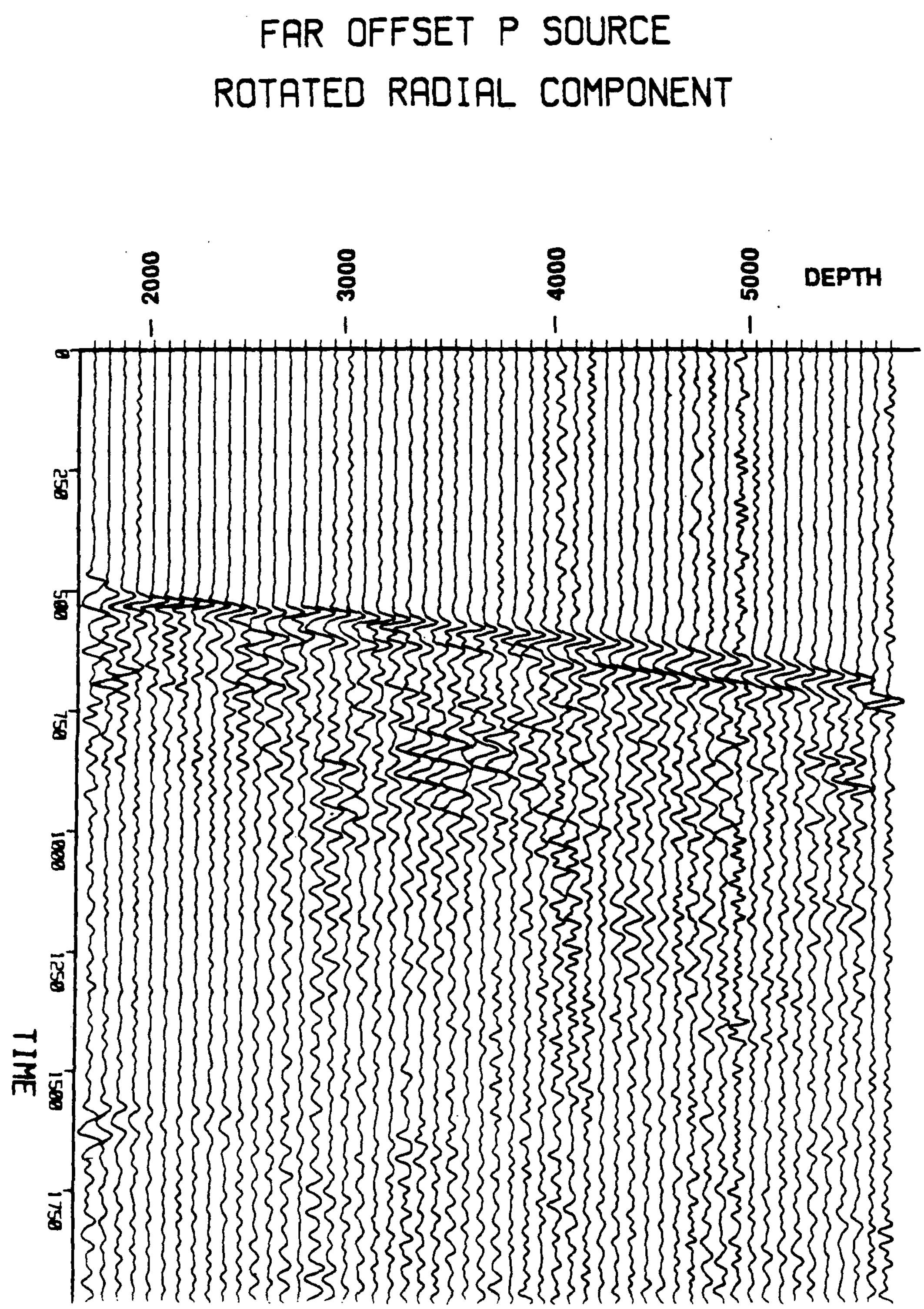

Figure 24a. Far-offset P source, radial component data.

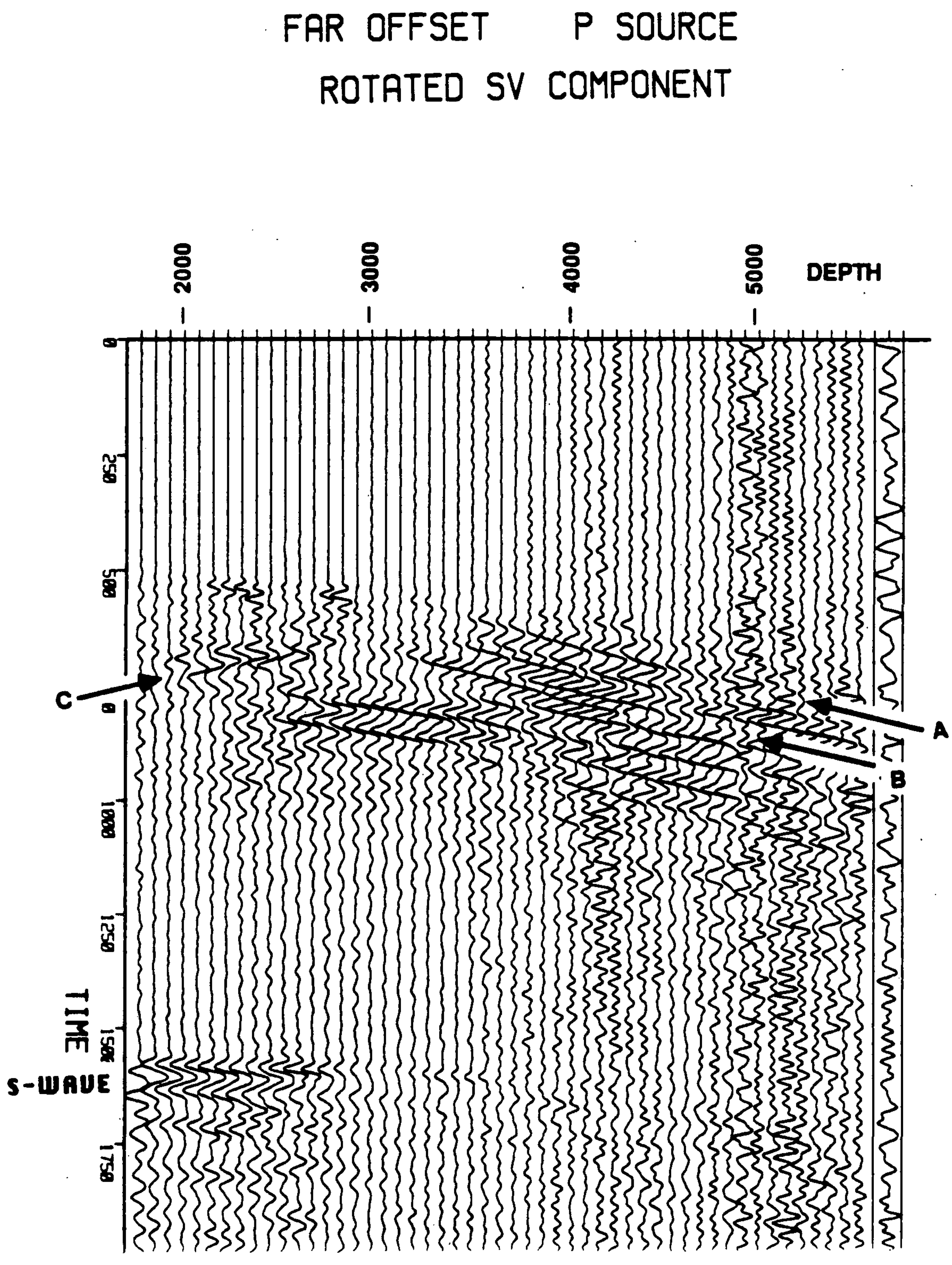

Figure 24b. Far-offset P source, SV component data.

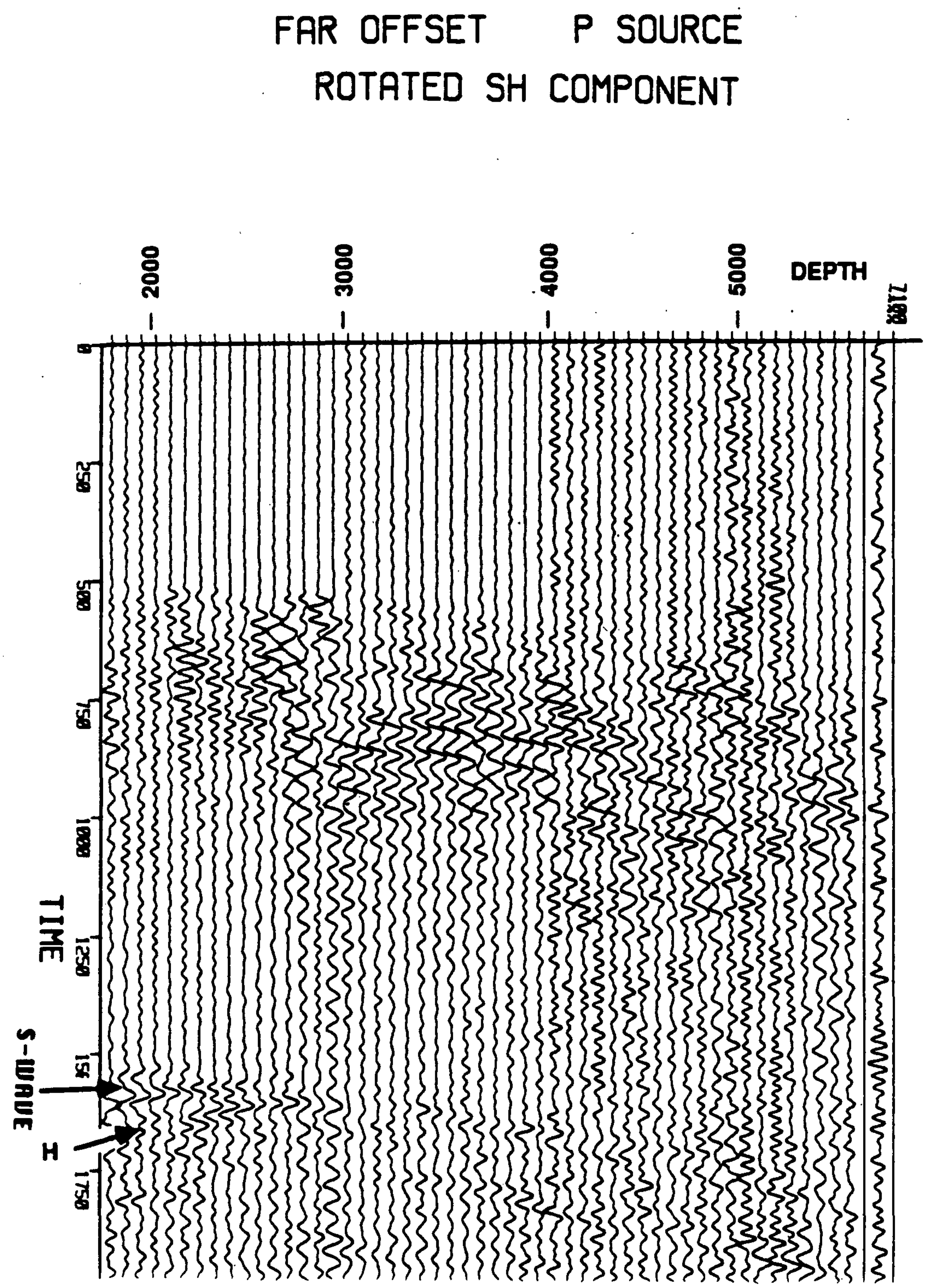

Figure 24c. Far-offset P source, SH component data.

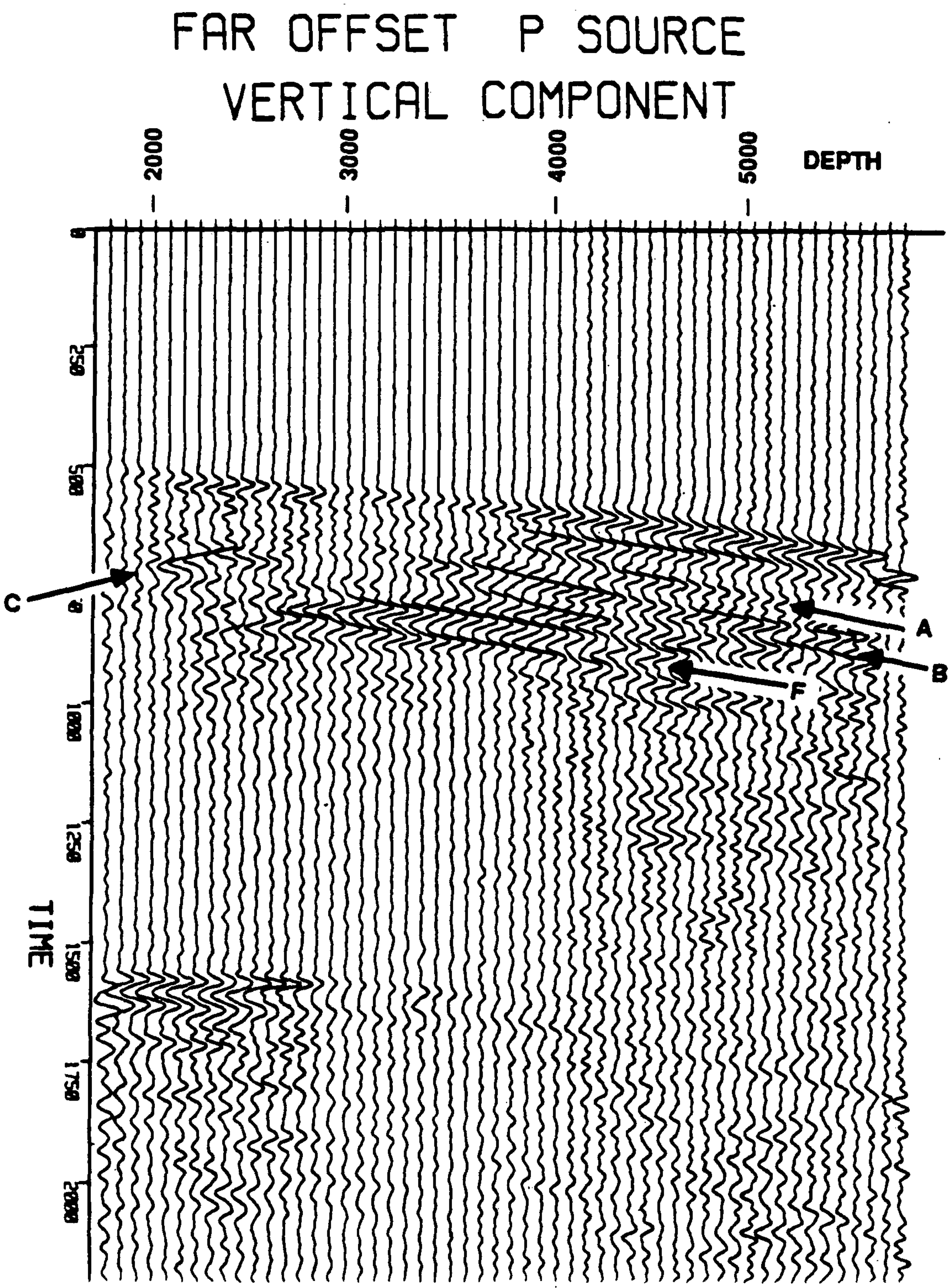

Figure 25. Far-offset P source, vertical component data.

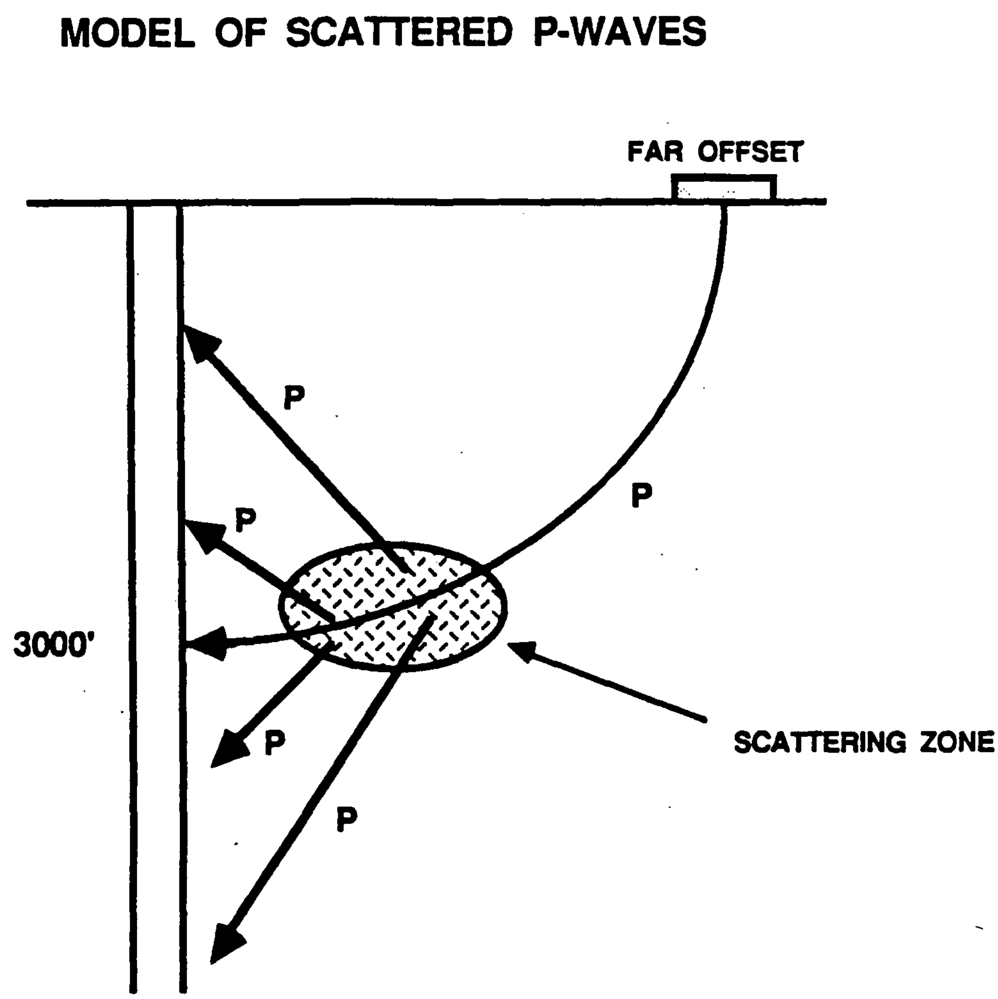

Figure 26. Model of scattered P-waves.

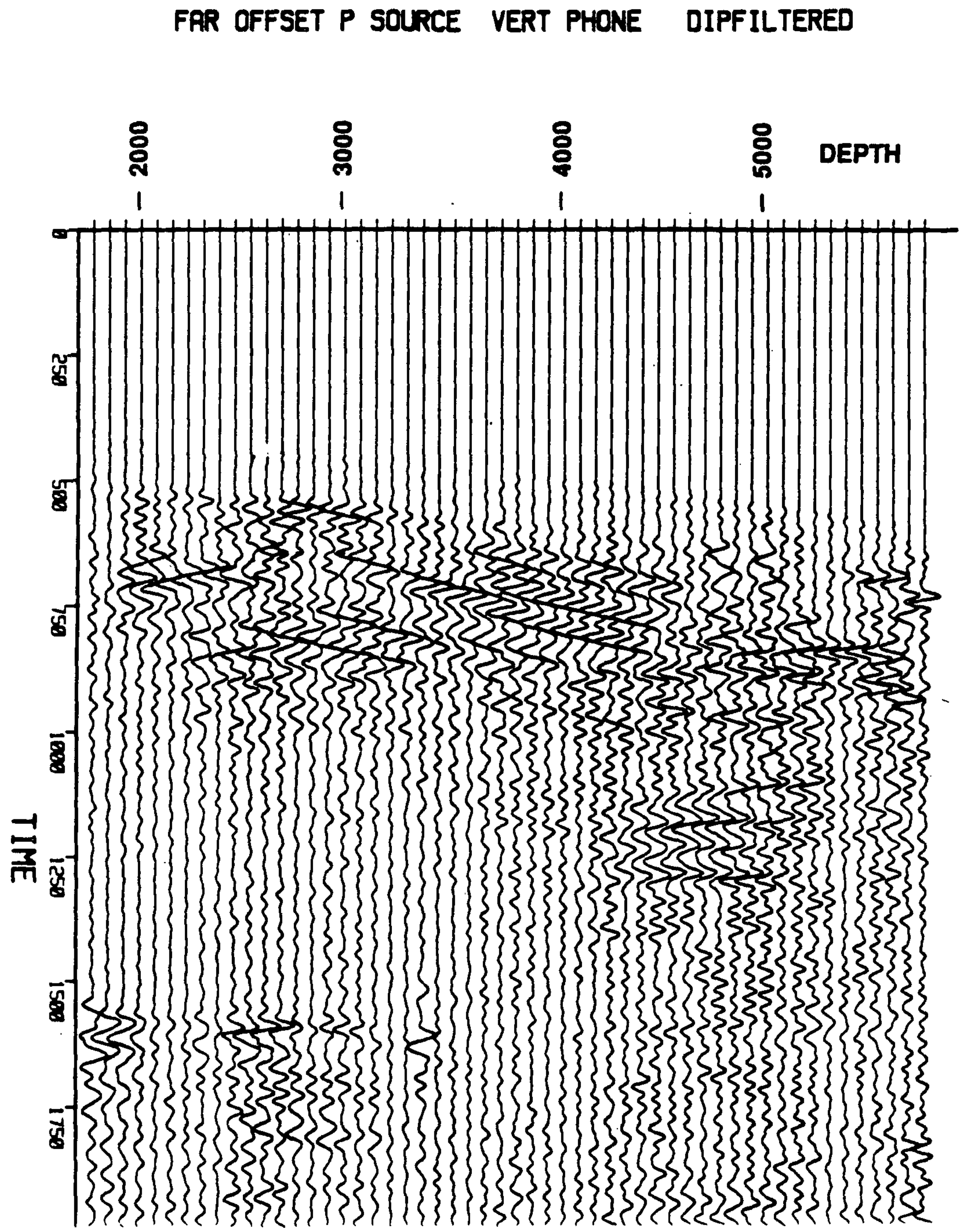

Figure 27. Far-offset P source, vertical component data, dipfiltered.

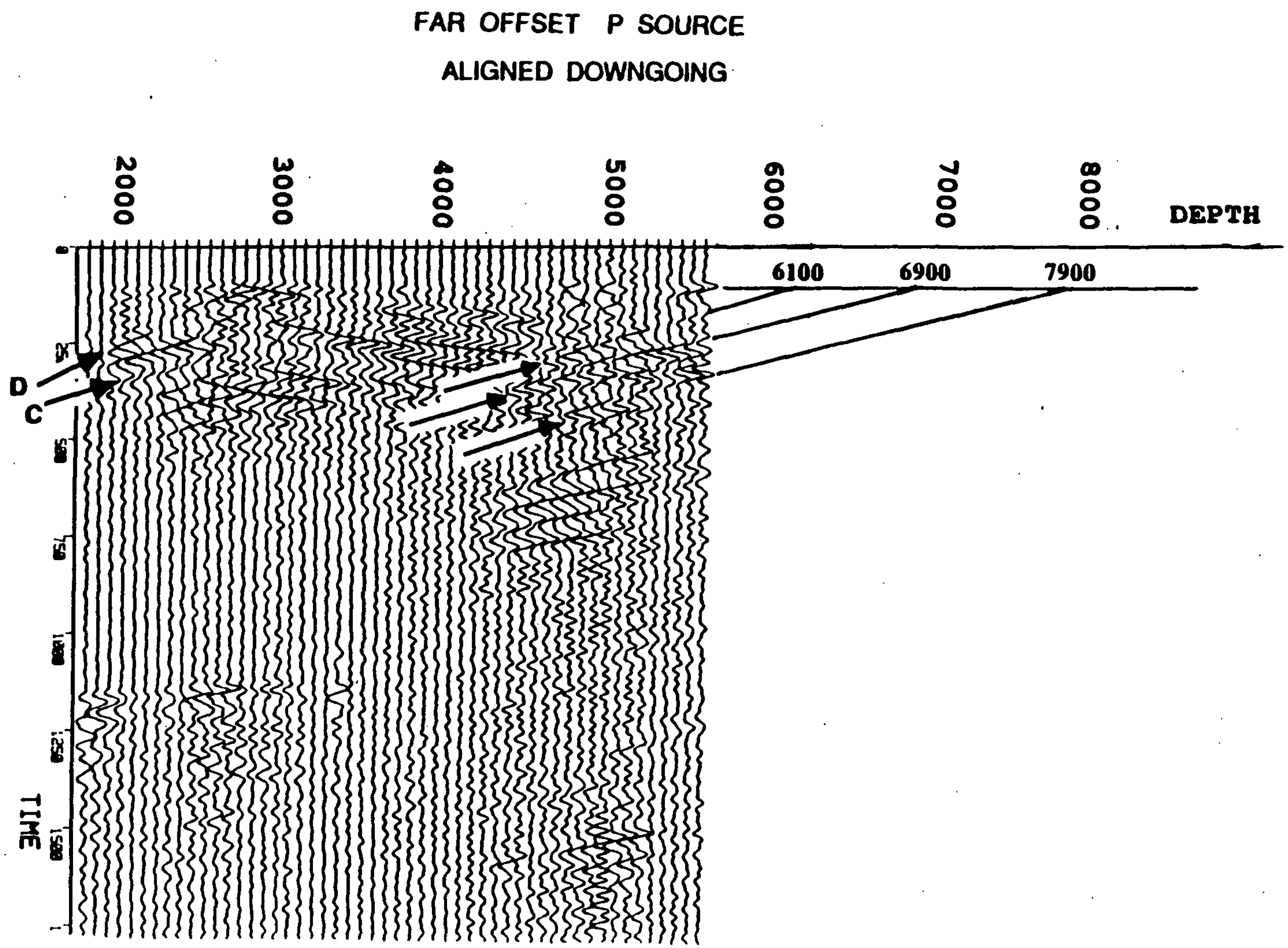

Figure 28. Reflector depth estimation for far-offset P source, vertical component data, dipfiltered.

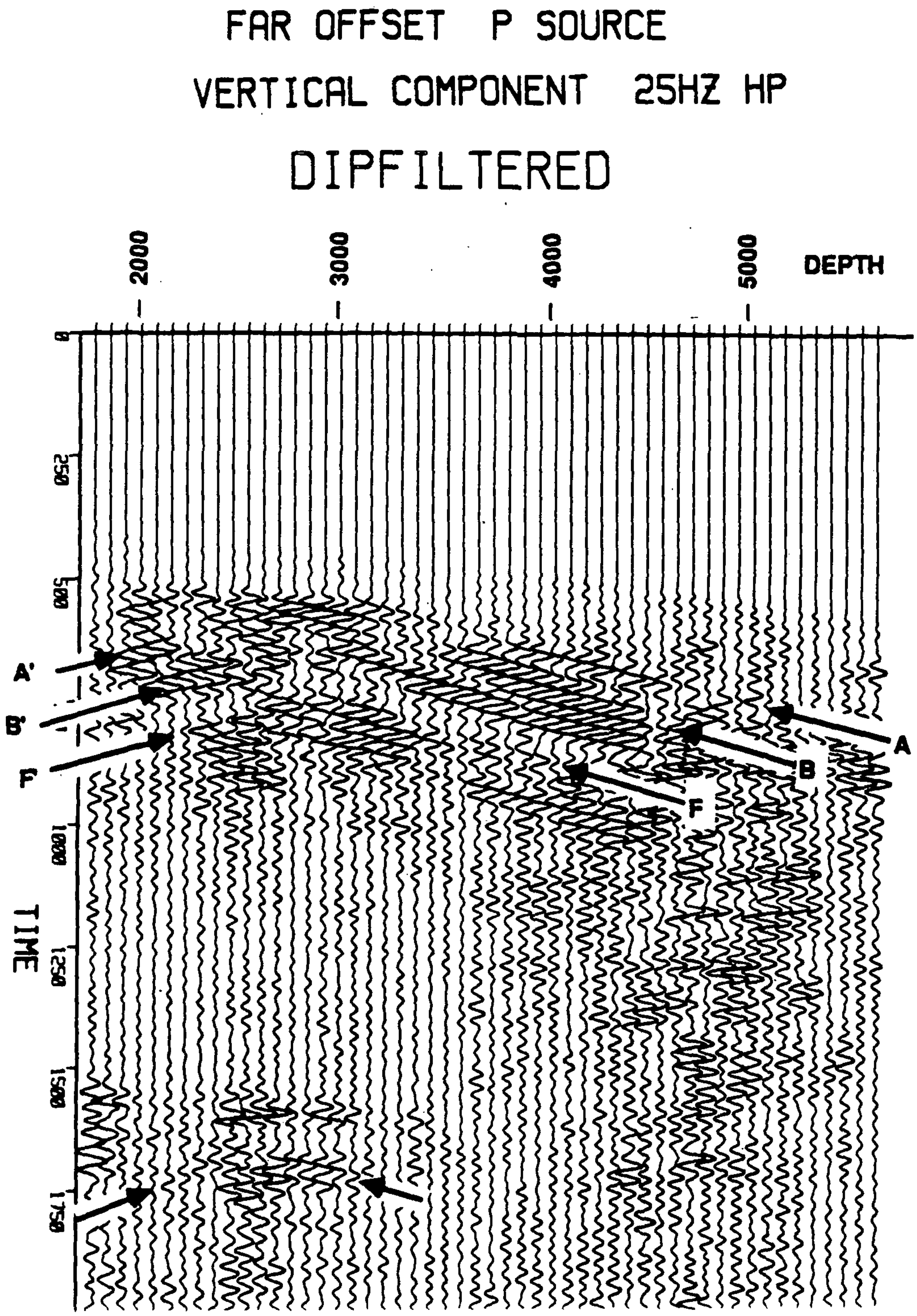

Figure 29. Far-offset P source, vertical component data, dipfiltered with 25 Hz high pass filter.

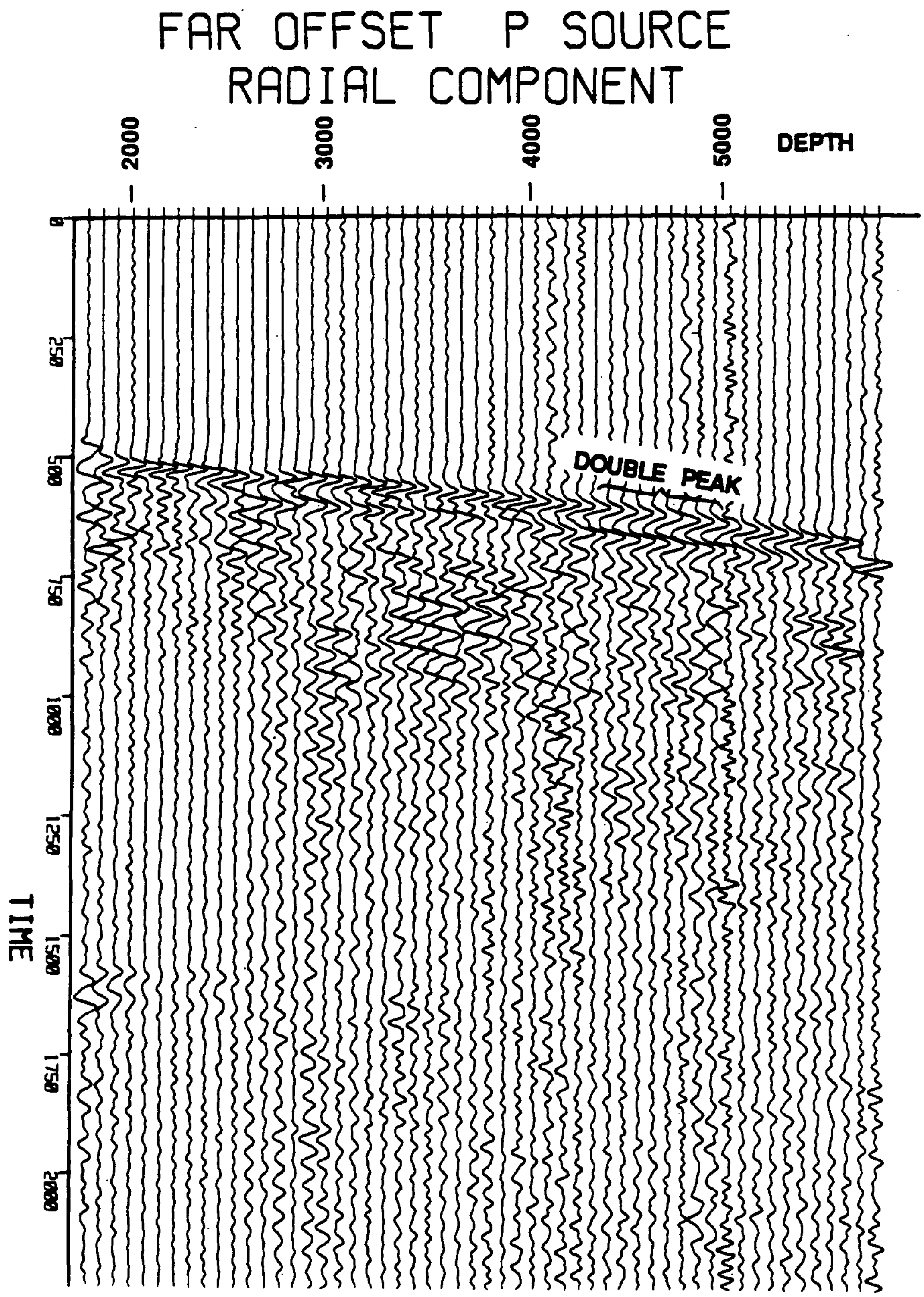

Figure 30a. Far-offset P source, radial component data.

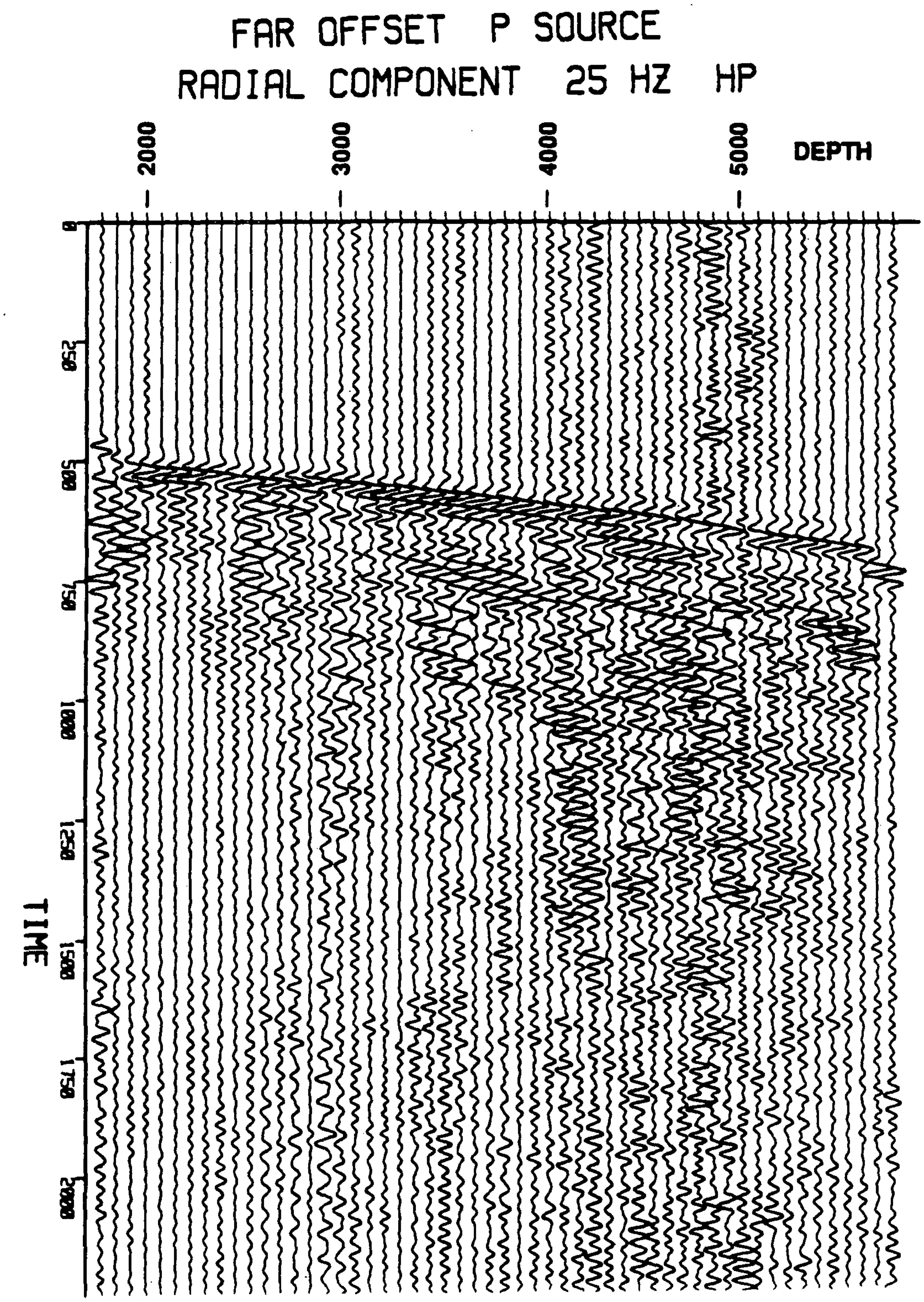

Figure 30b. Far-offset P source, radial component data with 25 Hz high pass filter.

3.5. FAR-OFFSET SH_t SOURCE DATA

Figures 31a, 31b and 31c show the rotated sections for the far-offset SH_t source. The shear wave arrival can be seen on all three components between 1.5 and 2.0 seconds. Between 2500' and 3500' there is very little moveout of the first arrival because the rays are turning and the angle of shear-wave incidence is near 90 degrees in this zone (see Table 5). The presence of a strong first arrival on both the SH and SV components is evidence of shear wave splitting, which will be discussed with the anisotropy effects. There is a discrete change in the character and time of the first arrival between 2200' and 2350' which is seen on the SH component (Figure 31a). This is probably an effect of raypath since the ray tracing (Figure 18b) shows a change in ray path near this depth with shadow zones between 2000' and 3000'.

The wavelet changes again at 3100' with a downgoing event emerging with different moveout than the direct shear arrival (event A). This event shows the same apparent velocity as the scattered P-wave energy seen for the far-offset P source. Apparently, the zone at 3000' is scattering P waves from incident shear waves. These scattered waves are seen more clearly on the SV component (Figure 31b), which has nearly vertical orientation.

Both the SH and SV components show downgoing multiples following the first arrivals. The radial component shows a poor first arrival, as expected, but there is low frequency downgoing energy below 3000' which is probably also associated with the P-wave scattering. An interesting effect is seen on the shallow traces at about 1.3 seconds where a coherent event is arriving before the first shear arrival. A possible interpretation is that this is also P-wave energy which has been scattered at some distance from the well, possibly by fracture zones, and has moved out ahead of the shear wave. Also seen on the radial component is a reflection from approximately 2500' (event J).

Deep reflection events are somewhat visible on the radial component. Inspection of the various components shows these reflections are strongest on the original vertical component. An estimate of the depth of reflection was made using the vertical component. Figure 32 shows an aligned dipfiltered section of the vertical component. Estimates were made for three events at 6800', 7500' and 8600'.

Later events can be seen, but they are probably multiples. In fact, the 8600' could easily be a multiple between the 6800' and 7500' reflectors, only its strength indicates it is a separate event.

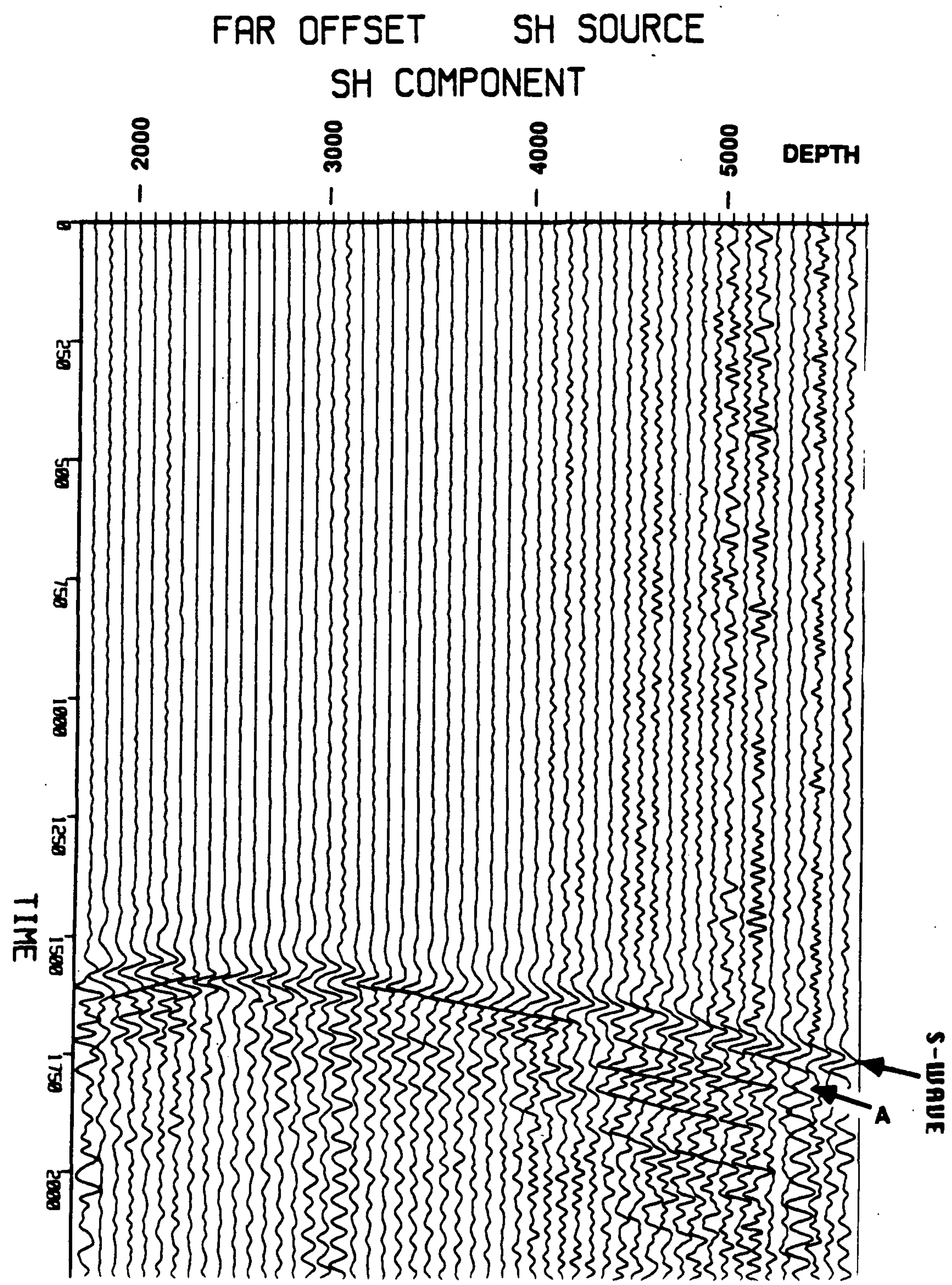

Figure 31a. Far-offset SH_t source, SH component data.

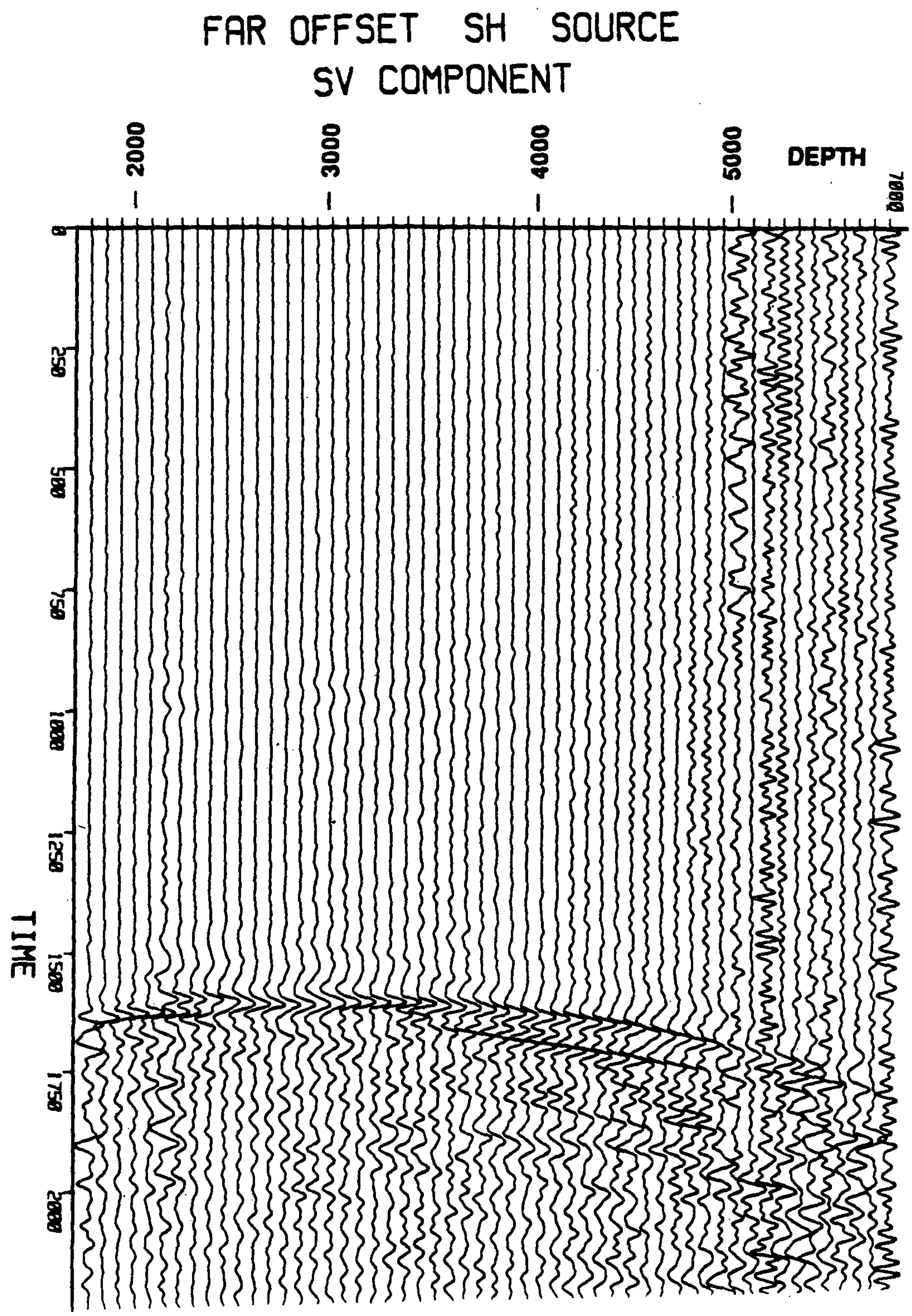

Figure 31b. Far-offset *SH*, **source, SV component data.**

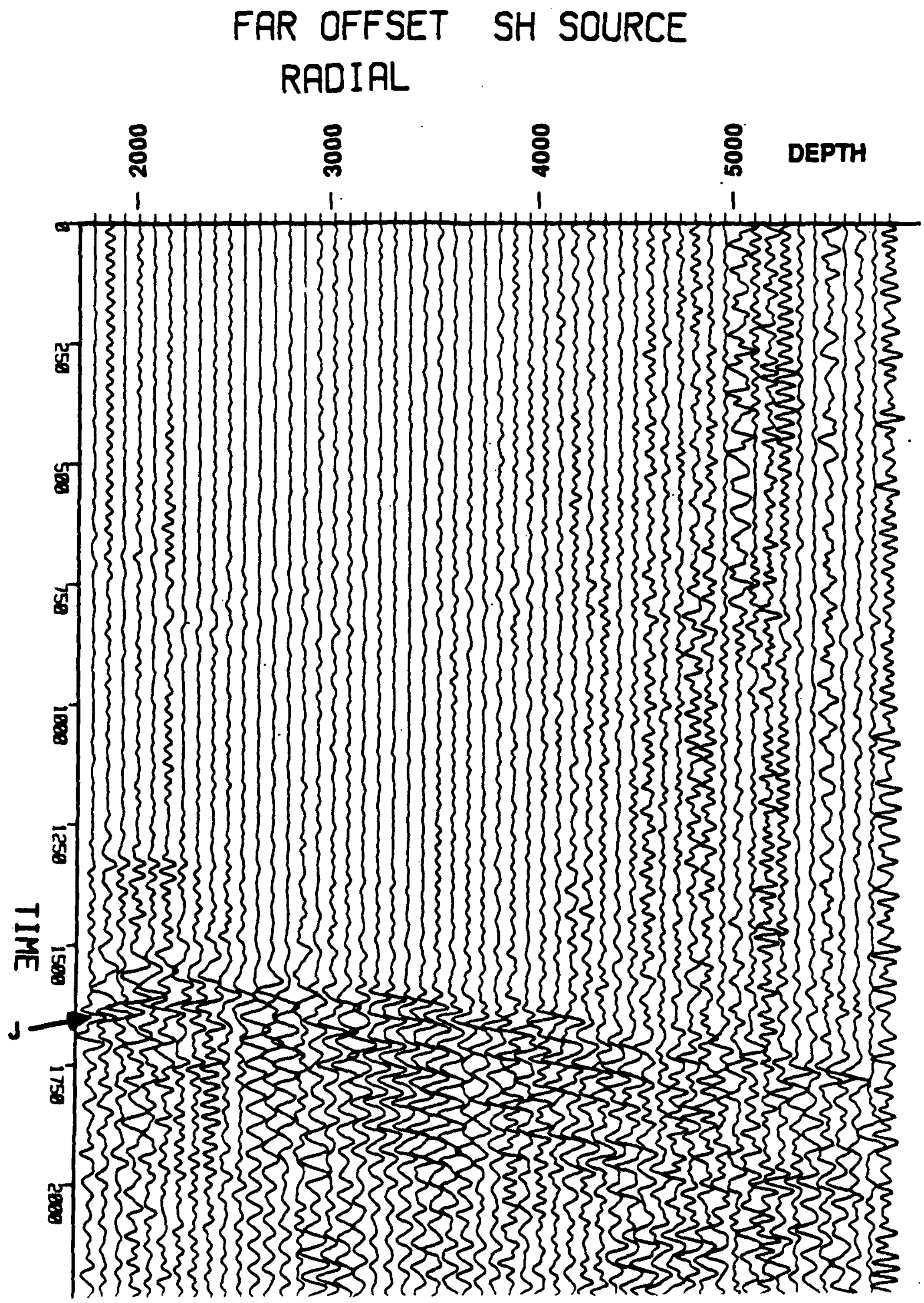

Figure 31c. Far-offset *SH,* source, radial component data.

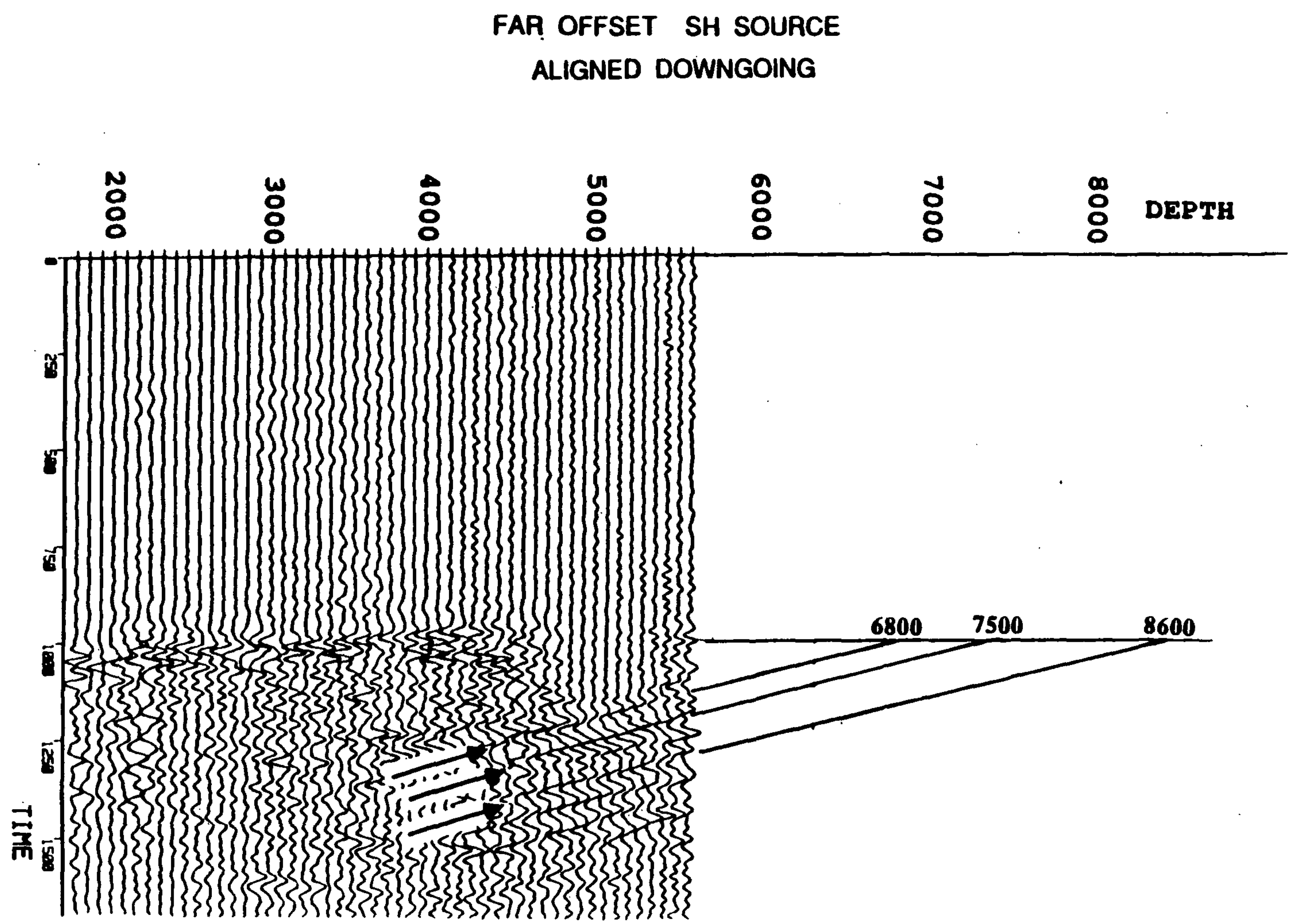

Figure 32. Estimated reflector depth from Far-offset *SH*, source, vertical component data with dipfilter and aligned first arrivals.

3.6. FAR-OFFSET *SV* SOURCE DATA

Figures 33a, 33b and 33c show the rotated component plots for the far-offset *SV* source. The first thing to notice is the strong first arrival and good signal to noise ratio on the SV component. Also, the SV component shows the first arrival having nearly simultaneous arrivals between 2000' and 2500', showing again the upturning of the ray path due to a steep velocity gradient. A possible reflection can be identified on the deep traces. The SH component shows the shear wave arrival but it is noiser with a high frequency event labeled A causing some interference. The event A may be scattered P energy propagating with a horizontal component.

The radial component shows some energy with the main shear arrival, and it also has two separate events before the shear arrival (labeled K and L). These events are probably scattered P-waves generated away from the well which have moved out in front of the shear waves . An estimate can be made of the distance from the well at which these scattered P waves were generated by using the known P and S velocities and the travel time difference. By assuming a straight ray path one can use the relation,

$$X = \frac{\Delta T \; V_P V_S}{V_P - V_S}$$

where

X = Distance of scatterer from well

ΔV = Travel time difference

V_P = P-wave average velocity

V_S = S-wave average velocity

Using this equation, the distance from the well to the scatter source was estimated at 1600' for event K, which would be roughly half the distance from the source to the 2000' depth receiver. Given the oblique incidence of the raypaths at this depth, it seems reasonable to assume the scatterer is mostly offset horizontally, and the lack of moveout of the scattered event also suggests horizontal offset. A separate scattered event is seen deeper on the radial component (event L). The same analysis gives a distance to this scatterer of 1500' from the receiver at 3000', which is probably also a dominantly horizontal offset.

The radial component of the *SV* source shows a strong reflection from below the deepest geophone depth. This reflection actually is stronger on the original vertical component, so this component is used for depth estimation. Figure 34 shows an aligned, dipfiltered section of the vertical component. Two reflector depths are estimated at 6800' and 8000'. Later upgoing events can be seen, but these are probably multiples.

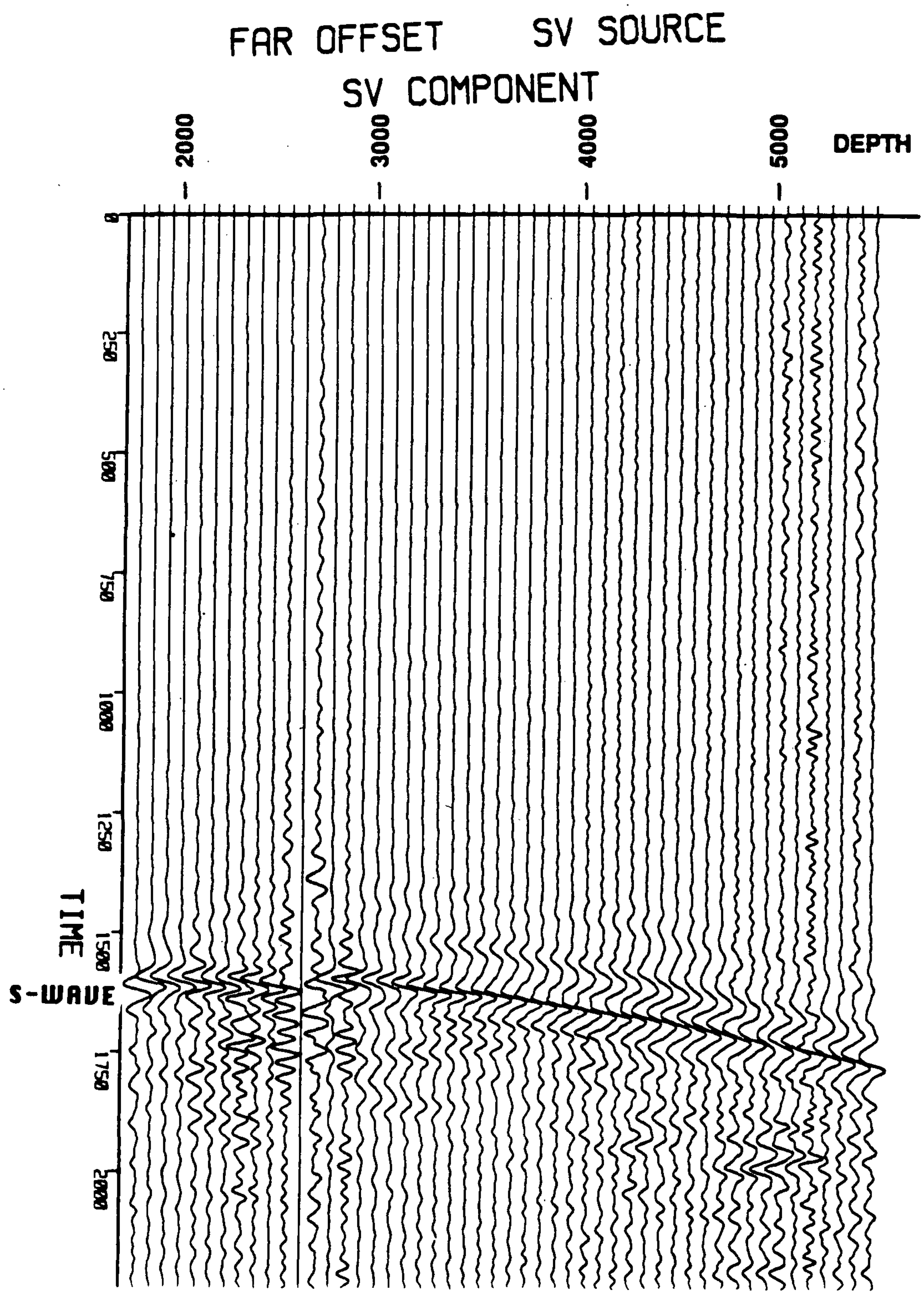

Figure 33a. Far-offset *SV* source, SV component data.

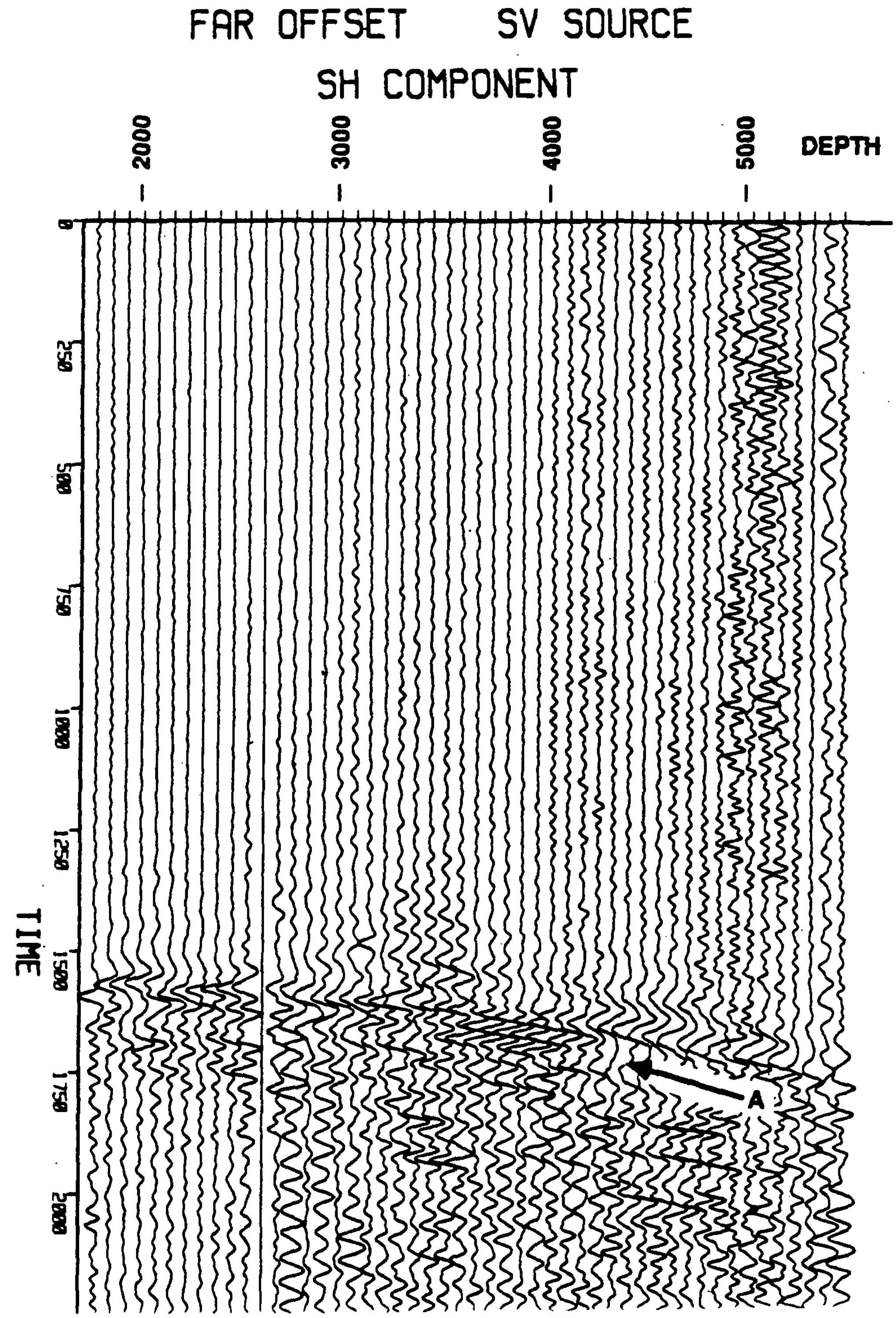

Figure 33b. Far-offset *SV* source, SH component data.

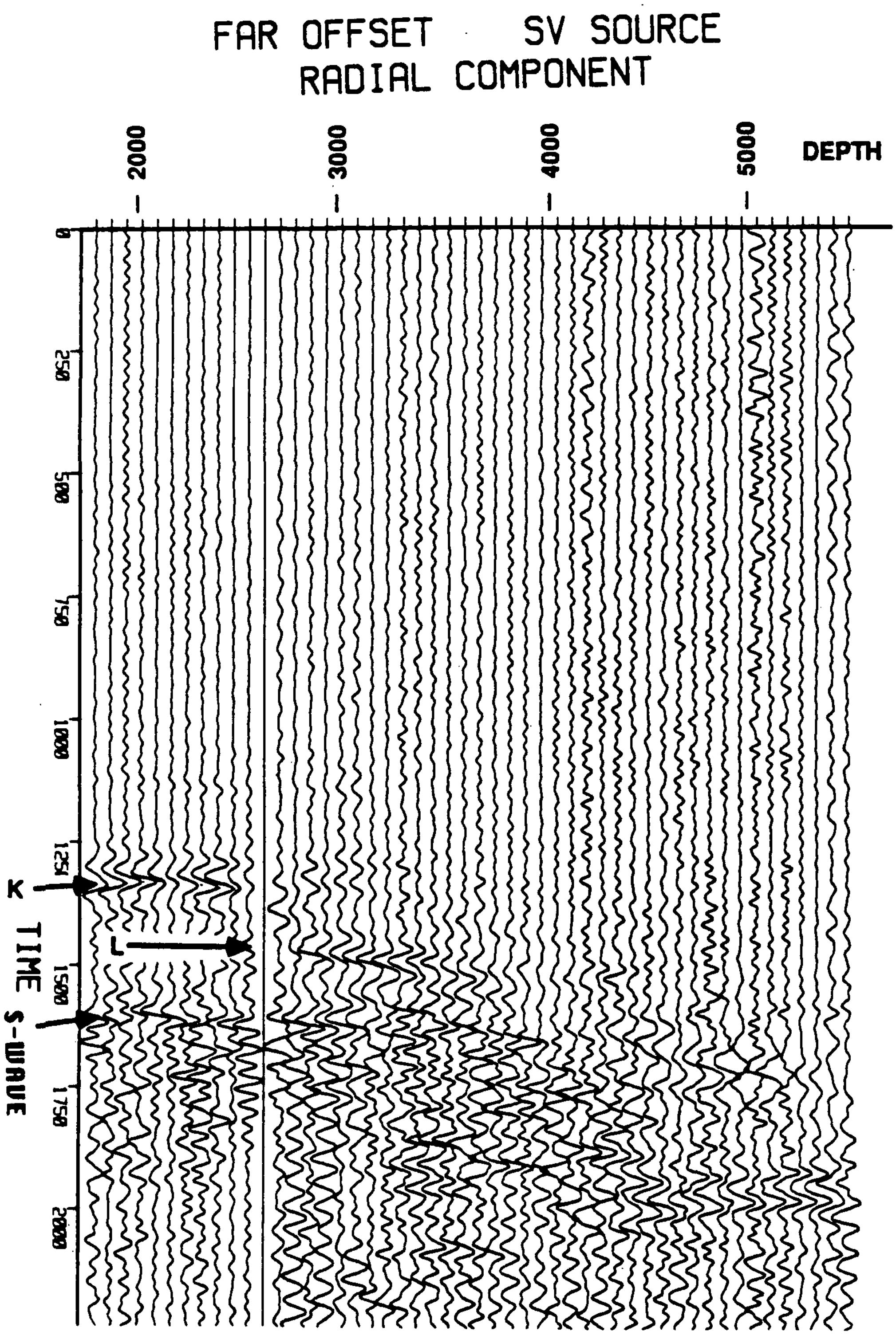

Figure 33c. Far-offset *SV* source, radial component data.

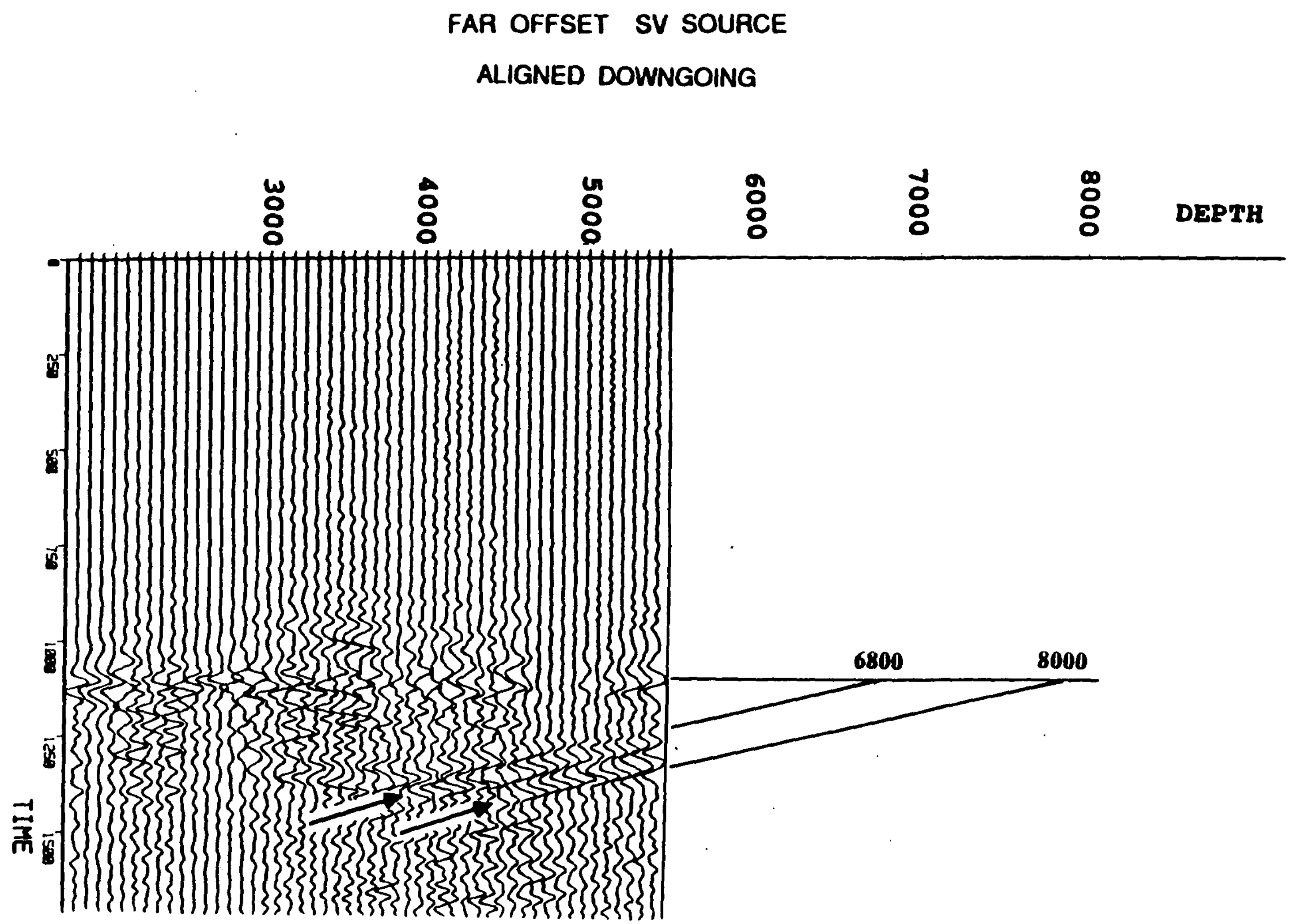

Figure 34. **Estimate of reflector depth for far-offset *SV* source, vertical component data with dipfilter and aligned first arrivals.**

CHAPTER 6

ANISOTROPY ANALYSIS

1. VELOCITY ANISOTROPY - NEAR-OFFSET DATA

As stated before, the near-offset shear sources are two polarizations of SH waves, labeled SH_r and SH_t. With these two polarizations of SH waves, it becomes possible to look for anisotropy in the horizontal plane, information rarely measurable in-situ. Two separate methods were used to look for anisotropy. The first is a simple travel time measurement used to look for velocity differences between orthogonal polarizations. This was done by picking first arrival times for both sources on the receiver component with the same polarization as the source, and comparing those times at depths where both were pickable. The first arrival was picked on the first trough for both sources. Figure 35 shows a plot of the travel time difference. The data available, from 4250' to 5650', shows that SH_r is faster with an apparent trend of increasing separation between SH_t and SH_r. The average travel time difference in this depth range is 9 msec which is approximately 0.5% velocity anisotropy. While this is not a large amount of anisotropy, it is consistent enough over this depth interval of 1400 feet to show the presence of an azimuthal polarization dependence of shear wave velocity in the horizontal layers of this area.

2. VELOCITY ANISOTROPY - FAR-OFFSET DATA

The far-offset SV source generates particle motion in the vertical plane. In fact, the oblique incidence of the raypaths indicate most of the motion is in the vertical plane. By comparing the data from the SH_t source with the SV source, any velocity difference between SH and SV polarizations can be detected. As with the near-offset data, the first step is to look at simple travel time differences between SH_t and SV sources. Again the travel time for each source was picked on the rotated coordinate on which the wave would arrive in an isotropic material, i.e. the SH_t was picked on the SH component and the SV source was picked on the SV component. Figure 36 shows the travel time difference at each depth where both sources could be picked, points are to the right of the zero line when SH_t is faster and to the left when SV is faster. The error of any one point is estimated at ±5 ms.

The dominant feature is a trend of SV motion becoming increasingly faster than SH motion. Another surprising feature is the crossover in travel time difference with the SV source having longer travel times shallow and SH_t source having longer travel times at depth. For the shallowest levels, from 1500' to 2100', the SH_t source becomes increasingly faster, but at 2275' there is a discrete jump to equal travel time. This jump corresponds to the changes in wavelet character, raypath and travel time for the SH_t source data. From 2275' to 3550' the travel times are approximately equal with the exception of an anomalous zone around 3250'. In this zone the SH_t motion is again faster. From 3250' to 5500' the SV motion becomes increasingly faster than the SH_t motion. The total velocity difference of 16 ms. at 5500' represents about 1% velocity anisotropy. As with the 0.5% horizontal plane anisotropy seen at the near-offset, this is a small but measurable amount. The overall trend of increasing separation between SH and SV is very evident.

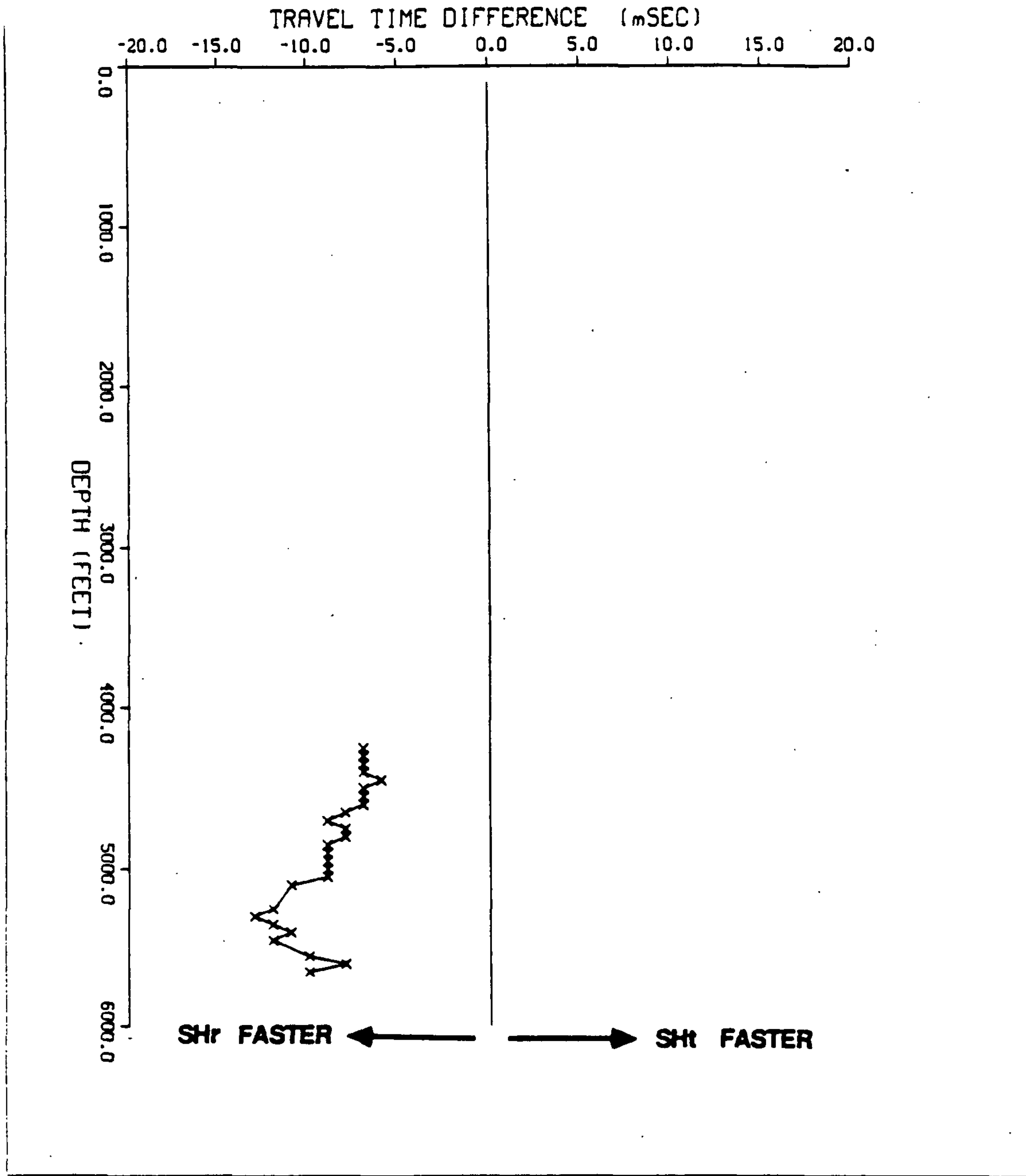

Figure 35. Travel time difference for near-offset shear sources. Data points are SH_r time minus SH_t time.

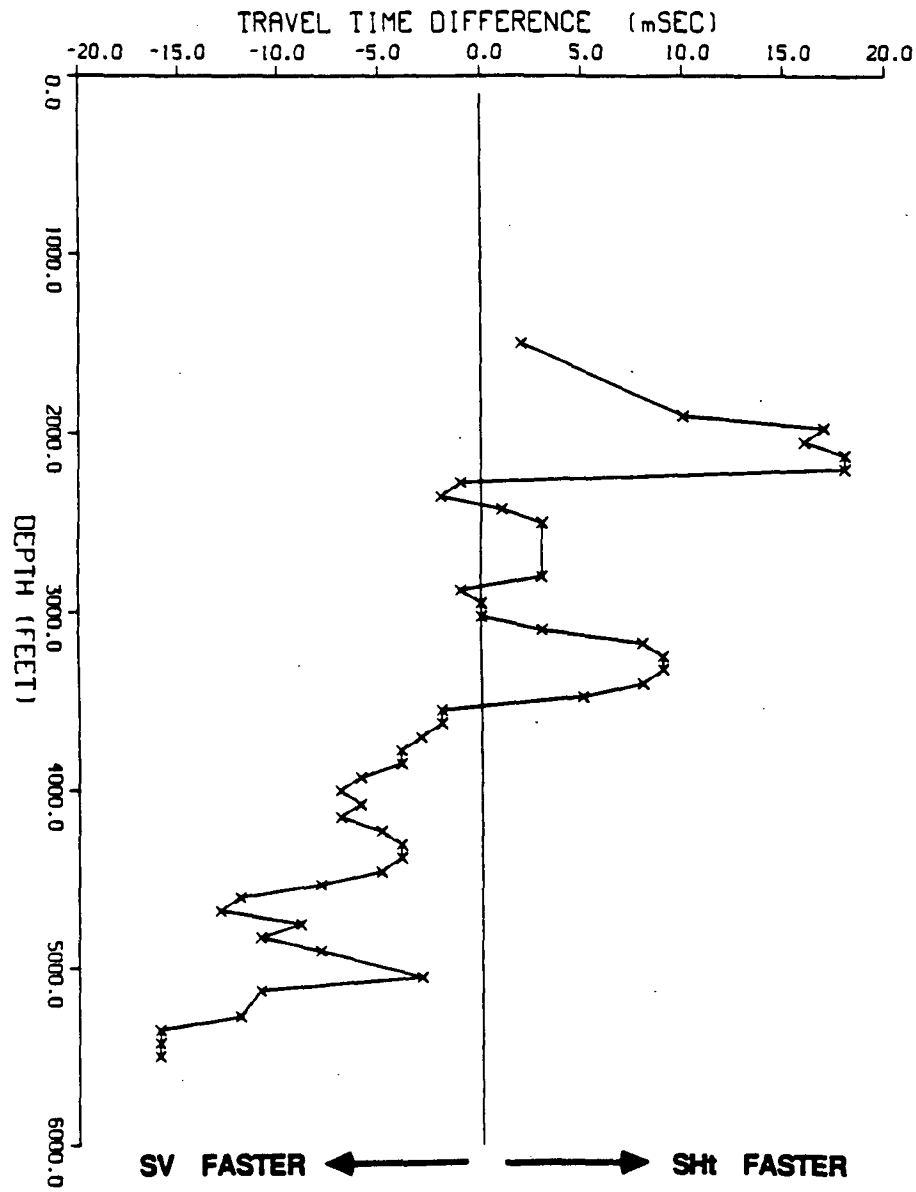

Figure 36. Travel time difference for far-offset shear sources. Data points are *SV* **time minus** SH_t **time.**

3. SHEAR-WAVE SPLITTING

It is the observation of particle motion which provides the second method of analyzing anisotropy. Given the observed velocity anisotropy, shear-wave splitting should be seen on plots of the first shear arrival's particle motion. The use of particle motion plots to study anisotropy effects has been well documented (Crampin 1985, Majer, et. al. 1986, etc). A three component geophone provides the ability to look at the particle motion within any 2-D plane or in its complete 3-D motion. Figure 37 illustrates the splitting of shear wave particle motion when a shear wave enters an anisotropic region. As described by Crampin (1985):

> A shear wave entering an anisotropic region necessarily splits into the two or more fixed polarizations which can propagate in the particular ray direction. These split phases propagate with different polarizations and different velocities, and on reentering an isotropic region the original waveform can not be reconstructed.

Figure 38 shows particle motion within the first arrival window for all three sources from the far offset at the 1900' level. These plots show the three 2-D slices which describe the complete particle motion plotted on the faces of a cube whose axes are the three components. The vertical axis is the radial component while the horizontal axes are the SH and SV components. The three plots on the cube faces are Radial vs SH, Radial vs SV and SH vs SV. This means the pure shear motion, SH vs SV, is shown on the bottom of the cube. While the SH vs SV plot is often the only one displayed in other studies, the radial component can provide much information about the three-dimensional nature of particle motion. It would be possible to plot the particle motion as a single three-dimensional path, but in practice this type of plot is difficult to interpret since it is significantly dependent on the angle at which it is viewed. Figure 38 is representative of the particle motion one would expect from isotropic propagation. The P-source first arrival has mostly radial motion, the SH-source arrival has mostly SH motion and the SV-source arrival has mostly SV motion.

The window used for these hodographs is approximately 70 milliseconds, although each arrival has a slightly different window length. The points plotted are two milliseconds apart. The first three points in time are circled to provide the correct identification of first motion. The software used for this display was a FORTRAN program, HODOS.FOR listed in Appendix 4. Since these plots are sensitive to signal-to-noise problems at any one level, their analysis should avoid individual levels which do not show correlation with nearby levels. Very good data quality is necessary before interpreting a single anomalous particle motion plot. The levels which were obviously distorted by noise are not displayed.

Appendix 2 contains the particle motion plots for all the sources and all depths with sufficient signal-to-noise ratio. A quick inspection shows the P-wave source arrivals are, as theory predicts, confined to the radial component. It is the particle motion of the shear arrivals which contains information about anisotropic propagation along the raypath. The following Tables summarize the important characteristics of the shear-wave particle motion plots displayed in Appendix 2, emphasizing both the SH-SV plane motion and the amount of radial motion.

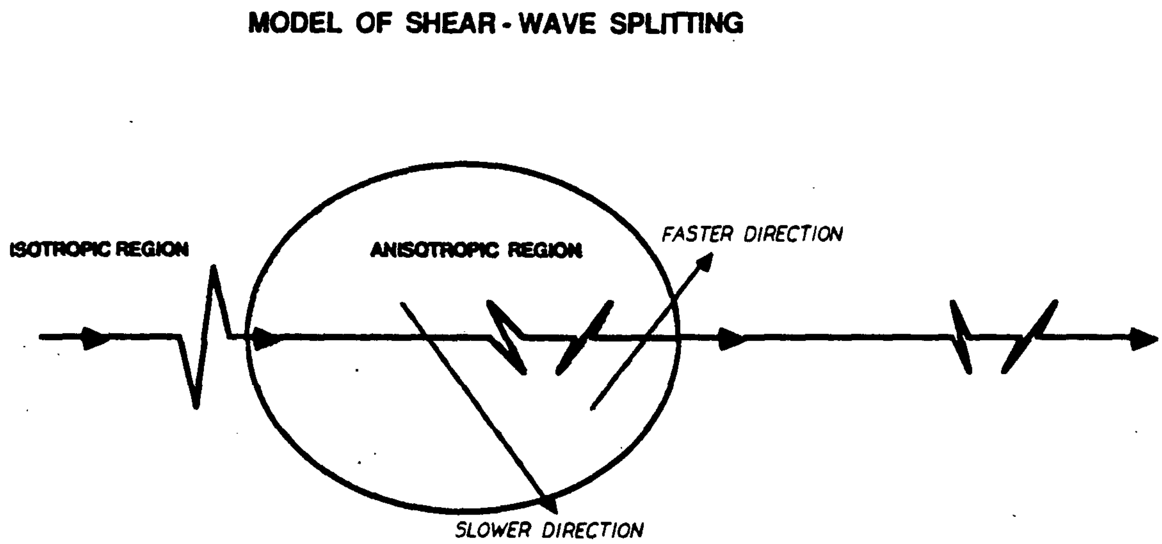

Figure 37. Model of shear-wave splitting in an anisotropic media. After Crampin, 1985.

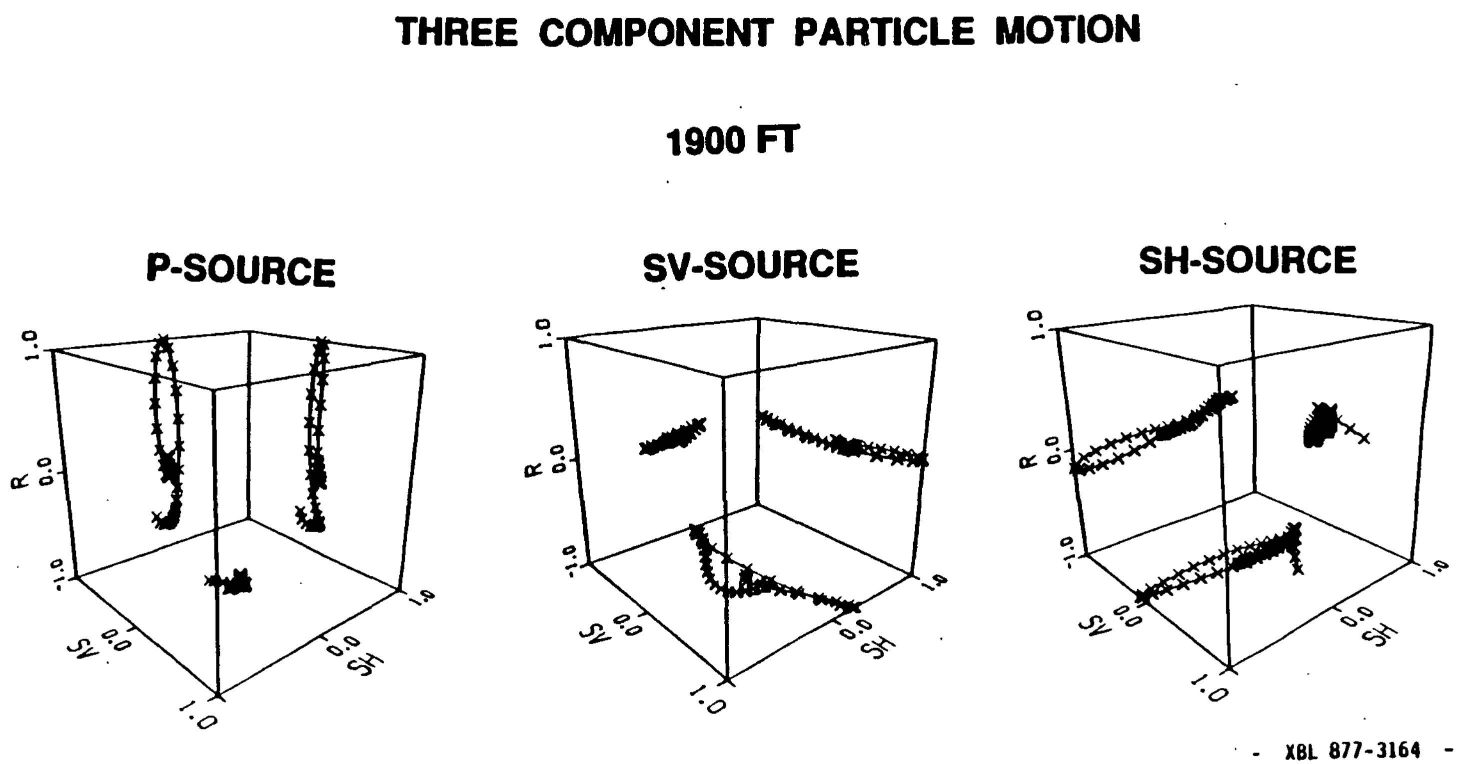

Figure 38. Three component particle motion for far-offset P, *SH*, and *SV* sources at 1900' depth level.

4. NEAR-OFFSET PARTICLE MOTION DESCRIPTIONS

4.1. SH_t SOURCE

NEAR-OFFSET SH_t SOURCE	
DEPTH (FEET)	DESCRIPTION
500	The SH-SV motion is fairly linear with dominant SH orientation. A strong radial component is seen in the Radial vs SH plane.
1000 - 2200	The first motion is SH, but the arrival then forms an ellipse rotated approximately 45 degrees from the SH axis.
2300 - 2500	The first motion is generally SH, but the dominant direction is SV with the motion more circular at 2450' and 2500'. Very little radial motion is observed.
2550 - 4000	These traces are too noisy to use particle motion analysis.
4050 - 4350	The motion is elliptical in the SV-SH plane with a dominant SH direction and no radial motion.
4400 - 4700	The SV and SH motion begins to be out of phase with each other and the amount of SV motion at each level decreases until at 4700' there is linear SH particle motion.
4800 - 5450	The shear motion is again elliptical with a dominant SH motion and little radial motion.
5450 - 5650	The SH and SV motions are about equal, though they are out of phase giving odd shapes. There is some radial motion at these levels and the first motion is always SH.

4.2. NEAR-OFFSET SH_r SOURCE

NEAR-OFFSET SH_r SOURCE	
DEPTH (FEET)	DESCRIPTION
3050 - 4200	These traces are too noisy for particle motion analysis.
4250 - 4350	The first motion is in the SV direction. At 4250' the SH motion is as large as the SV motion. The amount of SH motion decreases to a minimum at 4350'.
4400 - 4550	The SH motion increases to give circular polarization at 4550' with some radial energy.
4600 - 4800	The motion is split into two orthogonal polarizations, both rotated approximately 45 degrees from the SH and SV axis.
4850 - 5200	The two polarizations are approximately aligned with the SH and SV axis.
5350 - 5650	The motion takes on a figure 8 pattern with dominant polarization which rotates from aligned on SH to aligned on SV.

5. FAR-OFFSET PARTICLE MOTION DESCRIPTIONS

5.1. SH_t SOURCE

FAR-OFFSET SH_t SOURCE	
DEPTH (FEET)	DESCRIPTION
1500	The main arrival has very linear SH motion. Late in the arrival there is more elliptical motion.
1900 - 2200	Very linear SH motion with little radial motion.
2350 - 2875	The motion develops a significant SV component of motion. SH dominant elliptical motion continues to 2875' with radial motion at 2725' and 2800'.
2950 - 3100	The motion is nearly circular with all three components nearly equal in amplitude.
3175 - 3500	The radial motion decreases and the ellipse becomes more linear in the shear plane, with an SH direction.
3550 - 3775	The shear motion ellipse broadens as more SV motion is seen.
3925 - 4225	The first motion is SH, but the wavelet takes on SV and radial motion, and then returns to SH motion.
4300 - 4675	There is no radial motion, and the motion is elliptical with SV orientation.
4750 - 5275	The motion is still elliptical, but the direction of the orientation is rotated about 45 degrees from the axis and more radial motion is seen.
5350 - 5425	The shear motion is roughly a figure 8 aligned mainly with SH and with the latter part having large radial motion.
5575 - 5650	The shear motion is mainly aligned on the SH axis with strong SV and radial components.

5.2. FAR-OFFSET *SV* SOURCE

FAR-OFFSET *SV* SOURCE	
DEPTH (FEET)	DESCRIPTION
1500 - 2050	The shear motion is a fairly linear ellipse dominant SV motion.
2125 - 2500	The ellipse begins to rotate off of the SV axis and develop into two polarizations which are about 45 degrees apart. The later polarization has some radial motion.
2500 - 2800	These levels are too noisy for particle motion analysis.
2800 - 5500	The shear motion for all these depths is mostly linear SV motion. There is significant radial motion around 3025', 4525' and between 4900' and 5050'.

CHAPTER 7

INTERPRETATION OF ANISOTROPY ANALYSIS AND EVENT IDENTIFICATIONS

The interpretation of the various observations made with the VSP data is somewhat difficult because seismic data interpretation needs good geologic control, especially with the more experimental techniques such as particle motion analysis. Currently, only preliminary findings about the SSSDP are available. The available geologic information is shown in Figure 5 which has the fractional parts of sandstone, siltstone and claystone with the amount of alteration from sulfides, anhydrite, chlorite and epidote. Gaps such as the one from 6700' to 6900' are due to lost circulation which prevented mud logging and core samples. The interpretation of the seismic data will attempt to link the anisotropy analysis and the event identification. Among the factors which may affect the VSP data are the local stratigraphy, fracturing with or without fluid, and regional tectonic stress. Particular attention is paid to indications of fracture zones since this is one of the goals of the VSP. The interpretation separates the discussion of the horizontal plane anisotropy data from the *SV* vs SH_t anisotropy data.

1. HORIZONTAL PLANE ANISOTROPY - NEAR-OFFSET DATA

As discussed previously, the near-offset shear wave data represent a horizontal plane anisotropy experiment. Figure 39 shows a summary of the near-offset anisotropy data. Unfortunately, the data are incomplete since the SH_r source has no shallow data. The left column of Figure 39 shows the velocity information, the center and right hand columns shows the generalized particle motion description for first arrivals from the SH_t source and SH_r source, respectively.

There is a problem with interpreting near-offset particle motion analysis. The determination of the horizontal rotation angle theta is inaccurate for vertically incident waves. Therefore, the absolute orientation of the rotated SH and SV components may vary with depth. However, since the components are still orthogonal, non-linear motion implies there is shear wave splitting. Only the absolute orientation of the motion is unknown. For instance, the variation in ellipse orientation seen on SH_t source plots between 2000' and 2050' in Appendix 2 for may be due to incorrect rotation, but the non-linear motion still indicates anisotropy.

Between the surface and 2500', the elliptical nature of the particle motion plots shows shear-wave splitting within the horizontal plane. The observed splitting must be caused by horizontal plane anisotropy. A possible cause of this anisotropy is depositional alignment of mineral grains due to the dominate Northwestern flow of sediments from the Colorado river to the Salton Sea and its predecessors. Another possible cause is variation of the stress field within the Salton Trough caused by tectonic forces.

Below 4000' more information is available. The travel time information, which begins at 4250', shows the SH_t-generated wave is slower than the SH_r-generated wave. The particle motion plots for both sources show shear-wave splitting with two dominant polarizations of motion which appear to change phase with each other. A change in shape is interpreted as a phase change. The phase changes are probably due to the varying difference in travel time of each polarization. The changes in orientation of a given shape may be the rotation error.

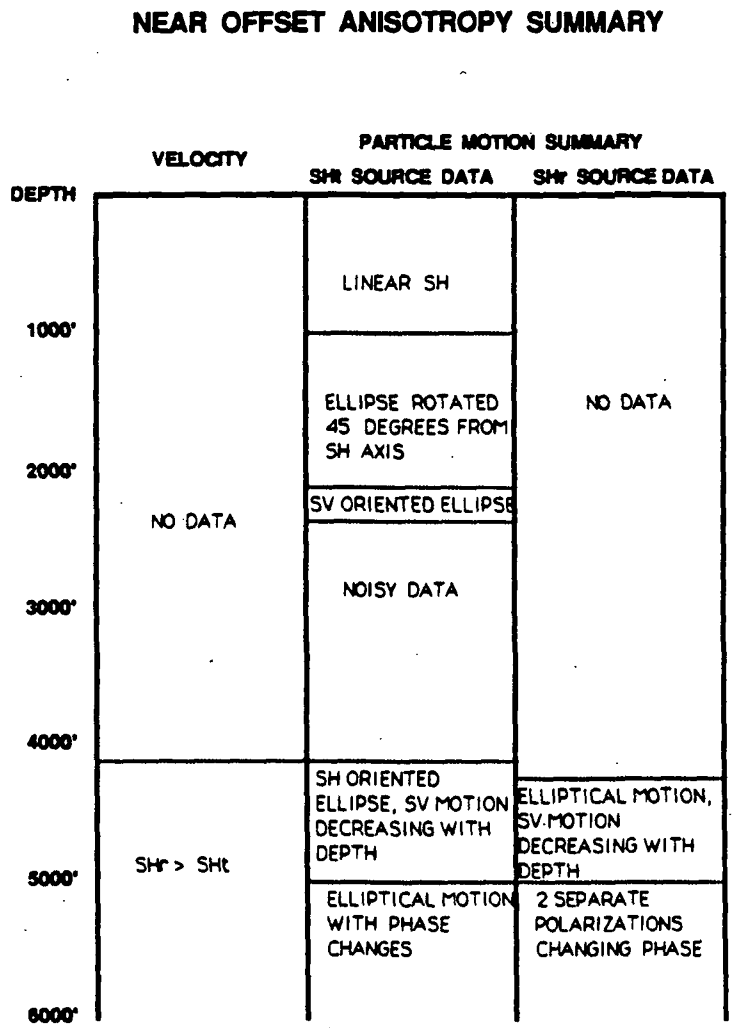

Figure 39. Near-offset anisotropy data summary.

2. *SV* VS SH_t ANISOTROPY - FAR-OFFSET DATA

The far-offset anisotropy data provide a much more complete data set. The results are outlined in Figure 40 which gives the travel time and particle motion summaries. The shallow zone above 1500' appears to be fairly isotropic with equal travel time to 1500' and linear particle motion for both sources' arrivals at 1500'. From 1900' to 2200' the SH_t-generated waves are increasingly faster than waves from the *SV* source. Between 2200' and 2500' the particle motion shows evidence of anisotropy, with the first shear arrival from the SH_t source developing SV motion and the *SV* source first arrival splitting into two polarizations. The travel time and particle motion information both indicate a change near 2200'. Velocity increases are seen for both P and S waves near 2200' with the S velocity showing a large increase. There are indications of reflections near 2200', but identification was not possible because of the lack of data between 1500' and 1900'. There does appears to be a general transition zone around 2200'. Geologically, from 1700' to 2100' there is the first anhydrite alteration, possibly marking the "cap rock" seen in the SSGF. The seismic effects may be related to the transition from anhydrite alteration in a mostly claystone layer to an alteration free sandstone layer at 2200'.

From 2200' to 3000' the *SV*- and SH_t-generated arrivals have approximately equal travel time indicating a relatively isotropic region. The SH_t source first arrival gives elliptical particle motion in this region with SV motion increasing with depth. SV motion in the SH_t-generated arrival is probably due to the local high of SV velocity (seen at 2200' in Figure 36) which causes SV motion to move into the SH_t-generated arrival. From 2500' to 2800' the poor signal-to-noise in the *SV* source data prevent seeing the transition from split *SV*-generated arrivals to linear *SV*-generated arrivals.

The zone from 2900' to 3200' has a number of anomalous properties. At 3000' a local high in the SH/SV velocity ratio develops with a peak SH/SV ratio at 3250'. The SH_t-generated first arrival gives nearly circular polarization in this zone, and both sources give a large amount of radial motion. Anomalous vertically scattered P-waves seen from the far-offset P source (Figure 27) appear to originate from about 2900' and indications of scattering from 3000' are seen on the SH_t source data.

The near-offset P source data show a reflection at 2900', and there is a high P velocity zone at 3000' to 3050' followed by a low velocity zone at 3200' to 3300'.

Figure 41 shows the hodographs for the SH_t source's first arrivals from 2875' to 3175'. The 2875' hodograph shows a narrow ellipse in the SH-SV plane with dominant SH motion. The amount of Radial and SV motion increases in the hodographs at 2950' and 3025', and then decreases at 3175' leaving the motion similar to the 2875' level. A possible interpretation of the increased radial energy is P-wave scattering. If the radial motion within these shear wave arrivals is caused by P-wave scattering, it would have to be caused by an inhomogeneity near the well since the higher P-wave velocity would cause the scattered P-wave energy to separate from the shear wave arrival.

A key finding relating to this anomalous zone is that the core from 3012'-3020' had an "open and permeable fracture zone " with indications that "this fracture zone presently contains a brine" (McKibben and Andes, 1986). There is anhydrite alteration above 2900' which may serve as an impermeable cap, and the nuclear porosity log showed an increase in percent porosity between 2900' and 3100' (Paillet, 1986). The lithology in this zone is mostly sandstone from 3000' to 3200' with some shale, siltstone and claystone. The anomalous seismic effects are most likely caused by a fluid filled fracture zone near the well.

Below 3300' the SH velocity decreases with respect to SV, and below 3500' the SH_t-generated wave has more total travel time than the SV-generated wave. The SH_t source first arrival particle motion becomes more linear from 3200' to 3500'. The effect of motion becoming more linear may be caused by phase changes between SH and SV motion since the major axis of the ellipse moves off the SH axis and then moves back to the SH axis as the motion becomes more circular from 3500' to 3800'.

After 3800' the particle motion of the SH_t-generated arrival develops an early SH motion and a later SV motion. This is seen on the hodographs from 3925' to 4150' in Appendix 2. A radial component of motion is seen developing from 4075' to 4225'. The separation of SH and SV motion is probably a local effect, possibly from aligned fractures which have slowed the SV motion more than that seen from the total travel time measurement. The observed radial motion could also result from fracturing which causes P-wave scattering. The P-wave scattering could be caused by SV motion since the radial motion and the SV motion occur at the same time within the first arrival. There are reflections from the near-offset shear-wave data generated between 4100' to 4200' (events R1 and G on Figures 22c and 21). The zone from 3900' to 4200' is associated with large anhydrite alteration and some epidote alteration which indicates hydrothermal activity and fracturing.

For the SH_t data below 4300', radial motion stops and shear motion becomes more circular. At 4600' and 4675' the shear motion ellipse actually takes on an SV orientation as the SH motion decreases. This effect is probably due to a local high in SV/SH velocity ratio at 4675'. At 4300' Poisson's ratio reaches a minimum and begins increasing after decreasing continuously.

From 4800' to 5650' both SH and SV motion are seen on arrivals from the SH_t source with the phase changing with depth giving varying shapes from circular to 'figure 8' motion at 5350' and 5425'. Large radial motion at 5500' and 5575' may be caused by local fracturing, and the radial motion again appears at the same time within the arrival window as SV motion. A P-wave reflection was also seen at 5450'. The seismic effects between 4500' and 5500' may be related to the epidote alteration which begins at 4400' and is indicative of strong hydrothermal process. The epidote alteration has a maximum of 1% at 4800', decreases to minimal amounts from 4200' to 4400' and increases to nearly 1% again from 5450' to 5600' and then is not detected until 6100' (see Figure 5).

One observation which may have regional implications is the consistent particle motion seen in the *SV* source first arrivals. Waves generated by the *SV* source motion are a stable propagation mode which only shows anisotropic effects in the 2100' to 2500' range. Below 2800' the *SV* source data have consistently linear SV motion in the SH-SV plane with some radial motion seen at various depths. The nearly isotropic propagation of SV polarized waves may be a regional effect since this polarization is oriented along the axis of the spreading center while the SH_t orientation is perpendicular to the axis. Another possible explanation is that all the anisotropy is in relatively thin horizontal beds to which the SV motion, with its long vertical wavelength, is not sensitive. More tests would be necessary to confirm either hypothesis. One such test would be conducting another VSP with a far-offset 90 degrees around the well from ours, giving the *SV* and SH_t sources opposite polarization from this survey, and then looking for linear SH or SV motion. If the SH motion is linear it would indicate a regional cause, and if the SV motion was still linear it would indicate a local bedding cause.

FAR OFFSET ANISOTROPY SUMMARY

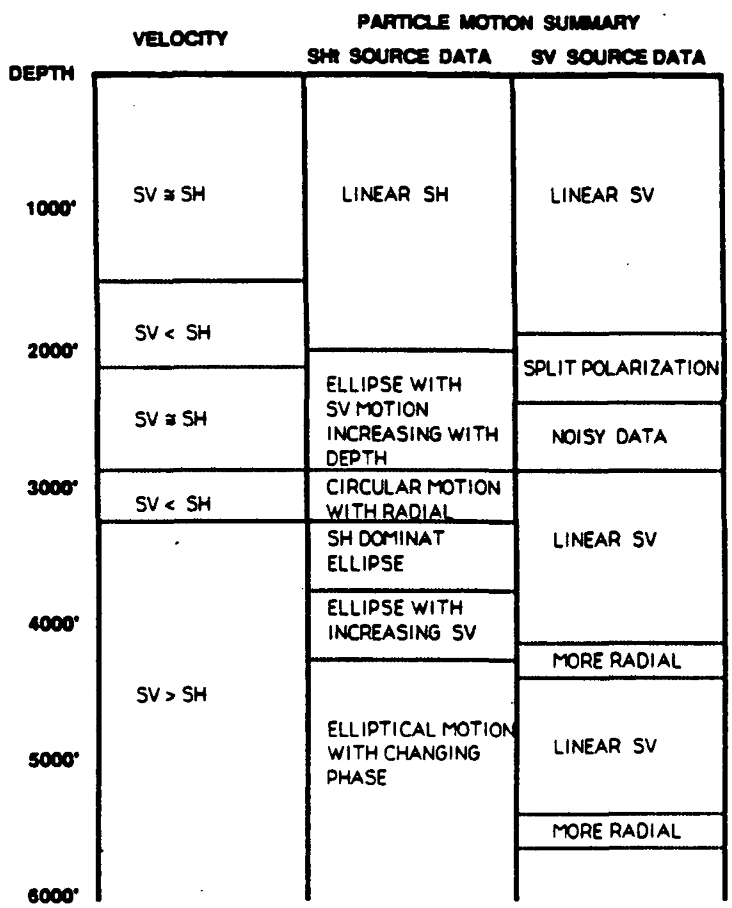

Figure 40. Far-offset anisotropy data summary.

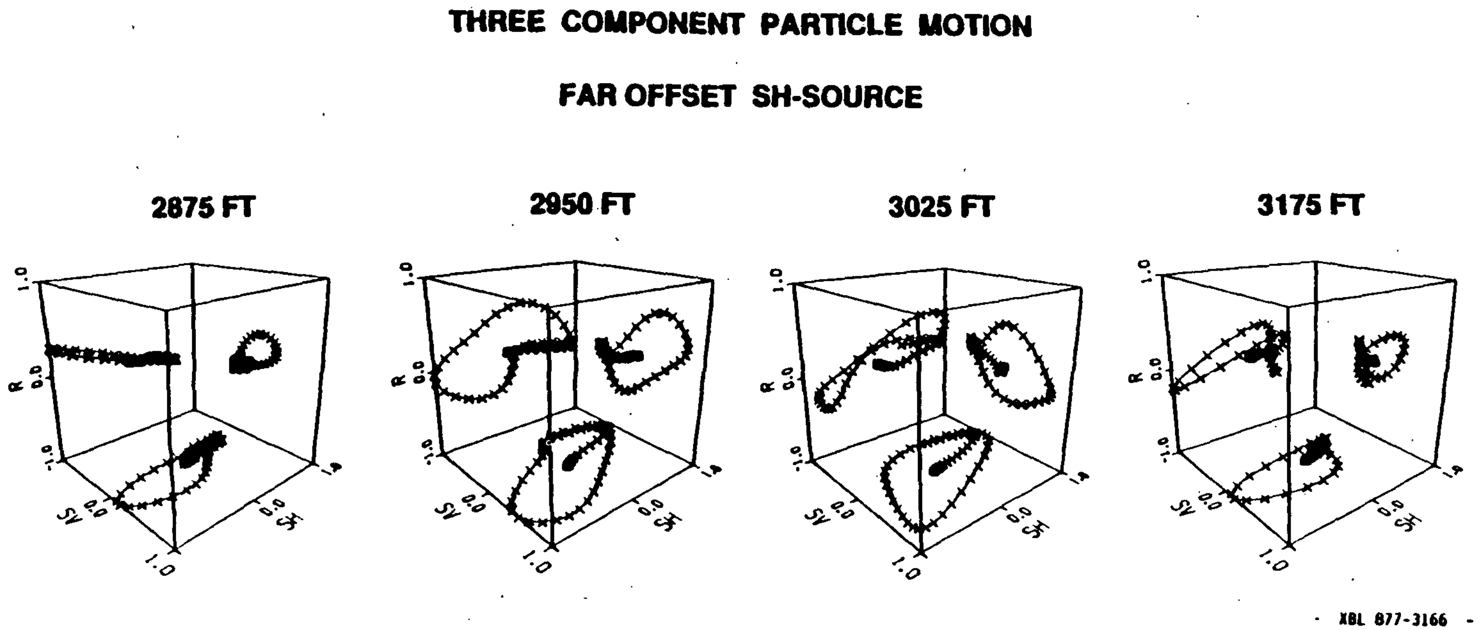

Figure 41. Three component particle motion from far-offset *SH*, source near 3000' depth zone.

CHAPTER 8

FRACTURE ORIENTATION USING POLARIZATION DIRECTION

In the previous section the particle motion of the first shear-wave arrival was used to analyze anisotropy. The presence of anisotropy is inferred by any variation in the direction of motion from the isotropic components of radial, SH and SV motion. Within the SSGF the anisotropy is probably affected by fracturing associated with hydrothermal alteration and fluid circulation. Since the specific orientation of any one fracture zone is unknown, a method of analyzing the VSP data to detect this orientation was used. The direction of shear-wave polarization after passing through an aligned set of fractures will be parallel and perpendicular to the plane of the fracture set (Crampin 1985, Majer et al. 1986). Using this information, an attempt was made to detect zones in which the first arrival particle motion became aligned in two directions while passing through some zone in the well. This requires computing the particle motion orientation as a function of time within the first arrival wavelet.

The data used in the previous analysis of particle motion could not be analyzed directly because the coordinate system used was the wavefront system whose orientation varied as a function of depth. What is needed to detect fracture orientation is a "borehole" coordinate system which has the same coordinate orientation at every depth. Such a coordinate system has components vertical (V), horizontal towards the source (H1), and horizontal transverse to the source (H2) as shown in Figure 9. The data traces were rotated into this system by the same rotation algorithm used previously. For borehole coordinates, the original vertical component is not altered while the two horizontals are rotated into H1 and H2 (see ROTBOR.FOR in Appendix 4 for FORTRAN code).

The data from the far-offset shear sources were rotated into borehole coordinates for orientation analysis. Once the traces were in borehole coordinates, the polarization direction could be compared from level to level. The computation of polarization direction as a function of time was accomplished with a modification of the covariance matrix analysis used to find the geophone rotation. A window of 15 samples length (30 msec) was passed through the first arrival wavelet moving 2 samples (4 msec) at a time. Each time the window moved, the direction of polarization within the window was computed. Because each depth had a different first arrival window length, the number of polarization computations varied with depth. The rectilinearity function was used to estimate the degree of accuracy of each calculation.

The complete listing of polarization directions with their rectilinearity function values for the far-offset shear sources is given in Appendix 3. The angle ϕ is in degrees down from vertical, and the angle θ is in degrees counterclockwise from the source azimuth, which is approximately S45E. The angle θ is non-unique since θ + 180 degrees is also an eigen vector solution (in other words, the fracture orientation forms a plane not a vector).

Careful reading of the polarization direction data shows a number of depths which have a unique direction with high rectilinearity value. It may be that some or all of these are related to localized fracture orientation, but it is also possible they are simply errors in rotation or thin bed multiple noise. There is one zone which gives some appearance of splitting the far-offset SH_t-generated arrival into distinct polarization directions over a range of depths. This zone is centered at 4000'. The data are displayed by plotting the polarization directions on a separate borehole axis system for each level. A unit length vector is plotted for each window's polarization computation. Figure 42 shows the orientations from 3775' to 4150' for arrivals from both the SH_t and SV sources.

The arrows in Figure 42 indicate the directions of polarization which develop for the SH_t source at 3925' and 4000'. Notations in Appendix 3 show how the wavelet switches between these two directions of polarizations (labeled D1 and D2) at progressively earlier times within the wavelet. This is the effect one would expect to see if one polarization direction represented a faster direction of propagation. The rectilinearity function also changes from nearly one at early times, to low values as the direction switches and then returns to nearly one late in the arrival wavelet. This indicates two coherent polarization directions which overlap within the wavelet. With no other evidence of a fracture zone at this depth, it is difficult to say what this polarization analysis represents. The consistent data over a range of depths would rule out rotation error or random noise. Interbed multiple interference could still be a source of error.

The polarization direction analysis provides another use. Figure 42 clearly shows the difference between arrivals from the SH_t source and the SV source. While the SH_t-generated arrivals have a varied polarization direction, the SV-generated arrivals have a very consistent direction at every depth. This is a display of the isotropic propagation of the SV-generated waves juxtaposed with the anisotropic propagation of the SH_t-generated waves. Figure 43 shows polarization direction plots for shallower depths. The difference between SH_t and SV data is again shown. The 1500' level in Figure 43 shows how the wavelet is polarized in an isotropic zone; the SV-generated motion is tilted because of the incident ray angle while the SH_t-generated motion is on the H2 axis which is parallel to the source motion.

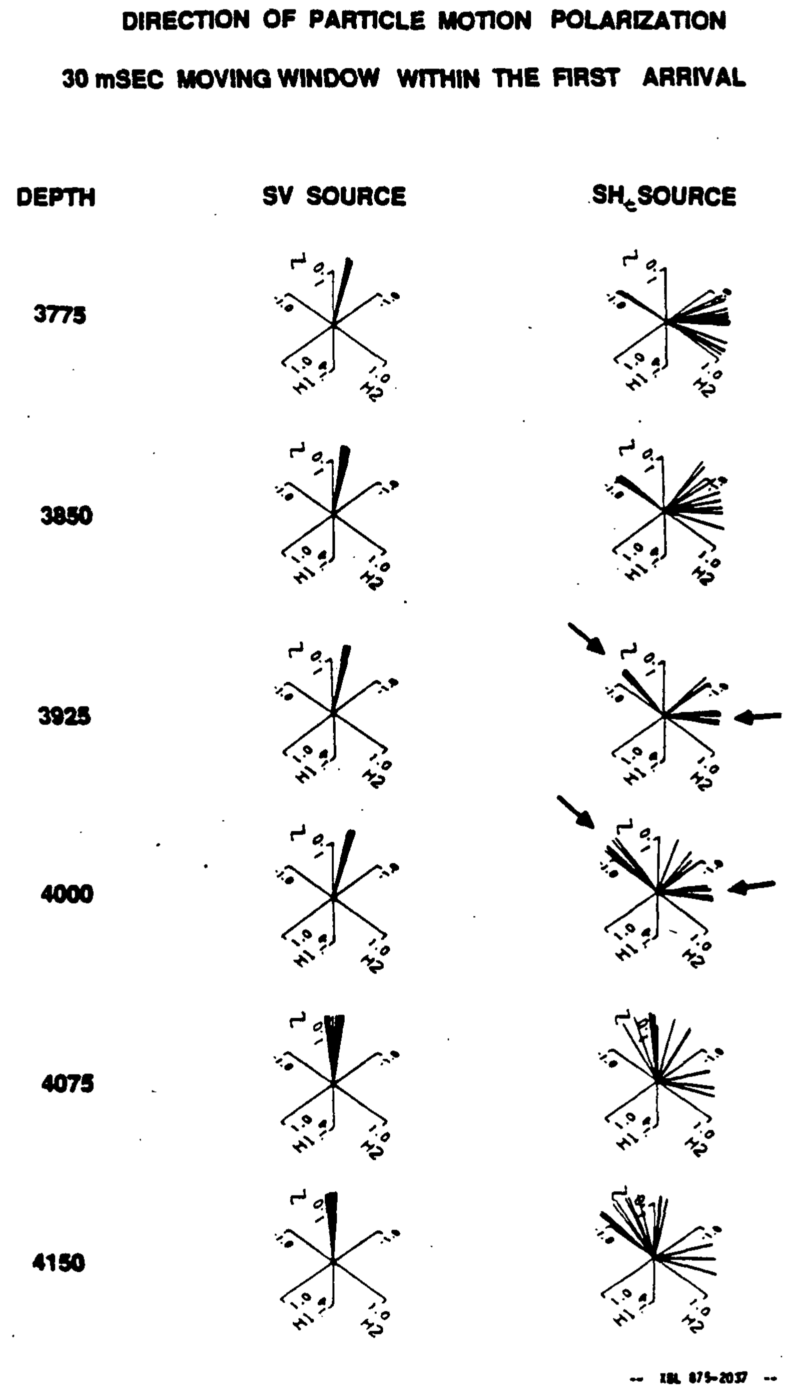

Figure 42. Direction of particle motion polarization for a 30 msec window within the first shear arrival for far-offset SH_t and SV sources near 4000' depth.

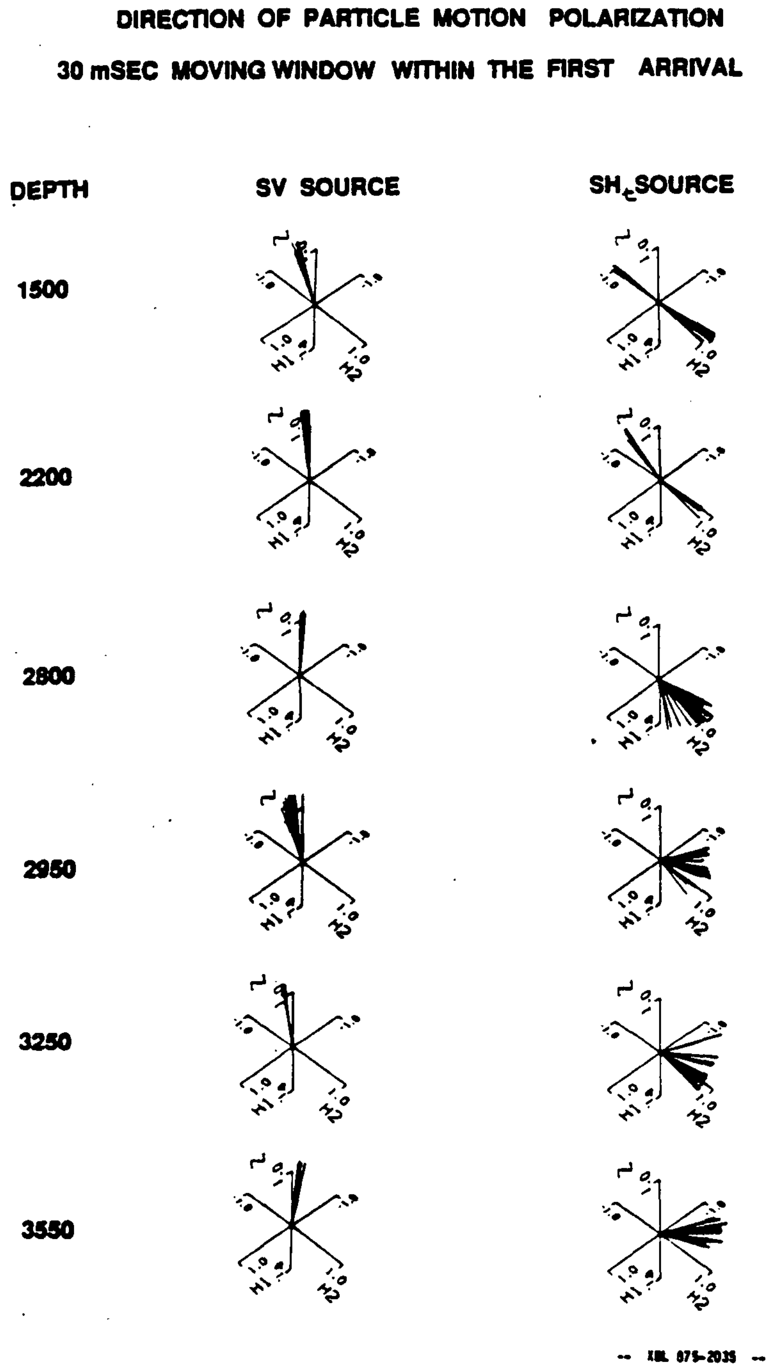

Figure 43. Direction of particle motion polarization for a 30 msec window within the first shear arrival for far-offset SH_t and SV sources.

CHAPTER 9

CONCLUSIONS - SUMMARY

This section is a summary of data analysis results for each of the stated goals of this thesis. The areas to be summarized are standard VSP analysis, anisotropy analysis, fracture detection and orientation analysis. At times these areas overlap and results are found to apply to more than one conclusion. All the results are brought together here in a summary of the seismic wave propagation effects seen with the SSSDP VSP.

1. STANDARD VSP ANALYSIS

The standard VSP analysis includes velocity analysis and identification of events seen on various profiles. The velocity analysis proved adequate for the modeling and event identification analysis used in this study. The P-wave velocities were accurate when compared to the other well information available. The S-wave velocities were sufficient for modeling although the poor data quality between 2500' and 4000' proved a hindrance especially when analyzing the anomalous zone around 3000'. The lack of accuracy in the near-offset θ determination may also have created some error in the first break picks. An error in θ will cause a phase shift on each of the three components. A phase shift would cause the first trough to be at the wrong time. The consistency of the first arrival indicates this error is small, however a change in wavelet character is seen on the last 4 traces of the shear source sections. This change may be a rotation error. The difficulty in determining θ from a near offset increases with depth as the raypath approaches vertical. The shear velocities determined from these deepest 4 levels and from the noisy levels between 2500' and 4000' are most likely to be inaccurate.

The identification of events was successful with all coherent events identifiable as reflections, multiples, tube waves, or the more unusual scattered waves. There are relatively few reflectors within the depths covered with the VSP and none were strong enough to be seen by all of the sources .

All the VSP sections did show reflections from below the deepest VSP level. The shallowest and most often seen reflection is from the 6700' to 6900' zone where the lost circulation indicates a fractured reservoir is located. The far-offset SH_t and SV data have a reflection from 6800' while the near-offset P-source data have a reflection from 7000' and the far-offset P-source data have a reflection from 6900'. The strength and consistent appearance of this reflection indicates that the fracture zone has an areal extent of at least a few hundred feet and that it is a relatively horizontal feature. A steeply dipping reflector would be seen to have curved moveout across the VSP section. Deeper reflectors were indicated on all the profiles, but their identification as reflections is not definite and their depth of origin can not be accurately assessed.

The detection of vertically scattered P-waves from the far-offset P-source was an indicative of a heterogeneity near 3000'. The scattered waves were the most obvious indication of the 3000' zone which also shows a reflection on the near-offset P-source survey and shows radial particle motion within the shear arrival. The anomalous seismic effects of this zone indicate fracturing.

2. ANISOTROPY ANALYSIS

The analysis of travel time for orthogonal polarizations of shear sources did find anisotropic propagation. The near-offset data, which was only useful over a limited depth range, shows anisotropy within the horizontal plane. The particle motion analysis of this data was ambiguous because the geophone component rotation is inaccurate at close offsets. However, both near-offset shear source first arrivals show non-linear particle motion, an effect which is only dependent on having orthogonal components which the near-offset rotation does provide. This non-linear particle motion shows horizontal plane anisotropy exists. The lack of accurately oriented components prevented analysis for any axis of symmetry within the horizontal plane. While the absolute orientation of the near-offset shear wave particle motion is questionable, splitting of the wave form is occurring. The horizontal plane anisotropy needs to be measured with an oriented geophone to obtain more information.

Anisotropy seen with the far-offset data is the more standard SH vs SV propagation anisotropy. The travel time data shows a crossover in velocity structure with SH propagation faster shallow and SV propagation faster at depth. There is also some localized structure seen in the travel time difference plot. Most notable is the local high in SH propagation velocity from 3000' to 3500'. This may be related to the anomalous zone around 3000' with ray path coverage spreading the effect to deeper levels.

The particle motion analysis showed the SV propagation mode to be an axis of symmetry with splitting of the SV motion only seen from 2100' to 2500'. Some zones did show significant radial motion in the shear arrival from the *SV* source which may be scattering of P-wave energy within the shear wavelet.

The SH_t-generated waves showed a complicated particle motion having SH, SV and radial motion whose relative amplitudes varied with depth. The SH_t-generated particle motion is indicative of anisotropic propagation. The amount of travel time difference between arrivals from SH_t and *SV* sources (up to 1%) can explain the shear wave splitting seen in the data from the SH_t source.

Given the SH_t data, the lack of splitting in the *SV*-generated first arrival is unusual. There is not enough separation in time to cause SH motion generated by the *SV* source to move out of the first arrival. The maximum travel time difference is 15 msec while the wavelets were analyzed with windows at least 50 msec long. The linearity of the motion in arrivals from the *SV* source does show that the *SV* source motion is an axis of anisotropy symmetry.

The splitting and travel time difference measured in the horizontal plane does indicate that the horizontal plane anisotropy needs to be included in future anisotropy studies. The *SV*-generated first-arrival particle motion has a component of motion with the polarization of the SH_r source. Strong anisotropy in the horizontal plane could be misinterpreted as SV vs SH anisotropy. This is especially true for surface reflection data using SH and SV sources because they have no horizontal plane information. In this survey, the horizontal plane anisotropy has half the effect of the SH-SV anisotropy (0.5% vs 1.0%).

3. FRACTURE DETECTION

The first discovery of interest to fracture detection is the strong reflection from the fractured reservoir between 6700' and 6900'; all the sections which could be dipfiltered showed a reflection from this zone. The strength of the reflections indicates that a surface seismic survey could track this event and possibly delineate the reservoir. The relative strength of the shear wave reflections on the vertical component points out the need for three component recording. It is unfortunate that VSP data could not be recorded through this zone to study its effects on seismic wave propagation.

The anomalous zone at 3000' shows the effects of fracturing. It is scattering P-waves from both P and S wave sources. The shear velocity anisotropy shows a local high just below this zone, an effect which indicates localized fracturing. The scattered P-wave events on the radial component of the *SV* source data (events K and L on Figure 33c), could lend themselves to inversion schemes to identify their source location with more accuracy.

The appearance of radial motion within the shear wave first arrival may also be an indication of P-wave scattering from fractures. Assuming the rotation is reasonably accurate, it would take severe anisotropy to cause any significant shear motion along the propagation direction. The scattering of P-energy by the shear wave seems a most likely explanation of the large amount of radial motion seen within the shear arrival at some depths.

4. FRACTURE ORIENTATION ANALYSIS

The attempt to find the orientation of some fracture zone with this data set was limited by the lack of a known zone within the depths surveyed. Given that limitation, the procedure of analyzing the particle motion orientation as a function of time within the first arrival did produce some interesting results. First, the display of particle motion direction proved to be a good graphic for the linearity of the *SV* source first arrival motion as compared to the SH_t source's first arrival motion. Within the SH_t's first arrival motion, one zone of split orientation was found. This zone, from approximately 3900' to 4200', gave the results which were expected for two polarizations of differing velocity. An estimate could be made of the absolute orientation of these two polarizations. No core data showed fracturing in this zone. However, this is a zone with anhydrite alteration indicating hydrothermal processes which could have associated fracturing outside the borehole. While no definitive conclusions could be reached about fracture orientation, the analysis technique does show enough promise to warrant further study in a more controlled situation.

REFERENCES

Ahmed, H., Dillon, P. B., Johnstad, S. E., and Johnston, C. D., 1986, Northern Viking Graben multilevel three-component walkaway VSPs - a case history, *First Break, v4*, n10, p9-27.

Babcock, E. A., 1971, Detection of active faulting using oblique infrared aerial photography in the Imperial Valley of California, *Geol. Soc. Am. Bull., v82*, p3189-3196.

Balch, A. H.,and Lee, M. W., (editors), 1984, *Vertical Seismic Profiling - Technique, Applications, and Case Histories*, International Human Resources Development Corporation, Boston, 488 pages.

Balch, A. H., Lee, M. W., Miller, J., J., and Ryder R. T., 1982, Use of vertical seismic profiles in seismic investigations of the earth, *Geophysics, v47*, p906-918.

Becker, D. F., and Perelberg A. I., 1987, Seismic detection of subsurface fractures, S.E.G. Midwest Meeting Abstract, *Geophysics, v52*, n5, p708.

Biehler, S., Kovach, R. L. and Allen, C. R., 1964, Geophysical framework of northern end of Gulf of California structural province, *Am. Assoc. Pet. Geol. Mem., v3*, p126-143.

Cassell, B. R., 1984, Vertical Seismic Profiles - An Introduction, *First Break, v2*, n11, p9-19.

Combs, J., and Hadley, D., 1977, Microearthquake investigation of the Mesa Geothermal Anomaly, Imperial Valley, California, *Geophysics, v42*, p17-33.

Crampin S., 1985, Evaluation of anisotropy by shear-wave splitting, *Geophysics, v50*, n1, p142-152.

Crampin S., Bush, I., Naville, C., Taylor D., 1986, Estimating the internal structure of reservoirs with shear-wave VSPs, *The Leading Edge, v5*, n11, p35-39.

Dillon, P.B., and Thomson, R. C., 1984, Offset source VSP surveys and their image reconstruction, *Geophys. Prosp., v32*, p790-811.

Douma, J., Helbig, K., 1987, What can the polarization of shear waves tell us?, *First Break v5*, n3, p95-104.

Elders, W. A., Rex, R. W., Meidav, T., Robinson, P. T,and Biehler, S., 1972, Crustal spreading in Southern California, *Science, v178*, p15-24.

Fitch, A. A., 1984, Interpretation of vertical seismic profiles, *First Break, v2*, n6, p19-23.

Frith, R. B., 1978, *A seismic refraction investigation of the Salton Sea Geothermal area Imperial Valley California*, M.S. Thesis, University of California, Riverside, Calif., 94pp, (unpublished).

Ganley, D. C., and Kanasewich, E. R., 1980, Measurement of absorption and dispersion from check shot surveys, *J. Geophys. Res., v85*, p5219-5226.

Gilpin, B. and Lee, T. C., 1978, A microearthquake study in the Salton Sea Geothermal area, California, *Bull. Seismol. Soc Am.*, *v68*, p441-450.

Griscom, A. and Muffler, L. J. P., 1971, Aeromagnetic map and interpretation of the Salton Sea geothermal area California, *U.S. Geol. Survey, Geophys. Invest. Map, GP 754.*

Hardage, B. A., 1981, An examination of tube wave noise in vertical seismic profiling data, *Geophysics, v46*, p892-903.

Hardage, B. A., 1985, *Vertical Seismic Profiling - Part A: Principles*, Geophysical Press Limited, London, 509 pages.

Kanasewich, E. R., 1981, *Time Sequence Analysis in Geophysics*, The University of Alberta Press, Edmonton, Canada, 480 pages.

Kassameyer, P. W., 1976, Preliminary interpretation of resistivity and seismic refraction data from the Salton Sea Geothermal Field, *Lawrence Livermore Natl. Lab., UCRL-52115*, Livermore, Calif.

Kelley, V. C. and Soske, J. L., 1936, Origin of the Salton volcanic domes, Salton Sea, California, *J. Geol.*, *v44*, p496-509.

Leary, P. C. and Henyey, T. L., 1985, Anisotropy and fracture zones about a geothermal well from P-wave velocity profiles, *Geophysics*, *v50*, n1, p25-36.

Lee, M. W. and Balch, A. H., 1983, Computer Processing Of Vertical Seismic Profile Data, *Geophysics, v48*, p272-287.

Majer, E. L., McEvilly T. V., Eastwood F., and Myer L., 1986, Fracture detection using P- and S-wave VSPs at the geysers geothermal Field, *Lawrence Berk. Lab. report #20100*, Berkeley, California.

Martin, Marshal A., 1987, Three-component seismic investigation of a fractured reservoir, Silo Field, Wyoming, S.E.G. Midwest Meeting Abstract, *Geophysics*, *v52*, n5, p708.

Meidav, T. and Furgeson, R., 1972, Resistivity studies of the Imperial Valley Geothermal area, California, *Geothermics*, *v1*, p47-62.

Meidav, T., West, R., Katzenstein, A. and Rostein, Y., 1976, An electrical resistivity survey of the Salton Sea Geothermal Field, Imperial Valley, California, *UCRL-13690*, *Lawrence Livermore Natl. Lab.*, Livermore, Calif.

McKibben, M. A., and Andes, J. P., 1986, Ore Mineralization and Related Fluid Inclusion Properties in the SSSDP Cores, Report to the SSSDP Principal Investigators' Session, *Geothermal Resources Council meeting*, September 1986, Palm Springs CA.

Muffler, L. J. P. and White, D. E., 1969, Active metamorphism of upper Cenozoic sediments in the Salton Sea Geothermal Field and the Salton Trough, Southeastern California, *Geol. Soc. Am. Bull.*, *v80*, p157-182.

Oristaglio M.L., 1985, A Guide to the current uses of vertical seismic profiles, *Geophysics, v50,* n12, p2473.

Palmer, T. D., Howard J. H., Lande D.P., editors, 1975, Geothermal development of the Salton Trough, California and Mexico, *Lawrence Livermore Laboratory report, UCRL - 51775*, Livermore, California.

Paillet, F. L., editor, 1986, Preliminary Report On Geophysical Well-Logging Activity On The Salton Sea Scientific Drilling Project, Imperial Valley, California, *U.S.G.S. Open-File Report 86-544*, U.S. Geological Survey, Denver, Co.

Peacock S., and Crampin S., 1985, Shear-wave vibrator signals in transversely isotropic shale, *Geophysics, v50,* n8, p1285-1293.

Randall, W., 1974, *An analysis of the subsurface structure and stratigraphy of the Salton Sea geothermal anomaly, Imperial Valley, California,* Ph.D. thesis, University of Calif., Riverside, Calif. (unpublished).

Schnapp, M. and Fuis, G. 1977, *Preliminary catalog of earthquakes in the Northern Imperial Valley, October 1, 1976 to December 31, 1976,* U.S. Geological Survey Seismological Laboratory, Pasadena, Calif.

Sharp, R. V., 1982, Tectonic setting of the Imperial Valley region, *USGS Professional Paper 1254,* U. S. Geological Survey.

Stewart, R. R., Turpening, R. M., and Toksoz, M. N., 1981, Study of a subsurface fracture zone by vertical seismic profiling, *Geophy. Res. Lett., v8,* p1132-1135.

Tatham, R. H., 1982, Vp/Vs and lithology, *Geophysics, v47,* p.336-344.

Thomsen L., 1986, Weak elastic anisotropy, *Geophysics, v51,* n10, p1954-1966.

Toksoz, M. N. and Stewart, R. R., editors, 1984, *Vertical Seismic Profiling - Part B - Advanced Concepts,* Geophysical Press, Amsterdam, 419 pages.

Towse, D. F. and Palmer, T. D., 1975, Summary of geology at the ERDA - Magma - SDG&E geothermal test site, *UCID-17008, Lawrence Livermore Natl. Lab.,* Livermore, Calif.

White, J. E., Monash, C., and Martineau - Nicoletis, L., 1983, Measured anisotropy in Pierre shale, *Geophysical Prospecting, v31,* n5, p709-725.

White, J. E., 1982, Computed waveforms in transversely isotropic media, *Geophysics, v47,* n5, p771-783.

Younker, L. W., Kasameyer, P. W. and Tewhey, J. D., 1982, Geological, geophysical and thermal characteristics of the Salton Sea Geothermal Field, California, *Jour. of Volc. and Geothermal research, v12,* p221-258.

APPENDIX 1

VELOCITY INFORMATION

All the tables and plots in appendix 1 use the following units:

Depths - Feet

Travel Time - Seconds

Velocity - Feet per Second

Ratios - unitless

TABLE 1-1 TRAVEL TIME MEASUREMENTS

Values Of 0.00 Indicate No Data

DEPTH	P TRAVEL TIME	SHr TRAVEL TIME	SHt TRAVEL TIME
500.	0.116	0.000	0.663
1000.	0.197	0.000	0.959
1500.	0.272	0.000	1.096
2000.	0.000	0.000	1.226
2050.	0.339	0.000	0.000
2100.	0.345	0.000	1.261
2150.	0.352	0.000	1.269
2200.	0.357	0.000	1.279
2250.	0.363	0.000	1.287
2300.	0.368	0.000	0.000
2350.	0.374	0.000	0.000
2400.	0.380	0.000	0.000
2450.	0.385	0.000	1.320
2500.	0.391	0.000	1.329
2550.	0.397	0.000	1.336
2600.	0.402	0.000	0.000
2650.	0.406	0.000	0.000
2700.	0.412	0.000	0.000
2750.	0.416	0.000	0.000
2800.	0.421	0.000	0.000
2850.	0.426	0.000	0.000
2900.	0.431	0.000	0.000
2950.	0.436	0.000	0.000
3000.	0.440	0.000	0.000
3050.	0.444	0.000	0.000
3100.	0.448	0.000	0.000
3150.	0.453	0.000	1.436
3200.	0.457	0.000	0.000
3250.	0.463	0.000	0.000
3300.	0.467	0.000	0.000
3350.	0.472	0.000	0.000
3400.	0.476	0.000	1.473
3450.	0.479	0.000	1.480
3500.	0.483	0.000	0.000
3550.	0.487	0.000	0.000
3600.	0.490	0.000	1.501
3650.	0.495	0.000	1.509
3700.	0.498	0.000	0.000
3750.	0.503	0.000	0.000
3800.	0.507	0.000	0.000
3850.	0.512	0.000	0.000
3900.	0.516	0.000	0.000
3950.	0.520	0.000	0.000
4000.	0.523	0.000	0.000
4050.	0.527	0.000	0.000
4100.	0.532	0.000	1.571
4150.	0.536	1.566	1.577
4200.	0.539	1.574	0.000
4250.	0.542	1.580	1.587
4300.	0.546	1.586	1.593
4350.	0.000	1.591	1.598
4400.	0.553	1.596	1.603
4450.	0.556	1.602	1.608
4500.	0.559	1.607	1.614
4550.	0.563	1.612	1.619
4600.	0.566	1.618	1.626
4650.	0.569	1.623	1.631
4700.	0.572	1.628	1.637
4750.	0.576	1.635	1.643
4800.	0.579	1.640	1.648
4850.	0.583	1.646	1.654
4900.	0.586	1.650	1.659
4950.	0.000	1.656	1.664
5000.	0.593	1.661	1.670
5050.	0.596	1.666	1.676
5100.	0.599	1.671	1.682
5150.	0.602	0.000	0.000
5200.	0.606	0.000	1.694
5250.	0.609	1.687	1.699
5300.	0.612	1.692	1.705
5350.	0.615	1.698	1.710
5400.	0.619	1.705	1.716
5450.	0.623	1.711	1.723
5500.	0.626	0.000	1.728
5550.	0.629	1.723	1.733
5600.	0.632	1.730	1.738
5650.	0.636	1.733	1.743

TABLE 1-2 AVERAGE VELOCITY CALCULATIONS

Values Of 0.00 Indicate No Data

DEPTH	P VELOCITY	SHr VELOCITY	SHt VELOCITY
500.	6027.	0.	893.
1000.	5300.	0.	1089.
1500.	6024.	0.	1398.
2000.	0.	0.	1650.
2050.	6112.	0.	0.
2100.	6149.	0.	1682.
2150.	6187.	0.	1711.
2200.	6219.	0.	1738.
2250.	6263.	0.	1764.
2300.	6303.	0.	0.
2350.	6334.	0.	0.
2400.	6366.	0.	0.
2450.	6396.	0.	1870.
2500.	6440.	0.	1896.
2550.	6487.	0.	1922.
2600.	6511.	0.	0.
2650.	6559.	0.	0.
2700.	6594.	0.	0.
2750.	6650.	0.	0.
2800.	6689.	0.	0.
2850.	6727.	0.	0.
2900.	6764.	0.	0.
2950.	6801.	0.	0.
3000.	6862.	0.	0.
3050.	6903.	0.	0.
3100.	6952.	0.	0.
3150.	6986.	0.	2284.
3200.	7033.	0.	0.
3250.	7049.	0.	0.
3300.	7090.	0.	0.
3350.	7120.	0.	0.
3400.	7171.	0.	2317.
3450.	7230.	0.	2340.
3500.	7273.	0.	0.
3550.	7316.	0.	0.
3600.	7372.	0.	2407.
3650.	7399.	0.	2427.
3700.	7464.	0.	0.
3750.	7479.	0.	0.
3800.	7518.	0.	0.
3850.	7542.	0.	0.
3900.	7580.	0.	0.
3950.	7618.	0.	0.
4000.	7670.	0.	0.
4050.	7708.	0.	0.
4100.	7727.	0.	2617.
4150.	7777.	2659.	2638.
4200.	7812.	2675.	0.
4250.	7861.	2697.	2686.
4300.	7896.	2718.	2708.
4350.	0.	2741.	2729.
4400.	7976.	2763.	2751.
4450.	8022.	2784.	2774.
4500.	8068.	2806.	2794.
4550.	8099.	2829.	2816.
4600.	8144.	2849.	2837.
4650.	8189.	2871.	2857.
4700.	8234.	2893.	2877.
4750.	8283.	2911.	2897.
4800.	8308.	2933.	2918.
4850.	8336.	2964.	2938.
4900.	8377.	2976.	2959.
4950.	0.	2998.	2980.
5000.	8447.	3018.	2999.
5050.	8488.	3037.	3020.
5100.	8529.	3057.	3037.
5150.	8569.	0.	0.
5200.	8600.	0.	3075.
5250.	8636.	3117.	3096.
5300.	8674.	3137.	3113.
5350.	8713.	3160.	3134.
5400.	8737.	3172.	3152.
5450.	8781.	3190.	3168.
5500.	8799.	0.	3188.
5550.	8838.	3228.	3207.
5600.	8873.	3242.	3227.
5650.	8910.	3265.	3246.

TABLE 1-3 100' INTERVAL VELOCITY CALCULATIONS

Values Of 0.00 Indicate No Data

DEPTH	P	DEPTH	SHr	DEPTH	SHt
1000.	6068.	0.	0.	1000.	2137.
0.	0.	0.	0.	1500.	3604.
1775.	8891.	0.	0.	0.	0.
1800.	8184.	0.	0.	2050.	2827.
2100.	7615.	0.	0.	2075.	3452.
2150.	8253.	0.	0.	2150.	5502.
2200.	9008.	0.	0.	2200.	5505.
2250.	9011.	0.	0.	0.	0.
2300.	9016.	0.	0.	0.	0.
2350.	8268.	0.	0.	0.	0.
2400.	8269.	0.	0.	2350.	6012.
2450.	9023.	0.	0.	2375.	5905.
2500.	9026.	0.	0.	2500.	6205.
2550.	9029.	0.	0.	0.	0.
2600.	11038.	0.	0.	0.	0.
2650.	9037.	0.	0.	0.	0.
2700.	9039.	0.	0.	0.	0.
2750.	11045.	0.	0.	0.	0.
2800.	9043.	0.	0.	0.	0.
2850.	9045.	0.	0.	0.	0.
2900.	9047.	0.	0.	0.	0.
2950.	11054.	0.	0.	0.	0.
3000.	12438.	0.	0.	0.	0.
3050.	12440.	0.	0.	0.	0.
3100.	11060.	0.	0.	2850.	5907.
3150.	11061.	0.	0.	0.	0.
3200.	9066.	0.	0.	0.	0.
3250.	9067.	0.	0.	0.	0.
3300.	11066.	0.	0.	0.	0.
3350.	11067.	0.	0.	3275.	6728.
3400.	14230.	0.	0.	3300.	6700.
3450.	14232.	0.	0.	0.	0.
3500.	12454.	0.	0.	0.	0.
3550.	14236.	0.	0.	3525.	7117.
3600.	12457.	0.	0.	3550.	6872.
3650.	12458.	0.	0.	0.	0.
3700.	12459.	0.	0.	0.	0.
3750.	11076.	0.	0.	0.	0.
3800.	11077.	0.	0.	0.	0.
3850.	11077.	0.	0.	0.	0.
3900.	12463.	0.	0.	0.	0.
3950.	14245.	0.	0.	0.	0.
4000.	14240.	0.	0.	0.	0.
4050.	11081.	0.	0.	3875.	7230.
4100.	12466.	0.	0.	3900.	7331.
4150.	14248.	0.	0.	0.	0.
4200.	14250.	4200.	6650.	4200.	9975.
4250.	14251.	4250.	8313.	4225.	9362.
0.	0.	4300.	9069.	4300.	9069.
4350.	14252.	4350.	9070.	4350.	9070.
4375.	14985.	4400.	9070.	4400.	9077.
4450.	16620.	4450.	9070.	4450.	9070.
4500.	14254.	4500.	9970.	4500.	9071.
4550.	14255.	4550.	9071.	4550.	9071.
4600.	16631.	4600.	9072.	4600.	8316.
4650.	16632.	4650.	9070.	4650.	8316.
4700.	14257.	4700.	8317.	4700.	8317.
4750.	14258.	4750.	8317.	4750.	9073.
4800.	14257.	4800.	9080.	4800.	9073.
4850.	14258.	4850.	9081.	4850.	9074.
0.	0.	4900.	9081.	4900.	9081.
4950.	14259.	4950.	9074.	4950.	9074.
4975.	14972.	5000.	9074.	5000.	9074.
5050.	16637.	5050.	9082.	5050.	8318.
5100.	16638.	0.	0.	0.	0.
5150.	16638.	0.	0.	5150.	8319.
5200.	14262.	5175.	9359.	5175.	8809.
5250.	14263.	5200.	9600.	5250.	9076.
5300.	16642.	5300.	9077.	5300.	9077.
5350.	14262.	5350.	7680.	5350.	9076.
5400.	12480.	5400.	7680.	5400.	7680.
5450.	14265.	0.	0.	5450.	8321.
5500.	16641.	5500.	8321.	5500.	9085.
5550.	16642.	5525.	7883.	5550.	9086.
5600.	16644.	5600.	9080.	5600.	9080.

TABLE 1-4 500' INTERVAL VELOCITY CALCULATIONS

Values Of 0.00 Indicate No Data

DEPTH	P	DEPTH	SHr	DEPTH	SHt
1426.	6922.	0.	0.	0.	0.
1700.	7512.	0.	0.	0.	0.
1975.	8233.	0.	0.	1975.	4190.
2000.	8304.	0.	0.	2250.	4811.
2300.	8547.	0.	0.	2275.	4956.
2350.	8701.	0.	0.	0.	0.
2400.	9187.	0.	0.	0.	0.
2450.	9023.	0.	0.	0.	0.
2500.	9366.	0.	0.	0.	0.
2550.	9369.	0.	0.	0.	0.
2600.	9551.	0.	0.	0.	0.
2650.	9741.	0.	0.	0.	0.
2700.	9938.	0.	0.	0.	0.
2750.	10143.	0.	0.	0.	0.
2800.	10577.	0.	0.	0.	0.
2850.	10809.	0.	0.	0.	0.
2900.	10581.	0.	0.	2850.	5967.
2950.	11064.	0.	0.	0.	0.
3000.	10585.	0.	0.	0.	0.
3050.	10817.	0.	0.	0.	0.
3100.	10819.	0.	0.	0.	0.
3150.	11061.	0.	0.	2975.	6172.
3200.	11577.	0.	0.	3000.	6210.
3250.	11578.	0.	0.	0.	0.
3300.	11580.	0.	0.	0.	0.
3350.	11857.	0.	0.	3075.	6333.
3400.	11858.	0.	0.	3400.	6823.
3450.	12149.	0.	0.	0.	0.
3500.	12464.	0.	0.	0.	0.
3550.	12465.	0.	0.	0.	0.
3600.	12467.	0.	0.	0.	0.
3650.	12468.	0.	0.	0.	0.
3700.	12155.	0.	0.	0.	0.
3750.	12460.	0.	0.	0.	0.
3800.	12461.	0.	0.	0.	0.
3850.	11869.	0.	0.	3850.	7121.
3900.	12463.	0.	0.	3900.	7331.
3950.	12160.	0.	0.	0.	0.
4000.	12784.	0.	0.	3950.	7670.
4050.	12786.	0.	0.	3975.	7716.
0.	0.	0.	0.	4000.	7843.
4150.	13470.	0.	0.	4025.	7956.
4200.	13863.	0.	0.	4050.	8059.
4250.	13864.	0.	0.	4075.	8073.
4300.	13865.	0.	0.	4100.	8160.
4350.	14071.	0.	0.	4350.	9237.
4400.	14072.	4400.	8601.	4400.	9230.
4450.	15117.	4450.	9230.	4425.	9140.
4500.	14073.	4500.	9071.	4500.	8909.
4550.	15119.	4550.	9239.	4550.	9071.
4575.	14033.	4600.	9240.	4600.	8910.
4650.	15120.	4650.	9240.	4650.	8910.
0.	0.	4700.	9415.	4700.	8910.
4750.	14077.	4750.	9241.	4750.	8911.
4800.	15122.	4800.	9241.	4800.	8911.
4850.	15123.	4850.	9410.	4850.	8755.
4900.	15123.	0.	0.	0.	0.
4950.	15124.	0.	0.	4950.	8756.
5000.	15124.	5000.	9690.	5000.	8912.
5050.	15125.	5050.	9690.	5050.	8758.
5100.	15590.	5100.	9418.	5100.	8913.
5150.	15120.	5150.	9075.	5150.	8757.
5175.	14840.	5200.	8914.	5200.	8461.
5250.	15127.	0.	0.	5250.	8807.
5300.	15127.	5300.	8768.	5300.	8807.
5350.	15128.	5350.	8461.	5350.	8916.
5400.	15128.	5375.	8857.	5375.	9002.

TABLE 1-5 AVERAGE VELOCITY RATIOS

Values Of 0.00 Or 1.00 Indicate No Data

DEPTH	P/SHr	SHr POISSON	DEPTH	P/SHt	SHt POISSON
500.	5.629	0.484	500.	0.000	1.000
1000.	4.068	0.470	1000.	0.000	1.000
1500.	4.029	0.467	1500.	0.000	1.000
2000.	0.000	0.000	2000.	0.000	0.000
2050.	0.000	1.000	2050.	0.000	1.000
2100.	3.665	0.460	2100.	0.000	1.000
2150.	3.605	0.458	2150.	0.000	1.000
2200.	3.583	0.458	2200.	0.000	1.000
2250.	3.546	0.457	2250.	0.000	1.000
2300.	0.000	1.000	2300.	0.000	1.000
2350.	0.000	1.000	2350.	0.000	1.000
2400.	0.000	1.000	2400.	0.000	1.000
2450.	3.420	0.453	2450.	0.000	1.000
2500.	3.399	0.453	2500.	0.000	1.000
2550.	3.365	0.452	2550.	0.000	1.000
2600.	0.000	1.000	2600.	0.000	1.000
2650.	0.000	1.000	2650.	0.000	1.000
2700.	0.000	1.000	2700.	0.000	1.000
2750.	0.000	1.000	2750.	0.000	1.000
2800.	0.000	1.000	2800.	0.000	1.000
2850.	0.000	1.000	2850.	0.000	1.000
2900.	0.000	1.000	2900.	0.000	1.000
2950.	0.000	1.000	2950.	0.000	1.000
3000.	0.000	1.000	3000.	0.000	1.000
3050.	0.000	1.000	3050.	0.000	1.000
3100.	0.000	1.000	3100.	0.000	1.000
3150.	3.170	0.445	3150.	0.000	1.000
3200.	0.000	1.000	3200.	0.000	1.000
3250.	0.000	1.000	3250.	0.000	1.000
3300.	0.000	1.000	3300.	0.000	1.000
3350.	0.000	1.000	3350.	0.000	1.000
3400.	3.096	0.442	3400.	0.000	1.000
3450.	3.090	0.441	3450.	0.000	1.000
3500.	0.000	1.000	3500.	0.000	1.000
3550.	0.000	1.000	3550.	0.000	1.000
3600.	3.063	0.440	3600.	0.000	1.000
3650.	3.048	0.440	3650.	0.000	1.000
3700.	0.000	1.000	3700.	0.000	1.000
3750.	0.000	1.000	3750.	0.000	1.000
3800.	0.000	1.000	3800.	0.000	1.000
3850.	0.000	1.000	3850.	0.000	1.000
3900.	0.000	1.000	3900.	0.000	1.000
3950.	0.000	1.000	3950.	0.000	1.000
4000.	0.000	1.000	4000.	0.000	1.000
4050.	0.000	1.000	4050.	0.000	1.000
4100.	2.963	0.436	4100.	0.000	1.000
4150.	2.948	0.435	4150.	2.925	0.434
4200.	0.000	1.000	4200.	2.920	0.434
4250.	2.920	0.434	4250.	2.916	0.433
4300.	2.910	0.433	4300.	2.906	0.433
4350.	0.000	0.000	4350.	0.000	0.000
4400.	2.899	0.432	4400.	2.886	0.432
4450.	2.892	0.432	4450.	2.881	0.432
4500.	2.887	0.432	4500.	2.876	0.431
4550.	2.878	0.431	4550.	2.863	0.431
4600.	2.871	0.431	4600.	2.869	0.430
4650.	2.860	0.431	4650.	2.852	0.430
4700.	2.862	0.430	4700.	2.846	0.430
4750.	2.852	0.430	4750.	2.839	0.429
4800.	2.846	0.430	4800.	2.832	0.429
4850.	2.837	0.429	4850.	2.822	0.428
4900.	2.831	0.429	4900.	2.816	0.428
4950.	0.000	0.000	4950.	0.000	0.000
5000.	2.816	0.428	5000.	2.801	0.427
5050.	2.810	0.428	5050.	2.795	0.427
5100.	2.808	0.427	5100.	2.790	0.426
5150.	0.000	1.000	5150.	0.000	1.000
5200.	2.800	0.427	5200.	0.000	1.000
5250.	2.790	0.426	5250.	2.770	0.425
5300.	2.786	0.426	5300.	2.765	0.425
5350.	2.780	0.426	5350.	2.761	0.425
5400.	2.772	0.425	5400.	2.754	0.424
5450.	2.766	0.425	5450.	2.746	0.424
5500.	2.760	0.424	5500.	0.000	1.000
5550.	2.765	0.424	5550.	2.739	0.423
5600.	2.760	0.424	5600.	2.737	0.423
5650.	2.745	0.423	5650.	2.729	0.422

TABLE 1-6 500' INTERVAL VELOCITY RATIOS

Values Of 0.00 Indicate No Data

DEPTH	P/SHr	SHr POISSON	DEPTH	P/SHt	SHt POISSON
0.	0.000	0.000	0.	0.000	0.000
0.	0.000	0.000	0.	0.000	0.000
1976.	1.966	0.326	0.	0.000	0.000
2000.	1.959	0.324	0.	0.000	0.000
2026.	1.920	0.314	0.	0.000	0.000
0.	0.000	0.000	0.	0.000	0.000
0.	0.000	0.000	0.	0.000	0.000
0.	0.000	0.000	0.	0.000	0.000
0.	0.000	0.000	0.	0.000	0.000
0.	0.000	0.000	0.	0.000	0.000
0.	0.000	0.000	0.	0.000	0.000
0.	0.000	0.000	0.	0.000	0.000
0.	0.000	0.000	0.	0.000	0.000
0.	0.000	0.000	0.	0.000	0.000
0.	0.000	0.000	0.	0.000	0.000
0.	0.000	0.000	0.	0.000	0.000
2860.	1.766	0.272	0.	0.000	0.000
0.	0.000	0.000	0.	0.000	0.000
0.	0.000	0.000	0.	0.000	0.000
0.	0.000	0.000	0.	0.000	0.000
0.	0.000	0.000	0.	0.000	0.000
2976.	1.734	0.261	0.	0.000	0.000
3000.	1.756	0.260	0.	0.000	0.000
0.	0.000	0.000	0.	0.000	0.000
0.	0.000	0.000	0.	0.000	0.000
3076.	1.774	0.267	0.	0.000	0.000
3400.	1.738	0.253	0.	0.000	0.000
0.	0.000	0.000	0.	0.000	0.000
0.	0.000	0.000	0.	0.000	0.000
0.	0.000	0.000	0.	0.000	0.000
0.	0.000	0.000	0.	0.000	0.000
0.	0.000	0.000	0.	0.000	0.000
0.	0.000	0.000	0.	0.000	0.000
0.	0.000	0.000	0.	0.000	0.000
0.	0.000	0.000	0.	0.000	0.000
3860.	1.667	0.219	0.	0.000	0.000
3900.	1.700	0.236	0.	0.000	0.000
0.	0.000	0.000	0.	0.000	0.000
3960.	1.660	0.216	4200.	0.000	0.000
3976.	1.647	0.200	4260.	0.000	0.000
0.	0.000	0.000	0.	0.000	0.000
4026.	1.621	0.193	4360.	0.000	0.000
4060.	1.623	0.194	4376.	0.000	0.000
4076.	1.641	0.204	4460.	0.000	0.000
4100.	1.618	0.191	4600.	0.000	0.000
4360.	1.580	0.172	4660.	0.000	0.000
4400.	1.588	0.172	4400.	1.706	0.230
4426.	1.622	0.193	4460.	1.636	0.202
4600.	1.647	0.200	4600.	1.618	0.191
4660.	1.667	0.219	4660.	1.636	0.202
4676.	1.649	0.209	4676.	1.596	0.176
4660.	1.697	0.234	4660.	1.636	0.202
0.	0.000	0.000	0.	0.000	0.000
4760.	1.647	0.200	4760.	1.680	0.172
4800.	1.697	0.234	4800.	1.636	0.202
4860.	1.727	0.248	4860.	1.606	0.163
0.	0.000	0.000	0.	0.000	0.000
49F0.	1.727	0.248	0.	0.000	0.000
5000.	1.697	0.234	6000.	1.676	0.163
F050.	1.727	0.248	6050.	1.676	0.163
5100.	1.760	0.258	6100.	1.656	0.213
5160.	1.727	0.248	6160.	1.667	0.219
5175.	1.738	0.249	6175.	1.649	0.209
5260.	1.768	0.261	0.	0.000	0.000
5300.	1.760	0.261	5300.	1.727	0.248
5360.	1.697	0.234	5360.	1.708	0.272
5376.	1.694	0.233	5376.	1.722	0.248

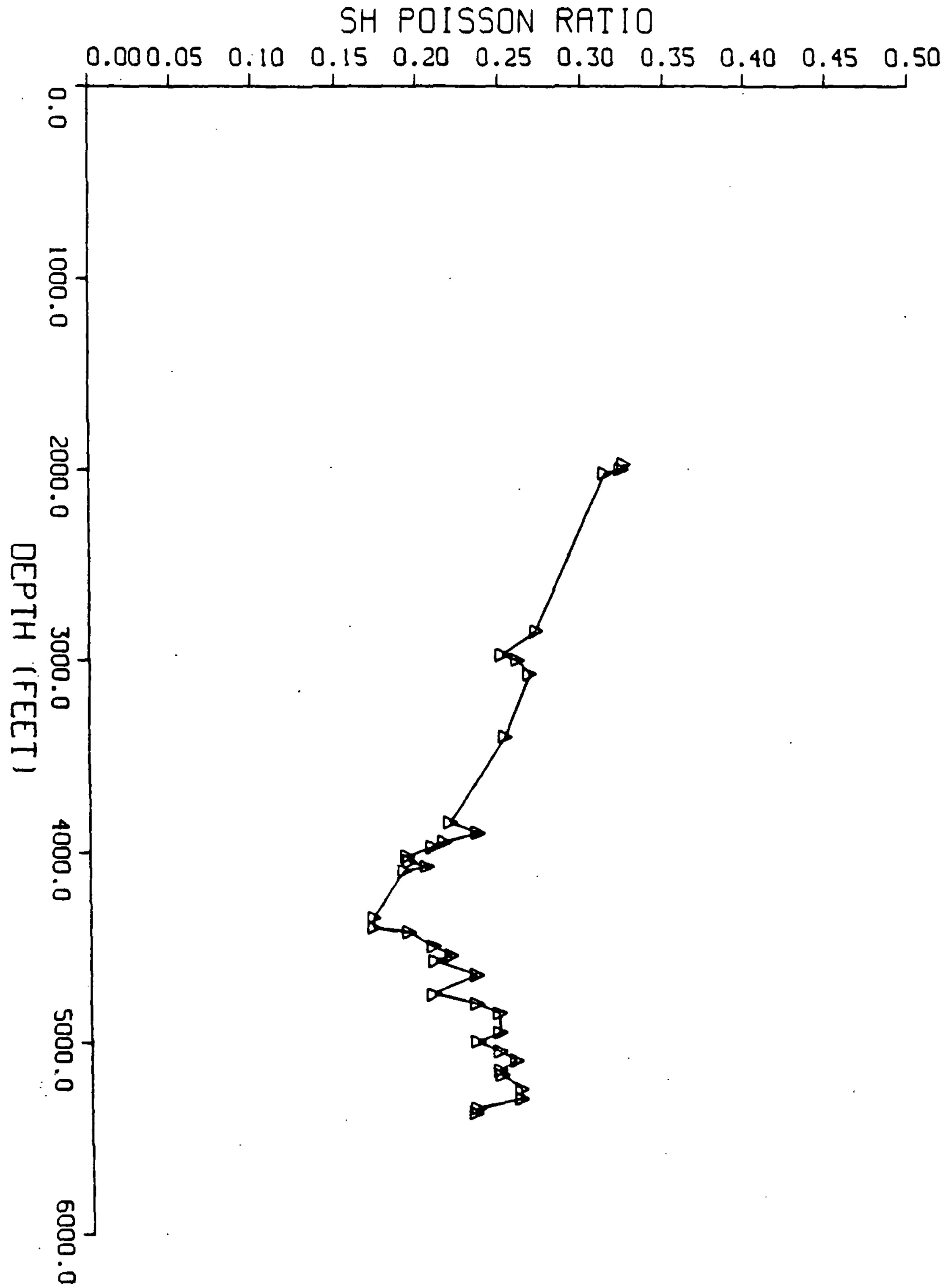

Figure 1-1 Interval Poisson's Ratio Calculated From SH_t Data With 500' Interval Spacing.

APPENDIX 2

PARTICLE MOTION HODOGRAPHS

The hodographs in this appendix are listed by level number instead of depth. The following tables cross-reference level number and depth for the various data sets. Table 3-1 is for all the far-offset data, while table 3-2 is for the near-offset P and SH_t source data and table 3-3 is for the near-offset SH_r source data.

Table 2-1

Far-Offset Data, All Sources

Level	Depth
1	1500
2	1900
3	1975
4	2050
5	2125
6	2200
7	2275
8	2350
9	2425
10	2500
11	2575
12	2650
13	2725
14	2800
15	2875
16	2950
17	3025
18	3100
19	3175
20	3250
21	3325
22	3400
23	3475
24	3550
25	3625
26	3700
27	3775
28	3850
29	3925
30	4000
31	4075
32	4150
33	4225
34	4300
35	4375
36	4450
37	4525
38	4600
39	4675
40	4750
41	4825
42	4900
43	4975
44	5050
45	5125
46	5200
47	5275
48	5350
49	5425
50	5500
51	5575
52	5650

Table 2-2

Near-Offset P and SH_t Data

Level	Depth
1	500
2	1000
3	1500
4	2000
5	2050
6	2100
7	2150
8	2200
9	2250
10	2300
11	2350
12	2400
13	2450
14	2500
15	2550
16	2600
17	2650
18	2700
19	2750
20	2800
21	2850
22	2900
23	2950
24	3000
25	3050
26	3100
27	3150
28	3200
29	3250
30	3300
31	3350
32	3400
33	3450
34	3500
35	3550
36	3600
37	3650
38	3700
39	3750
40	3800

Table 2-2

Near-Offset P and SH_t Data

Level	Depth
41	3850
42	3900
43	3950
44	4000
45	4050
46	4100
47	4150
48	4200
49	4250
50	4300
51	4350
52	4400
53	4450
54	4500
55	4550
56	4600
57	4650
58	4700
59	4750
60	4800
61	4850
62	4900
63	4950
64	5000
65	5050
66	5100
67	5150
68	5200
69	5250
70	5300
71	5350
72	5400
73	5450
74	5500
75	5550
76	5600
77	5650

Table 2-3

Near-Offset SH_r Data

Level	Depth
1	3050
2	3100
3	3150
4	3200
5	3250
6	3300
7	3350
8	3400
9	3450
10	3500
11	3550
12	3600
13	3650
14	3700
15	3750
16	3800
17	3850
18	3900
19	3950
20	4000
21	4050
22	4100
23	4150
24	4200
25	4250
26	4300
27	4350
28	4400
29	4450
30	4500
31	4550
32	4600
33	4650
34	4700
35	4750
36	4800
37	4850
38	4900
39	4950
40	5000
41	5050
42	5100
43	5150
44	5200
45	5250
46	5300
47	5350
48	5400
49	5450
50	5500
51	5550
52	5600
53	5650

FAR OFFSET P-WAVE SOURCE

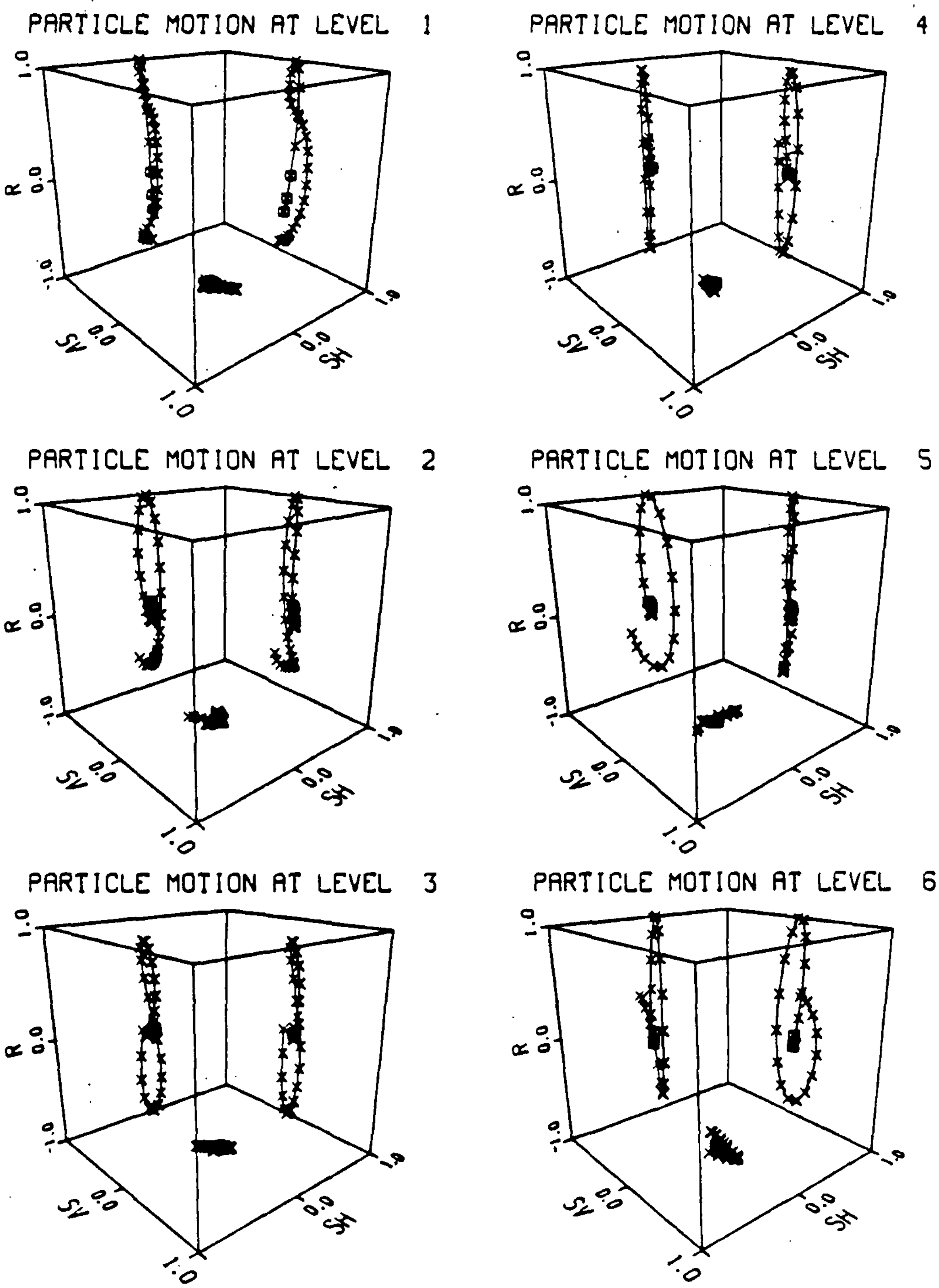

FAR OFFSET P-WAVE SOURCE

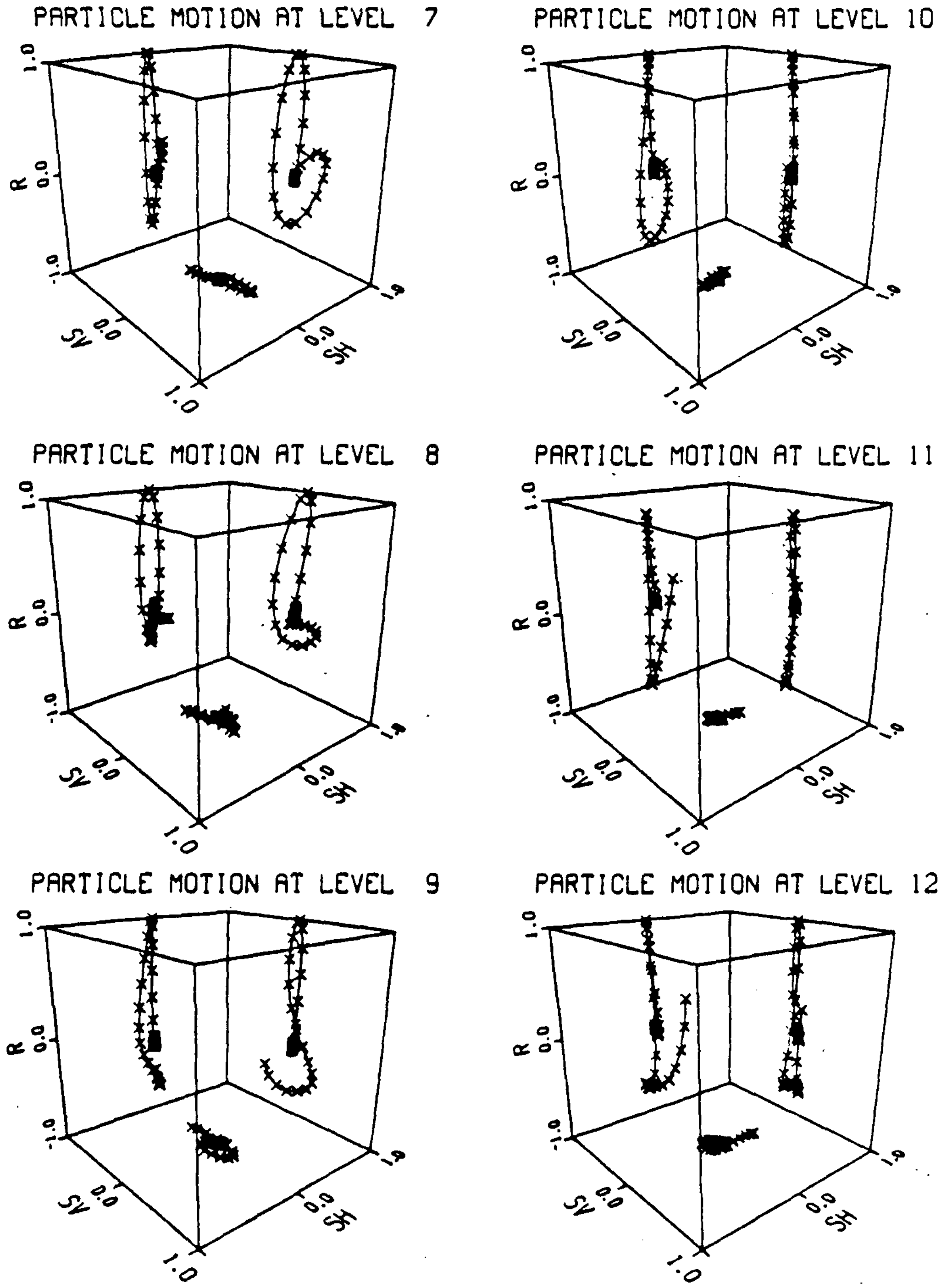

FAR OFFSET P-WAVE SOURCE

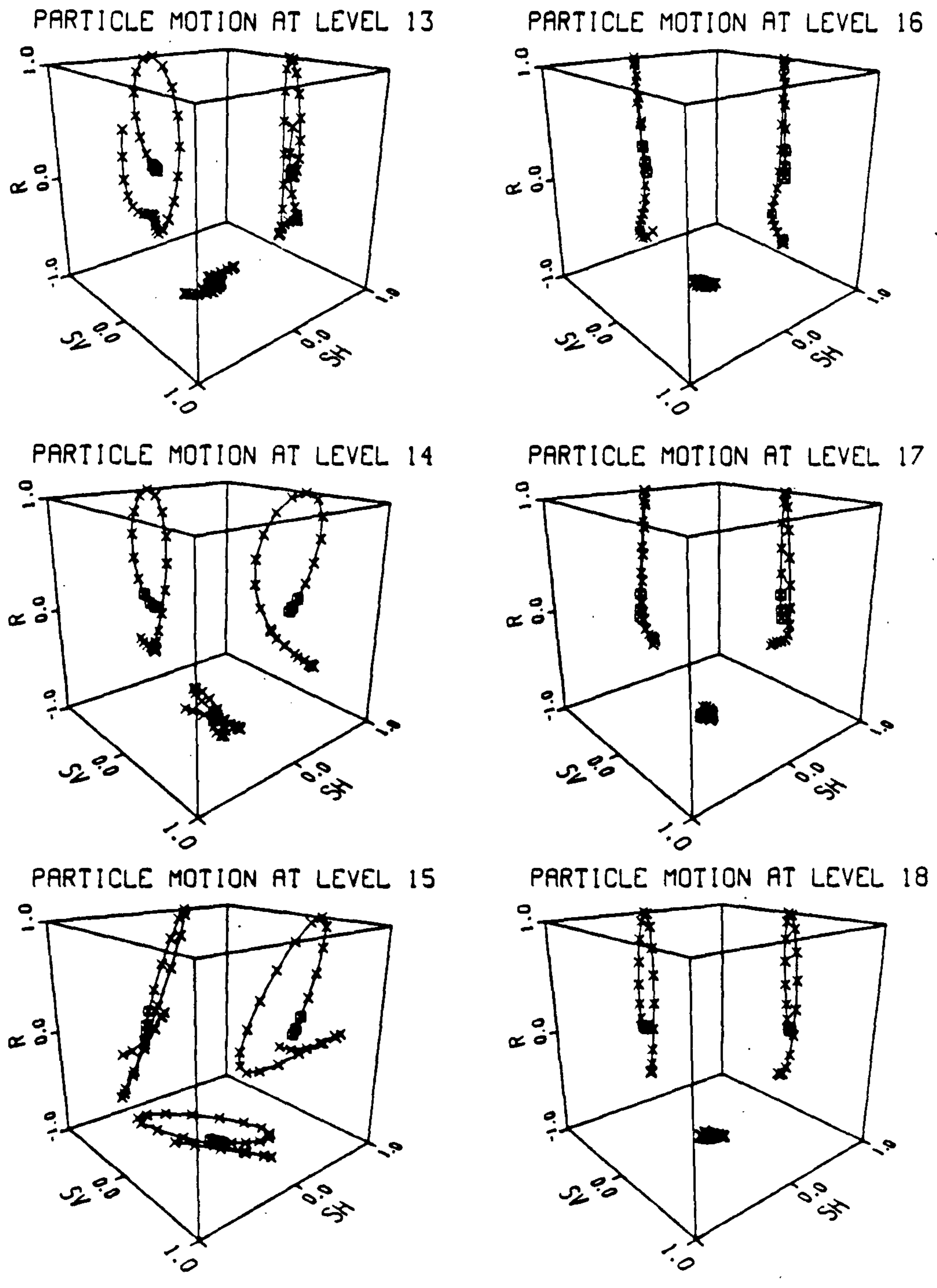

FAR OFFSET P-WAVE SOURCE

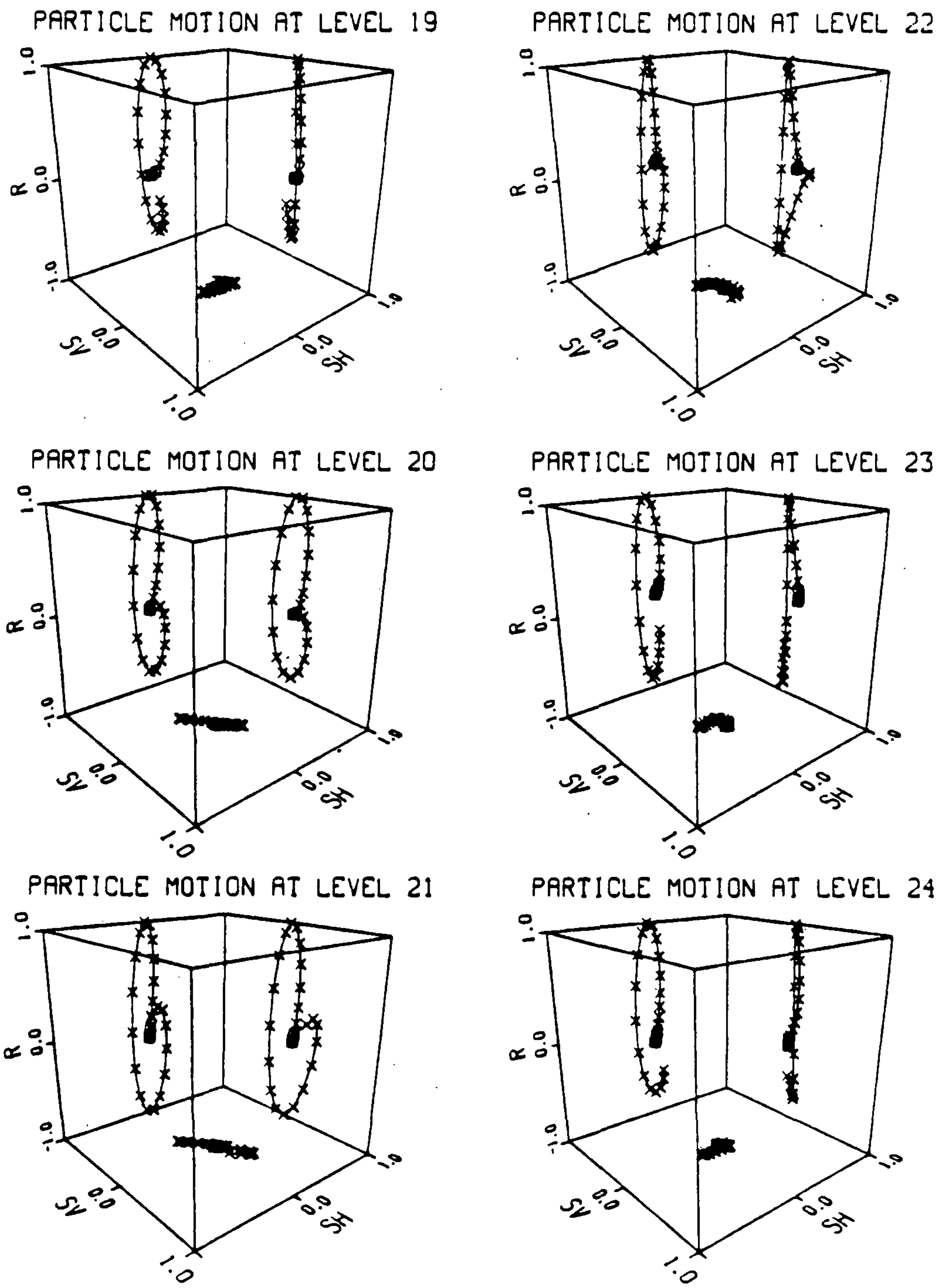

FAR OFFSET P-WAVE SOURCE

PARTICLE MOTION AT LEVEL 25

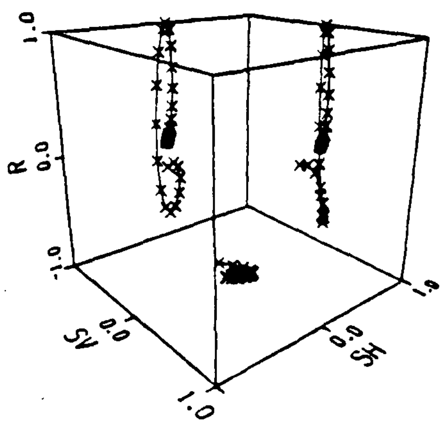

PARTICLE MOTION AT LEVEL 28

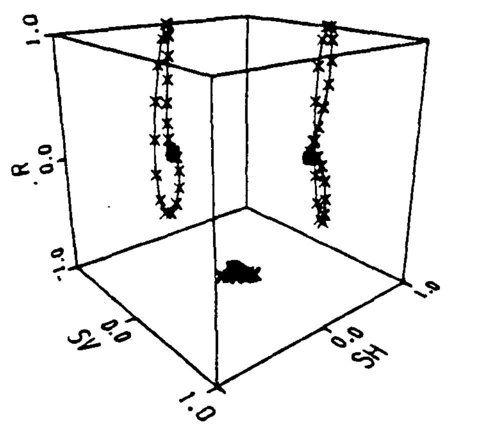

PARTICLE MOTION AT LEVEL 26

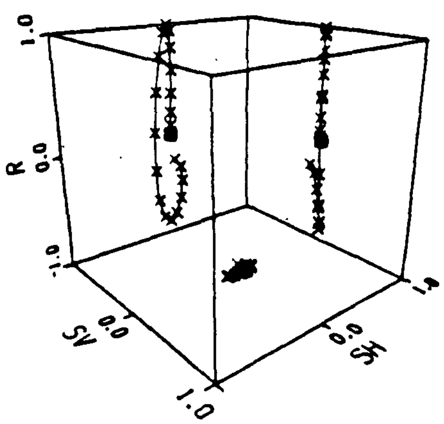

PARTICLE MOTION AT LEVEL 29

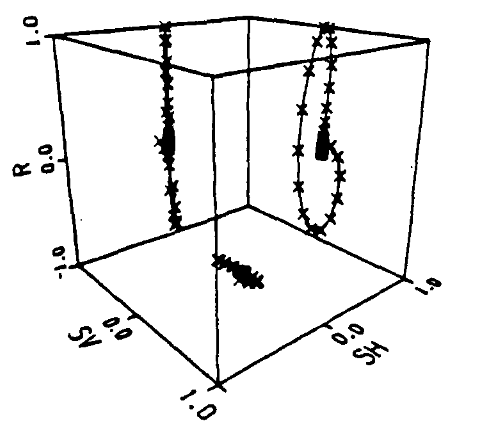

PARTICLE MOTION AT LEVEL 27

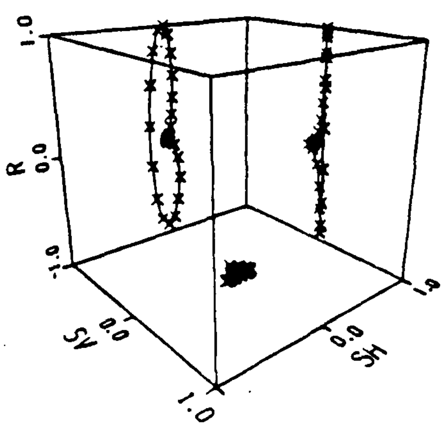

PARTICLE MOTION AT LEVEL 30

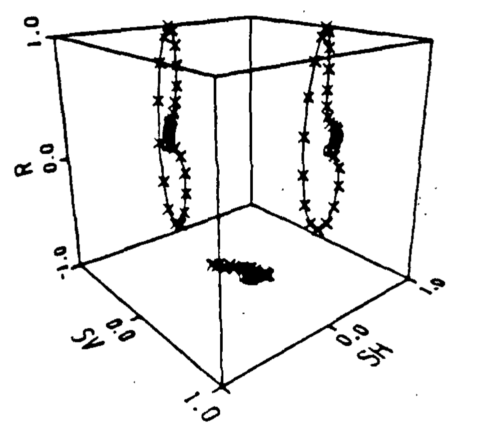

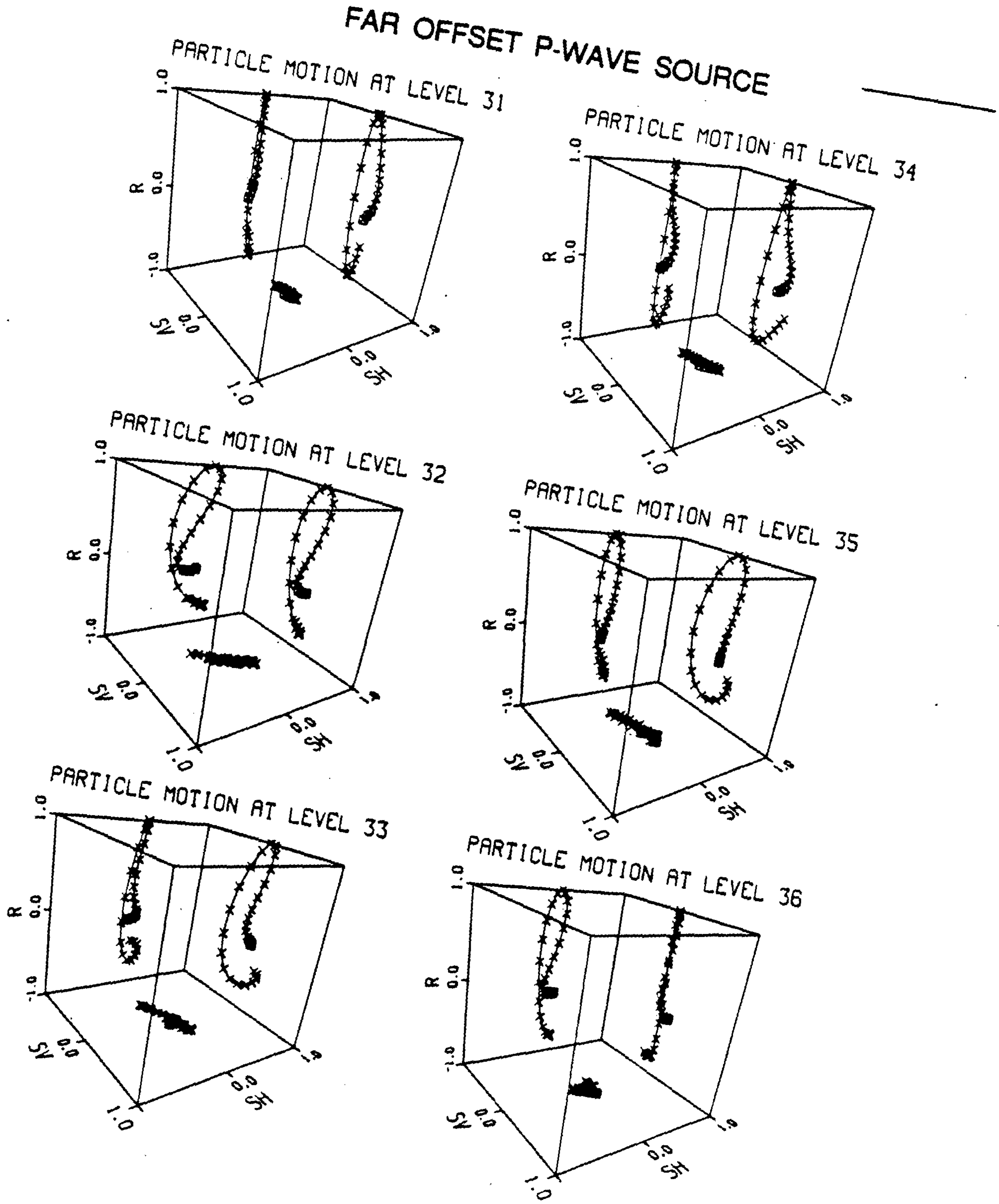
FAR OFFSET P-WAVE SOURCE
PARTICLE MOTION AT LEVEL 31
PARTICLE MOTION AT LEVEL 32
PARTICLE MOTION AT LEVEL 33
PARTICLE MOTION AT LEVEL 34
PARTICLE MOTION AT LEVEL 35
PARTICLE MOTION AT LEVEL 36
R
SV
SH
1.0
0.0
-1.0

FAR OFFSET P-WAVE SOURCE

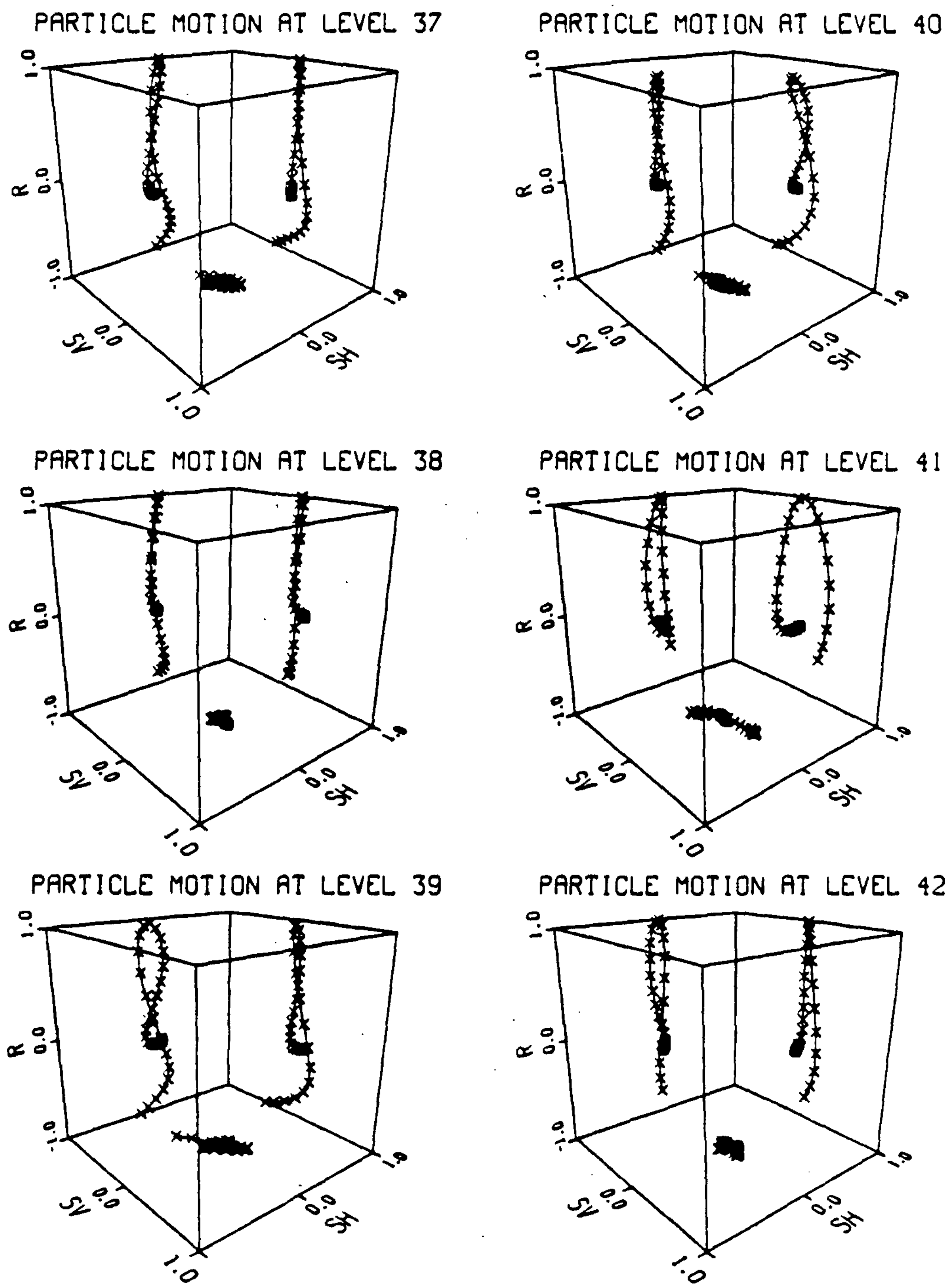

FAR OFFSET P-WAVE SOURCE

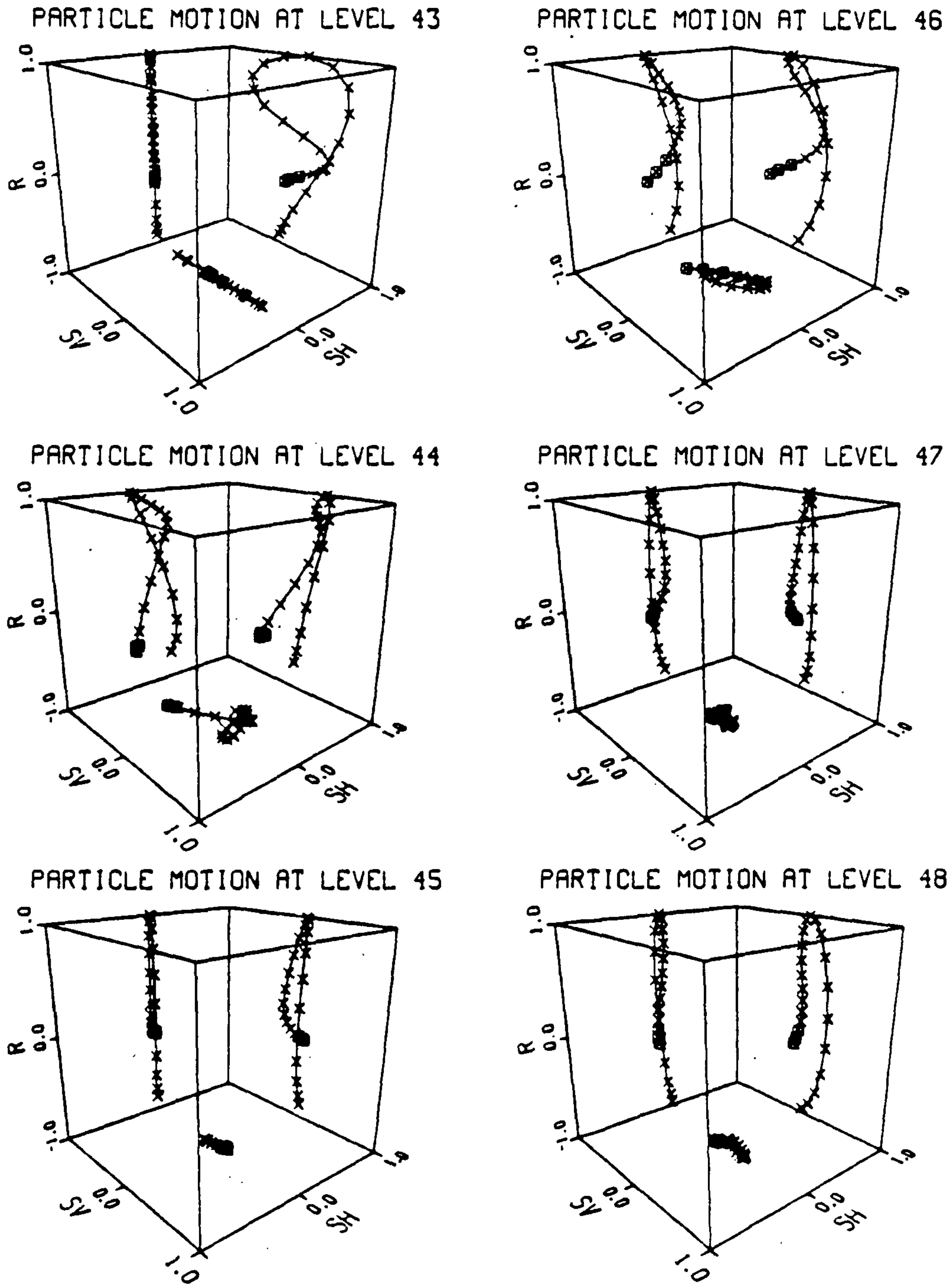

FAR OFFSET P-WAVE SOURCE

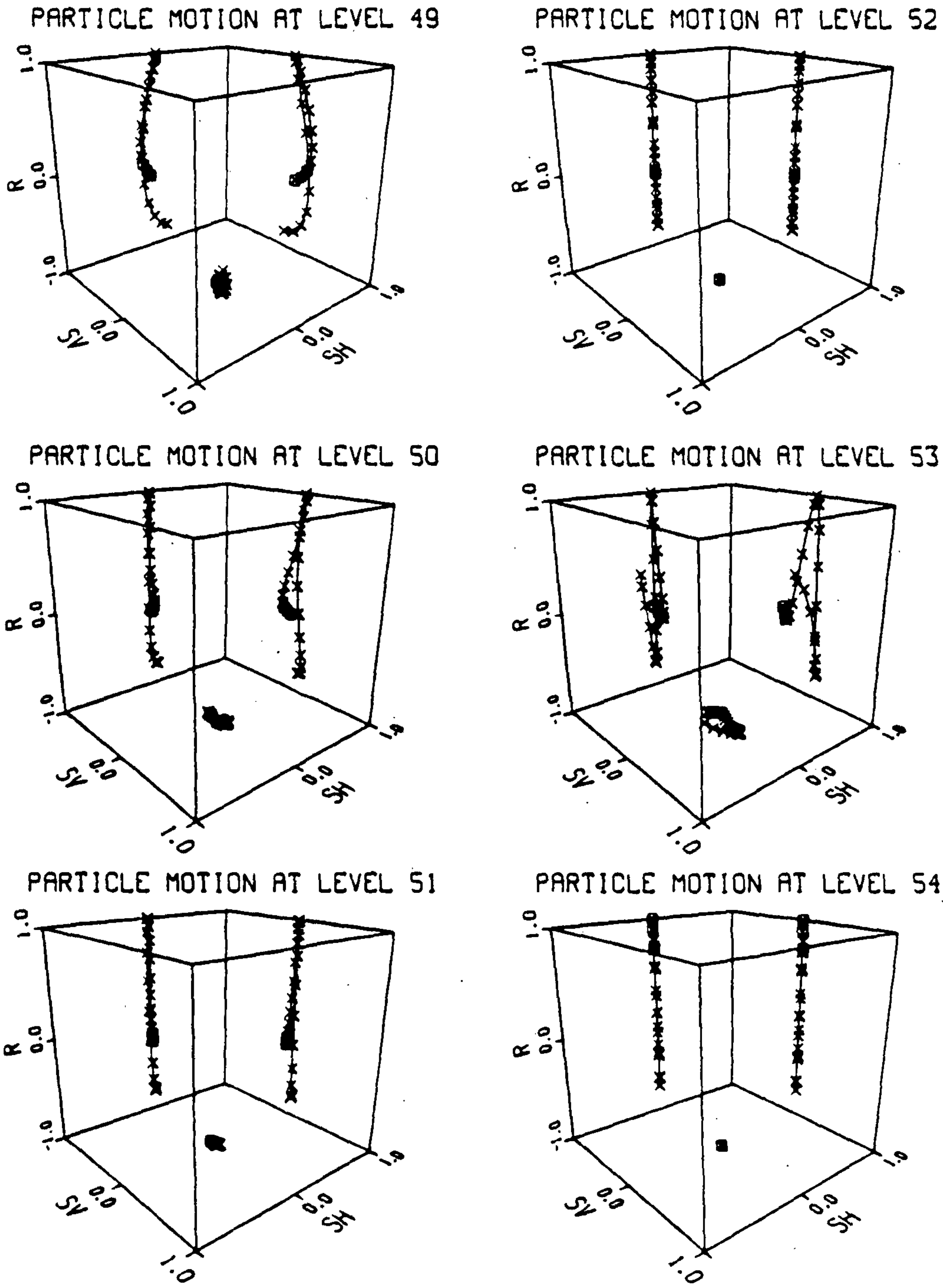

FAR OFFSET SV SOURCE

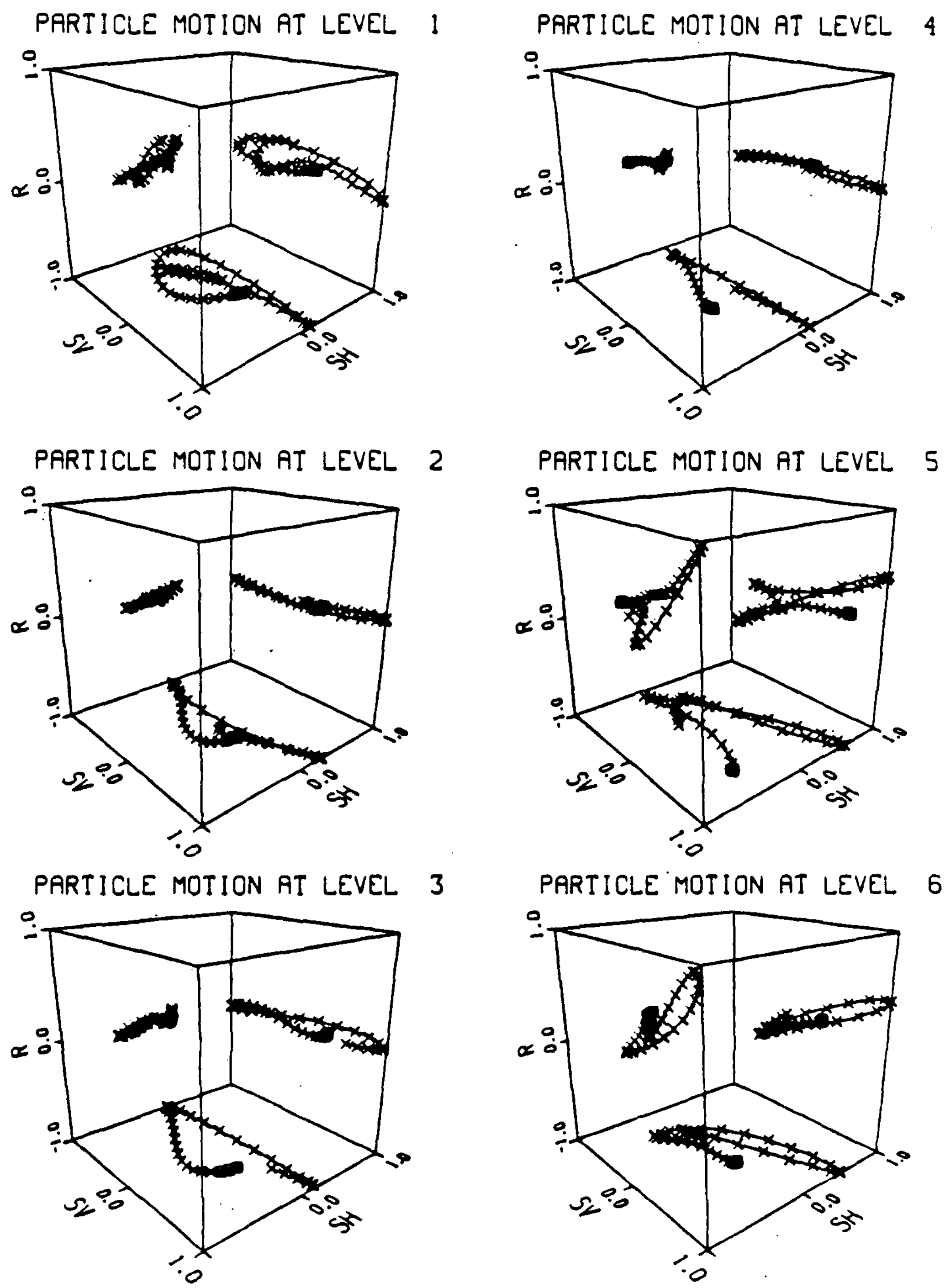

FAR OFFSET SV SOURCE

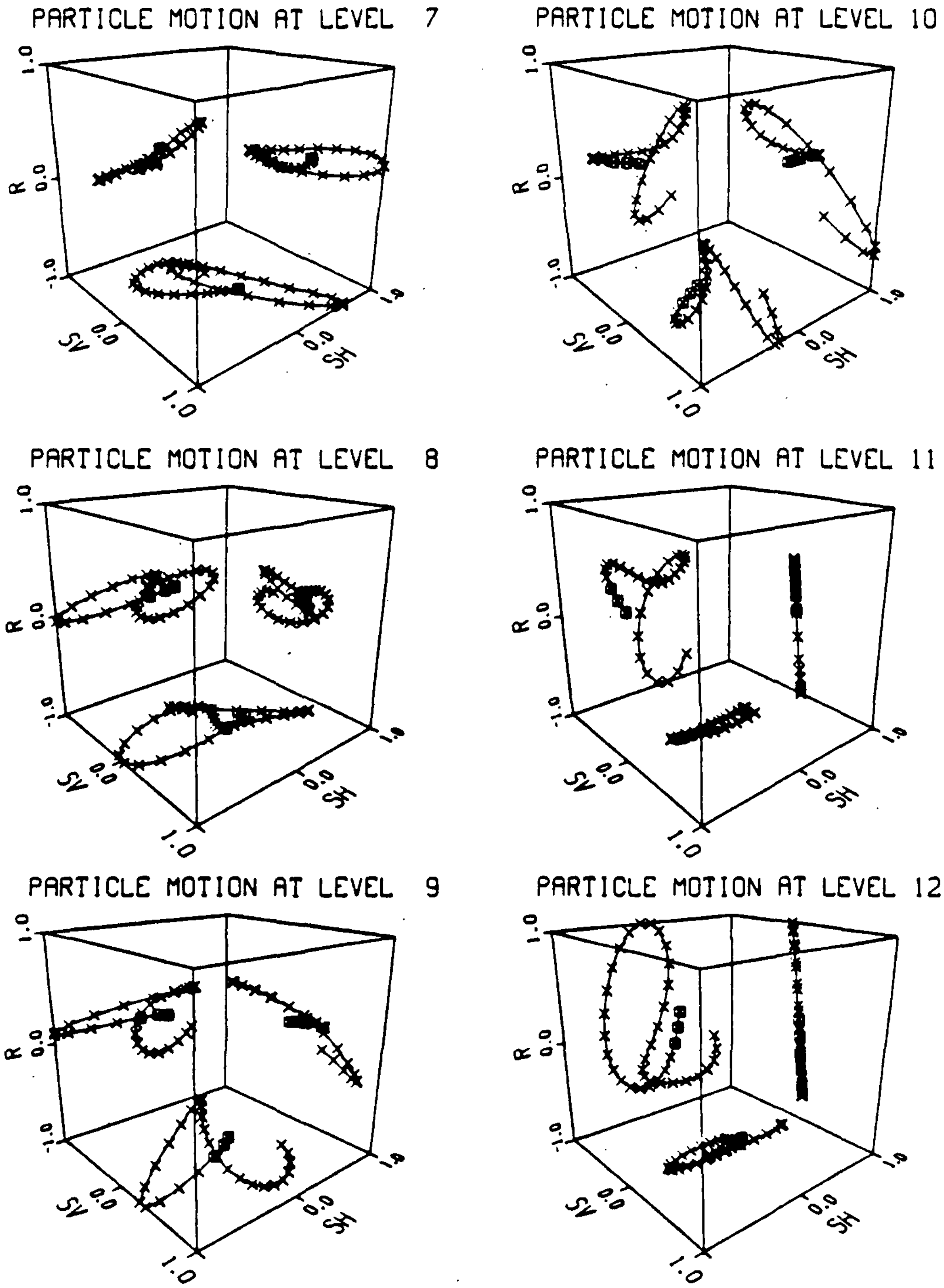

FAR OFFSET SV SOURCE

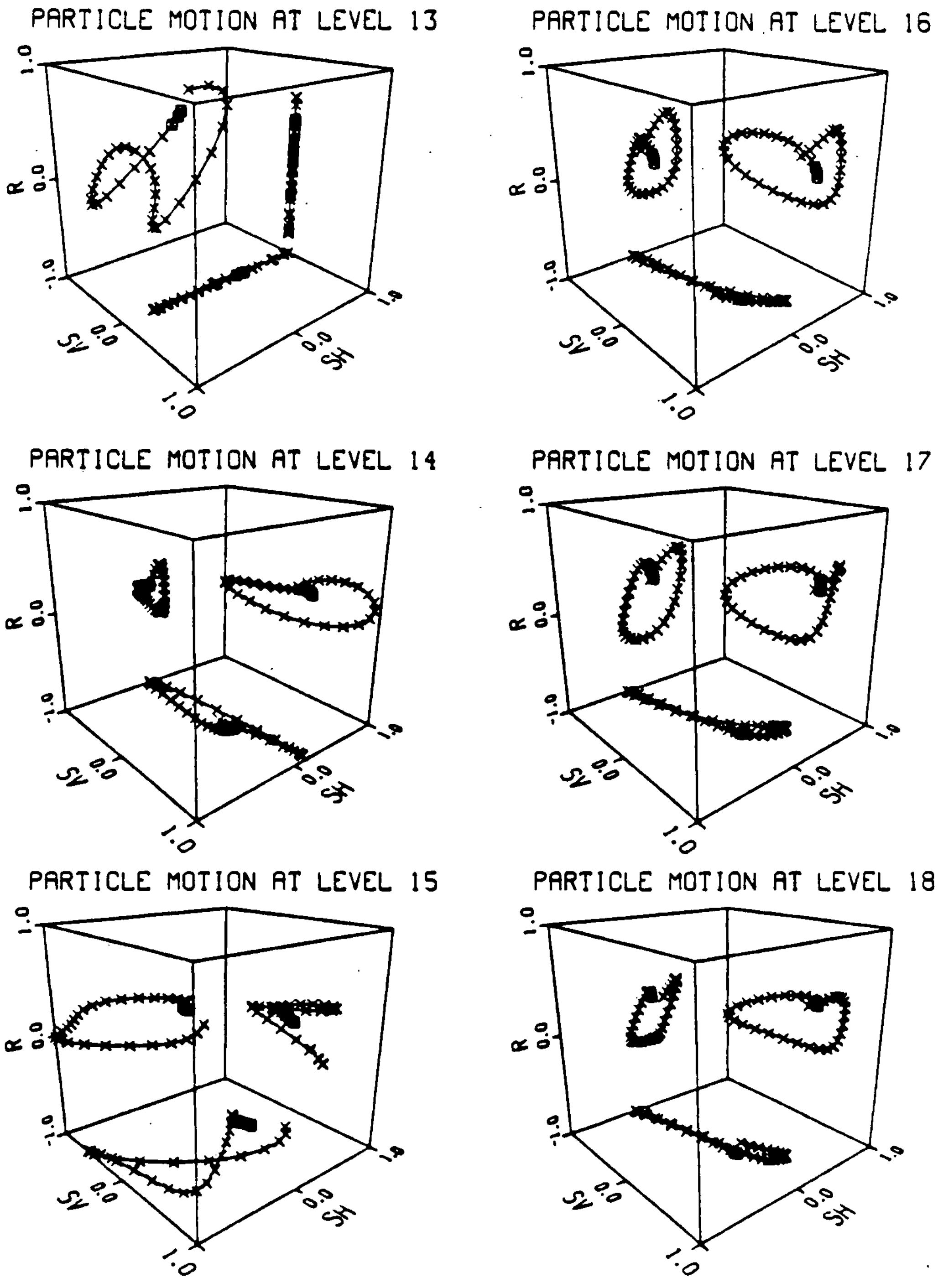

FAR OFFSET SV SOURCE

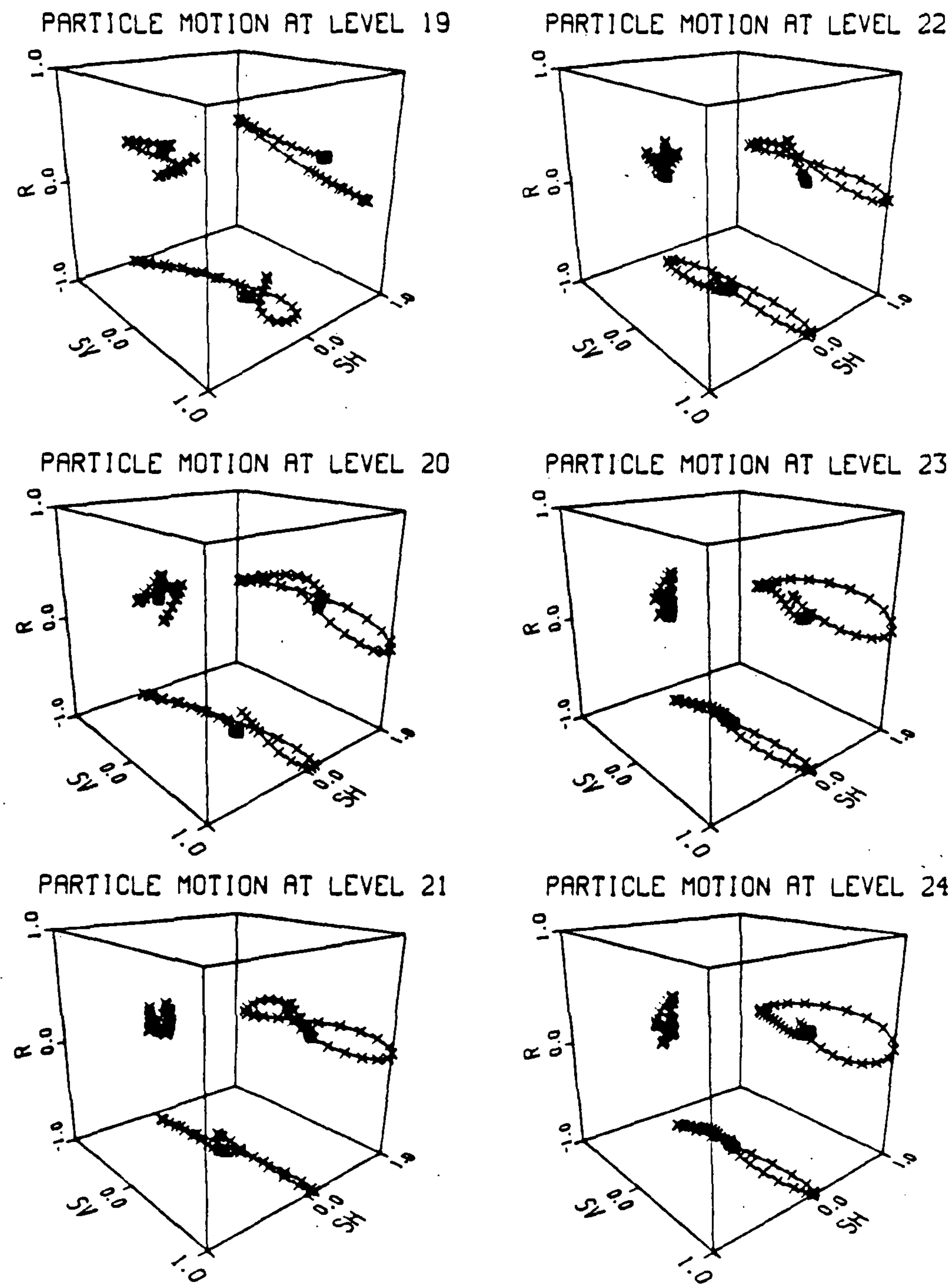

FAR OFFSET SV SOURCE

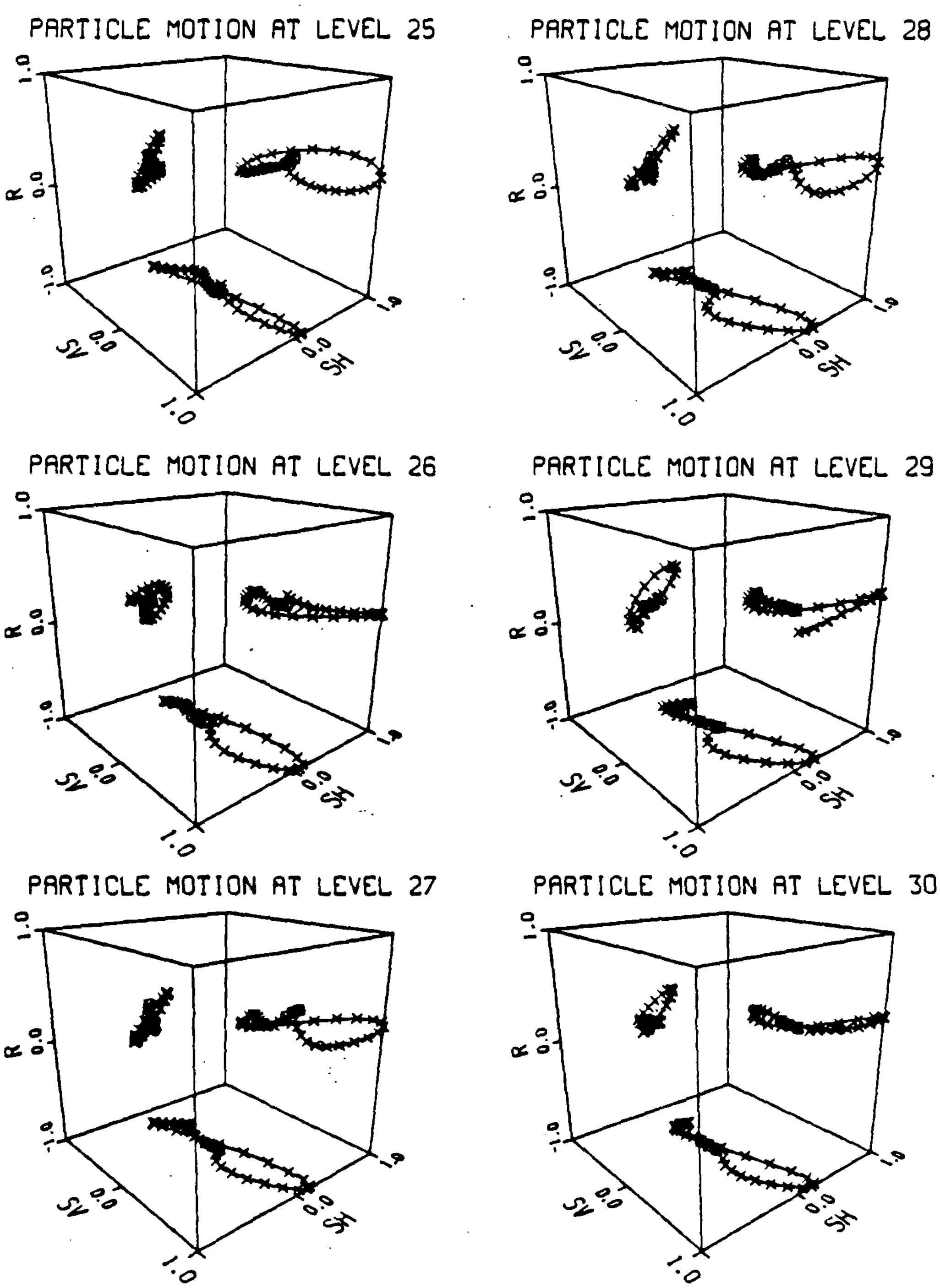

FAR OFFSET SV SOURCE

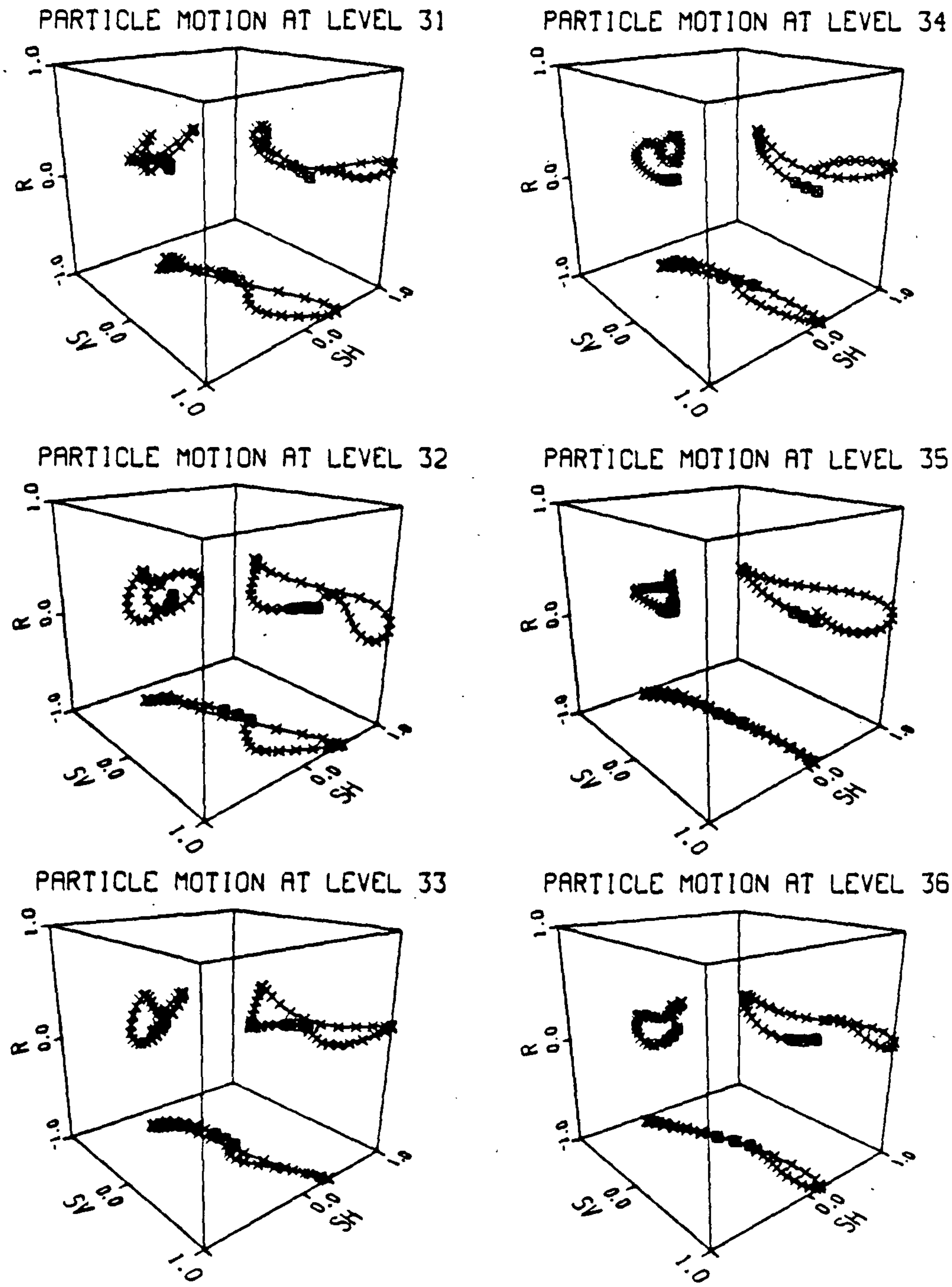

FAR OFFSET SV SOURCE

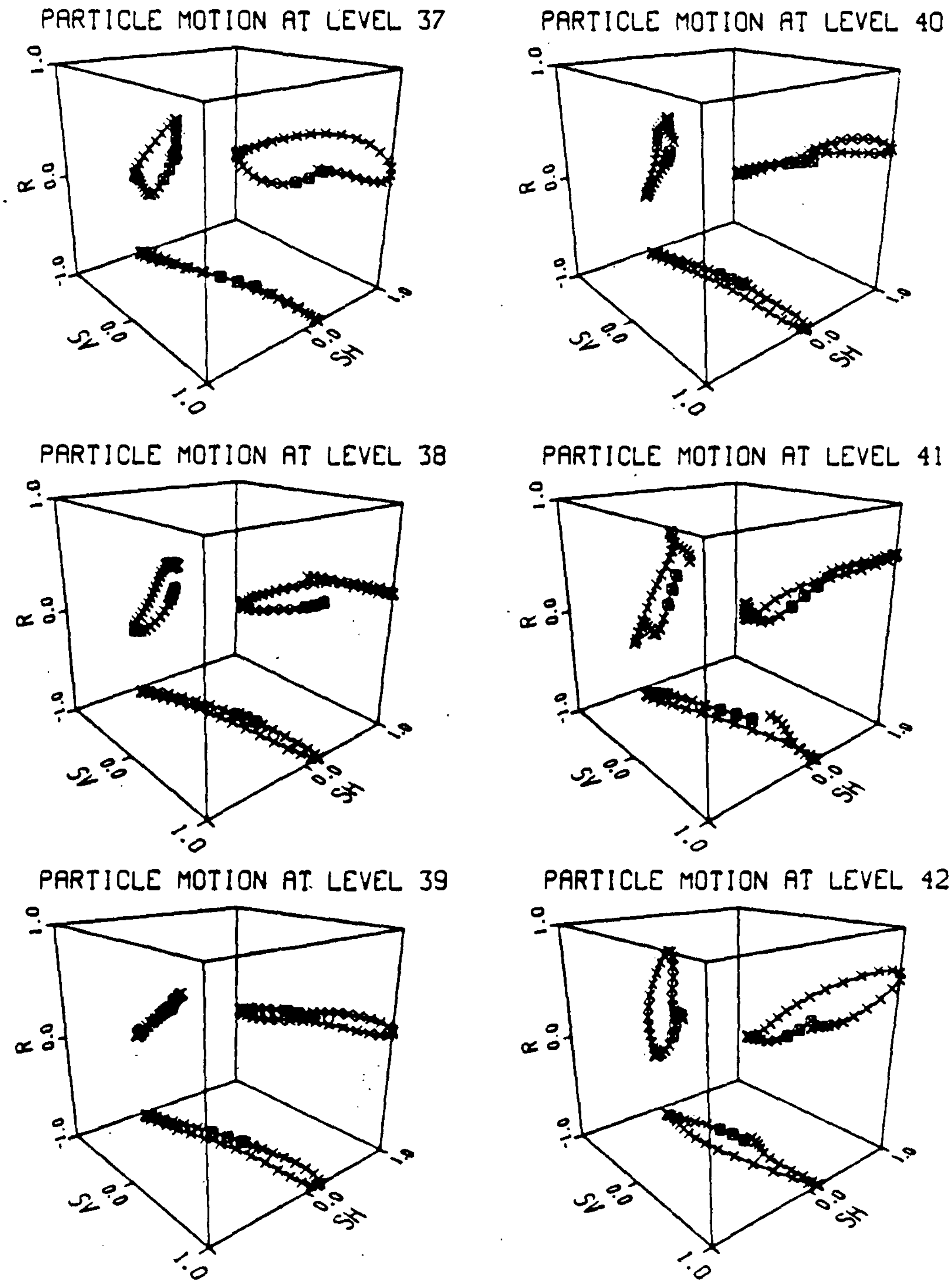

FAR OFFSET SV SOURCE

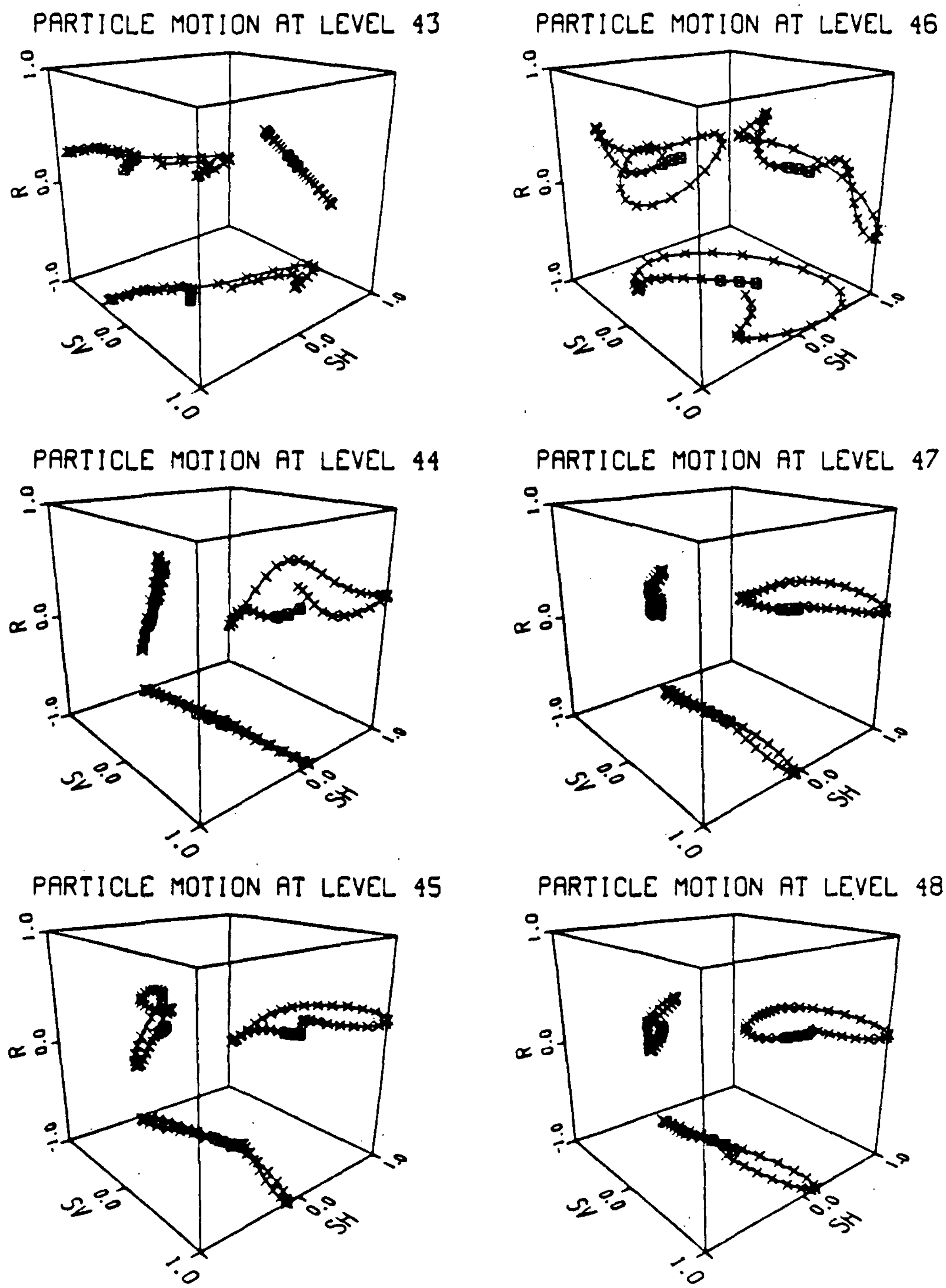

FAR OFFSET SV SOURCE

PARTICLE MOTION AT LEVEL 49

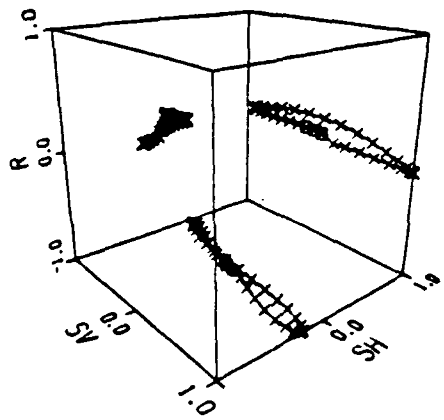

PARTICLE MOTION AT LEVEL 50

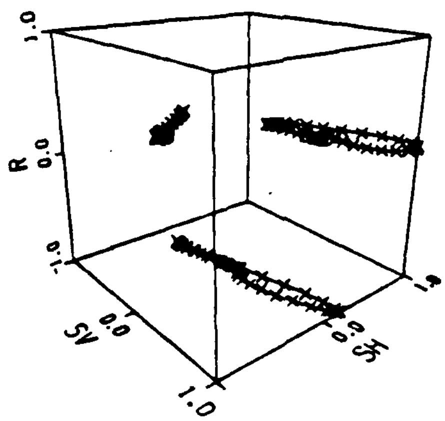

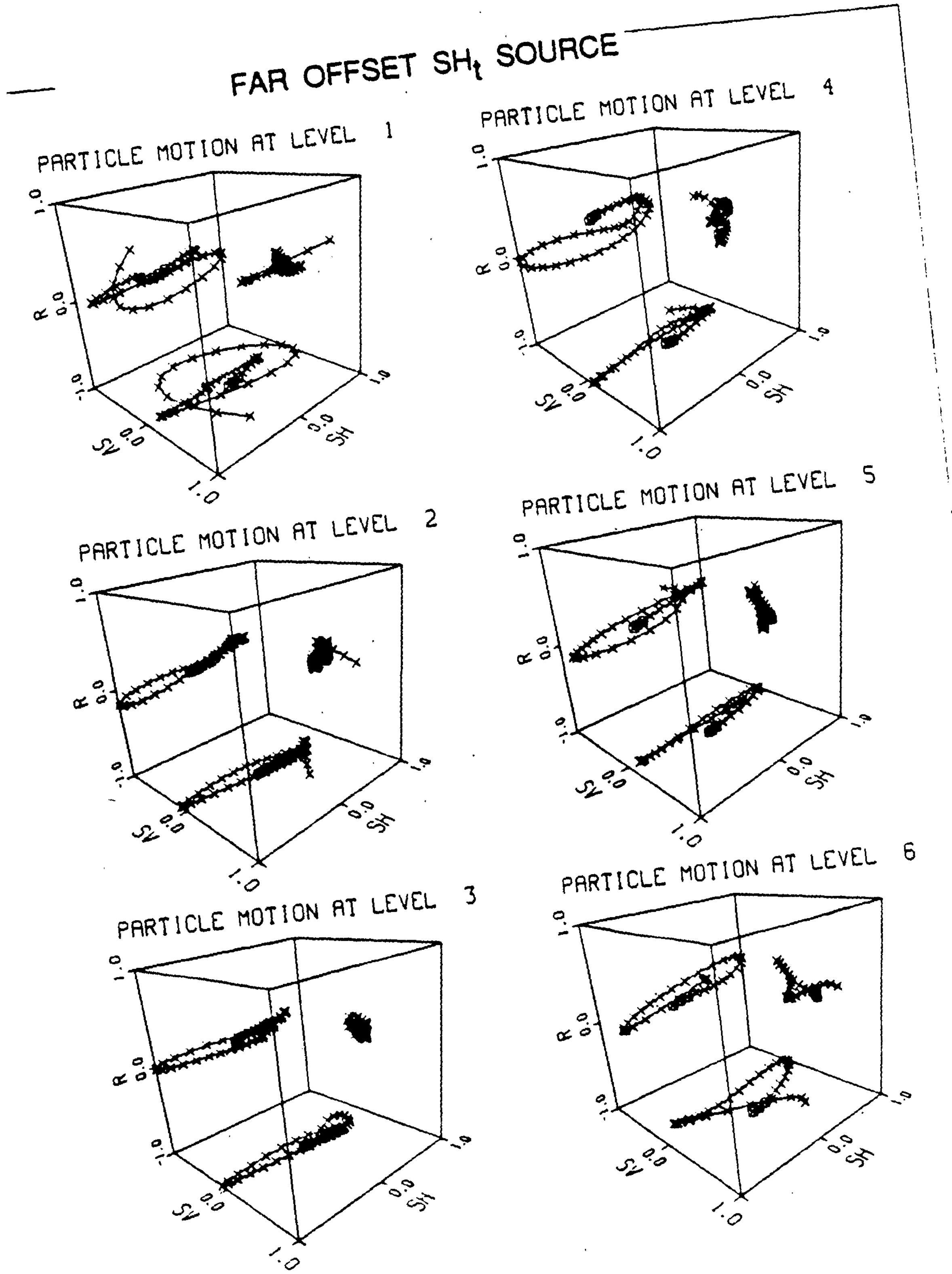
FAR OFFSET SH_t SOURCE
PARTICLE MOTION AT LEVEL 1
PARTICLE MOTION AT LEVEL 2
PARTICLE MOTION AT LEVEL 3
PARTICLE MOTION AT LEVEL 4
PARTICLE MOTION AT LEVEL 5
PARTICLE MOTION AT LEVEL 6
R
SV
SH
1.0
0.0
-1.0

FAR OFFSET SH_t SOURCE

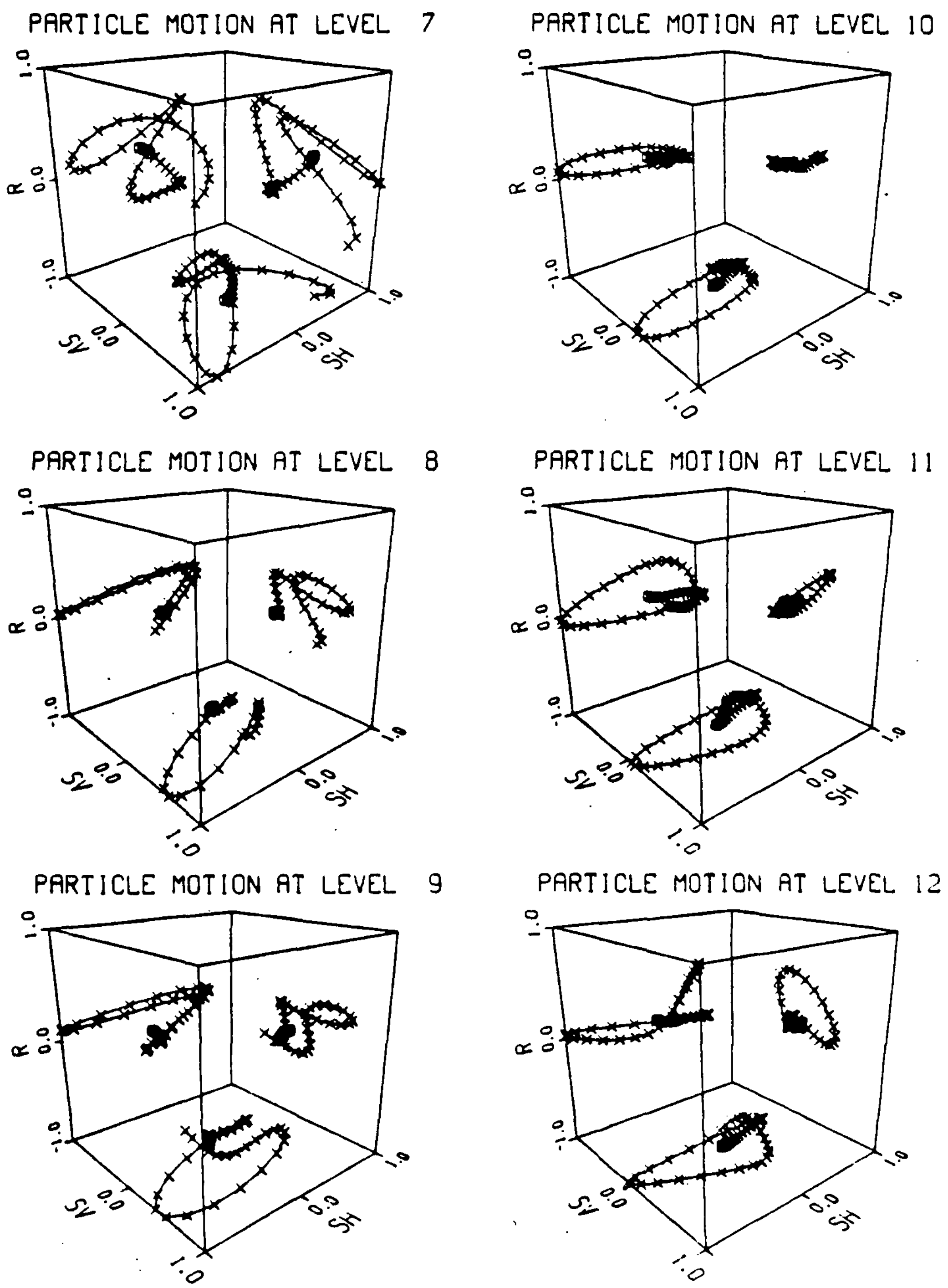

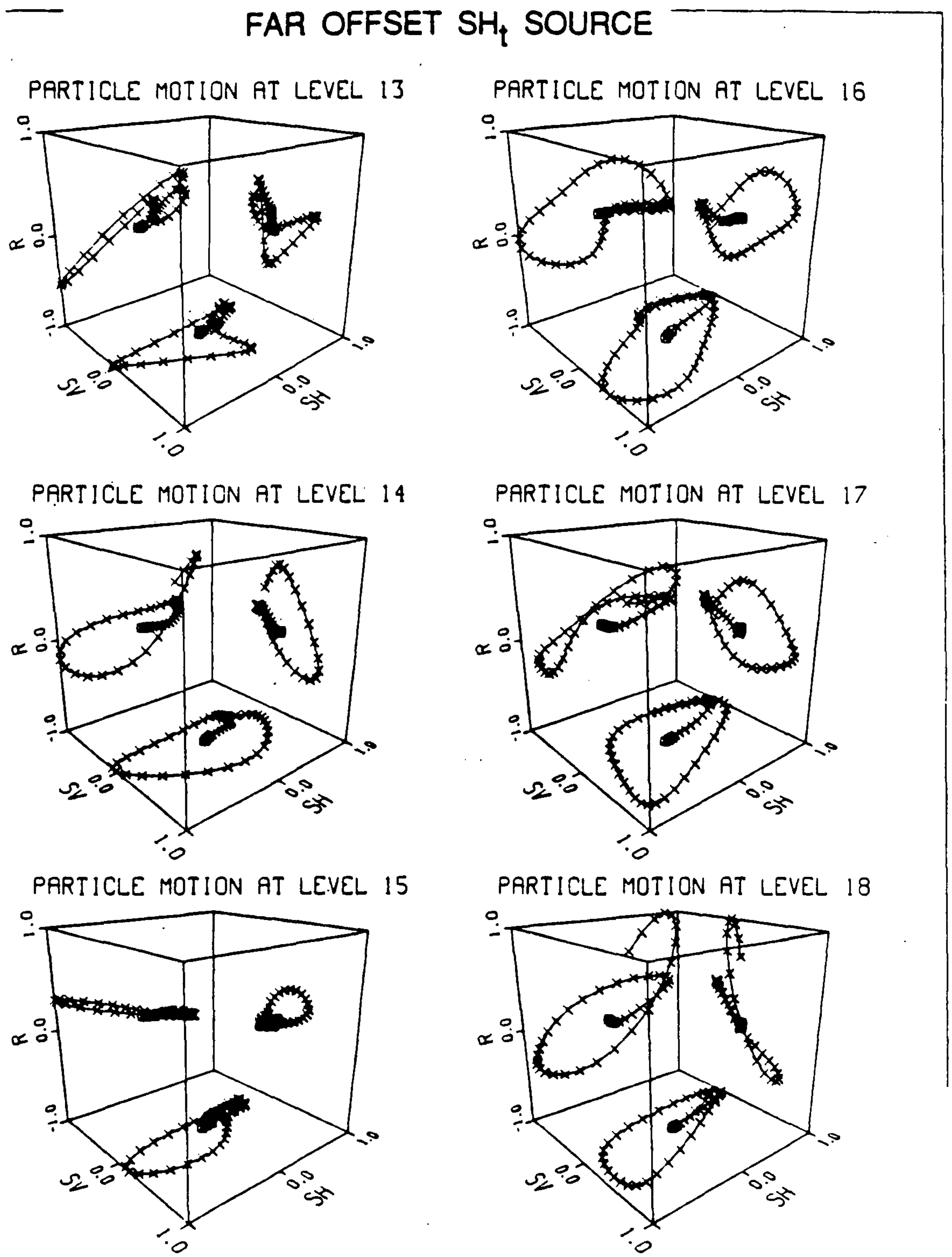
FAR OFFSET SH_t SOURCE
PARTICLE MOTION AT LEVEL 13
PARTICLE MOTION AT LEVEL 16
PARTICLE MOTION AT LEVEL 14
PARTICLE MOTION AT LEVEL 17
PARTICLE MOTION AT LEVEL 15
PARTICLE MOTION AT LEVEL 18
R
SV
SH
1.0
0.0
-1.0

FAR OFFSET SH_t SOURCE

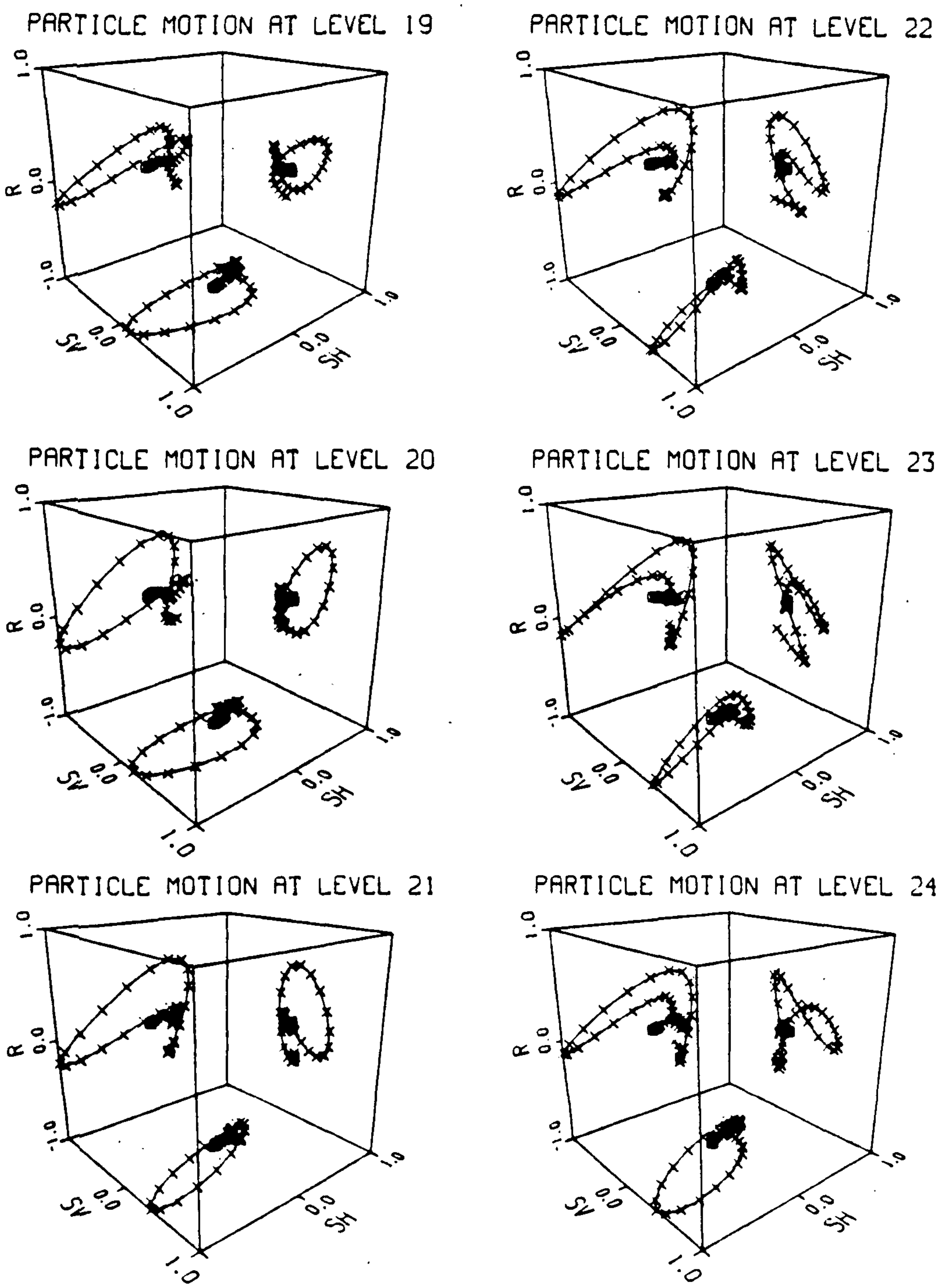

FAR OFFSET SH_t SOURCE

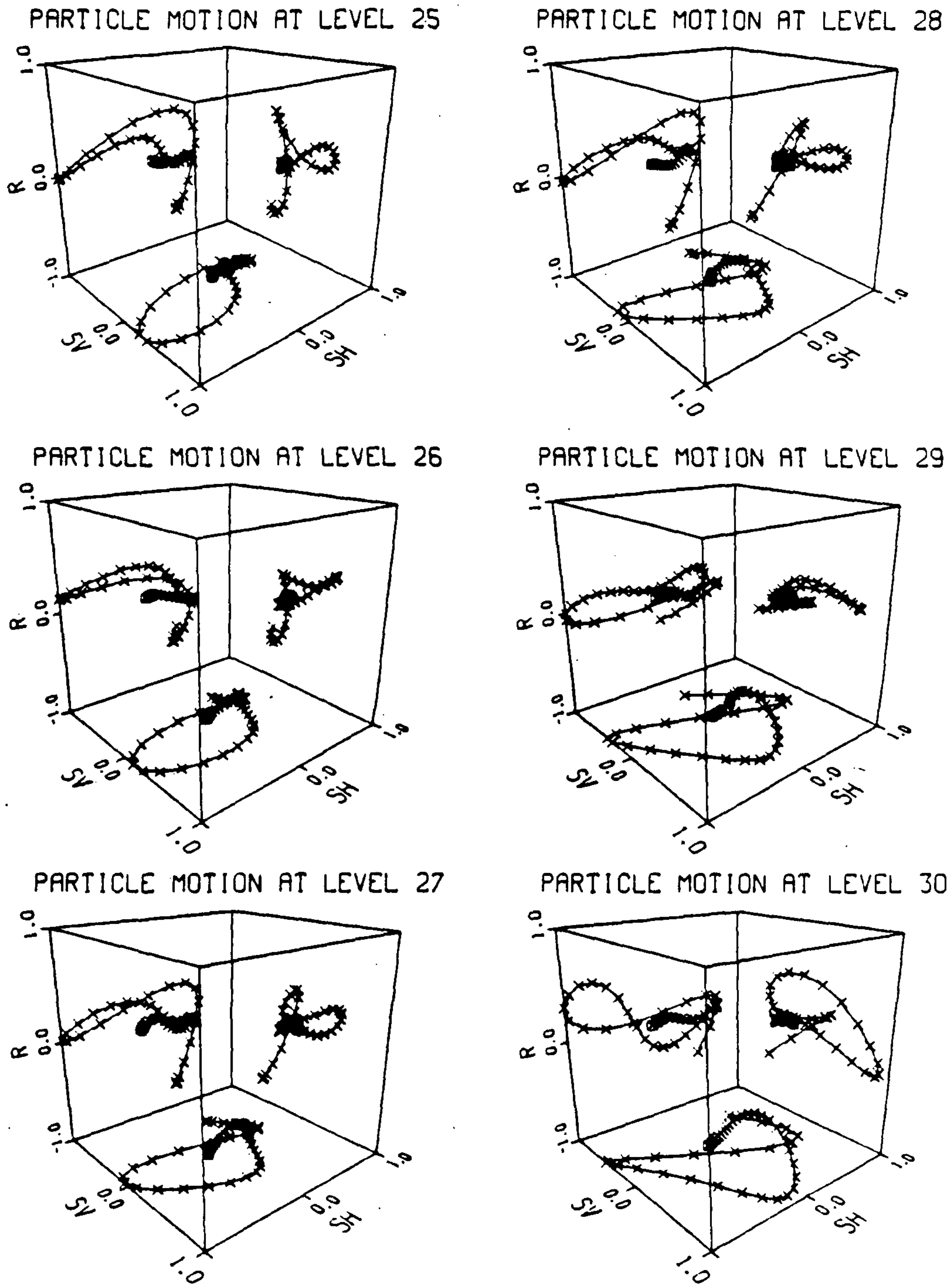

FAR OFFSET SH_t SOURCE

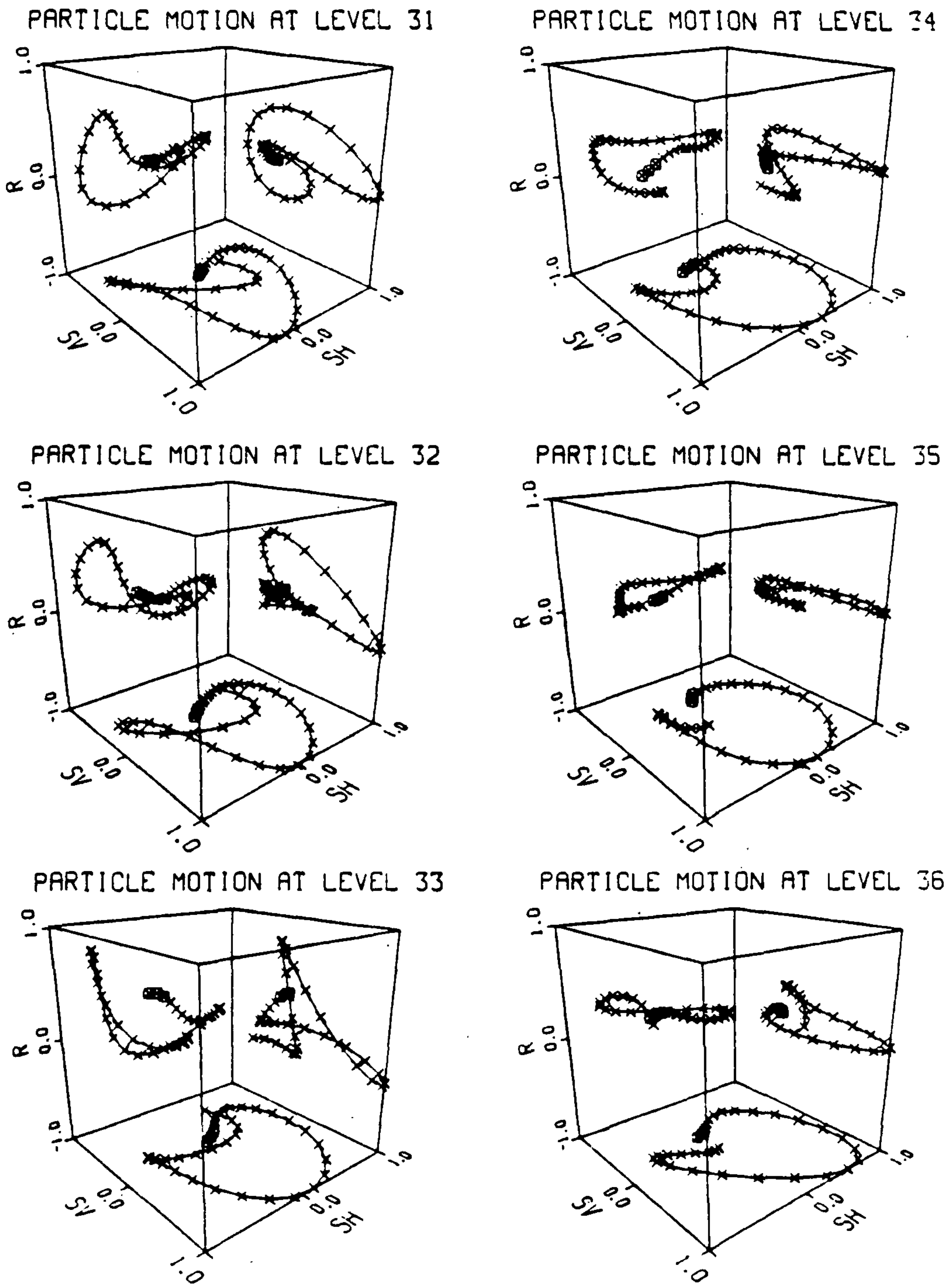

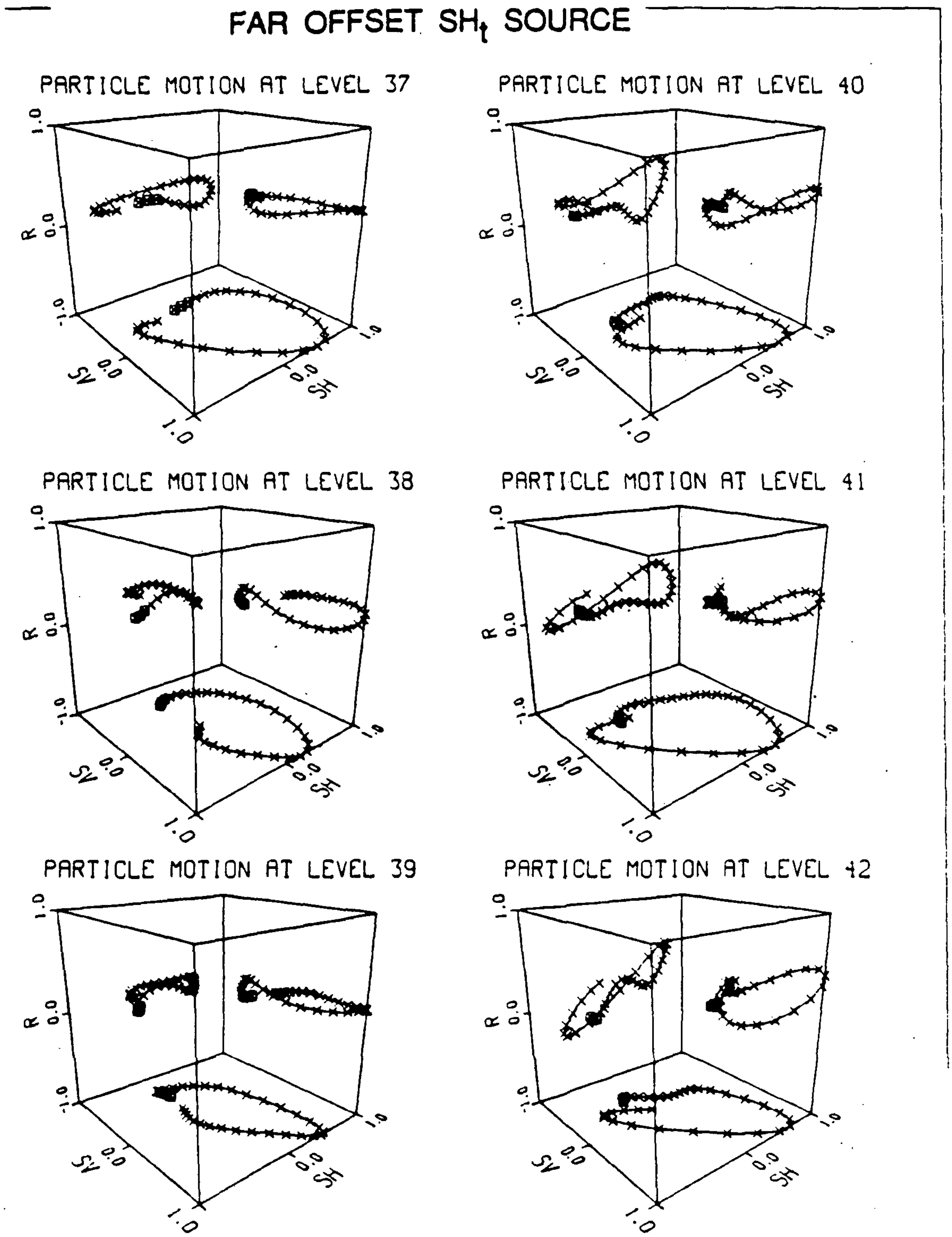
FAR OFFSET SH$_t$ SOURCE
PARTICLE MOTION AT LEVEL 37
PARTICLE MOTION AT LEVEL 40
PARTICLE MOTION AT LEVEL 38
PARTICLE MOTION AT LEVEL 41
PARTICLE MOTION AT LEVEL 39
PARTICLE MOTION AT LEVEL 42
R
SV
SH
1.0
0.0
-1.0

FAR OFFSET SH_t SOURCE

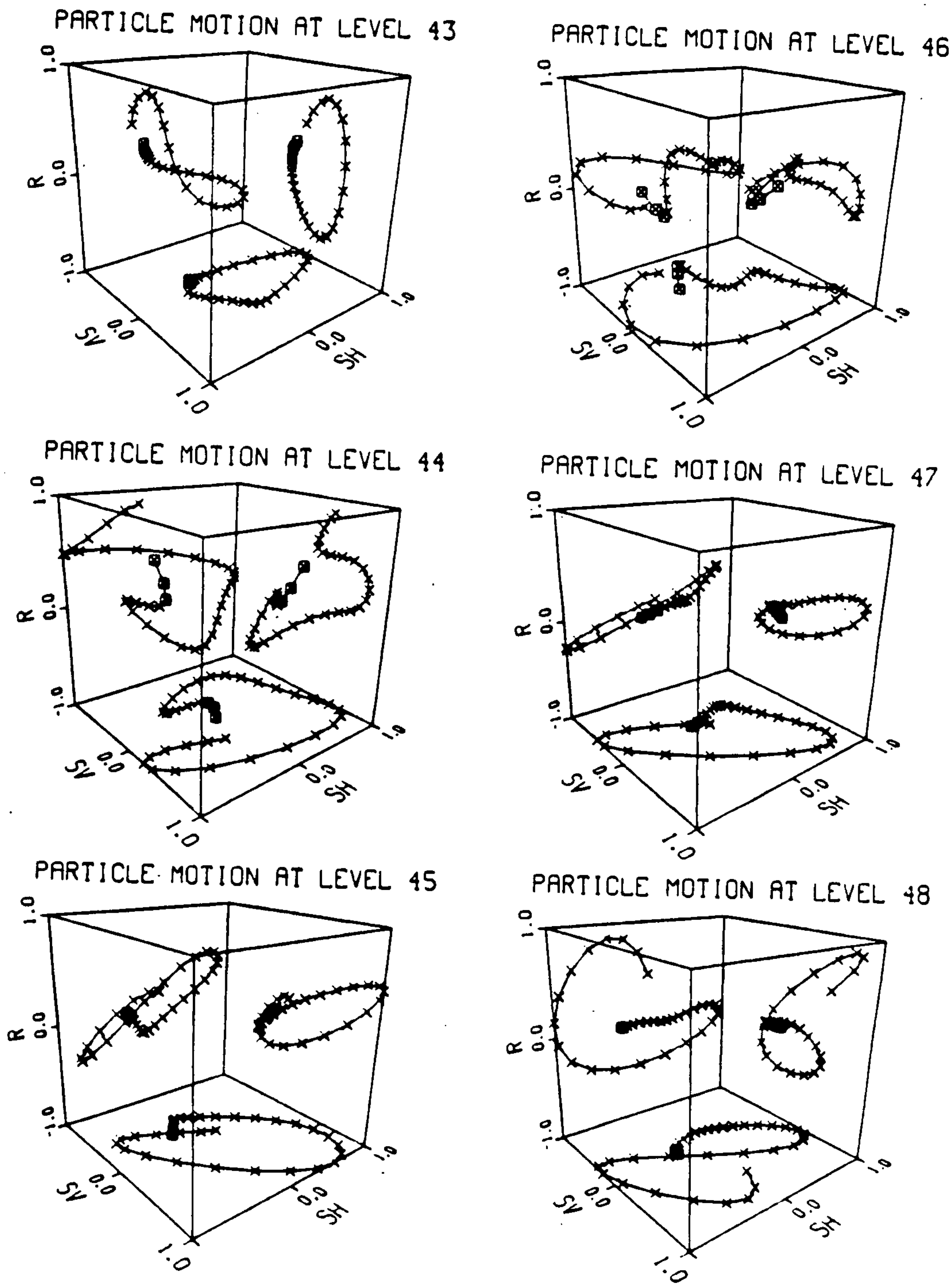

FAR OFFSET SH_t SOURCE

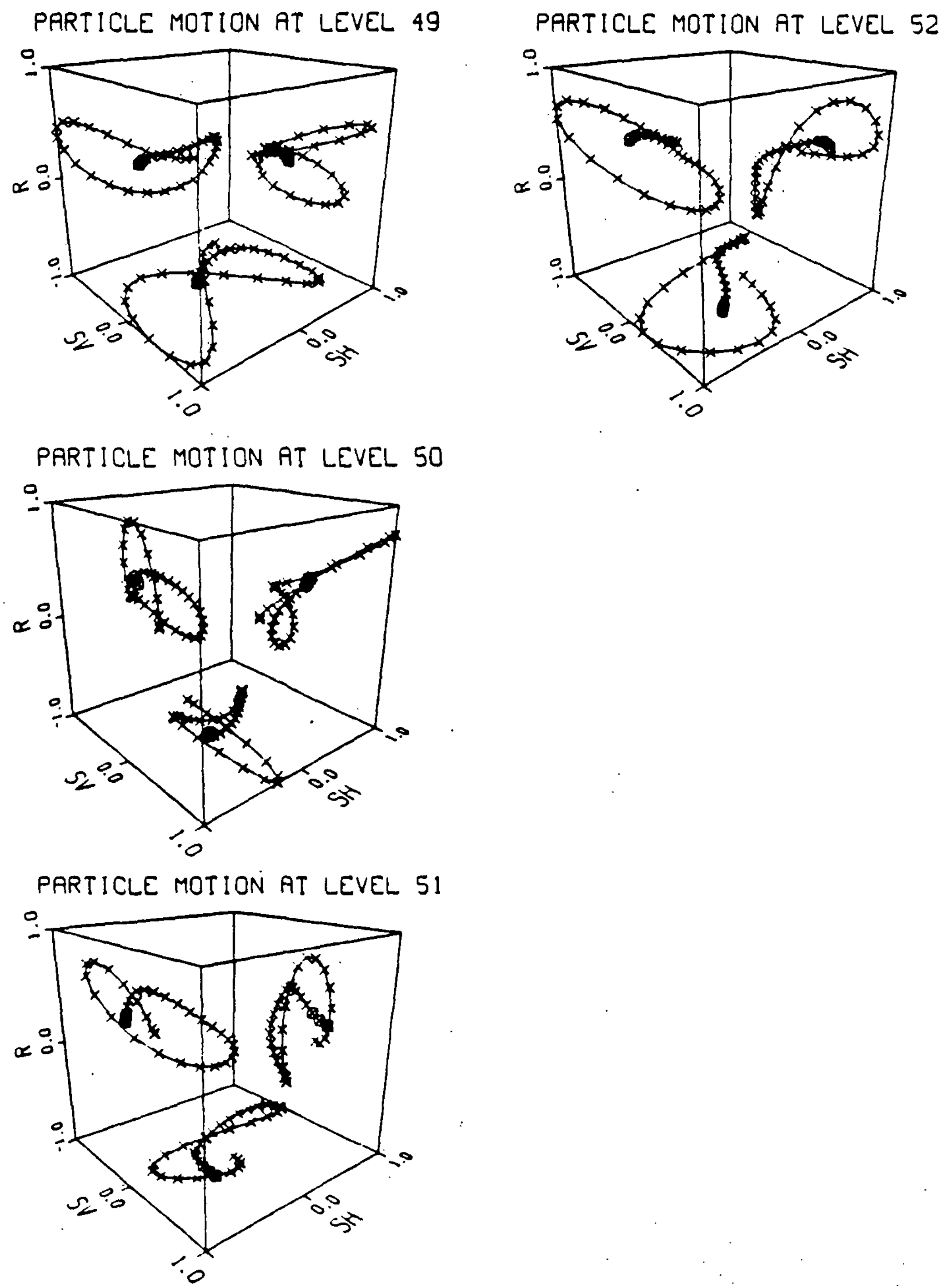

NEAR OFFSET P-WAVE SOURCE

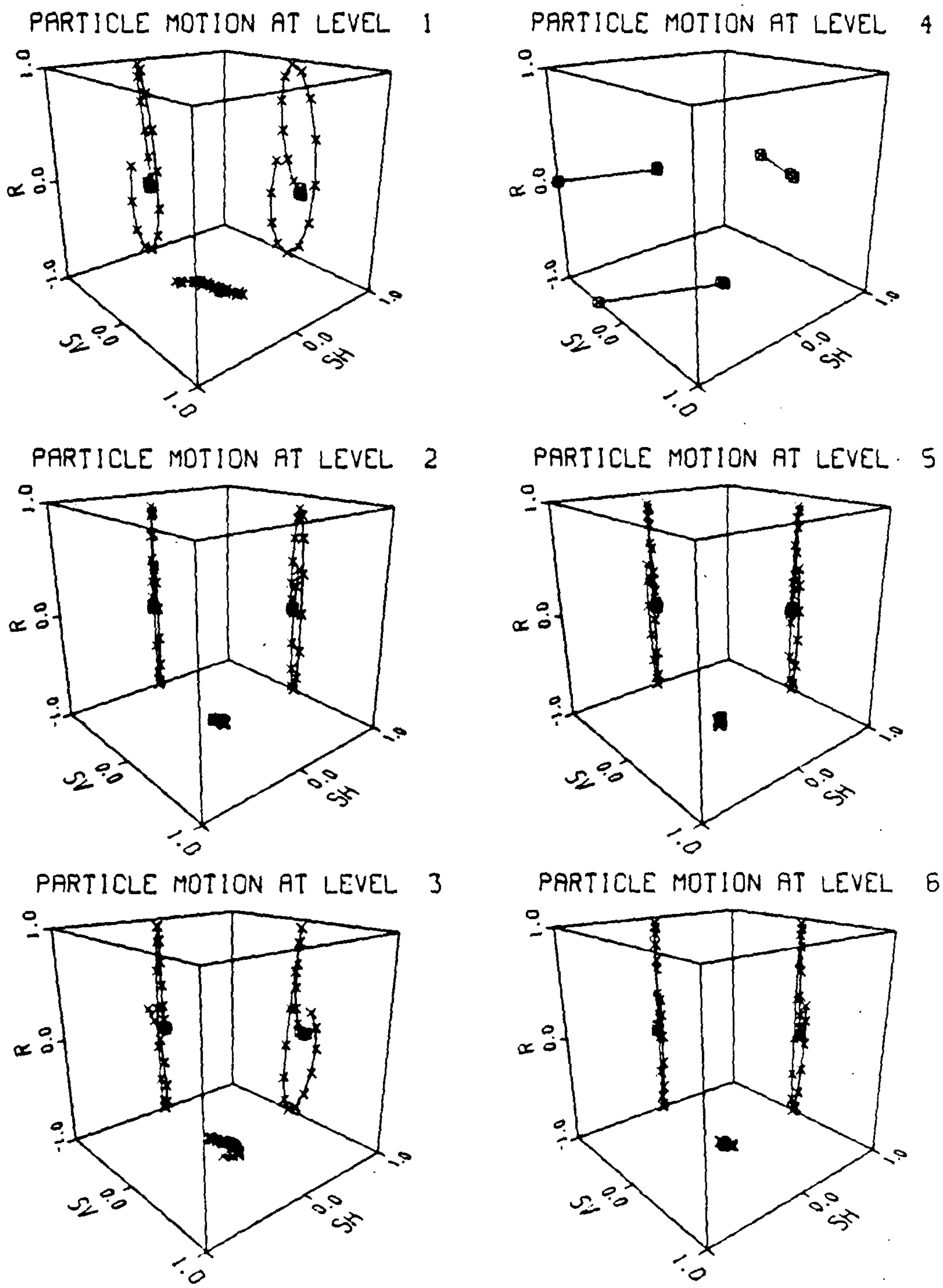

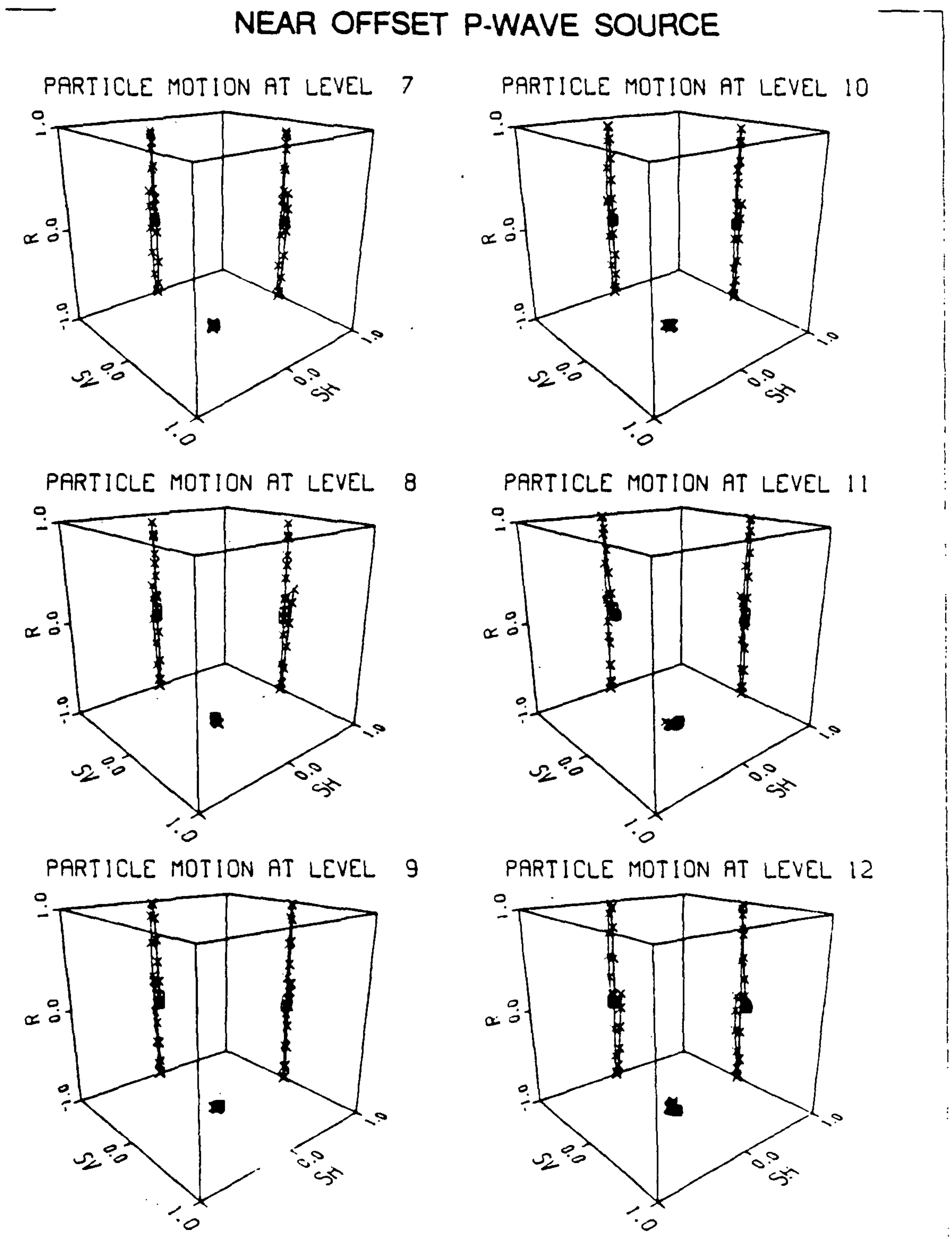
NEAR OFFSET P-WAVE SOURCE
PARTICLE MOTION AT LEVEL 7
PARTICLE MOTION AT LEVEL 10
PARTICLE MOTION AT LEVEL 8
PARTICLE MOTION AT LEVEL 11
PARTICLE MOTION AT LEVEL 9
PARTICLE MOTION AT LEVEL 12
R
SV
SH
1.0
0.0
-1.0

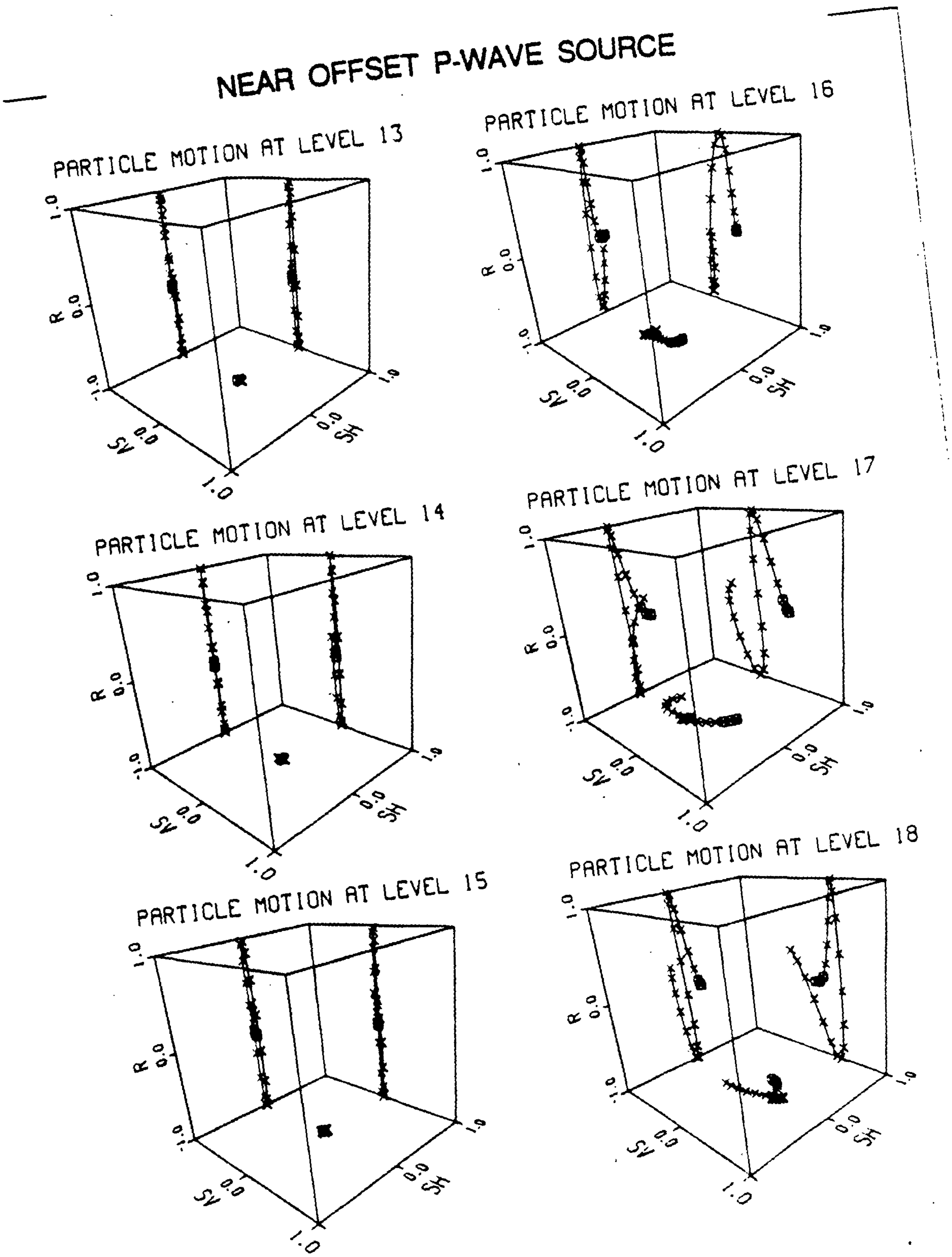
NEAR OFFSET P-WAVE SOURCE
PARTICLE MOTION AT LEVEL 13
PARTICLE MOTION AT LEVEL 14
PARTICLE MOTION AT LEVEL 15
PARTICLE MOTION AT LEVEL 16
PARTICLE MOTION AT LEVEL 17
PARTICLE MOTION AT LEVEL 18
R
SV
SH
1.0
0.0
-1.0

NEAR OFFSET P-WAVE SOURCE

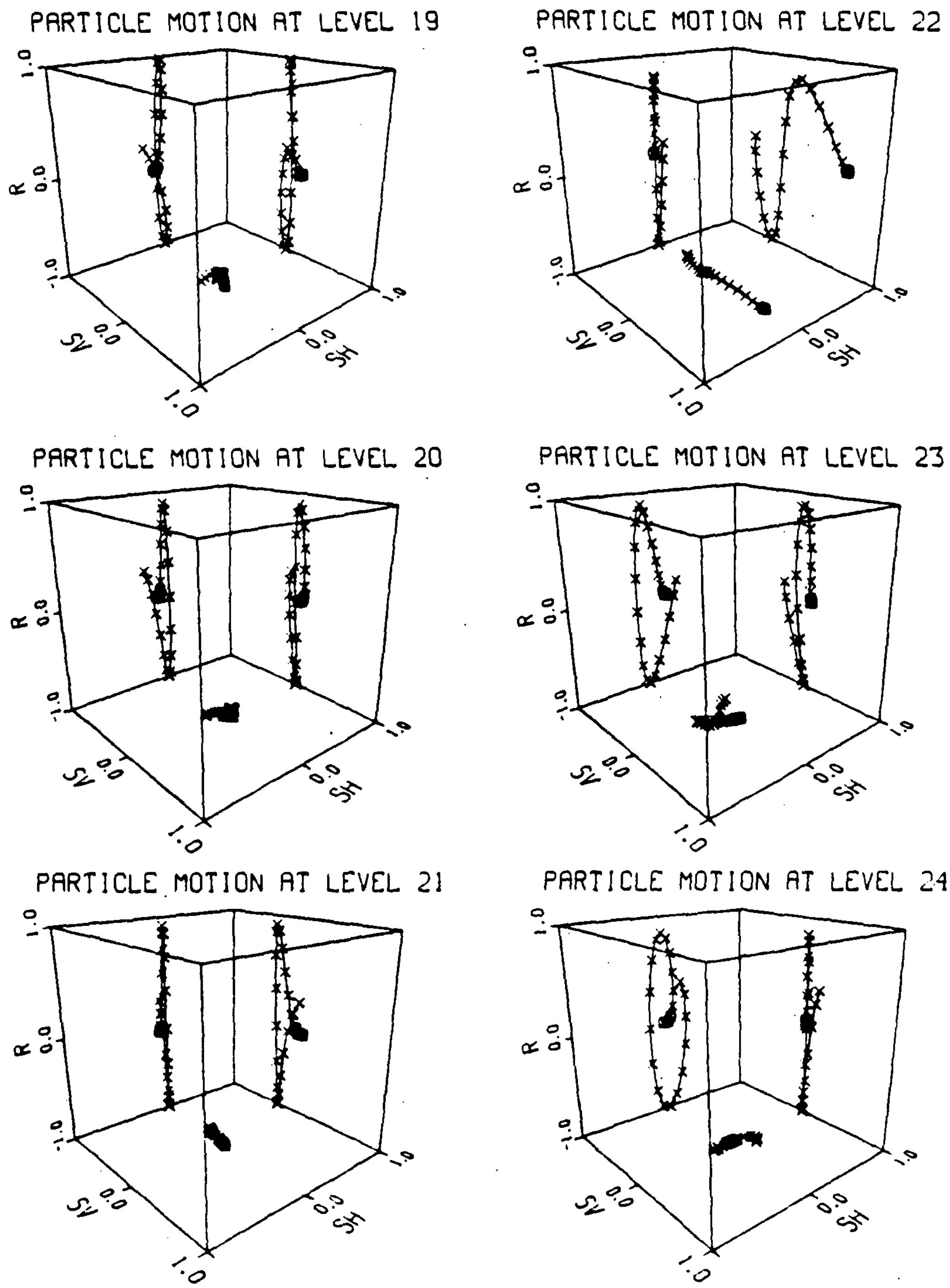

NEAR OFFSET P-WAVE SOURCE

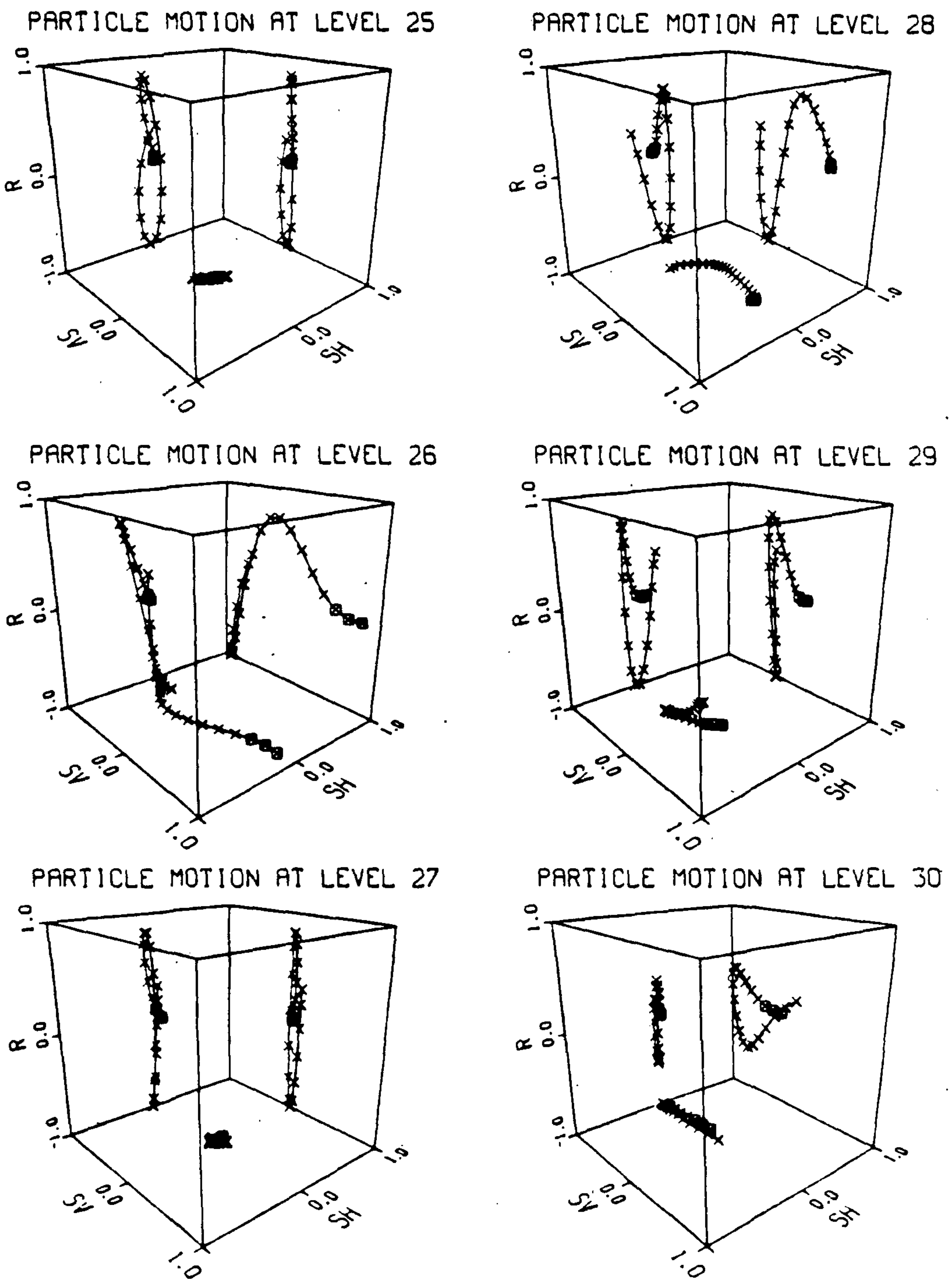

NEAR OFFSET P-WAVE SOURCE

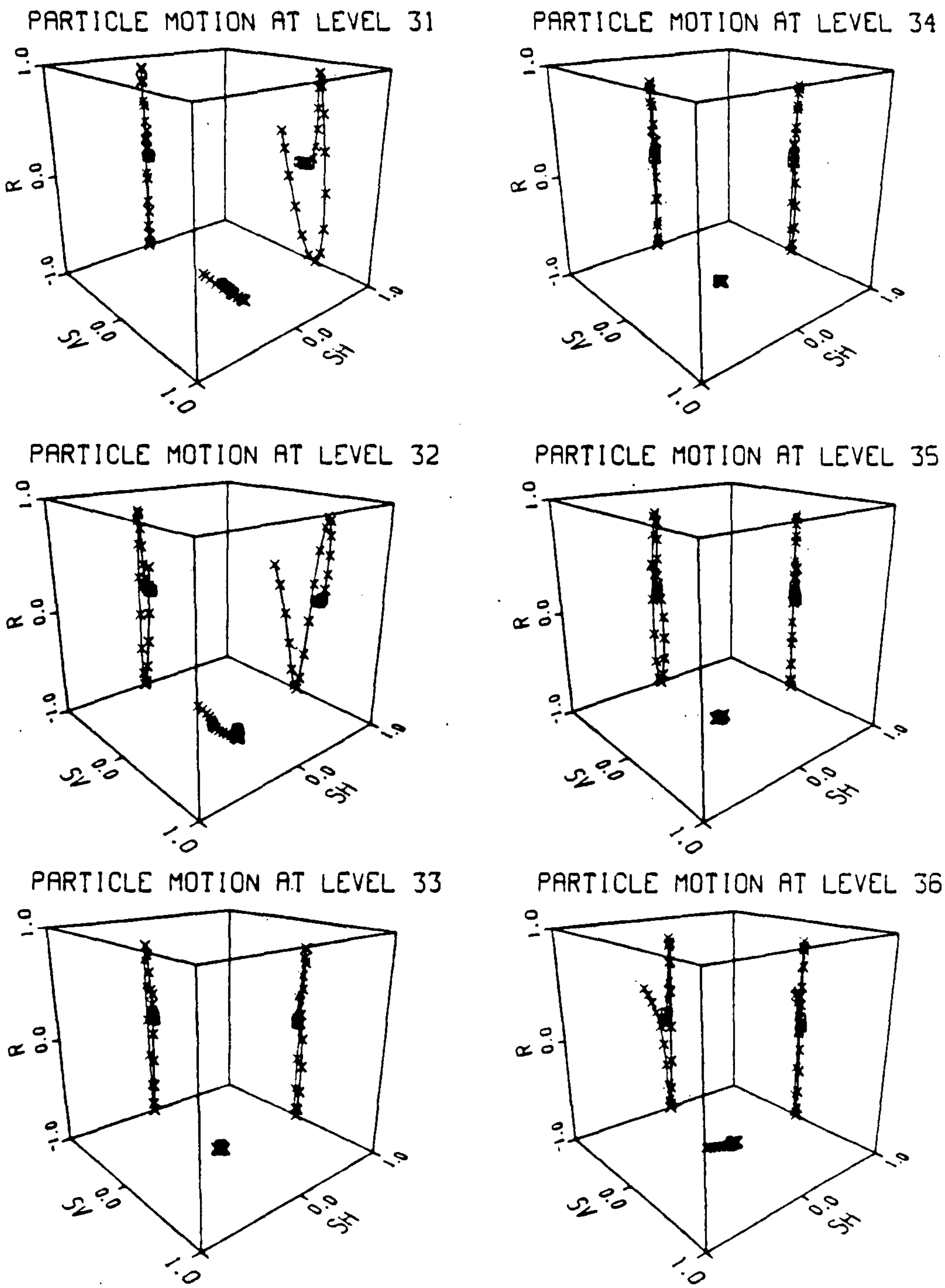

NEAR OFFSET P-WAVE SOURCE

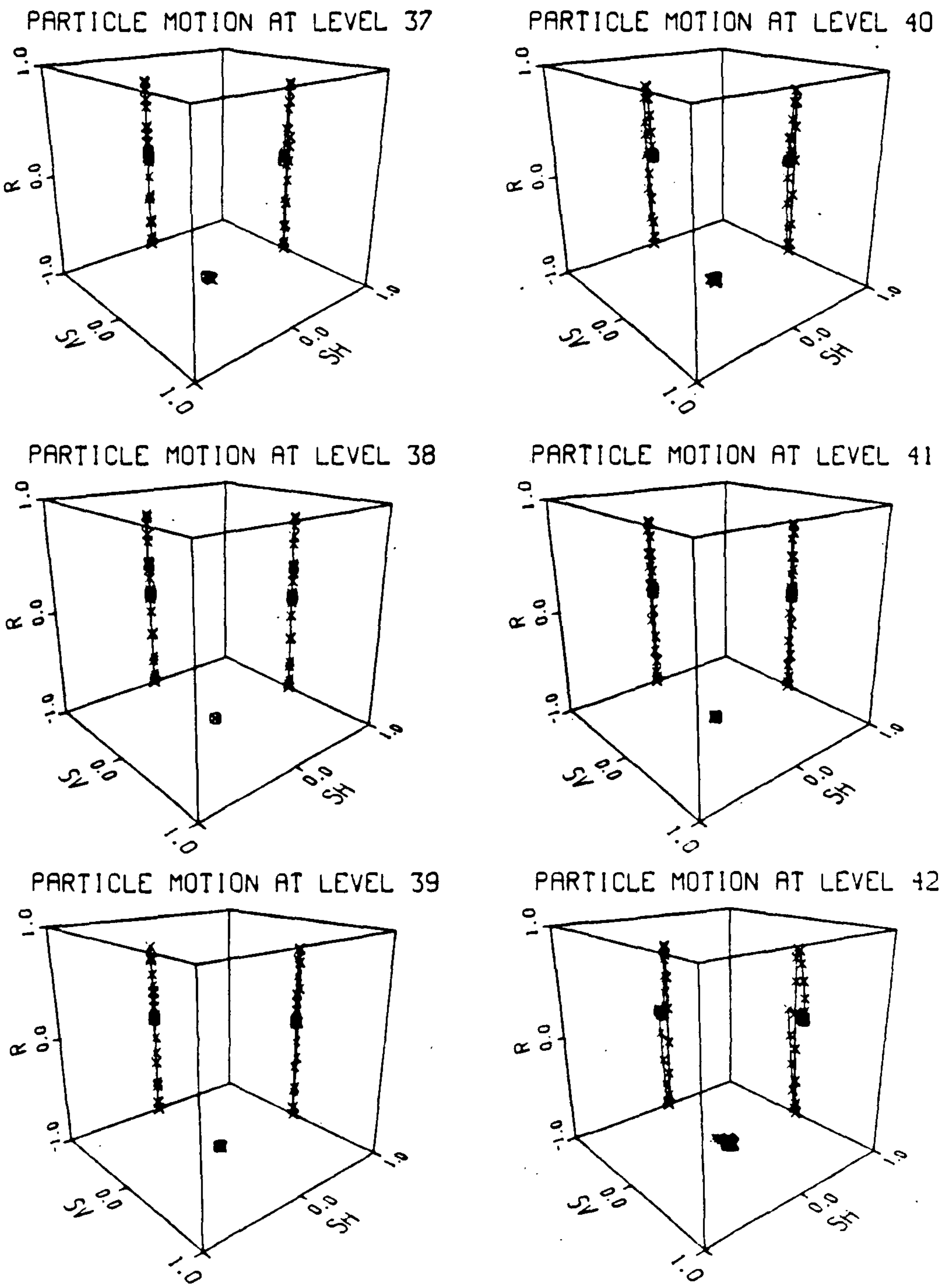

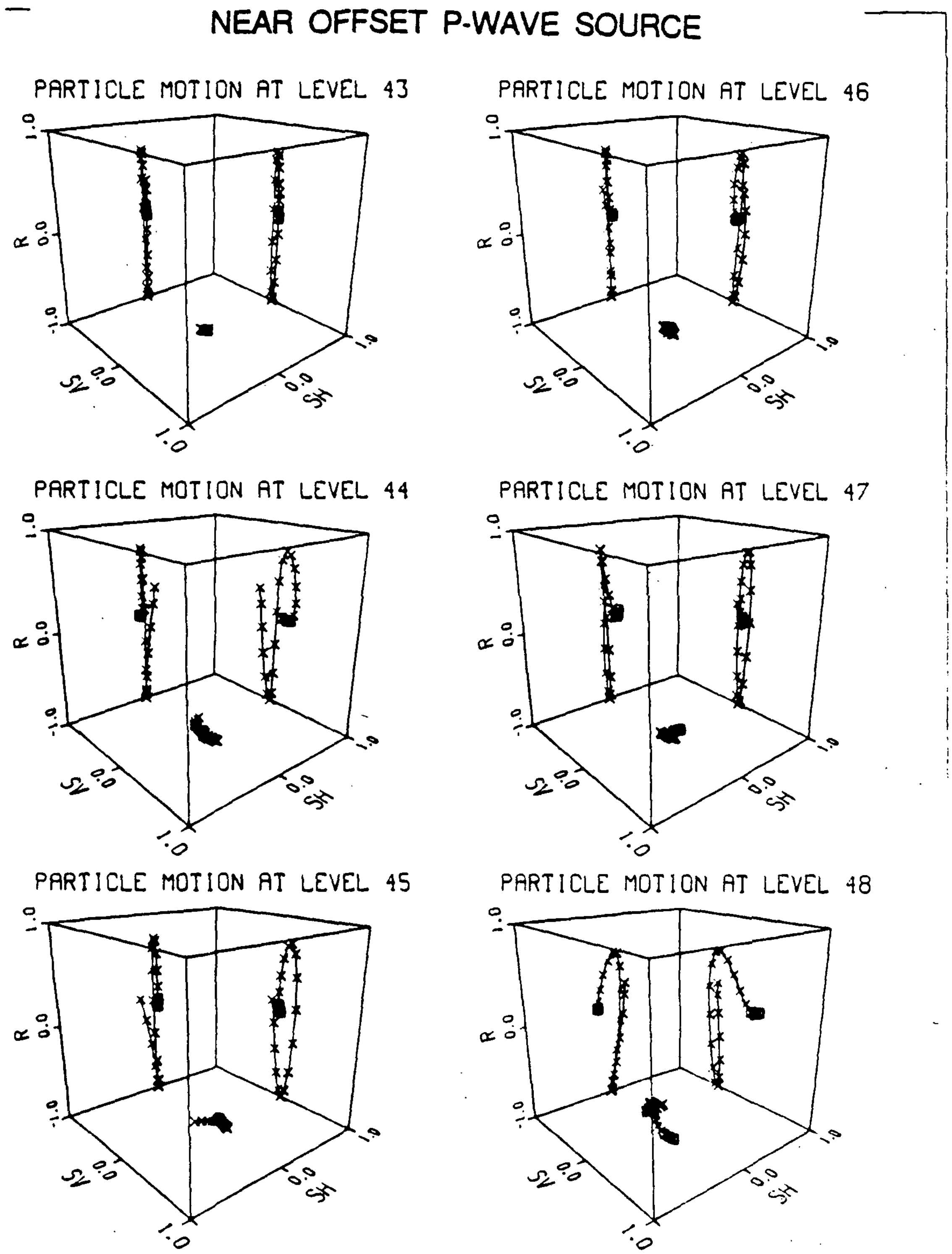
NEAR OFFSET P-WAVE SOURCE
PARTICLE MOTION AT LEVEL 43
PARTICLE MOTION AT LEVEL 46
PARTICLE MOTION AT LEVEL 44
PARTICLE MOTION AT LEVEL 47
PARTICLE MOTION AT LEVEL 45
PARTICLE MOTION AT LEVEL 48
R
SV
SH
1.0
0.0
-1.0

NEAR OFFSET P-WAVE SOURCE

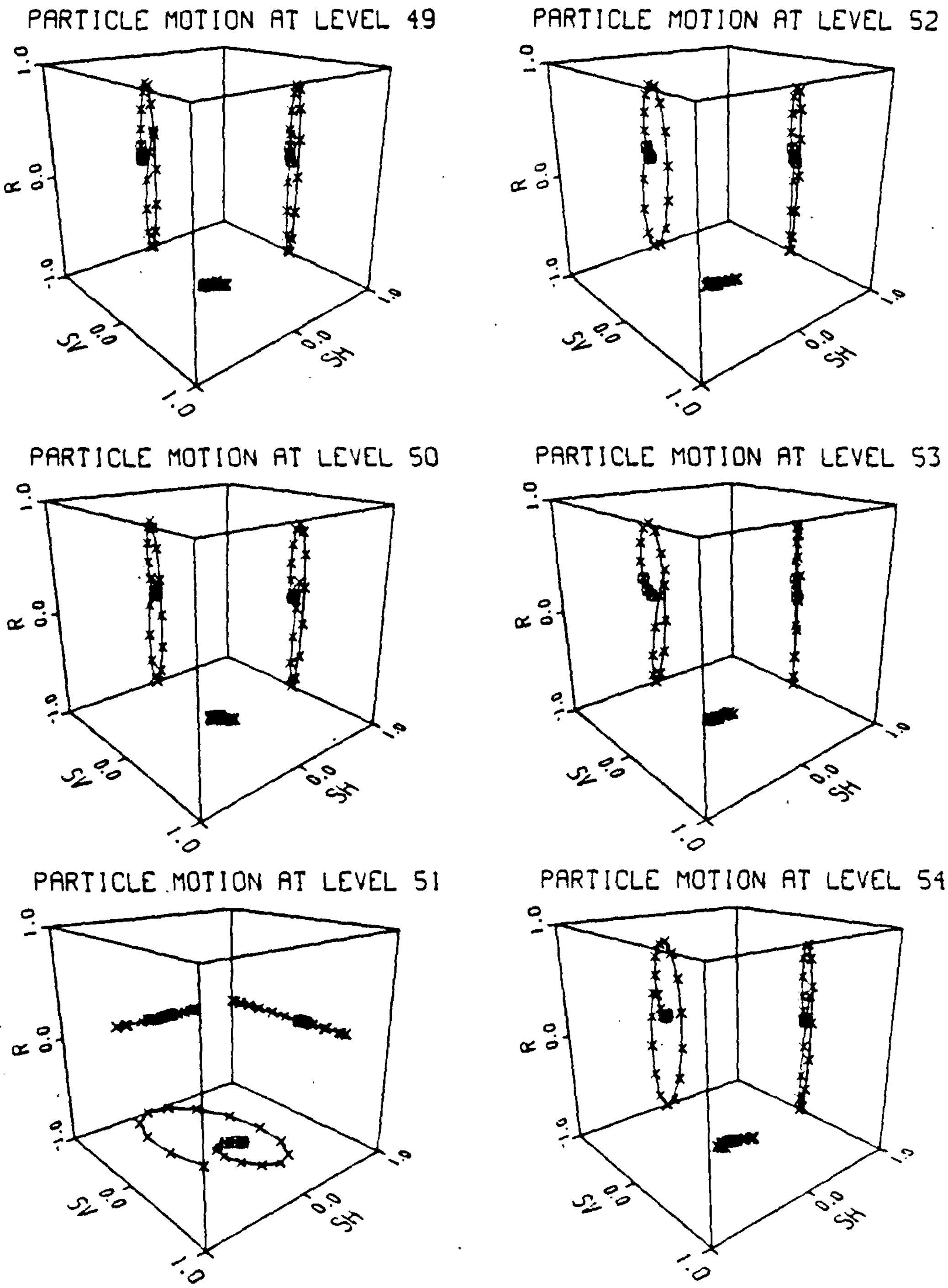

NEAR OFFSET P-WAVE SOURCE

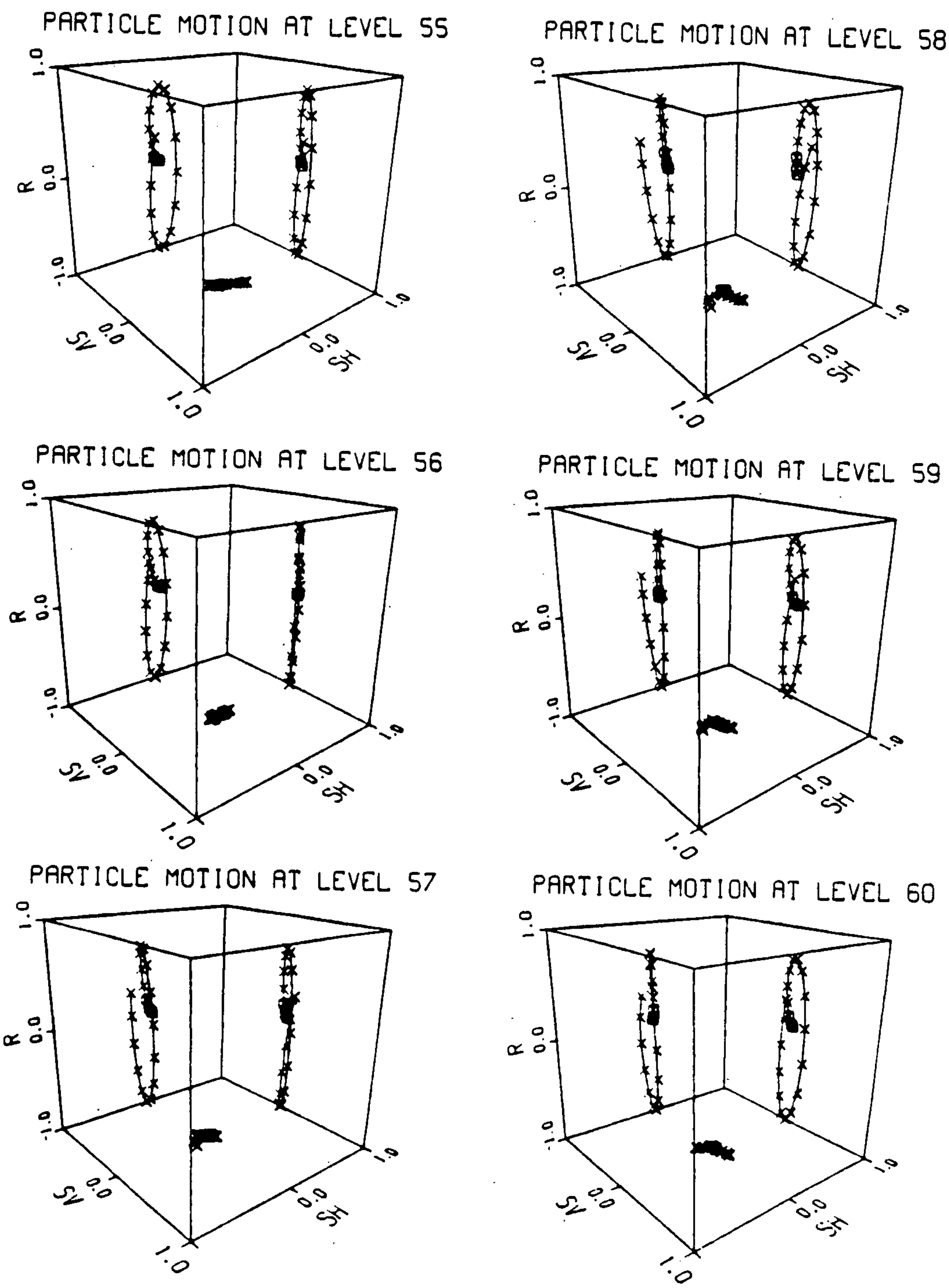

NEAR OFFSET P-WAVE SOURCE

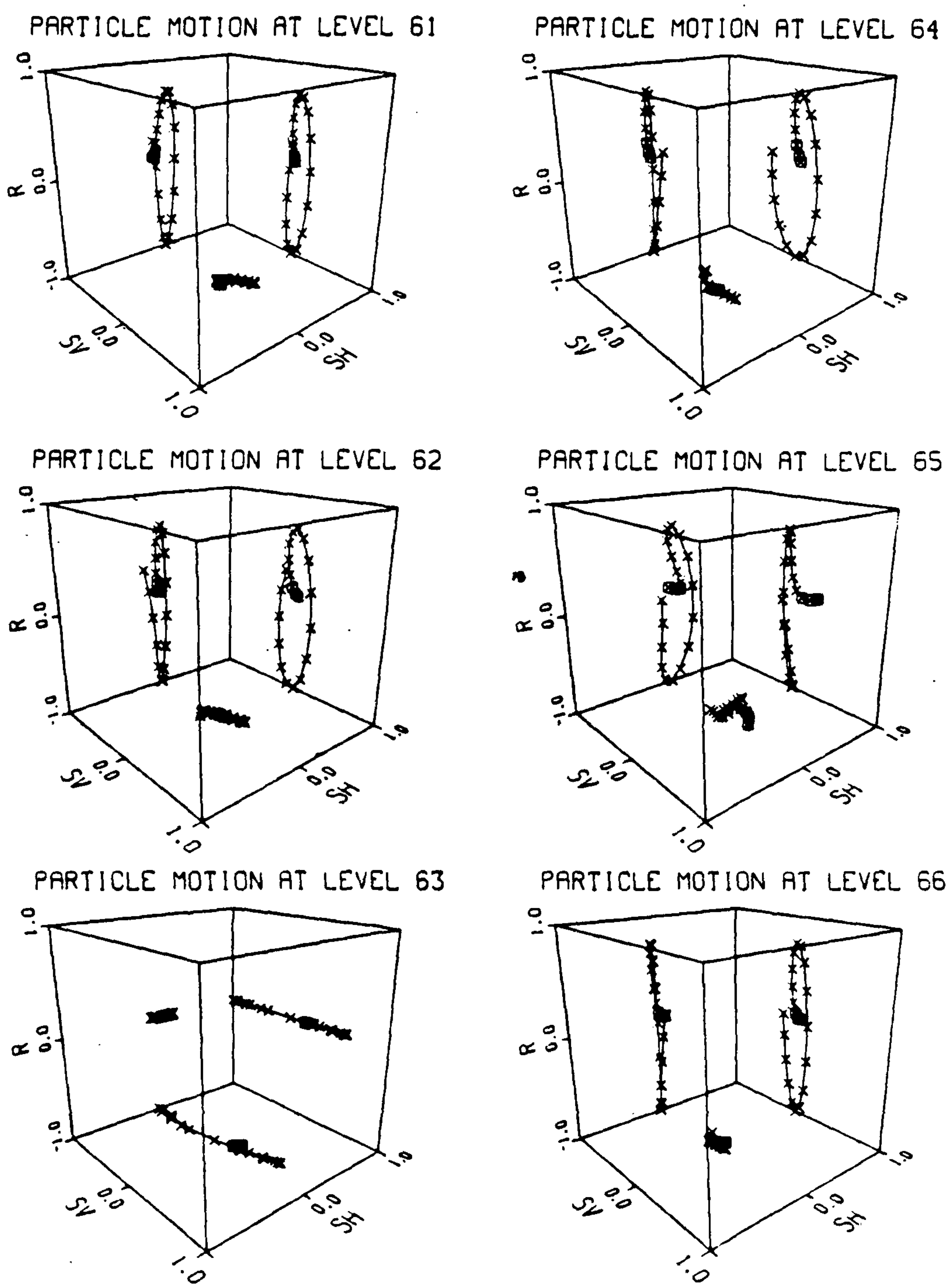

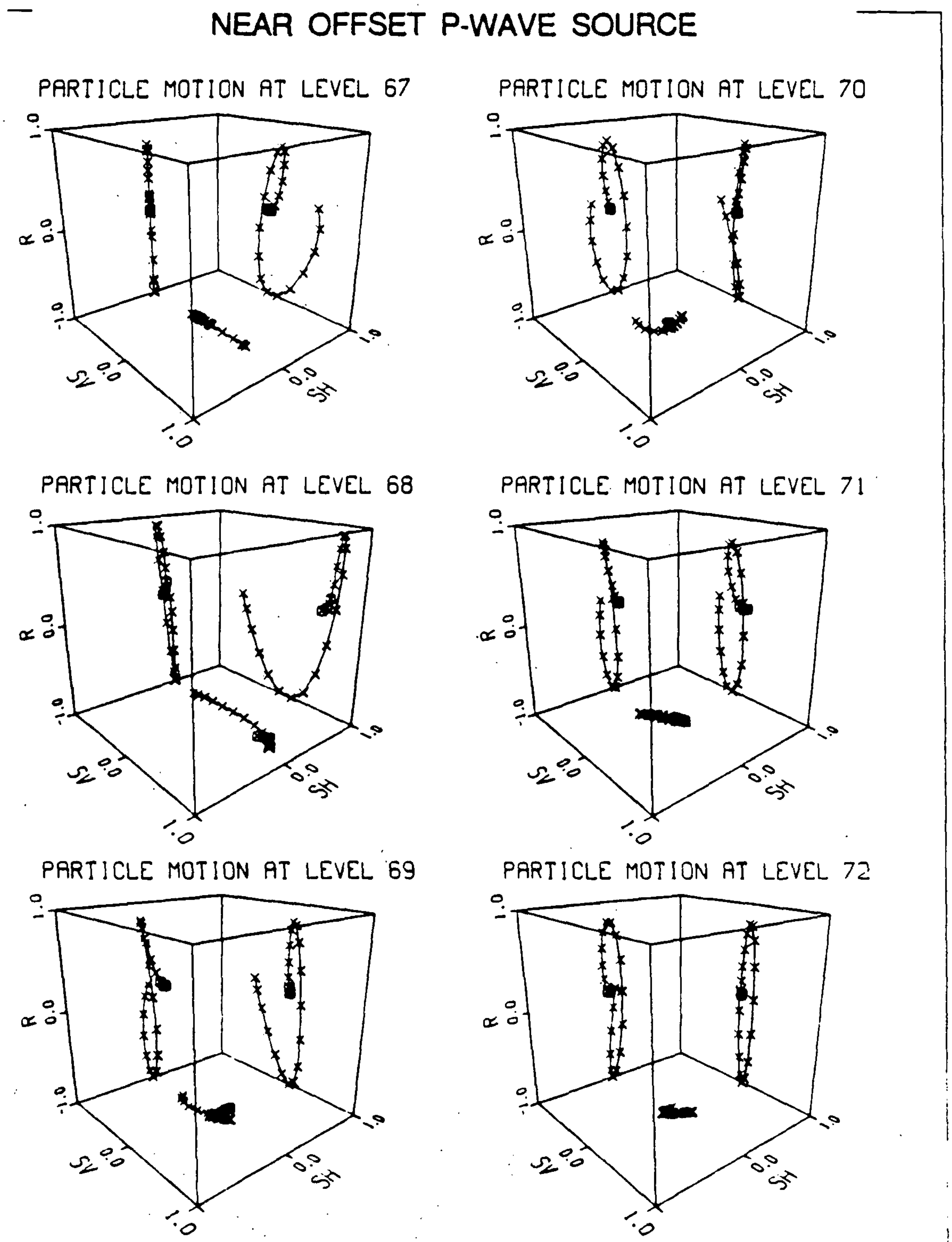
NEAR OFFSET P-WAVE SOURCE
PARTICLE MOTION AT LEVEL 67
PARTICLE MOTION AT LEVEL 70
PARTICLE MOTION AT LEVEL 68
PARTICLE MOTION AT LEVEL 71
PARTICLE MOTION AT LEVEL 69
PARTICLE MOTION AT LEVEL 72
R
SV
SH
1.0
0.0
-1.0

NEAR OFFSET P-WAVE SOURCE

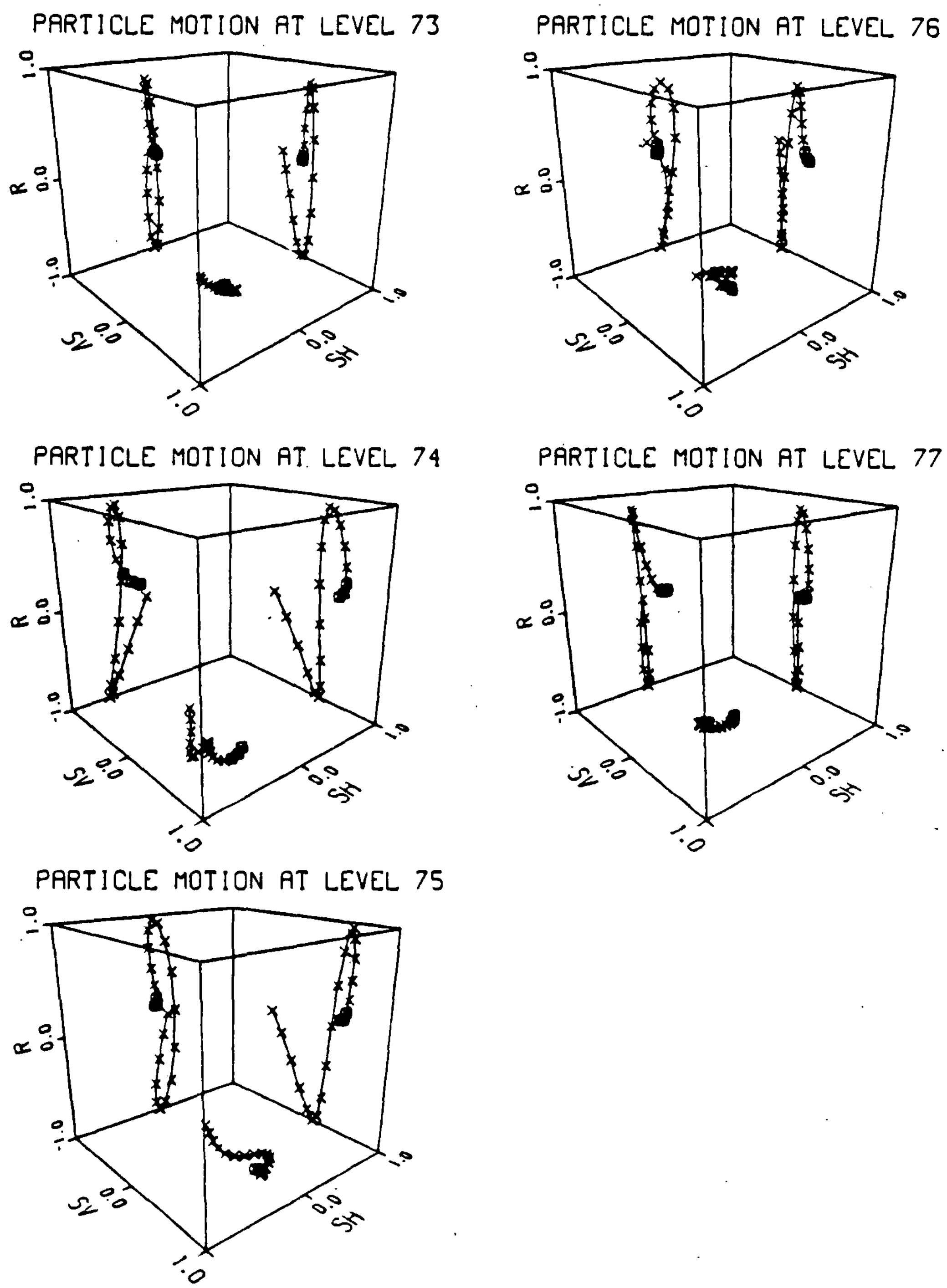

NEAR OFFSET SH_t SOURCE

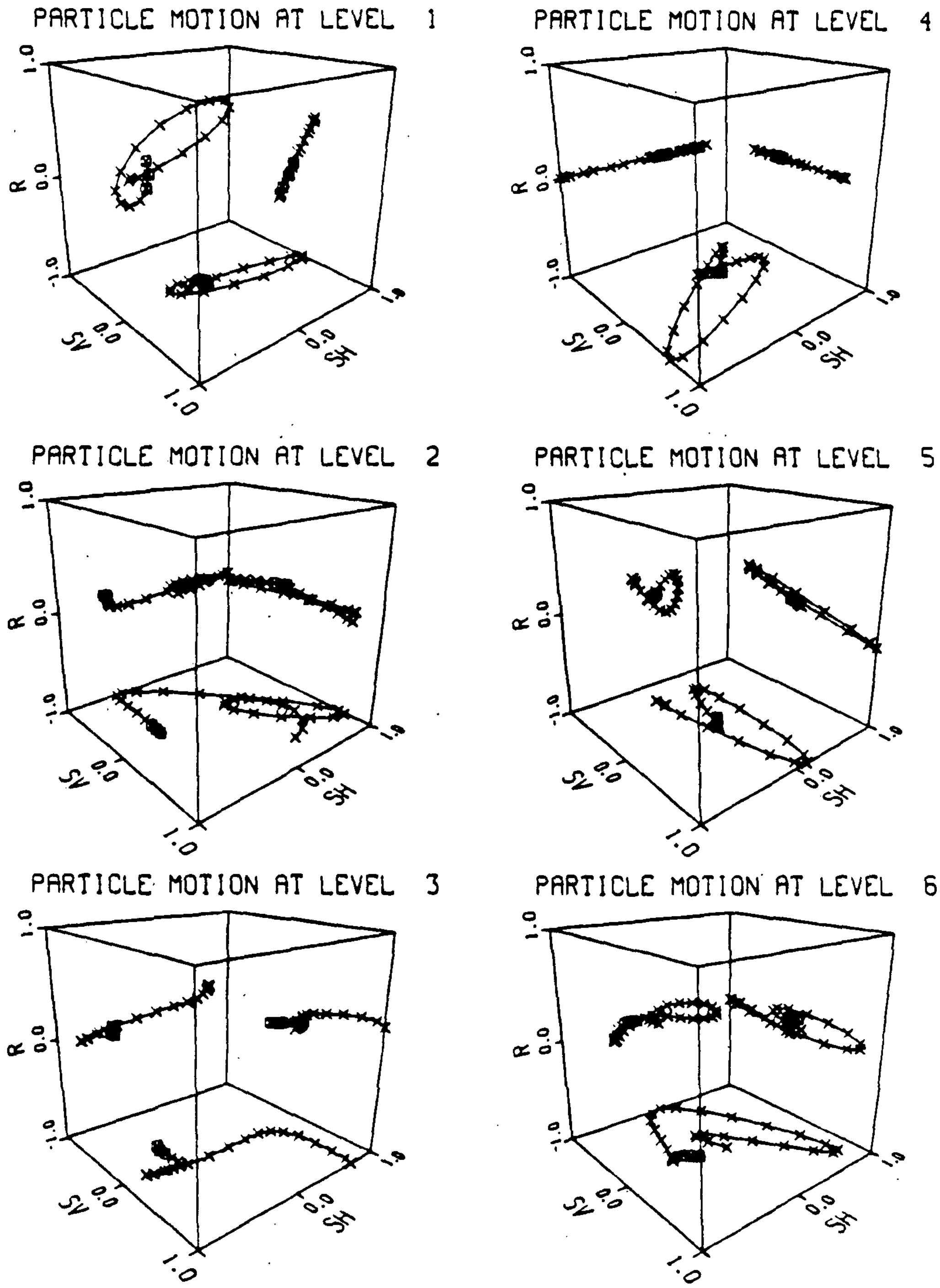

NEAR OFFSET SH_t SOURCE

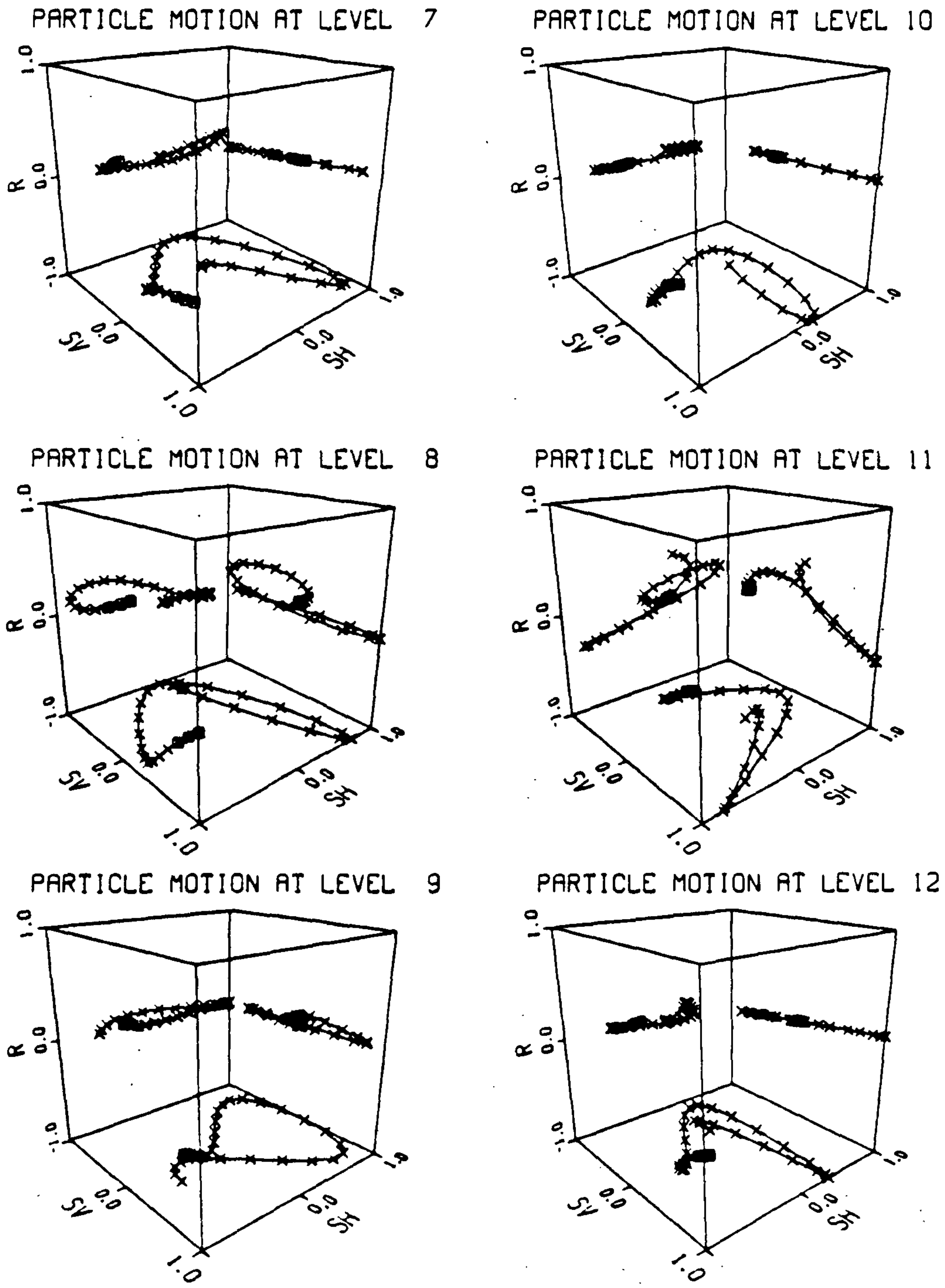

NEAR OFFSET SH_t SOURCE

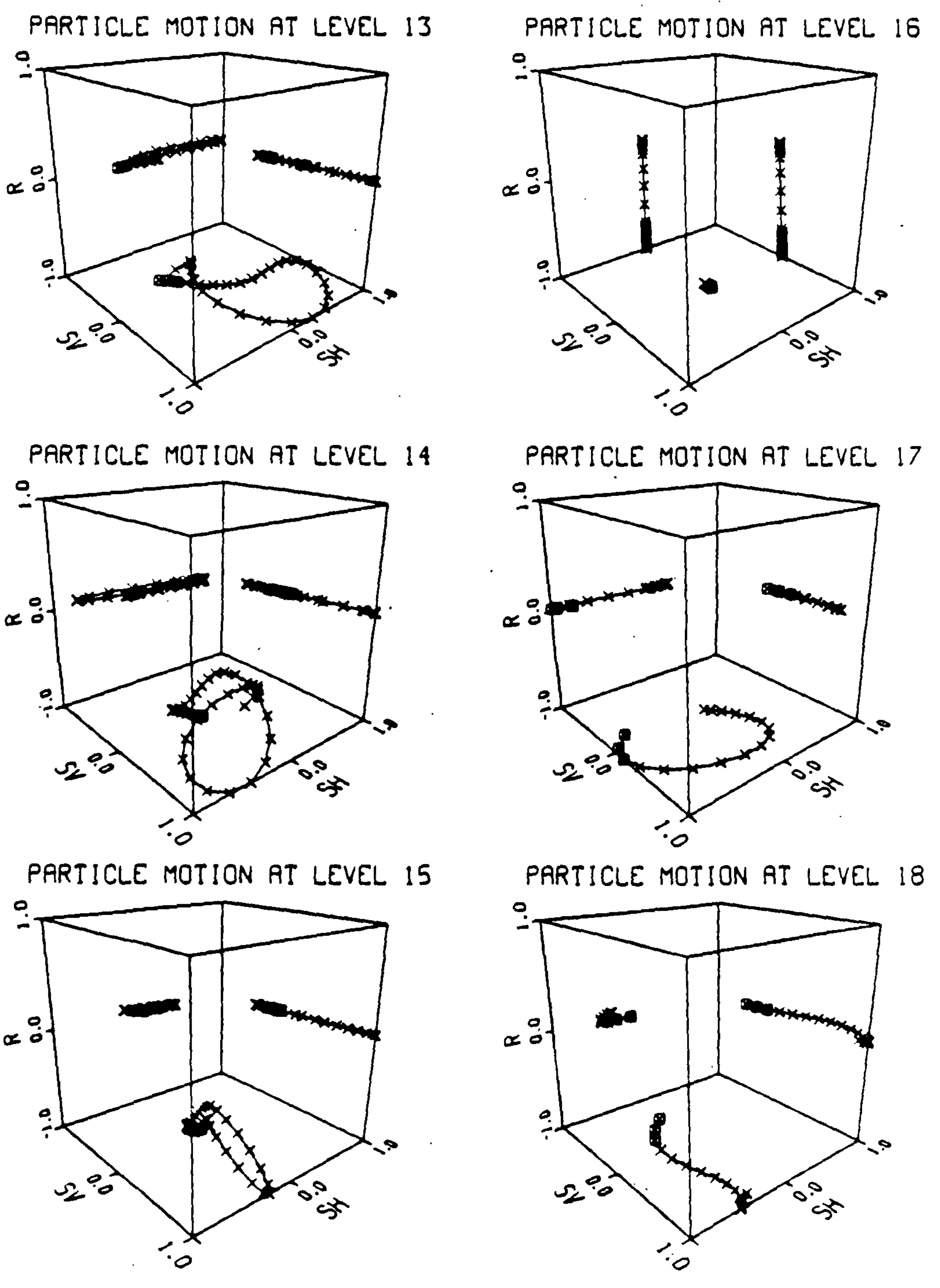

NEAR OFFSET SH_t SOURCE

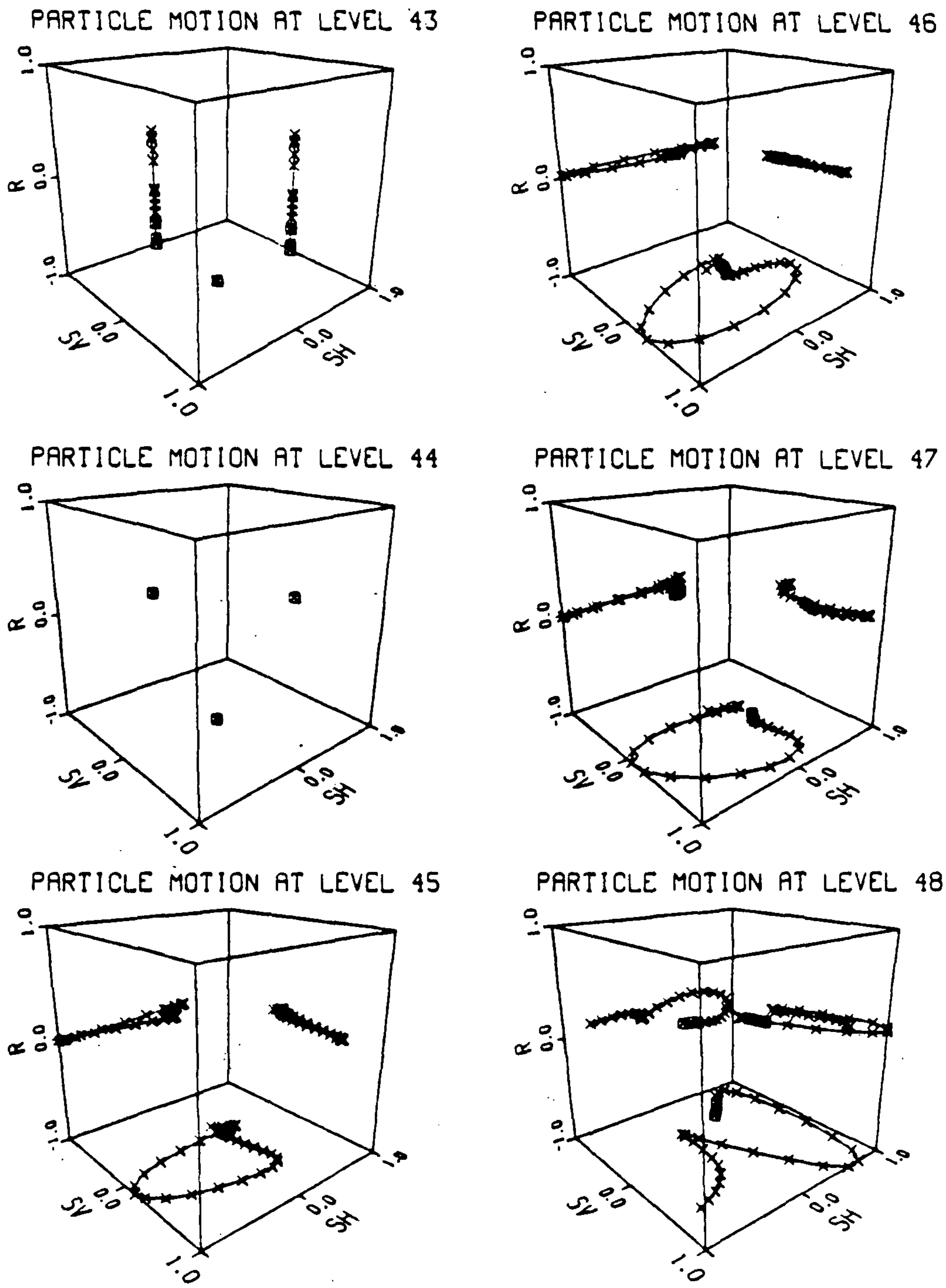

NEAR OFFSET SH$_t$ SOURCE

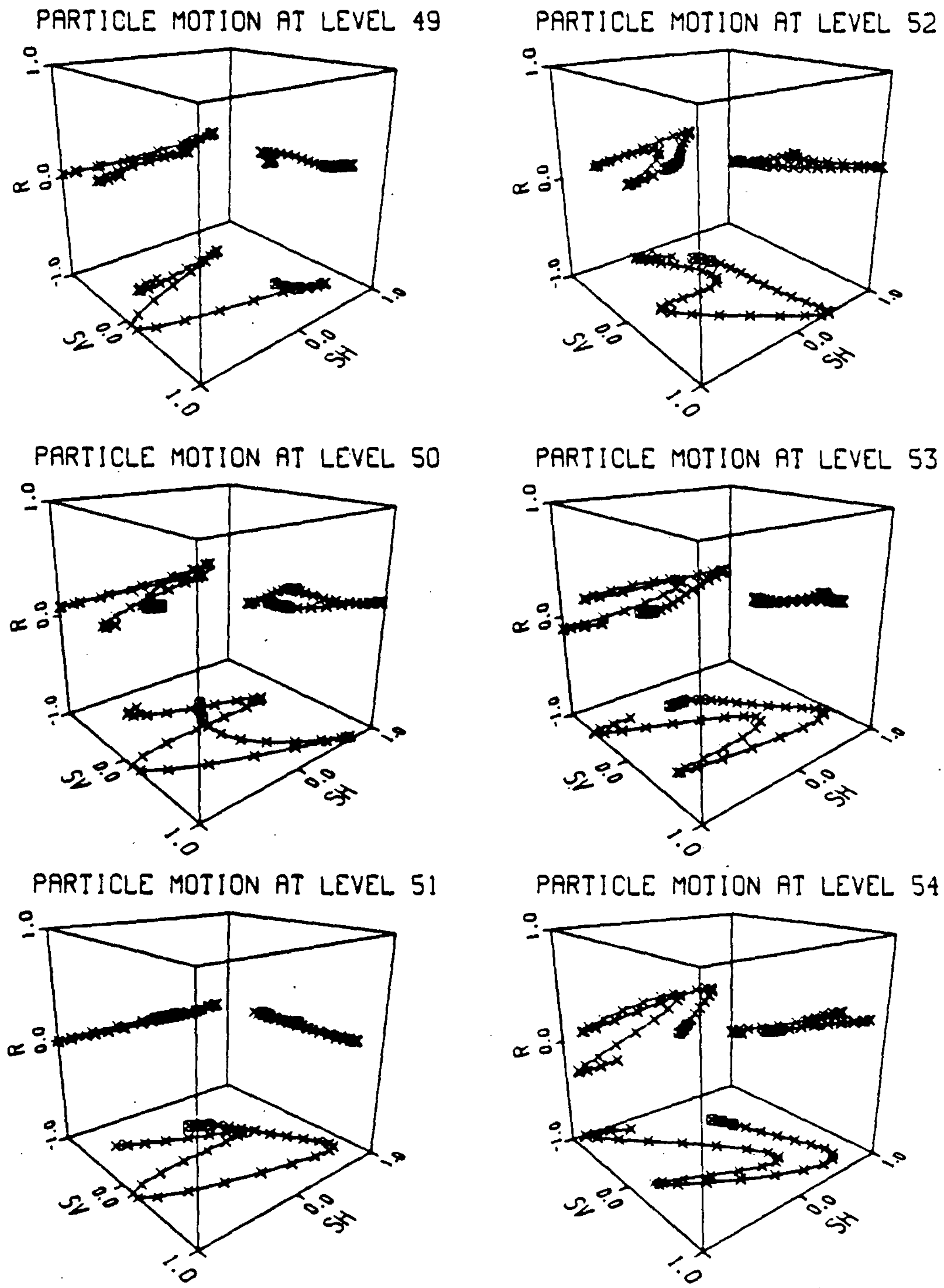

NEAR OFFSET SH$_t$ SOURCE

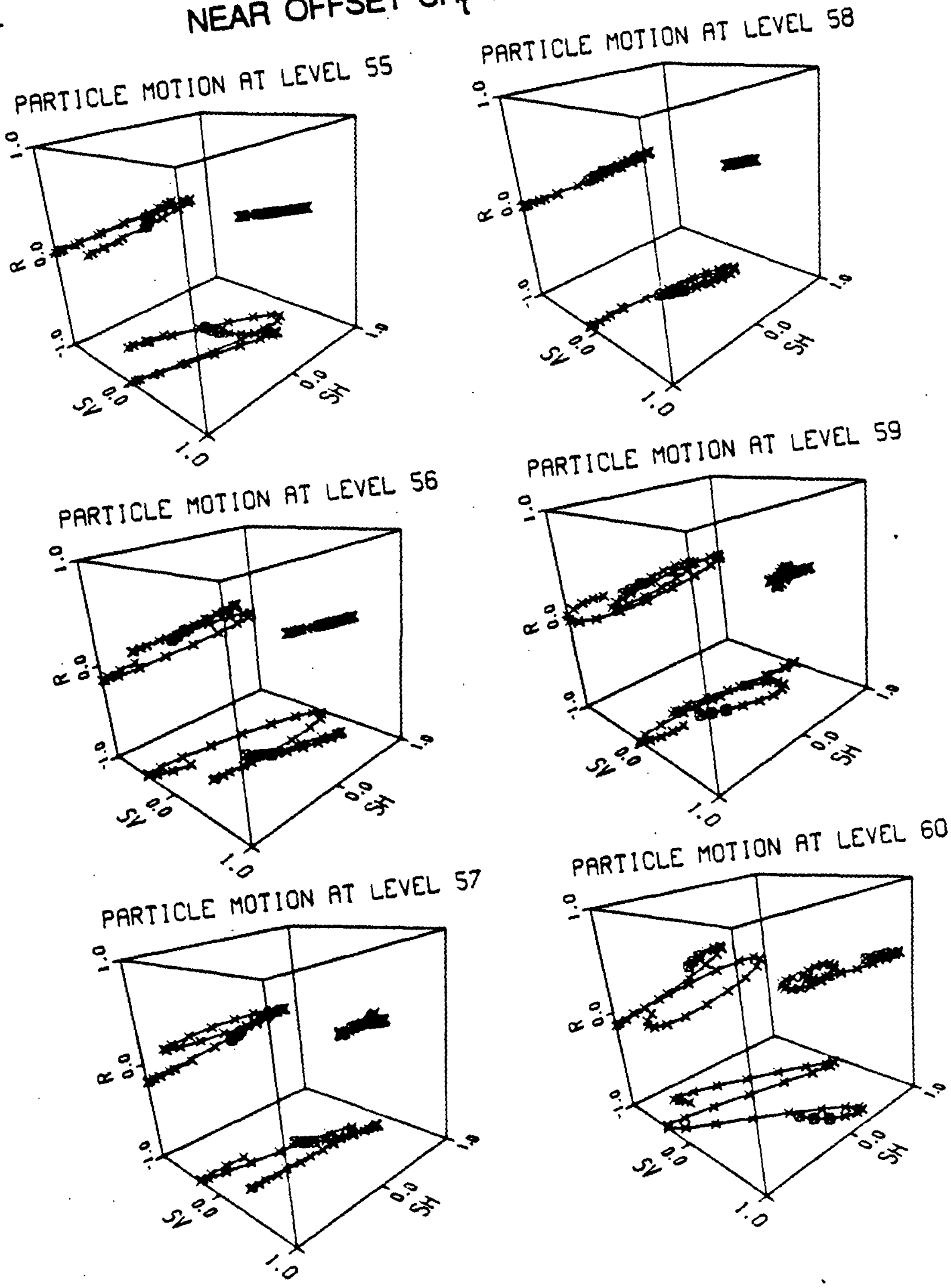

NEAR OFFSET SH_t SOURCE

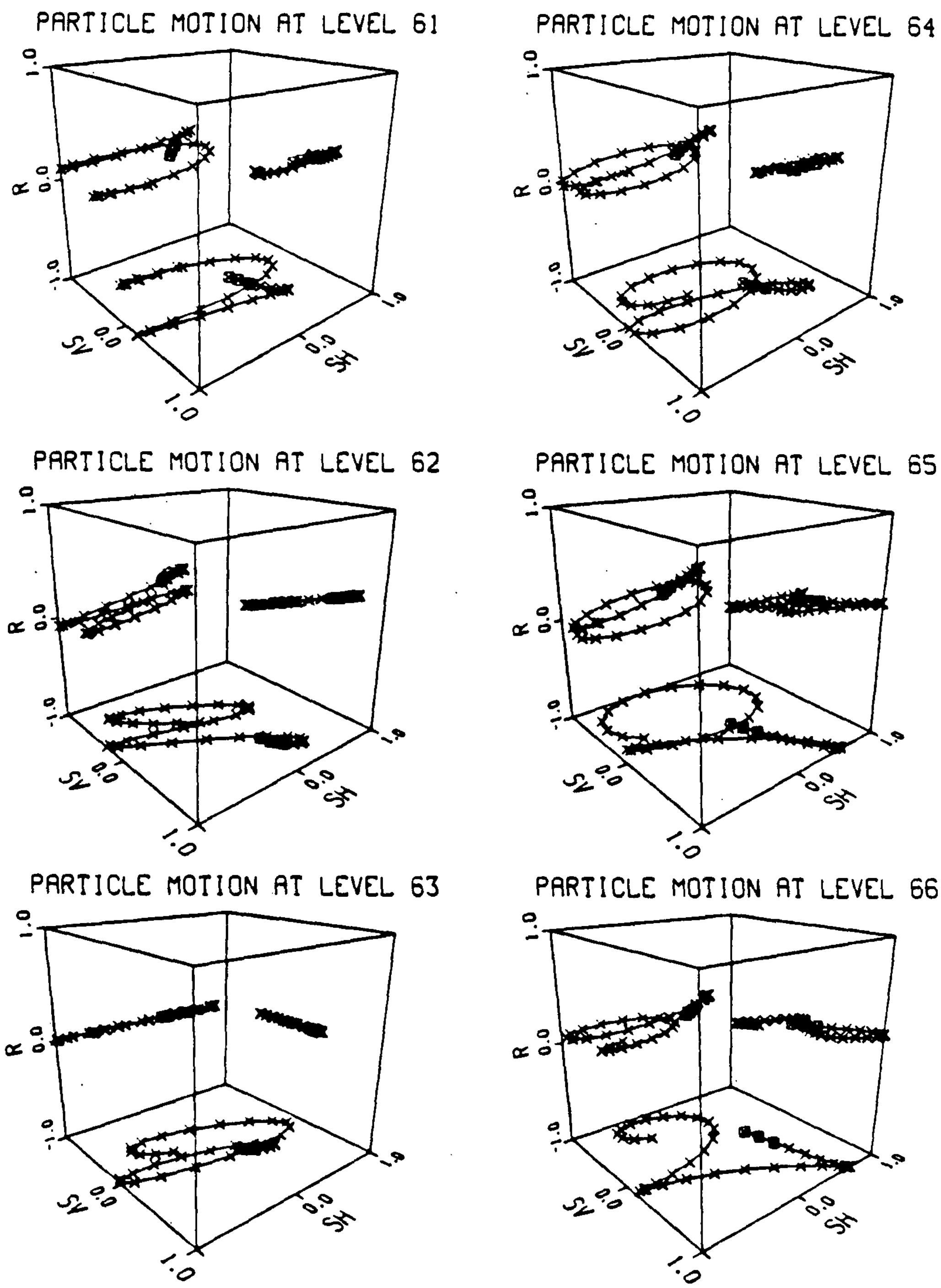

NEAR OFFSET SH_t SOURCE

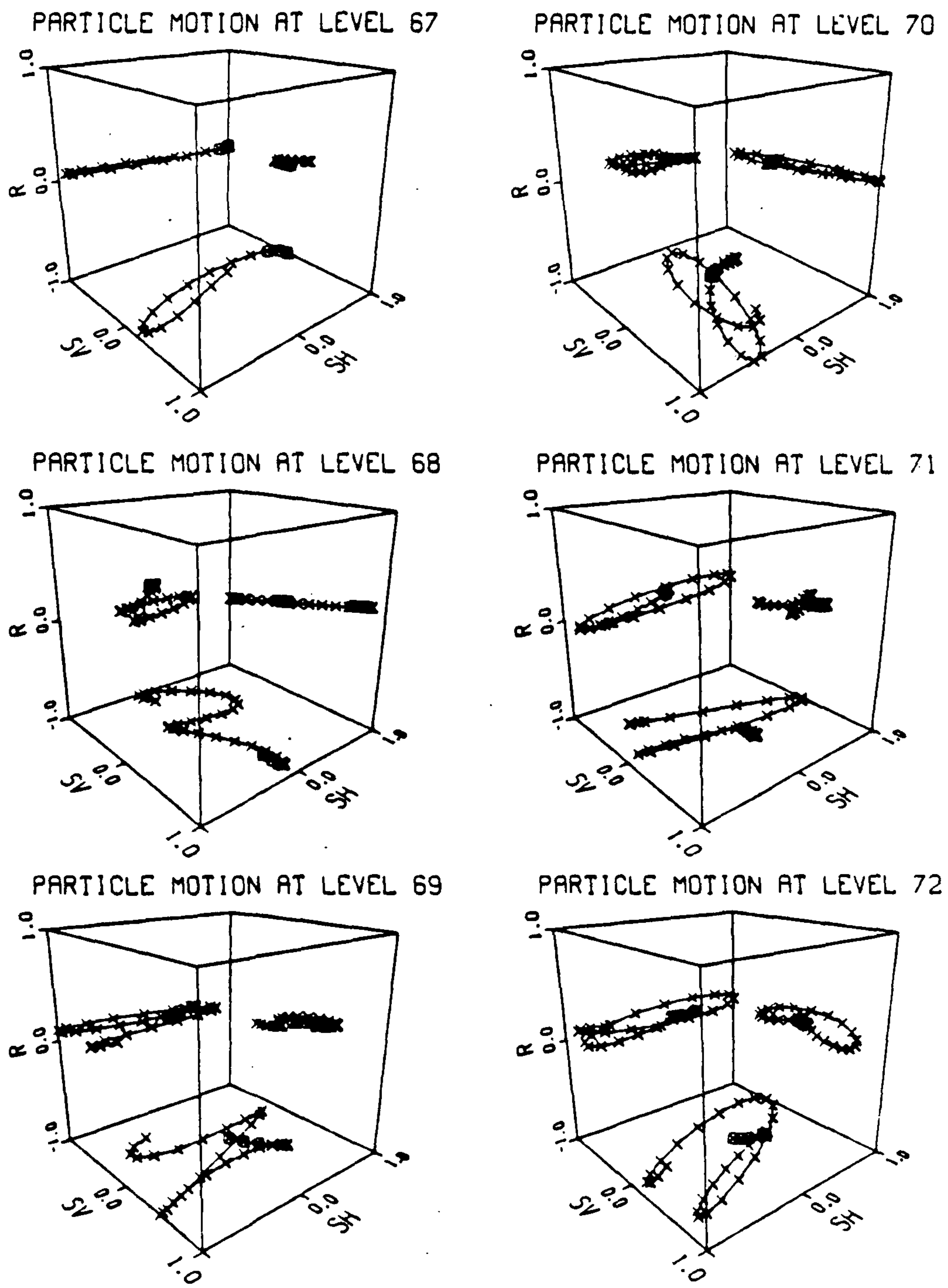

NEAR OFFSET SH_t SOURCE

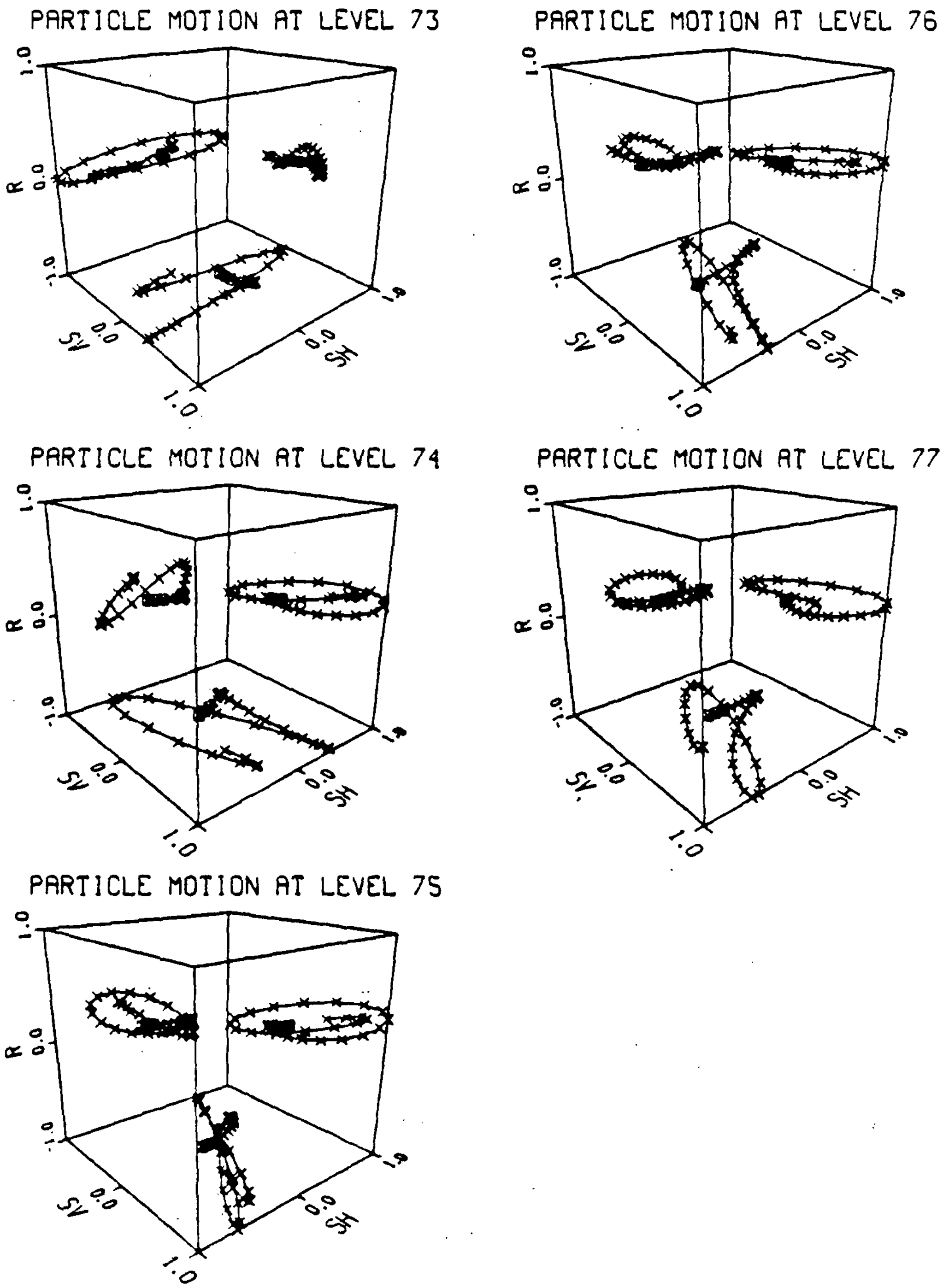

NEAR OFFSET SH_r SOURCE

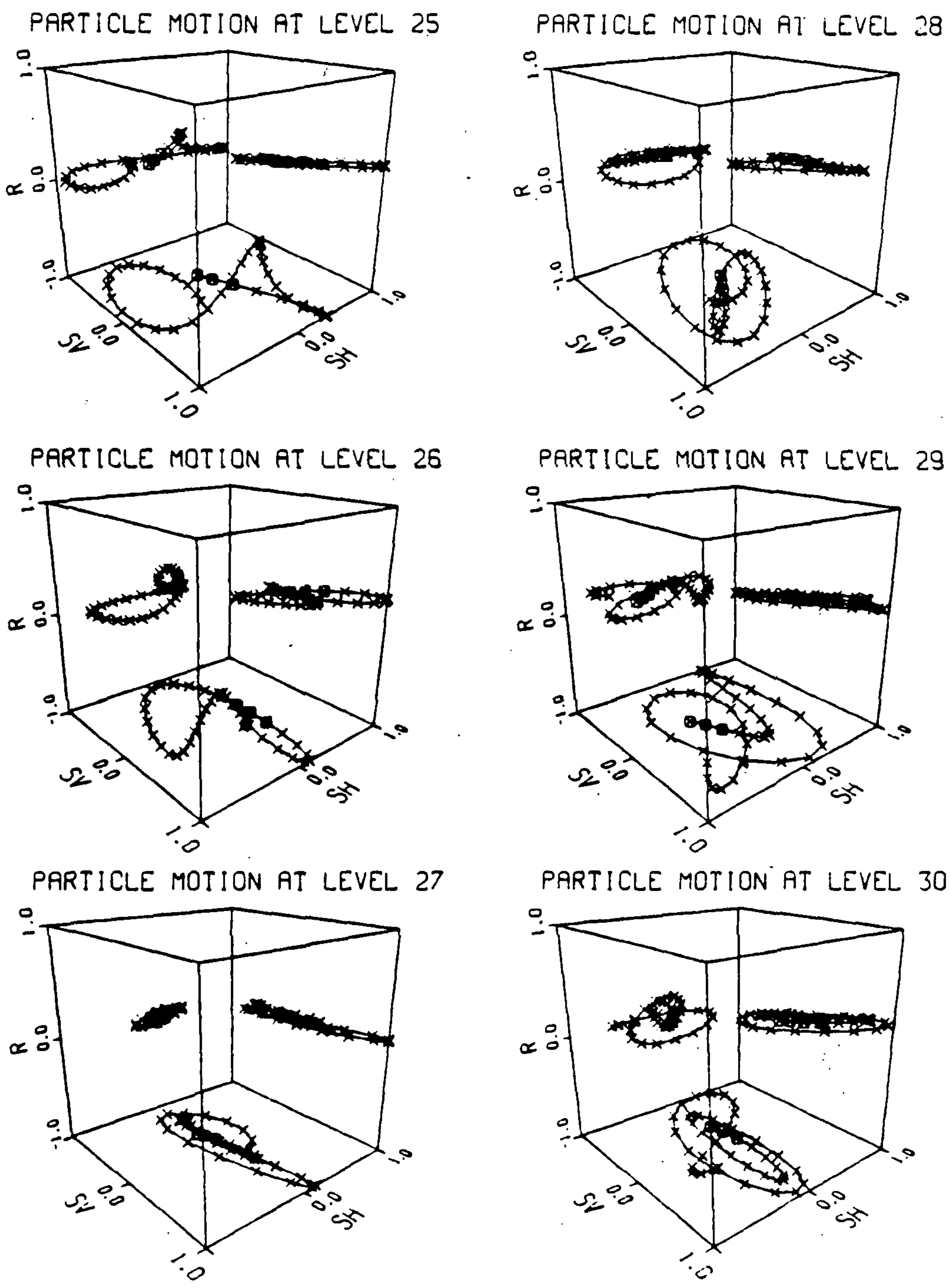

NEAR OFFSET SH_r SOURCE

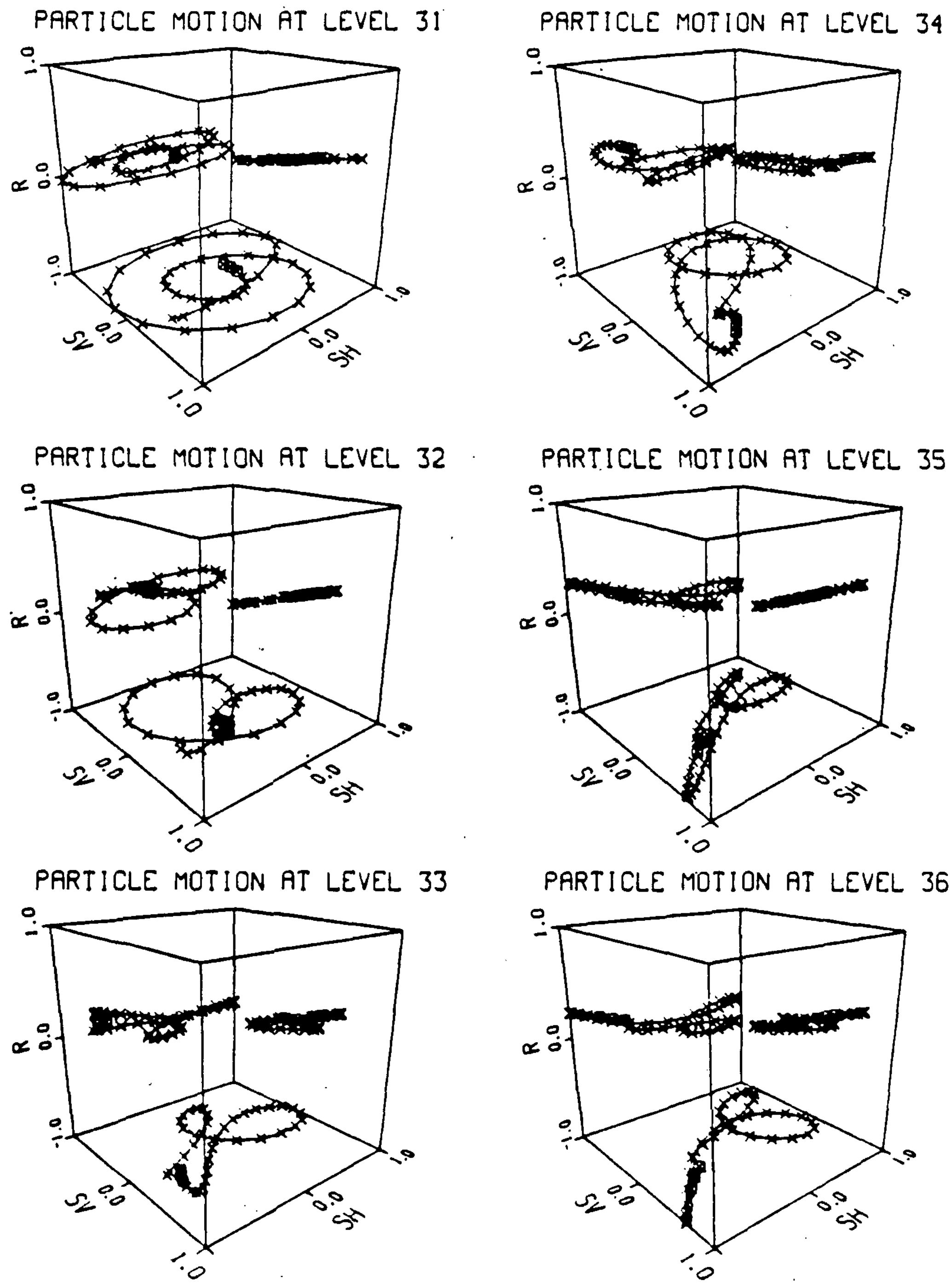

NEAR OFFSET SH_r SOURCE

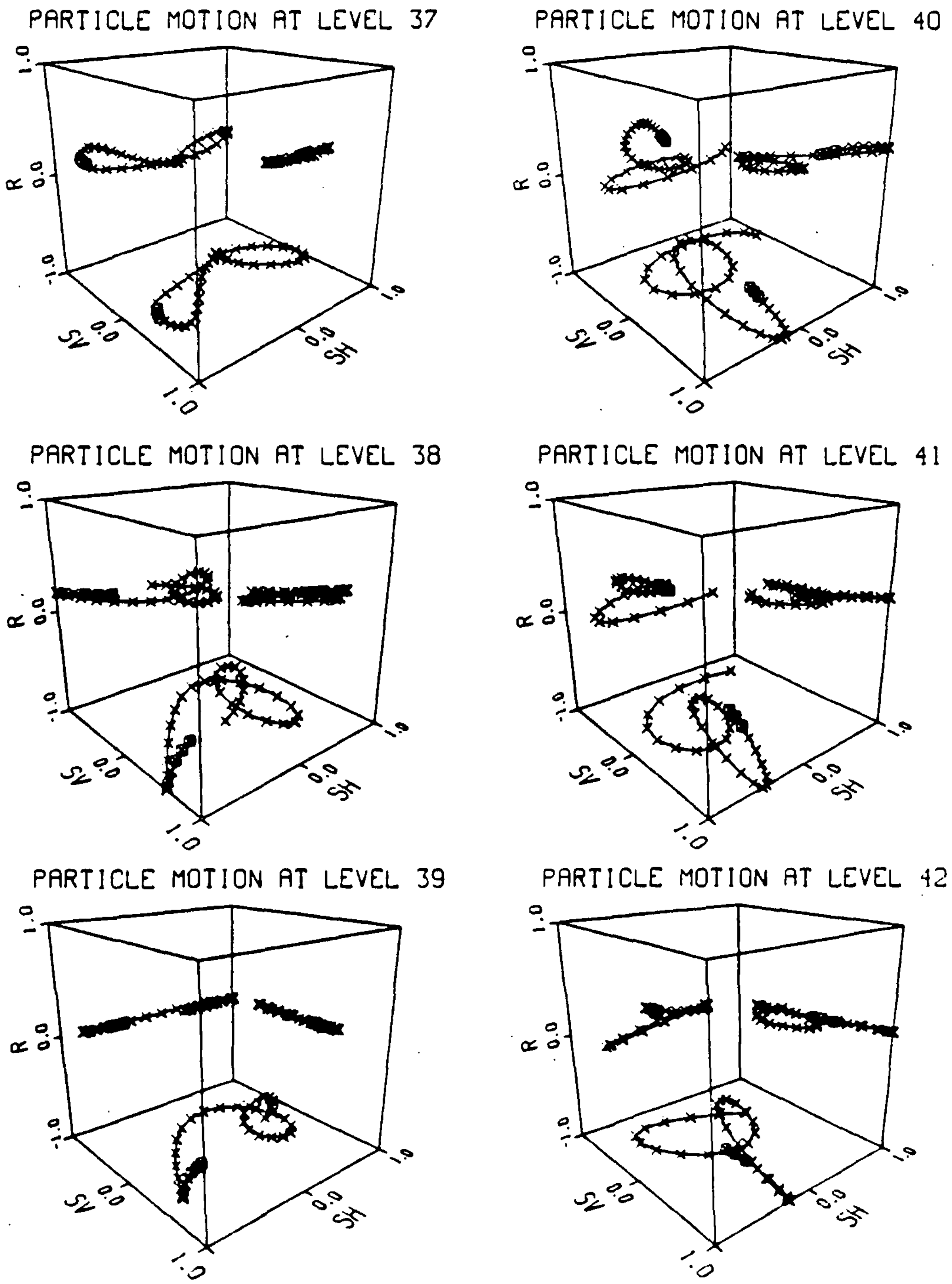

NEAR OFFSET SH_r SOURCE

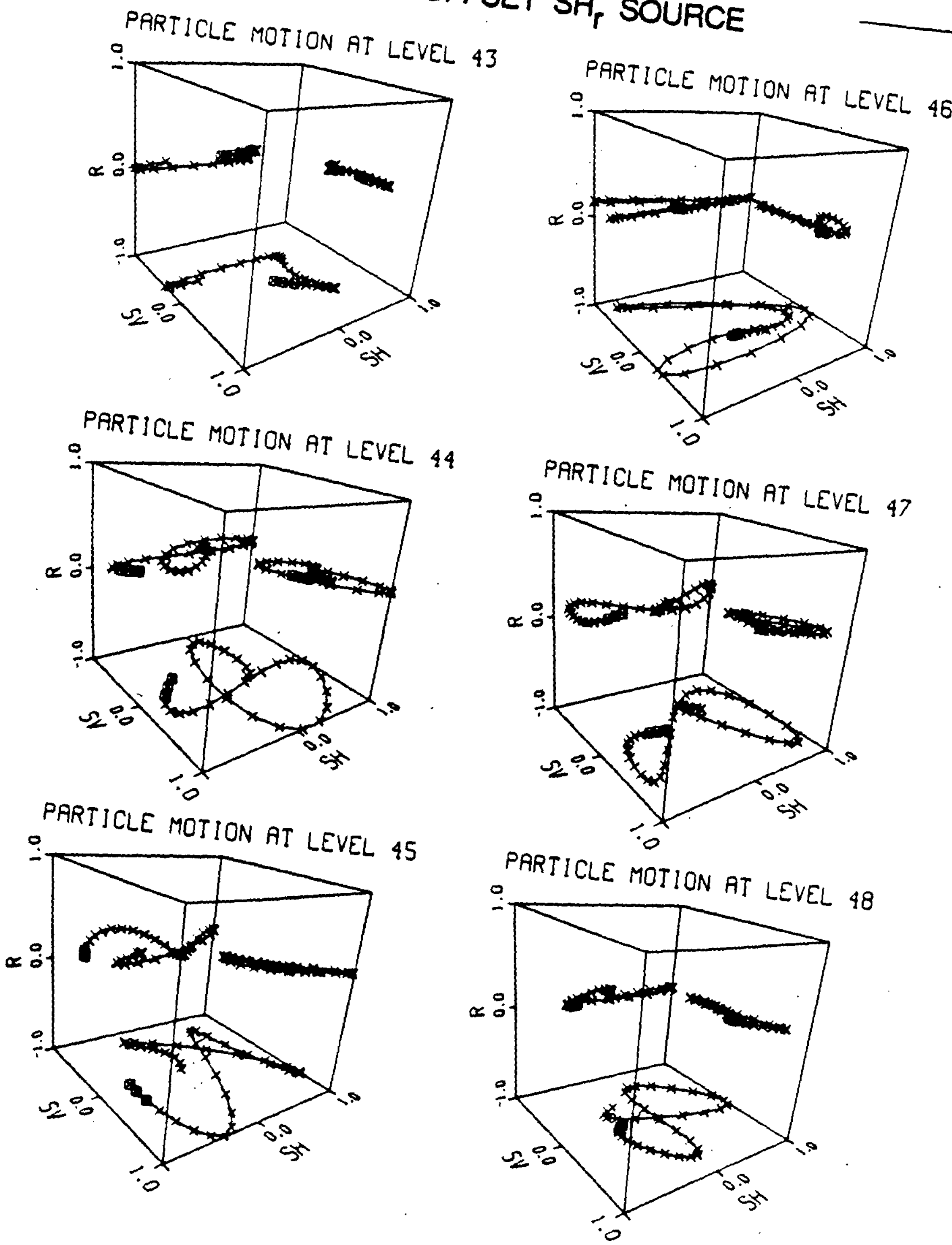

NEAR OFFSET SH_r SOURCE

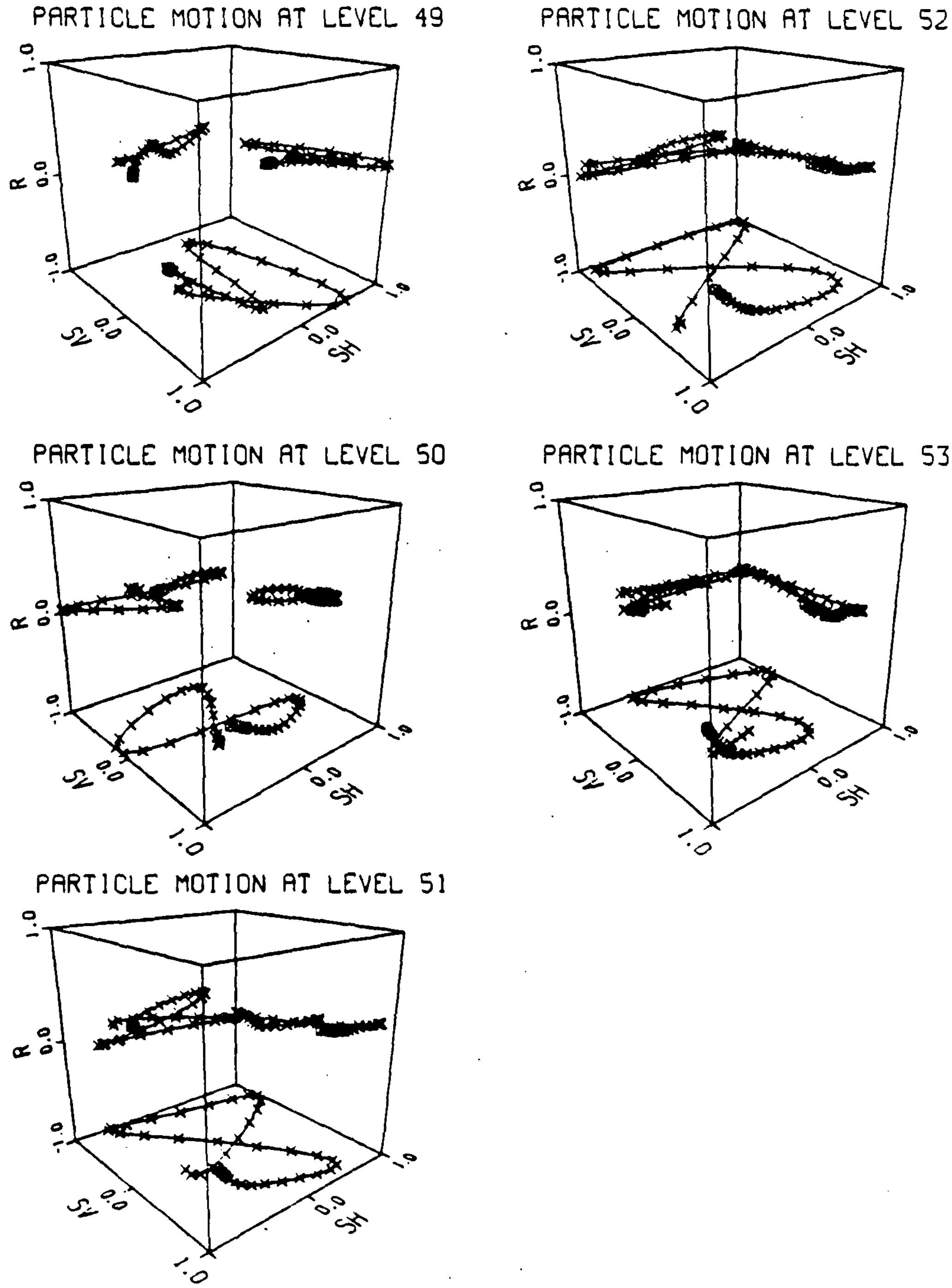

APPENDIX 3

POLARIZATION DIRECTION -- DATA AND PLOTS

The data in this appendix are listed by level number instead of depth. The following table cross-references level number and depth for the far-offset shear sources used in the polarization analysis.

Table 3-1

Far-Offset Data

Level	Depth
1	1500
2	1900
3	1975
4	2050
5	2125
6	2200
7	2275
8	2350
9	2425
10	2500
11	2575
12	2650
13	2725
14	2800
15	2875
16	2950
17	3025
18	3100
19	3175
20	3250
21	3325
22	3400
23	3475
24	3550
25	3625
26	3700
27	3775
28	3850
29	3925

Table 3-1

Far-Offset Data

Level	Depth
30	4000
31	4075
32	4150
33	4225
34	4300
35	4375
36	4450
37	4525
38	4600
39	4675
40	4750
41	4825
42	4900
43	4975
44	5050
45	5125
46	5200
47	5275
48	5350
49	5425
50	5500
51	5575
52	5650

FAR OFFSET SH_t SOURCE

LEVEL	WINDOW	PHI	THETA	F
1	1	84.272	77.929	0.980
1	2	84.734	77.979	0.979
1	3	84.782	78.376	0.980
1	4	84.511	79.982	0.979
1	5	84.720	84.268	0.970
1	6	87.483	89.875	0.969
1	7	89.240	-90.142	0.983
1	8	89.080	-92.033	0.992
1	9	89.683	87.296	0.984
1	10	88.637	-92.309	0.968
1	11	84.982	-91.556	0.955
1	12	86.161	-90.662	0.964
1	13	89.445	90.456	0.929
1	14	85.565	91.690	0.787
1	15	88.348	92.183	0.553
1	16	82.681	-88.706	0.498
1	17	87.289	-87.381	0.505
2	1	83.687	-102.496	0.974
2	2	83.417	-103.259	0.984
2	3	83.309	-103.292	0.990
2	4	83.146	-103.113	0.994
2	5	82.885	-103.118	0.995
2	6	82.694	-103.365	0.994
2	7	82.822	-103.178	0.993
2	8	83.493	-100.950	0.990
2	9	84.568	-97.165	0.990
2	10	85.086	-96.815	0.996
2	11	84.670	-96.840	0.996
2	12	83.668	-98.252	0.992
2	13	82.625	-99.090	0.986
2	14	82.037	-99.301	0.979
2	15	81.970	-99.469	0.974
2	16	82.056	-100.214	0.970
2	17	82.084	-101.558	0.964
2	18	83.099	-102.793	0.950
2	19	87.530	-102.869	0.931
2	20	86.956	78.046	0.946
2	21	86.155	78.811	0.968
3	1	84.444	-98.847	0.994
3	2	84.642	-97.016	0.988
3	3	84.541	-95.719	0.982
3	4	84.520	-95.100	0.975
3	5	84.999	-94.906	0.972
3	6	86.010	-94.458	0.974
3	7	86.656	-93.463	0.981
3	8	86.399	-92.476	0.987
3	9	85.601	-91.726	0.990
3	10	84.591	-91.269	0.989
3	11	83.931	-91.170	0.986
3	12	84.140	-91.168	0.980
3	13	84.678	-90.943	0.977
3	14	84.735	-90.747	0.975
3	15	84.813	-91.487	0.970
3	16	87.557	-94.358	0.951
3	17	85.648	82.658	0.941
4	1	87.868	80.997	0.985
4	2	87.429	82.302	0.894

FAR OFFSET SH_t SOURCE

LEVEL	WINDOW	PHI	THETA	F
4	3	87.533	81.589	0.889
4	4	87.640	80.644	0.902
4	5	87.405	81.530	0.924
4	6	86.982	83.687	0.937
4	7	86.920	85.267	0.938
4	8	87.611	85.044	0.939
4	9	88.369	83.747	0.951
4	10	87.956	83.699	0.969
4	11	86.703	85.443	0.980
4	12	85.573	87.349	0.983
4	13	84.193	87.116	0.980
4	14	80.119	82.806	0.947
5	1	83.896	76.976	0.979
5	2	84.117	77.142	0.979
5	3	84.544	77.786	0.980
5	4	84.711	78.402	0.981
5	5	84.956	78.888	0.980
5	6	86.148	79.338	0.978
5	7	88.642	79.513	0.980
5	8	89.046	-100.739	0.985
5	9	88.533	-100.545	0.979
5	10	89.335	-99.857	0.974
5	11	89.898	79.444	0.975
6	1	72.953	78.620	0.952
6	2	72.395	78.075	0.947
6	3	72.372	78.891	0.940
6	4	73.068	77.971	0.925
6	5	75.536	77.203	0.885
6	6	82.152	76.326	0.821
6	7	86.013	-103.265	0.798
6	8	75.300	-101.284	0.873
6	9	70.722	-99.885	0.955
6	10	68.412	-100.384	0.976
7	1	56.803	134.608	0.920
7	2	57.350	138.893	0.930
7	3	56.839	144.261	0.874
7	4	54.744	149.846	0.783
7	5	51.064	155.343	0.736
7	6	45.701	161.557	0.732
7	7	38.332	171.106	0.229
7	8	63.460	29.331	0.426
7	9	67.105	29.485	0.574
7	10	56.765	33.613	0.536
7	11	38.050	55.686	0.689
7	12	37.437	71.740	0.810
7	13	39.982	80.644	0.822
7	14	41.820	88.117	0.804
7	15	42.201	95.088	0.822
7	16	43.170	98.171	0.881
7	17	45.949	97.362	0.771
7	18	54.468	99.448	0.395
8	1	46.976	85.554	0.641
8	2	56.217	86.767	0.742
8	3	61.620	89.132	0.897
8	4	59.824	90.177	0.947
8	5	57.337	91.777	0.958

FAR OFFSET SH_t SOURCE

LEVEL	WINDOW	PHI	THETA	F
8	6	56.292	93.300	0.938
8	7	57.540	93.759	0.893
8	8	60.111	93.099	0.865
8	9	61.495	92.252	0.849
8	10	60.264	91.665	0.806
9	1	46.319	144.824	0.612
9	2	53.182	104.925	0.515
9	3	56.169	91.425	0.606
9	4	60.612	88.496	0.701
9	5	69.246	90.855	0.887
9	6	68.238	92.876	0.951
9	7	64.212	94.733	0.958
9	8	61.355	96.500	0.898
9	9	62.453	96.996	0.789
9	10	67.548	95.581	0.712
9	11	71.084	94.146	0.699
9	12	70.412	93.643	0.673
9	13	69.521	92.009	0.528
9	14	77.064	-107.976	0.386
9	15	66.982	-116.125	0.813
10	1	71.785	98.176	0.997
10	2	72.744	98.329	0.998
10	3	72.723	98.517	0.998
10	4	71.585	99.101	0.993
10	5	71.829	99.219	0.959
10	6	77.481	96.523	0.914
10	7	81.876	93.846	0.937
10	8	80.737	93.910	0.956
10	9	77.899	95.115	0.951
10	10	75.566	96.211	0.930
10	11	75.015	96.454	0.899
10	12	76.029	96.066	0.879
10	13	76.258	96.266	0.877
10	14	74.556	97.646	0.870
10	15	71.739	99.907	0.829
10	16	69.994	101.341	0.719
10	17	74.876	97.540	0.583
10	18	78.790	93.939	0.621
10	19	73.681	95.160	0.699
11	1	75.645	94.452	0.998
11	2	74.530	95.945	0.995
11	3	73.132	97.222	0.985
11	4	72.934	97.362	0.952
11	5	76.525	94.749	0.902
11	6	81.632	91.059	0.897
11	7	83.670	89.340	0.919
11	8	83.192	89.220	0.929
11	9	81.699	89.760	0.912
11	10	80.454	90.271	0.861
11	11	80.273	90.314	0.788
11	12	80.521	90.148	0.724
11	13	79.557	90.769	0.670
11	14	75.501	93.343	0.592
11	15	65.988	100.290	0.470
11	16	54.533	110.779	0.386
11	17	54.446	110.842	0.310
11	18	66.421	99.990	0.407

FAR OFFSET SH_t SOURCE

LEVEL	WINDOW	PHI	THETA	F
11	19	68.826	98.491	0.644
12	1	78.734	97.809	0.994
12	2	77.531	97.755	0.996
12	3	76.306	97.754	0.992
12	4	77.206	97.375	0.969
12	5	82.238	96.394	0.946
12	6	86.521	95.196	0.952
12	7	87.828	93.730	0.963
12	8	87.806	91.815	0.964
12	9	87.273	89.852	0.938
12	10	87.918	88.902	0.876
12	11	89.318	88.974	0.822
12	12	89.839	-92.212	0.794
12	13	89.679	81.903	0.752
12	14	86.448	66.942	0.688
12	15	81.441	52.296	0.666
12	16	79.808	47.750	0.663
13	1	78.117	67.432	0.942
13	2	76.039	64.009	0.969
13	3	74.451	60.819	0.974
13	4	73.291	58.925	0.962
13	5	75.363	59.902	0.929
13	6	81.809	61.793	0.920
13	7	85.836	61.867	0.938
13	8	86.647	61.545	0.949
13	9	86.341	61.669	0.944
13	10	87.465	62.542	0.903
13	11	89.097	-116.533	0.824
13	12	86.873	-116.812	0.768
13	13	87.134	-117.756	0.719
13	14	88.452	-118.205	0.571
13	15	47.887	72.516	0.063
13	16	16.528	115.463	0.461
13	17	37.136	93.887	0.356
14	1	77.931	88.915	0.916
14	2	73.984	85.204	0.916
14	3	70.495	82.808	0.915
14	4	67.691	80.745	0.903
14	5	66.902	79.106	0.850
14	6	73.334	80.895	0.749
14	7	85.180	84.490	0.756
14	8	89.872	83.849	0.836
14	9	89.147	80.541	0.869
14	10	86.203	76.740	0.834
14	11	83.288	74.143	0.740
14	12	82.916	73.864	0.643
14	13	84.952	73.504	0.609
14	14	86.373	6[illegible].810	0.625
14	15	83.521	60.449	0.651
14	16	82.534	53.473	0.662
14	17	84.866	51.034	0.654
15	1	80.788	-97.420	0.990
15	2	79.886	-97.496	0.986
15	3	79.000	-97.548	0.982
15	4	77.853	-97.836	0.972
15	5	77.832	-98.852	0.939

FAR OFFSET SH_t SOURCE

LEVEL	WINDOW	PHI	THETA	F
15	6	83.107	-99.449	0.910
15	7	86.819	-97.667	0.940
15	8	85.133	-95.828	0.957
15	9	82.042	-94.703	0.952
15	10	79.546	-94.174	0.930
15	11	78.449	-94.075	0.906
15	12	78.185	-94.006	0.894
15	13	77.003	-93.519	0.896
15	14	73.667	-92.584	0.896
15	15	68.949	-91.773	0.888
15	16	67.324	-92.353	0.865
15	17	70.997	-94.029	0.868
15	18	73.844	-94.819	0.913
16	1	71.056	90.483	0.962
16	2	68.432	89.519	0.915
16	3	66.431	89.276	0.864
16	4	64.416	89.514	0.824
16	5	61.175	88.905	0.769
16	6	56.855	82.760	0.622
16	7	64.555	67.006	0.468
16	8	72.945	65.931	0.595
16	9	69.460	73.735	0.707
16	10	63.592	80.084	0.746
16	11	58.324	84.931	0.745
16	12	54.367	89.101	0.721
16	13	51.776	92.710	0.683
16	14	50.194	95.226	0.648
16	15	49.184	97.513	0.623
16	16	48.971	100.368	0.597
16	17	49.950	101.796	0.547
16	18	53.217	97.593	0.474
17	1	72.453	83.744	0.971
17	2	69.031	81.315	0.943
17	3	66.615	79.568	0.884
17	4	66.354	79.058	0.812
17	5	68.415	78.266	0.757
17	6	71.143	74.718	0.729
17	7	72.573	68.067	0.718
17	8	71.407	62.491	0.726
17	9	68.249	62.184	0.753
17	10	64.701	64.884	0.797
17	11	61.314	66.916	0.831
17	12	58.157	67.718	0.840
17	13	56.231	67.668	0.820
17	14	57.255	67.428	0.782
17	15	60.846	68.309	0.751
17	16	64.891	69.962	0.737
17	17	69.120	70.640	0.723
18	1	72.224	75.531	0.947
18	2	70.653	73.168	0.920
18	3	70.969	73.256	0.872
18	4	73.803	74.970	0.839
18	5	76.843	75.299	0.844
18	6	77.746	73.631	0.857
18	7	76.466	70.836	0.858
18	8	73.863	67.643	0.852
18	9	71.858	64.476	0.846

FAR OFFSET SH_t SOURCE

LEVEL	WINDOW	PHI	THETA	F
18	10	70.816	61.704	0.847
18	11	69.901	60.200	0.849
18	12	69.103	59.724	0.866
18	13	69.944	57.235	0.895
18	14	73.103	52.058	0.914
18	15	77.580	46.784	0.917
19	1	69.873	91.458	0.964
19	2	68.004	86.905	0.958
19	3	66.126	85.453	0.948
19	4	68.946	84.272	0.919
19	5	77.423	79.973	0.905
19	6	79.815	78.130	0.938
19	7	78.044	79.009	0.946
19	8	75.981	80.750	0.908
19	9	76.320	81.740	0.816
19	10	79.223	80.785	0.744
19	11	80.034	79.698	0.745
19	12	76.565	81.079	0.734
19	13	67.811	88.502	0.646
19	14	53.630	114.719	0.561
20	1	64.717	100.211	0.968
20	2	66.288	93.893	0.960
20	3	66.322	90.842	0.963
20	4	65.271	91.234	0.952
20	5	71.603	84.022	0.861
20	6	79.236	75.388	0.899
20	7	78.188	76.296	0.942
20	8	75.200	80.179	0.905
20	9	73.902	82.379	0.757
20	10	76.622	78.630	0.585
20	11	79.687	74.029	0.557
20	12	78.429	75.195	0.566
20	13	72.838	82.661	0.467
20	14	58.386	123.322	0.329
21	1	66.716	99.799	0.981
21	2	66.107	95.604	0.972
21	3	65.461	91.685	0.963
21	4	65.064	91.512	0.947
21	5	69.594	85.908	0.934
21	6	72.668	77.624	0.961
21	7	70.890	77.035	0.982
21	8	68.594	79.774	0.962
21	9	68.140	80.704	0.876
21	10	69.918	76.138	0.784
21	11	70.842	73.016	0.783
21	12	69.992	73.978	0.783
21	13	67.945	76.237	0.703
21	14	64.903	81.784	0.446
22	1	65.928	103.317	0.991
22	2	66.193	102.693	0.994
22	3	66.391	99.036	0.978
22	4	66.296	95.741	0.941
22	5	67.134	96.317	0.925
22	6	68.739	90.666	0.945
22	7	68.082	84.548	0.971
22	8	66.894	84.537	0.984

FAR OFFSET SH_t SOURCE

LEVEL	WINDOW	PHI	THETA	F
22	9	66.353	86.800	0.966
22	10	66.318	85.697	0.898
22	11	66.168	81.386	0.861
22	12	66.276	80.728	0.875
22	13	66.481	81.870	0.857
22	14	66.179	83.037	0.749
22	15	66.775	85.061	0.434
22	16	72.370	4.683	0.141
23	1	74.678	106.237	0.990
23	2	74.691	105.671	0.994
23	3	74.586	102.452	0.958
23	4	74.300	100.446	0.868
23	5	71.874	103.856	0.844
23	6	67.355	95.477	0.905
23	7	66.534	87.611	0.945
23	8	67.414	86.562	0.962
23	9	68.093	87.542	0.942
23	10	66.836	84.140	0.867
23	11	65.661	79.871	0.850
23	12	66.365	79.935	0.867
23	13	67.295	79.409	0.798
23	14	67.481	75.932	0.547
23	15	61.981	13.883	0.156
24	1	62.755	112.663	0.955
24	2	63.047	113.000	0.977
24	3	63.884	111.172	0.982
24	4	65.220	109.216	0.929
24	5	65.100	111.404	0.808
24	6	58.652	119.246	0.763
24	7	52.307	111.361	0.828
24	8	54.963	96.445	0.871
24	9	59.804	91.689	0.902
24	10	62.820	92.579	0.910
24	11	62.894	93.136	0.909
24	12	61.090	89.969	0.856
24	13	61.047	87.243	0.860
24	14	63.277	87.209	0.846
24	15	66.768	90.425	0.739
24	16	72.209	106.713	0.495
24	17	80.392	138.090	0.453
25	1	69.262	109.192	0.967
25	2	70.008	109.571	0.977
25	3	71.146	108.513	0.978
25	4	71.122	108.698	0.916
25	5	65.602	115.250	0.822
25	6	58.295	119.190	0.873
25	7	58.569	110.392	0.898
25	8	63.873	102.273	0.890
25	9	68.846	100.320	0.883
25	10	70.632	101.047	0.868
25	11	69.275	99.184	0.846
25	12	69.102	96.134	0.839
25	13	72.093	93.433	0.837
25	14	77.095	95.382	0.764
25	15	83.918	107.898	0.571
26	1	64.493	114.692	0.968

FAR OFFSET SH_t SOURCE

LEVEL	WINDOW	PHI	THETA	F	
26	2	65.945	114.332	0.978	
26	3	67.869	113.305	0.969	
26	4	69.531	112.250	0.912	
26	5	68.838	113.533	0.774	
26	6	62.031	121.934	0.651	
26	7	57.127	127.199	0.709	
26	8	61.238	119.027	0.755	
26	9	69.017	110.047	0.770	
26	10	74.812	106.512	0.775	
26	11	76.841	106.626	0.776	
26	12	76.359	106.757	0.809	
26	13	77.031	105.384	0.873	
26	14	79.851	104.691	0.923	
26	15	83.347	106.714	0.911	
26	16	84.809	116.178	0.754	
27	1	60.436	118.103	0.928	
27	2	62.364	114.692	0.947	
27	3	64.501	111.958	0.948	
27	4	67.087	110.746	0.928	D1
27	5	69.456	110.010	0.874	
27	6	69.877	109.206	0.736	
27	7	63.281	112.329	0.527	
27	8	50.891	125.754	0.512	
27	9	55.578	125.051	0.603	
27	10	69.949	112.214	0.609	
27	11	82.542	101.453	0.641	
27	12	87.964	98.196	0.667	
27	13	88.289	98.859	0.693	
27	14	87.481	97.216	0.764	
27	15	88.312	93.849	0.869	
27	16	89.728	-87.034	0.907	D2
27	17	87.900	-85.120	0.725	
28	1	54.240	116.509	0.861	
28	2	58.876	110.820	0.851	
28	3	63.479	107.230	0.805	D1
28	4	66.308	104.517	0.660	
28	5	61.883	105.164	0.378	
28	6	34.887	133.380	0.274	
28	7	34.721	144.560	0.421	
28	8	47.770	128.222	0.374	
28	9	80.169	102.061	0.364	
28	10	86.193	-87.981	0.520	
28	11	84.534	-88.504	0.585	
28	12	86.695	-87.053	0.647	D2
28	13	87.763	-90.031	0.761	
28	14	87.466	-92.769	0.876	
28	15	86.460	-92.530	0.868	
28	16	85.314	-92.625	0.490	
29	1	60.845	104.969	0.919	
29	2	64.604	99.367	0.828	
29	3	66.565	97.549	0.650	D1
29	4	58.354	103.342	0.417	
29	5	40.338	120.007	0.395	
29	6	36.075	125.007	0.469	
29	7	40.262	120.566	0.427	
29	8	62.472	104.456	0.217	
29	9	79.161	-93.672	0.348	

FAR OFFSET SH_t SOURCE

LEVEL	WINDOW	PHI	THETA	F	
29	10	75.043	-96.319	0.476	D2
29	11	78.013	-95.313	0.556	
29	12	79.917	-94.058	0.712	
29	13	78.657	-94.342	0.873	
29	14	77.450	-94.550	0.937	
29	15	75.993	-95.898	0.882	
30	1	58.228	102.009	0.914	D1
30	2	63.732	99.761	0.860	
30	3	66.185	99.285	0.686	
30	4	53.773	99.737	0.428	
30	5	31.777	102.488	0.442	
30	6	27.399	108.492	0.514	
30	7	27.677	115.981	0.459	
30	8	14.637	134.512	0.164	
30	9	43.809	-73.275	0.295	D2
30	10	51.337	-75.943	0.410	
30	11	61.742	-76.648	0.466	
30	12	68.685	-75.637	0.639	
30	13	68.506	-79.415	0.816	
30	14	68.085	-81.417	0.898	
31	1	65.195	98.383	0.781	D1
31	2	71.372	96.269	0.551	
31	3	52.112	102.110	0.201	
31	4	23.332	129.883	0.363	
31	5	25.042	137.994	0.462	
31	6	26.317	148.060	0.446	
31	7	19.625	-177.446	0.389	
31	8	20.351	-127.718	0.473	
31	9	25.487	-123.162	0.528	
31	10	33.593	-122.623	0.466	D2
31	11	40.901	-107.867	0.452	
31	12	56.425	-97.166	0.822	
31	13	56.973	-97.332	0.721	
32	1	55.076	113.144	0.815	D1
32	2	65.379	107.059	0.720	
32	3	77.412	102.733	0.465	
32	4	57.466	-88.606	0.049	
32	5	10.283	-165.304	0.305	
32	6	12.041	171.015	0.370	
32	7	12.417	-155.434	0.341	
32	8	21.675	-97.014	0.435	D2
32	9	27.070	-84.033	0.575	
32	10	30.000	-81.998	0.579	
32	11	39.226	-78.261	0.483	
32	12	57.559	-72.630	0.577	
32	13	61.676	-71.838	0.841	
32	14	61.206	-73.117	0.908	
33	1	72.802	105.279	0.604	
33	2	83.355	101.412	0.238	
33	3	15.620	-173.021	0.144	
33	4	14.712	154.995	0.276	
33	5	12.430	157.512	0.227	
33	6	24.046	-100.877	0.255	
33	7	30.679	-82.020	0.471	
33	8	31.919	-68.174	0.533	
33	9	38.459	-58.618	0.467	

FAR OFFSET SH_t SOURCE

LEVEL	WINDOW	PHI	THETA	F
33	10	56.718	-55.757	0.495
33	11	65.385	-56.514	0.764
33	12	64.981	-53.909	0.919
33	13	65.512	-51.481	0.914
34	1	72.232	97.129	0.596
34	2	88.408	-93.485	0.461
34	3	65.217	-106.777	0.367
34	4	49.178	-121.012	0.342
34	5	45.291	-127.253	0.325
34	6	48.252	-121.379	0.373
34	7	47.292	-117.498	0.504
34	8	43.252	-118.416	0.584
34	9	40.487	-120.367	0.542
34	10	45.812	-110.987	0.365
34	11	70.474	-88.524	0.504
34	12	71.141	-87.486	0.771
34	13	67.101	-91.026	0.698
35	1	60.361	-116.835	0.374
35	2	46.411	-132.641	0.390
35	3	41.905	-142.317	0.356
35	4	45.194	-136.668	0.346
35	5	47.444	-131.836	0.480
35	6	44.386	-136.964	0.640
35	7	41.418	-145.749	0.717
35	8	40.727	-153.779	0.651
35	9	46.075	-146.883	0.395
36	1	66.471	-93.241	0.491
36	2	53.061	-106.689	0.574
36	3	47.810	-114.444	0.583
36	4	48.112	-114.579	0.558
36	5	51.661	-108.906	0.608
36	6	51.838	-106.510	0.713
36	7	48.765	-107.751	0.757
36	8	45.152	-109.441	0.700
36	9	46.155	-100.709	0.520
37	1	62.746	-111.138	0.552
37	2	55.826	-121.338	0.585
37	3	53.103	-126.843	0.596
37	4	52.965	-127.602	0.618
37	5	53.114	-126.433	0.682
37	6	51.700	-127.230	0.743
37	7	49.112	-129.697	0.745
38	1	27.343	-147.773	0.431
38	2	30.924	-137.333	0.531
38	3	33.432	-141.574	0.618
38	4	36.235	-147.262	0.669
38	5	38.290	-160.835	0.700
38	6	38.910	-153.382	0.731
38	7	38.773	-158.019	0.771
38	8	39.327	-166.328	0.811
39	1	41.403	-160.176	0.784
39	2	41.541	-149.361	0.739
39	3	42.868	-141.463	0.776
39	4	44.318	-140.497	0.822

FAR OFFSET SH_t SOURCE

LEVEL	WINDOW	PHI	THETA	F
39	5	45.810	-141.513	0.863
39	6	46.938	-142.347	0.877
39	7	47.272	-143.190	0.900
39	8	46.948	-144.966	0.915
39	9	46.568	-147.998	0.913
39	10	46.316	-151.771	0.892
40	1	37.521	-174.248	0.449
40	2	45.394	154.624	0.423
40	3	55.334	136.968	0.222
40	4	59.443	-120.564	0.330
40	5	59.376	-130.464	0.623
40	6	57.833	-135.514	0.725
40	7	56.535	-137.823	0.753
40	8	56.635	-137.035	0.755
40	9	57.388	-134.651	0.760
40	10	57.154	-134.719	0.765
40	11	55.251	-137.865	0.738
41	1	67.227	-96.158	0.159
41	2	85.516	-87.637	0.436
41	3	80.371	-94.436	0.599
41	4	72.067	-104.556	0.650
41	5	63.647	-114.436	0.659
41	6	57.590	-120.806	0.657
41	7	54.824	-123.532	0.660
41	8	55.140	-124.251	0.671
41	9	55.440	-125.138	0.721
41	10	53.194	-126.822	0.744
42	1	70.358	-126.941	0.392
42	2	77.383	-120.472	0.636
42	3	72.168	-127.992	0.785
42	4	67.097	-133.804	0.831
42	5	63.597	-136.378	0.828
42	6	63.299	-136.595	0.810
42	7	65.693	-135.542	0.823
42	8	66.474	-135.288	0.856
42	9	64.898	-136.281	0.866
43	1	75.596	-64.740	0.774
43	2	73.903	-61.585	0.877
43	3	70.139	-59.022	0.915
43	4	67.513	-57.769	0.905
43	5	67.410	-57.240	0.872
43	6	68.494	-55.382	0.860
43	7	67.889	-52.255	0.864
43	8	64.873	-48.915	0.857
44	1	74.513	163.087	0.749
44	2	77.841	153.849	0.680
44	3	82.730	144.015	0.498
44	4	87.813	-53.661	0.289
44	5	74.585	-78.856	0.176
44	6	68.767	-91.501	0.104
44	7	76.725	-76.367	0.181
44	8	76.667	-80.360	0.396
44	9	76.035	-81.554	0.488
44	10	78.053	-73.410	0.439

FAR OFFSET SH_t SOURCE

LEVEL	WINDOW	PHI	THETA	F
45	1	62.525	-143.842	0.540
45	2	73.176	-130.296	0.680
45	3	72.946	-132.055	0.812
45	4	70.105	-136.109	0.854
45	5	67.353	-138.871	0.847
45	6	66.721	-138.736	0.811
45	7	69.416	-136.196	0.799
45	8	71.016	-134.980	0.830
45	9	69.605	-135.783	0.848
45	10	67.369	-137.397	0.824
46	1	75.488	173.749	0.427
46	2	87.478	-98.887	0.091
46	3	76.992	-101.377	0.735
46	4	71.035	-103.453	0.859
46	5	68.176	-107.077	0.823
46	6	69.024	-104.270	0.714
46	7	70.582	-100.462	0.739
46	8	68.780	-106.865	0.775
47	1	89.792	72.873	0.523
47	2	78.532	-122.459	0.675
47	3	72.868	-128.545	0.753
47	4	70.082	-130.947	0.770
47	5	72.122	-129.051	0.772
47	6	75.640	-125.819	0.823
47	7	75.530	-125.273	0.868
47	8	74.067	-125.868	0.871
48	1	78.512	99.114	0.606
48	2	86.297	90.910	0.742
48	3	85.299	-94.213	0.806
48	4	78.388	-95.898	0.833
48	5	74.724	-95.381	0.838
48	6	75.460	-97.143	0.832
48	7	77.138	-102.495	0.849
48	8	75.778	-102.834	0.878
48	9	73.295	-97.066	0.845
48	10	71.880	-85.356	0.582
48	11	76.921	-52.910	0.306
49	1	77.840	102.935	0.720
49	2	89.283	89.073	0.613
49	3	79.789	-99.963	0.594
49	4	75.112	-100.806	0.626
49	5	74.251	-102.041	0.686
49	6	72.947	-110.321	0.797
49	7	70.973	-113.895	0.888
49	8	68.940	-107.736	0.818
49	9	71.130	-86.837	0.578
49	10	80.362	-61.249	0.613
49	11	83.937	-55.155	0.701
49	12	85.580	-54.639	0.695
49	13	87.775	-53.086	0.748
50	1	86.855	-47.955	0.930
50	2	83.367	-45.186	0.938
50	3	80.826	-43.860	0.927
50	4	80.399	-44.037	0.917
50	5	80.356	-44.460	0.922

FAR OFFSET SH_t SOURCE

LEVEL	WINDOW	PHI	THETA	F
50	6	79.202	-44.233	0.876
50	7	75.815	-44.334	0.794
50	8	73.350	-42.081	0.753
50	9	86.144	-25.013	0.710
50	10	84.435	165.438	0.838
50	11	83.349	167.183	0.874
50	12	83.260	166.991	0.877
50	13	83.039	167.265	0.909
51	1	89.889	123.356	0.738
51	2	83.177	-59.166	0.831
51	3	78.374	-60.267	0.870
51	4	75.390	-59.560	0.891
51	5	74.525	-57.816	0.909
51	6	74.526	-57.556	0.932
51	7	72.147	-59.946	0.944
51	8	67.501	-61.496	0.947
51	9	63.656	-60.218	0.939
51	10	61.315	-57.518	0.913
51	11	60.012	-55.238	0.865
52	1	83.643	141.051	0.938
52	2	88.244	137.496	0.947
52	3	86.626	-43.526	0.945
52	4	83.555	-41.802	0.943
52	5	82.656	-39.757	0.940
52	6	81.471	-41.565	0.899
52	7	78.164	-46.902	0.876
52	8	75.825	-48.260	0.893
52	9	75.873	-45.278	0.885
52	10	77.752	-40.891	0.835
52	11	80.636	-38.112	0.756
52	12	82.222	-39.844	0.760

FAR OFFSET SH_t SOURCE

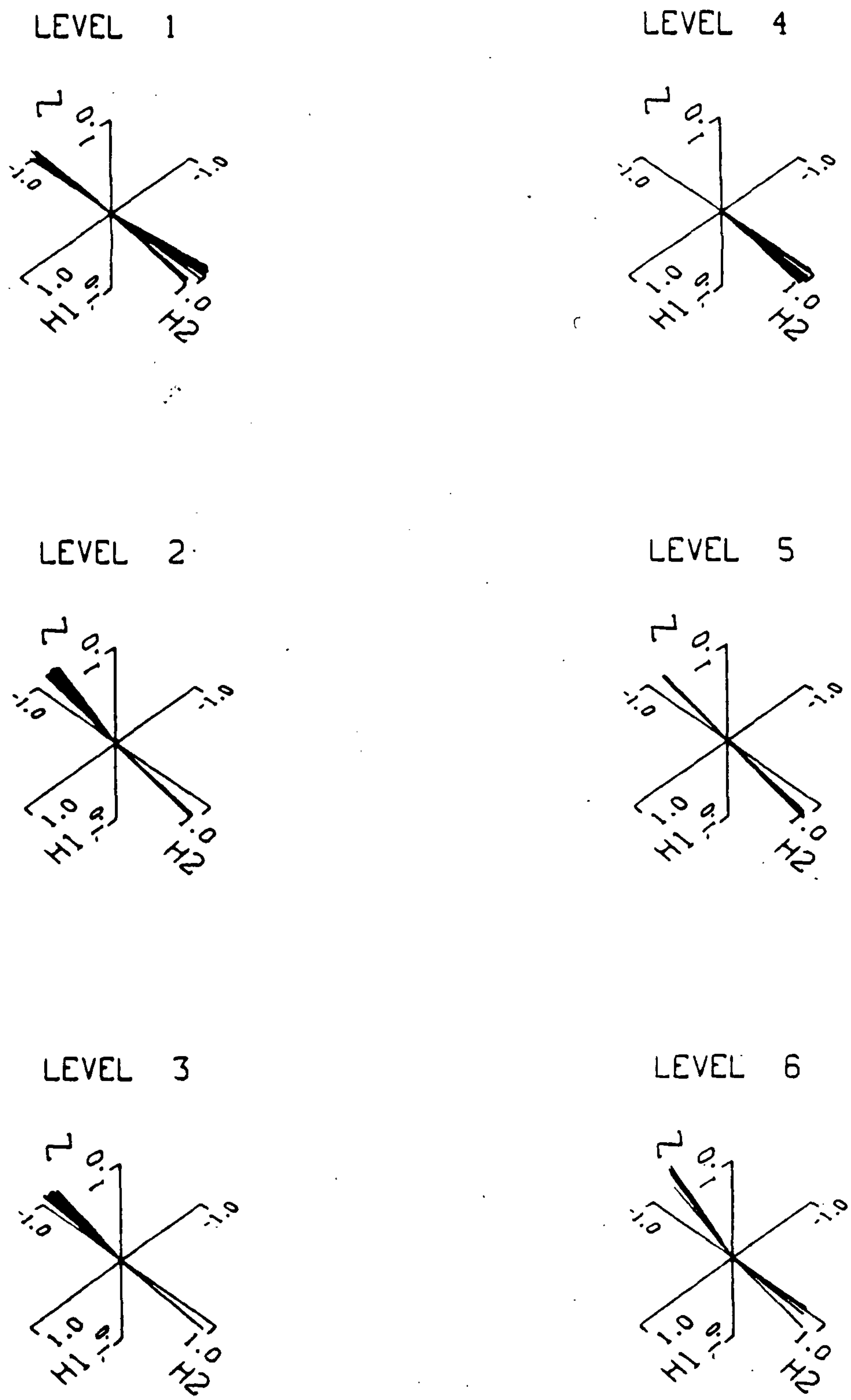

FAR OFFSET SH_t SOURCE

LEVEL 7

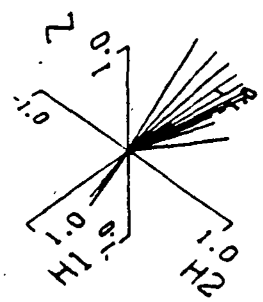

LEVEL 10

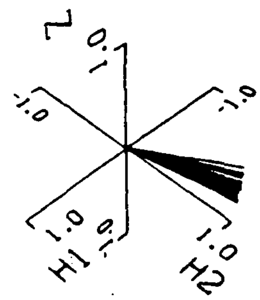

LEVEL 8

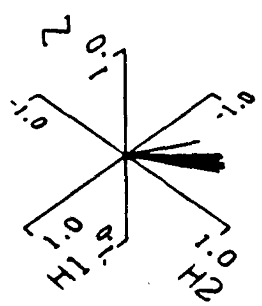

LEVEL 11

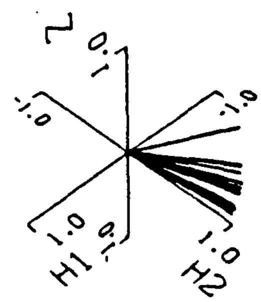

LEVEL 9

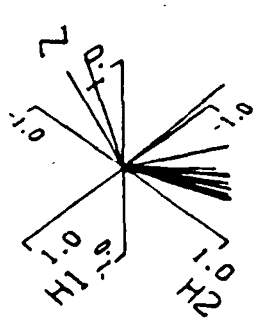

LEVEL 12

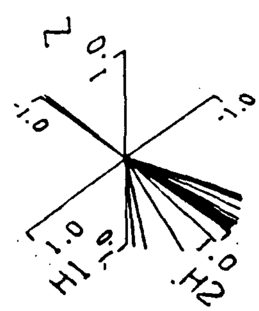

FAR OFFSET SH_t SOURCE

LEVEL 13

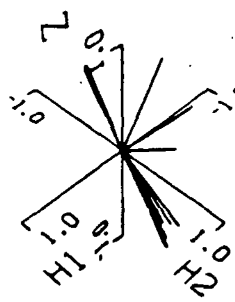

LEVEL 14

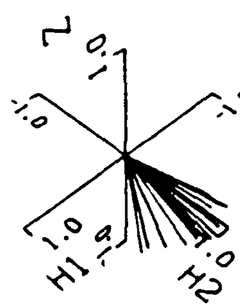

LEVEL 15

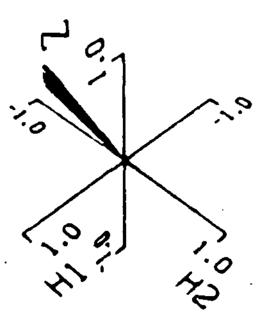

LEVEL 16

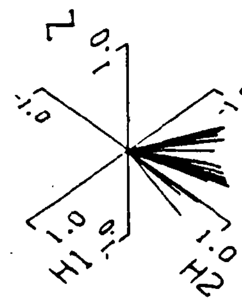

LEVEL 17

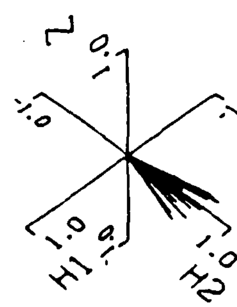

LEVEL 18

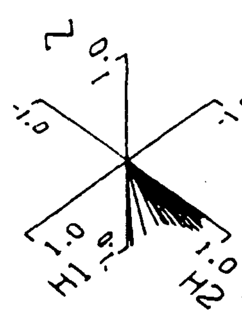

FAR OFFSET SH_t SOURCE

LEVEL 19

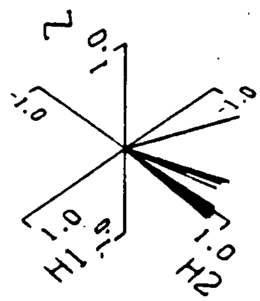

LEVEL 20

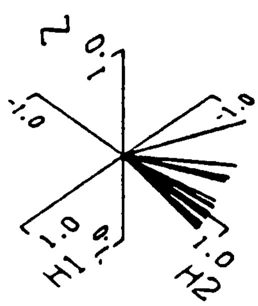

LEVEL 21

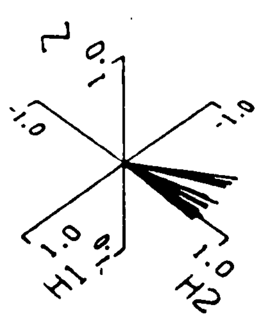

LEVEL 22

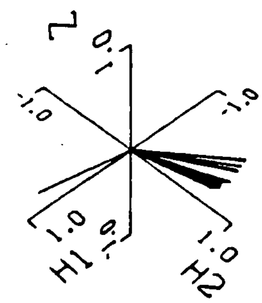

LEVEL 23

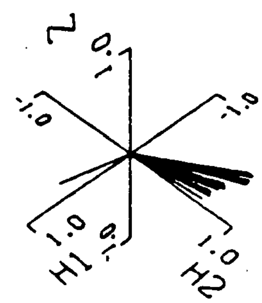

LEVEL 24

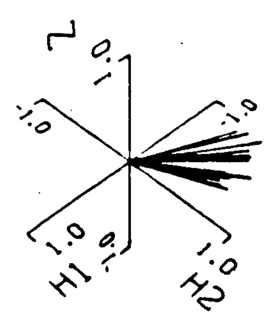

FAR OFFSET SH_t SOURCE

LEVEL 25

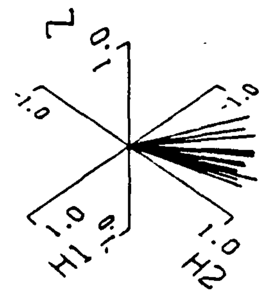

LEVEL 26

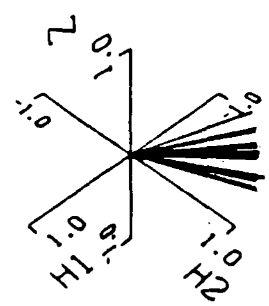

LEVEL 27

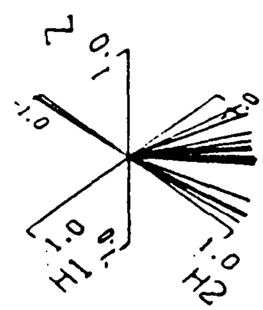

LEVEL 28

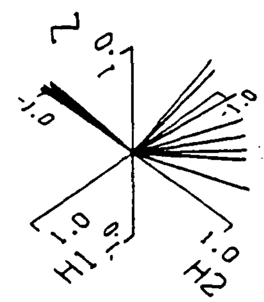

LEVEL 29

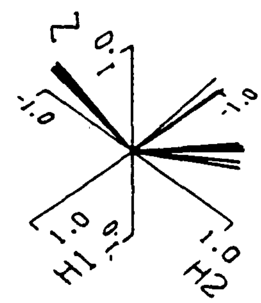

LEVEL 30

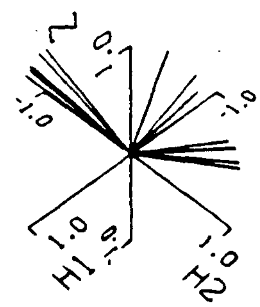

FAR OFFSET SH_t SOURCE

LEVEL 31

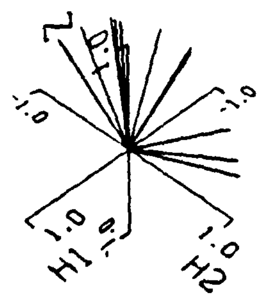

LEVEL 34

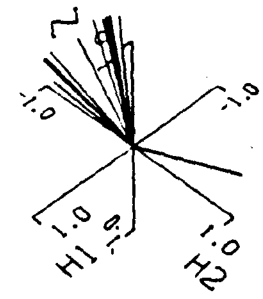

LEVEL 32

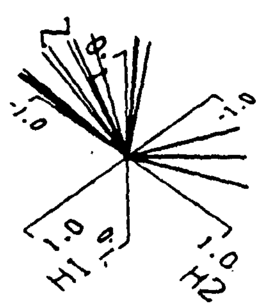

LEVEL 35

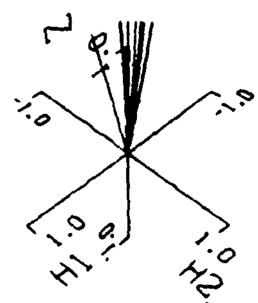

LEVEL 33

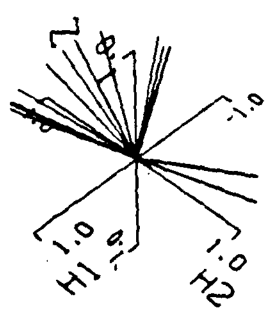

LEVEL 36

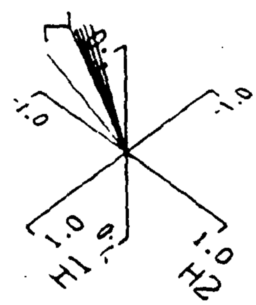

FAR OFFSET SH_t SOURCE

LEVEL 37

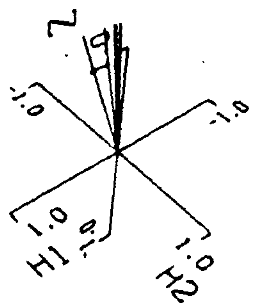

LEVEL 38

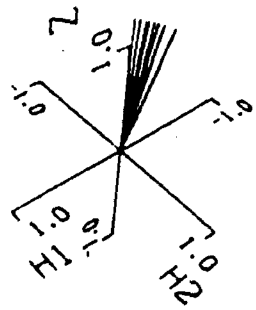

LEVEL 39

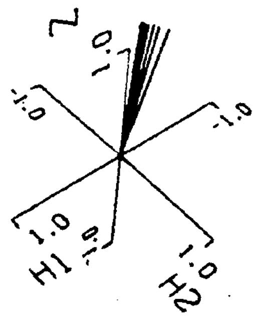

LEVEL 40

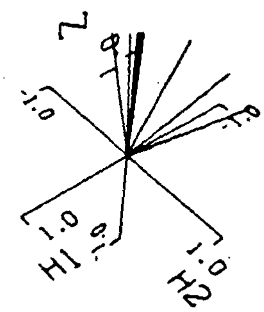

LEVEL 41

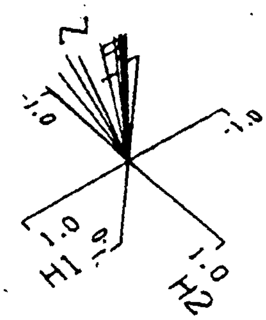

LEVEL 42

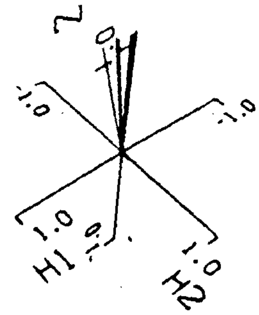

FAR OFFSET SH_t SOURCE

LEVEL 43

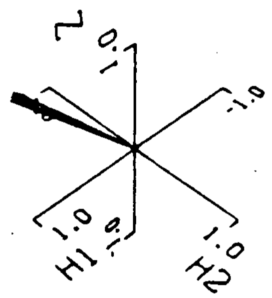

LEVEL 46

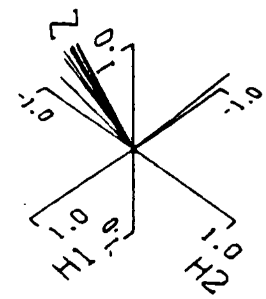

LEVEL 44

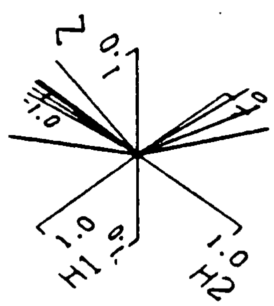

LEVEL 47

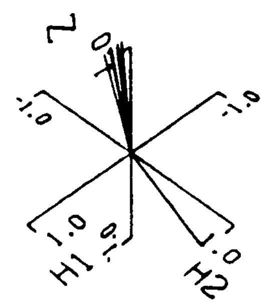

LEVEL 45

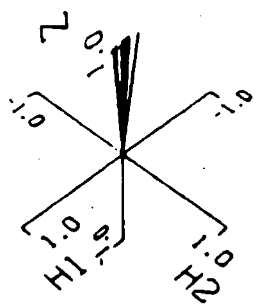

LEVEL 48

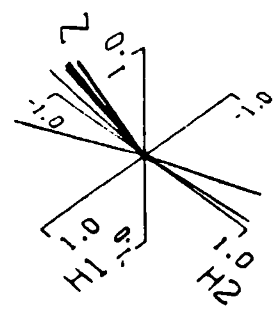

FAR OFFSET SH_t SOURCE

LEVEL 49

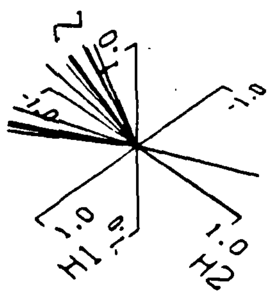

LEVEL 52

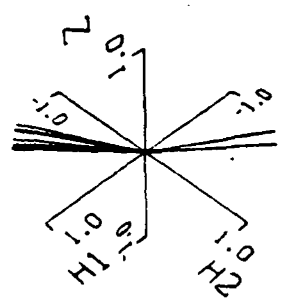

LEVEL 50

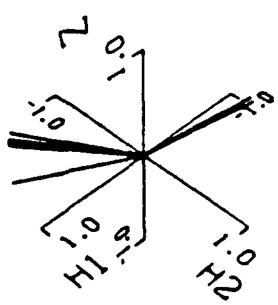

LEVEL 51

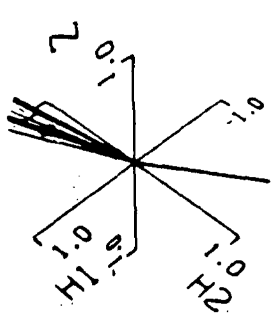

FAR OFFSET SV SOURCE

LEVEL	WINDOW	PHI	THETA	F
1	1	23.441	-80.311	0.737
1	2	14.471	-67.225	0.739
1	3	12.480	-32.624	0.726
1	4	12.688	-28.491	0.716
1	5	12.358	-36.088	0.766
1	6	11.889	-30.328	0.858
1	7	13.013	-16.586	0.913
1	8	14.867	-11.891	0.927
1	9	15.873	-18.501	0.923
1	10	16.307	-32.203	0.931
1	11	16.609	-40.660	0.960
1	12	16.569	-39.132	0.985
1	13	16.411	-36.952	0.983
1	14	15.753	-45.681	0.969
1	15	16.184	-69.746	0.952
1	16	18.580	-85.462	0.969
1	17	18.885	-83.069	0.941
1	18	18.331	-76.493	0.894
2	1	5.714	62.379	0.602
2	2	6.948	63.843	0.765
2	3	5.938	60.686	0.852
2	4	4.304	56.699	0.909
2	5	3.560	56.813	0.953
2	6	4.162	58.390	0.983
2	7	3.974	49.800	0.990
2	8	2.172	-2.472	0.977
2	9	4.521	-74.908	0.971
2	10	8.178	-88.952	0.980
2	11	10.756	-92.507	0.991
2	12	11.642	-92.119	0.990
2	13	11.530	-91.584	0.985
3	1	4.593	19.307	0.510
3	2	2.863	19.379	0.704
3	3	1.353	36.148	0.815
3	4	1.203	68.458	0.887
3	5	1.966	75.252	0.936
3	6	2.636	81.041	0.961
3	7	2.301	99.433	0.964
3	8	1.291	161.201	0.967
3	9	2.863	-116.645	0.953
3	10	6.130	-94.487	0.955
4	1	5.656	104.091	0.856
4	2	3.120	117.797	0.921
4	3	2.386	120.860	0.963
4	4	2.305	122.160	0.982
4	5	1.822	153.969	0.980
4	6	2.194	-138.011	0.977
4	7	3.851	-103.028	0.979
4	8	5.842	-87.611	0.981
4	9	7.969	-80.895	0.984
5	1	13.248	-168.095	0.760
5	2	19.260	-150.547	0.861
5	3	23.265	-144.161	0.924
5	4	26.843	-136.565	0.948
5	5	29.060	-130.811	0.957
5	6	29.668	-128.026	0.964

FAR OFFSET SV SOURCE

LEVEL	WINDOW	PHI	THETA	F
5	7	30.382	-125.862	0.966
5	8	31.914	-122.787	0.964
5	9	33.534	-119.051	0.961
5	10	32.842	-116.946	0.946
5	11	29.736	-116.170	0.928
5	12	25.772	-113.802	0.916
5	13	21.478	-106.305	0.898
6	1	38.382	-123.593	0.866
6	2	38.368	-124.985	0.924
6	3	37.305	-127.534	0.941
6	4	37.270	-127.719	0.923
6	5	38.248	-124.142	0.917
6	6	37.364	-123.042	0.938
6	7	35.381	-125.800	0.952
6	8	34.228	-128.870	0.958
6	9	34.094	-129.845	0.956
6	10	34.570	-128.462	0.955
6	11	34.574	-127.866	0.969
6	12	33.481	-129.476	0.986
6	13	32.190	-132.604	0.991
7	1	52.372	-98.652	0.901
7	2	46.201	-97.552	0.873
7	3	41.446	-96.931	0.831
7	4	39.459	-96.621	0.801
7	5	39.217	-96.834	0.804
7	6	37.143	-98.928	0.850
7	7	33.460	-102.524	0.909
7	8	30.906	-104.159	0.938
7	9	29.830	-103.608	0.943
7	10	30.510	-102.995	0.943
7	11	32.290	-103.401	0.954
7	12	32.354	-103.781	0.969
7	13	30.298	-103.269	0.973
7	14	27.238	-101.672	0.971
8	1	86.114	-89.965	0.785
8	2	87.045	-90.199	0.760
8	3	86.333	-89.976	0.770
8	4	81.111	-87.973	0.766
8	5	66.446	-82.886	0.729
8	6	47.279	-83.618	0.727
8	7	54.804	-98.113	0.775
8	8	60.924	-96.888	0.923
8	9	62.430	-93.291	0.947
8	10	62.844	-92.371	0.906
8	11	60.718	-94.291	0.862
8	12	57.481	-95.522	0.843
8	13	55.331	-94.451	0.822
9	1	56.195	89.071	0.717
9	2	49.293	84.254	0.732
9	3	47.244	81.401	0.728
9	4	42.909	76.872	0.718
9	5	32.669	65.316	0.815
9	6	27.738	56.662	0.952
9	7	26.055	52.660	0.953
9	8	22.072	39.433	0.888

FAR OFFSET SV SOURCE

LEVEL	WINDOW	PHI	THETA	F
10	1	62.481	94.790	0.833
10	2	50.747	85.171	0.766
10	3	43.171	71.728	0.789
10	4	39.996	58.924	0.864
10	5	36.888	49.668	0.936
10	6	33.369	43.811	0.953
10	7	32.625	37.616	0.967
10	8	33.181	30.585	0.971
11	1	54.736	135.000	0.000
11	2	54.736	135.000	0.000
11	3	54.736	135.000	0.000
11	4	54.736	135.000	0.000
11	5	54.736	135.000	0.000
11	6	54.736	135.000	0.000
11	7	54.736	135.000	0.000
11	8	54.736	135.000	0.000
12	1	54.736	135.000	0.000
12	2	54.736	135.000	0.000
12	3	54.736	135.000	0.000
12	4	54.736	135.000	0.000
12	5	54.736	135.000	0.000
12	6	54.736	135.000	0.000
12	7	54.736	135.000	0.000
12	8	54.736	135.000	0.000
12	9	54.736	135.000	0.000
12	10	54.736	135.000	0.000
12	11	54.736	135.000	0.000
12	12	54.736	135.000	0.000
13	1	54.736	135.000	0.000
13	2	54.736	135.000	0.000
13	3	54.736	135.000	0.000
13	4	54.736	135.000	0.000
13	5	54.736	135.000	0.000
13	6	54.736	135.000	0.000
13	7	54.736	135.000	0.000
13	8	54.736	135.000	0.000
13	9	54.736	135.000	0.000
13	10	54.736	135.000	0.000
14	1	8.490	-137.145	0.946
14	2	8.545	-146.666	0.963
14	3	9.421	-154.880	0.968
14	4	9.962	-157.311	0.962
14	5	9.153	-151.739	0.950
14	6	8.339	-143.069	0.960
14	7	9.096	-142.329	0.956
14	8	11.388	-146.502	0.955
14	9	14.439	-148.380	0.942
14	10	16.570	-145.433	0.924
15	1	61.489	-106.450	0.879
15	2	57.061	-100.436	0.913
15	3	60.537	-99.595	0.931
15	4	69.725	-100.961	0.849
15	5	85.941	-104.156	0.710
15	6	81.312	72.344	0.713
15	7	79.472	70.364	0.750

FAR OFFSET SV SOURCE

LEVEL	WINDOW	PHI	THETA	F
15	8	79.459	68.787	0.784
15	9	74.452	68.084	0.840
15	10	67.732	69.333	0.882
16	1	16.465	-54.030	0.939
16	2	15.444	-69.798	0.937
16	3	15.616	-79.971	0.920
16	4	15.820	-81.825	0.894
16	5	16.068	-77.829	0.876
16	6	16.987	-76.372	0.874
16	7	18.807	-81.596	0.872
16	8	29.555	-135.000	0.851
16	9	25.514	-101.635	0.799
16	10	27.535	-110.081	0.752
16	11	27.200	-114.964	0.760
16	12	26.896	-120.059	0.809
17	1	17.478	-95.818	0.859
17	2	19.315	-103.811	0.882
17	3	20.985	-108.136	0.878
17	4	21.596	-108.411	0.855
17	5	21.408	-106.508	0.837
17	6	21.957	-107.265	0.837
17	7	24.630	-112.481	0.833
17	8	30.207	-119.885	0.808
17	9	36.417	-125.903	0.775
17	10	37.716	-127.382	0.768
17	11	35.033	-126.171	0.810
17	12	33.366	-127.140	0.884
18	1	15.260	-106.156	0.924
18	2	16.026	-108.497	0.937
18	3	16.527	-108.136	0.940
18	4	16.385	-105.199	0.937
18	5	16.711	-102.366	0.929
18	6	15.163	-101.702	0.920
18	7	15.329	-102.400	0.905
18	8	16.971	-104.109	0.872
18	9	20.194	-107.559	0.834
18	10	22.644	-110.987	0.832
18	11	24.009	-114.520	0.858
19	1	19.665	-64.898	0.962
19	2	20.360	-64.566	0.975
19	3	20.486	-62.924	0.983
19	4	20.950	-61.976	0.987
19	5	21.289	-62.978	0.992
19	6	20.583	-63.761	0.992
19	7	18.526	-62.312	0.979
19	8	15.020	-56.332	0.963
19	9	12.070	-45.207	0.963
19	10	12.618	-44.019	0.939
20	1	14.694	-102.227	0.950
20	2	14.795	-101.946	0.958
20	3	14.691	-99.578	0.962
20	4	15.102	-101.189	0.974
20	5	14.787	-104.783	0.990
20	6	12.872	-104.140	0.987
20	7	10.174	-95.640	0.975

FAR OFFSET SV SOURCE

LEVEL	WINDOW	PHI	THETA	F
20	8	8.149	-77.193	0.971
20	9	7.896	-61.047	0.973
21	1	11.720	-65.421	0.968
21	2	11.707	-66.620	0.970
21	3	11.352	-70.049	0.970
21	4	10.121	-79.205	0.981
21	5	8.713	-84.036	0.993
21	6	7.684	-79.490	0.992
21	7	7.465	-67.077	0.985
21	8	7.844	-55.264	0.982
21	9	7.713	-50.480	0.981
21	10	7.592	-45.298	0.979
22	1	15.006	-60.074	0.966
22	2	13.271	-58.505	0.963
22	3	13.356	-59.336	0.960
22	4	12.820	-64.730	0.971
22	5	10.555	-65.944	0.983
22	6	8.171	-58.027	0.986
22	7	6.889	-44.153	0.984
22	8	6.774	-34.712	0.981
22	9	7.275	-35.174	0.979
22	10	7.828	-34.407	0.978
23	1	7.070	-140.825	0.920
23	2	6.979	-127.224	0.947
23	3	6.149	-112.971	0.961
23	4	6.817	-113.297	0.951
23	5	9.569	-129.376	0.940
23	6	10.264	-136.143	0.953
23	7	8.161	-137.867	0.957
23	8	5.388	-140.733	0.946
23	9	3.780	-152.027	0.930
23	10	4.349	-163.822	0.924
23	11	4.649	-166.029	0.937
24	1	15.948	-171.920	0.964
24	2	14.019	-162.832	0.959
24	3	12.126	-158.065	0.960
24	4	12.283	-154.661	0.960
24	5	15.651	-153.692	0.939
24	6	16.885	-154.248	0.952
24	7	14.785	-155.461	0.956
24	8	11.802	-158.266	0.944
24	9	9.933	-163.914	0.922
24	10	10.267	-168.419	0.908
24	11	10.847	-169.272	0.918
25	1	28.344	-172.992	0.984
25	2	27.422	-167.368	0.968
25	3	26.441	-165.558	0.969
25	4	27.418	-164.269	0.973
25	5	29.620	-162.170	0.974
25	6	29.264	-160.669	0.979
25	7	26.747	-160.622	0.977
25	8	23.589	-162.522	0.968
25	9	21.162	-166.096	0.955
25	10	20.824	-168.694	0.944

FAR OFFSET SV SOURCE

LEVEL	WINDOW	PHI	THETA	F
26	1	14.571	-164.159	0.984
26	2	16.416	-167.004	0.980
26	3	16.680	-169.391	0.975
26	4	16.686	-163.385	0.971
26	5	18.365	-156.374	0.974
26	6	19.734	-156.594	0.980
26	7	19.891	-163.274	0.977
26	8	19.273	-171.465	0.963
26	9	18.282	-176.972	0.945
26	10	17.615	-177.166	0.939
27	1	24.879	-173.302	0.981
27	2	26.754	-166.725	0.980
27	3	27.973	-165.197	0.979
27	4	27.888	-164.978	0.978
27	5	28.716	-161.607	0.975
27	6	31.055	-157.686	0.984
27	7	32.035	-157.207	0.994
27	8	31.196	-159.221	0.989
27	9	29.134	-162.838	0.970
27	10	26.994	-166.349	0.944
27	11	26.267	-167.290	0.931
28	1	25.560	-169.541	0.981
28	2	27.576	-162.089	0.973
28	3	28.507	-159.602	0.971
28	4	27.984	-157.556	0.967
28	5	30.575	-151.807	0.959
28	6	34.715	-149.157	0.974
28	7	35.485	-150.404	0.988
28	8	34.183	-153.291	0.977
28	9	32.229	-157.098	0.940
28	10	30.610	-160.232	0.897
28	11	30.207	-160.973	0.881
29	1	18.110	-174.036	0.951
29	2	19.795	-169.871	0.959
29	3	22.296	-164.630	0.952
29	4	23.143	-165.333	0.945
29	5	23.378	-166.914	0.938
29	6	28.557	-159.095	0.928
29	7	34.326	-155.611	0.958
29	8	36.237	-157.548	0.983
29	9	36.221	-160.727	0.968
29	10	35.547	-163.867	0.927
30	1	19.632	-170.680	0.977
30	2	20.233	-170.695	0.982
30	3	21.435	-168.706	0.983
30	4	22.597	-169.693	0.986
30	5	23.580	-172.324	0.978
30	6	26.843	-167.603	0.966
30	7	31.286	-161.814	0.973
30	8	33.268	-161.180	0.988
30	9	33.561	-163.359	0.988
30	10	33.227	-166.850	0.974
30	11	32.616	-169.712	0.961
31	1	28.065	-121.575	0.957
31	2	24.591	-122.275	0.968

FAR OFFSET SV SOURCE

LEVEL	WINDOW	PHI	THETA	F
31	3	24.126	-124.321	0.964
31	4	25.310	-126.409	0.960
31	5	24.480	-127.010	0.952
31	6	22.814	-128.719	0.951
31	7	26.924	-135.500	0.933
31	8	32.541	-140.715	0.947
31	9	34.910	-144.140	0.976
31	10	35.269	-147.332	0.980
31	11	34.182	-150.202	0.960
31	12	32.743	-151.532	0.950
32	1	35.052	-139.214	0.916
32	2	31.316	-137.226	0.910
32	3	28.585	-134.142	0.917
32	4	26.382	-128.858	0.934
32	5	23.596	-121.680	0.953
32	6	21.347	-117.272	0.969
32	7	23.492	-122.962	0.932
32	8	28.149	-128.358	0.932
32	9	30.008	-129.579	0.952
32	10	29.588	-130.681	0.958
32	11	28.462	-133.670	0.946
32	12	27.673	-137.603	0.937
32	13	27.242	-139.752	0.937
33	1	39.452	-153.801	0.951
33	2	36.098	-151.165	0.932
33	3	33.399	-148.390	0.917
33	4	31.698	-144.407	0.915
33	5	29.561	-138.406	0.919
33	6	25.806	-132.266	0.936
33	7	24.203	-135.971	0.942
33	8	28.527	-146.160	0.928
33	9	33.311	-150.691	0.948
33	10	35.361	-152.253	0.976
33	11	36.562	-153.161	0.984
33	12	35.006	-153.687	0.974
33	13	34.627	-153.795	0.966
34	1	31.654	-130.373	0.905
34	2	29.410	-130.067	0.940
34	3	26.764	-129.069	0.963
34	4	24.637	-128.092	0.975
34	5	22.893	-126.296	0.976
34	6	20.999	-123.334	0.972
34	7	19.557	-125.103	0.973
34	8	20.794	-137.782	0.973
34	9	25.080	-150.645	0.971
34	10	29.233	-157.472	0.979
34	11	31.546	-160.579	0.979
34	12	32.119	-161.798	0.978
34	13	32.017	-162.396	0.981
35	1	32.096	-147.653	0.970
35	2	31.072	-148.993	0.983
35	3	29.992	-149.956	0.991
35	4	28.971	-149.548	0.991
35	5	28.202	-148.634	0.988
35	6	28.307	-150.598	0.983
35	7	30.057	-157.640	0.967

FAR OFFSET SV SOURCE

LEVEL	WINDOW	PHI	THETA	F
35	8	32.866	-165.369	0.965
35	9	34.587	-169.140	0.972
35	10	34.553	-169.136	0.973
35	11	33.590	-167.525	0.967
35	12	32.486	-166.306	0.960
35	13	31.142	-165.664	0.958
36	1	37.950	-148.415	0.956
36	2	36.778	-148.314	0.966
36	3	35.641	-147.809	0.978
36	4	34.072	-146.766	0.988
36	5	32.480	-145.390	0.992
36	6	32.143	-145.467	0.989
36	7	33.516	-149.233	0.984
36	8	34.956	-155.059	0.985
36	9	35.336	-160.059	0.985
36	10	35.221	-162.984	0.983
36	11	35.387	-163.845	0.984
36	12	35.865	-163.911	0.987
36	13	35.967	-164.401	0.988
37	1	45.388	-157.794	0.960
37	2	44.435	-156.556	0.966
37	3	43.006	-155.146	0.974
37	4	41.023	-153.659	0.979
37	5	39.481	-152.033	0.974
37	6	39.675	-150.838	0.958
37	7	41.449	-151.556	0.942
37	8	42.445	-154.549	0.938
37	9	41.451	-158.158	0.940
37	10	39.874	-160.403	0.939
37	11	39.024	-160.669	0.944
37	12	38.498	-159.984	0.955
37	13	37.289	-159.378	0.969
38	1	52.324	-158.955	0.975
38	2	51.903	-158.684	0.981
38	3	51.346	-158.253	0.987
38	4	50.662	-157.274	0.992
38	5	49.924	-155.865	0.993
38	6	49.181	-154.952	0.991
38	7	48.242	-156.602	0.984
38	8	46.707	-161.844	0.979
38	9	44.980	-166.355	0.984
38	10	44.020	-167.347	0.987
38	11	44.137	-166.727	0.990
38	12	44.852	-166.035	0.992
38	13	45.411	-165.454	0.991
39	1	44.495	-157.586	0.993
39	2	45.194	-157.097	0.994
39	3	45.803	-156.539	0.995
39	4	46.345	-156.068	0.996
39	5	46.846	-155.876	0.996
39	6	46.948	-156.767	0.991
39	7	45.989	-159.817	0.981
39	8	44.499	-164.015	0.980
39	9	43.944	-166.329	0.987
39	10	44.505	-166.206	0.989
39	11	45.415	-165.229	0.986

FAR OFFSET SV SOURCE

LEVEL	WINDOW	PHI	THETA	F
39	12	46.087	-164.441	0.981
40	1	48.874	-168.087	0.993
40	2	49.250	-167.566	0.996
40	3	49.380	-166.881	0.997
40	4	49.538	-166.162	0.998
40	5	49.953	-165.633	0.998
40	6	50.348	-165.991	0.995
40	7	49.694	-168.431	0.987
40	8	47.800	-172.764	0.983
40	9	46.675	-175.918	0.989
40	10	47.171	-176.622	0.994
40	11	48.276	-176.196	0.992
40	12	49.038	-175.560	0.989
40	13	49.327	-174.824	0.984
41	1	48.907	-160.317	0.982
41	2	49.723	-159.419	0.986
41	3	49.726	-158.137	0.990
41	4	48.881	-156.443	0.994
41	5	48.654	-155.020	0.993
41	6	49.858	-155.062	0.992
41	7	51.276	-157.367	0.989
41	8	51.507	-161.587	0.984
41	9	51.005	-166.211	0.986
41	10	51.024	-169.174	0.991
41	11	51.732	-169.447	0.996
41	12	52.449	-167.972	0.989
42	1	59.891	-171.862	0.986
42	2	59.449	-170.941	0.989
42	3	58.491	-169.387	0.986
42	4	57.738	-168.465	0.972
42	5	58.811	-169.665	0.948
42	6	61.995	-172.404	0.936
42	7	63.981	-173.824	0.945
42	8	63.782	-174.077	0.952
42	9	62.990	-174.435	0.954
42	10	62.558	-174.930	0.958
42	11	62.251	-174.832	0.961
42	12	61.438	-173.808	0.965
43	1	56.560	-90.000	0.988
43	2	55.558	-90.000	0.994
43	3	55.590	-90.000	0.995
43	4	56.443	-90.000	0.994
43	5	59.225	-90.000	0.980
43	6	62.290	-90.000	0.970
43	7	63.311	-90.000	0.971
43	8	62.850	-90.000	0.965
43	9	61.863	-90.000	0.958
43	10	61.494	-90.000	0.961
43	11	61.918	-90.000	0.965
44	1	56.697	-169.781	0.993
44	2	55.463	-169.781	0.990
44	3	54.181	-169.781	0.970
44	4	54.389	-169.781	0.940
44	5	55.902	-169.781	0.922
44	6	56.624	-169.781	0.911

FAR OFFSET SV SOURCE

LEVEL	WINDOW	PHI	THETA	F
44	7	53.920	-169.781	0.892
44	8	48.979	-169.781	0.891
44	9	46.780	-169.781	0.900
44	10	46.506	-169.781	0.916
44	11	45.712	-169.781	0.948
44	12	44.383	-169.781	0.977
44	13	43.201	-169.781	0.986
45	1	55.735	-167.970	0.987
45	2	55.048	-167.132	0.992
45	3	54.266	-166.681	0.993
45	4	54.200	-166.115	0.984
45	5	55.078	-165.046	0.975
45	6	55.917	-164.546	0.970
45	7	54.896	-167.634	0.965
45	8	52.249	-175.581	0.960
45	9	50.684	177.346	0.961
45	10	50.574	175.087	0.963
45	11	50.926	175.730	0.969
45	12	50.819	176.360	0.973
45	13	49.969	175.768	0.970
46	1	47.963	-109.312	0.932
46	2	46.201	-113.235	0.936
46	3	44.131	-119.494	0.910
46	4	41.360	-122.212	0.832
46	5	41.964	-118.482	0.712
46	6	48.677	-116.258	0.678
46	7	49.823	-122.716	0.721
46	8	44.865	-132.644	0.720
46	9	38.386	-144.712	0.653
46	10	33.203	-157.780	0.552
46	11	32.491	-162.372	0.489
46	12	35.207	-158.884	0.582
47	1	55.458	-177.541	0.988
47	2	54.459	-176.785	0.987
47	3	53.249	-176.388	0.986
47	4	52.422	-175.744	0.978
47	5	52.773	-174.258	0.964
47	6	54.004	-173.118	0.956
47	7	54.167	-174.807	0.958
47	8	53.111	-178.649	0.961
47	9	52.369	178.212	0.962
47	10	52.341	177.002	0.964
47	11	52.430	177.016	0.971
48	1	58.737	-169.385	0.971
48	2	57.406	-168.630	0.967
48	3	55.780	-167.907	0.963
48	4	53.822	-167.014	0.958
48	5	52.258	-165.152	0.949
48	6	52.439	-162.388	0.940
48	7	53.297	-162.066	0.947
48	8	53.080	-164.476	0.958
48	9	52.571	-167.296	0.963
48	10	52.503	-169.252	0.963
48	11	52.711	-169.977	0.966
49	1	55.613	165.183	0.997

FAR OFFSET SV SOURCE

LEVEL	WINDOW	PHI	THETA	F
49	2	54.800	165.677	0.995
49	3	54.333	165.565	0.991
49	4	54.549	165.376	0.986
49	5	55.128	166.109	0.982
49	6	55.323	167.760	0.981
49	7	55.037	168.631	0.981
49	8	54.991	167.497	0.982
49	9	55.530	165.442	0.984
49	10	56.111	164.148	0.987
50	1	50.896	-168.329	0.998
50	2	50.474	-167.920	0.999
50	3	49.921	-167.764	0.999
50	4	49.585	-167.823	0.997
50	5	50.171	-167.395	0.994
50	6	51.853	-166.238	0.990
50	7	53.060	-165.710	0.992
50	8	53.172	-166.377	0.993
50	9	52.934	-167.700	0.992
50	10	52.925	-168.852	0.988
50	11	53.048	-169.309	0.985

FAR OFFSET SV SOURCE

LEVEL 1

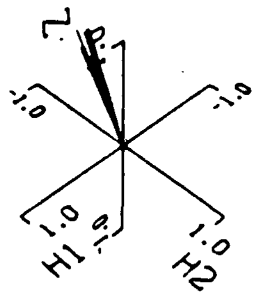

LEVEL 4

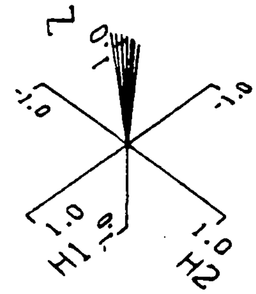

LEVEL 2

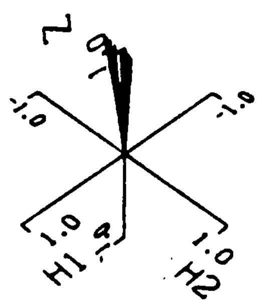

LEVEL 5

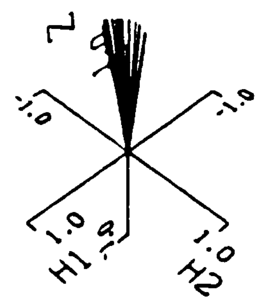

LEVEL 3

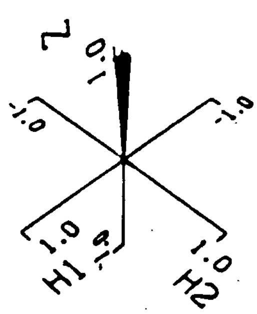

LEVEL 6

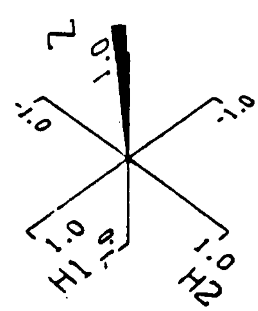

FAR OFFSET SH_t SOURCE

LEVEL 7

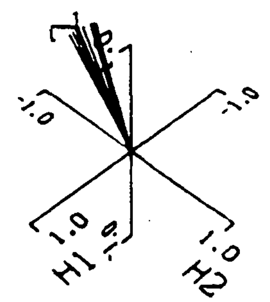

LEVEL 8

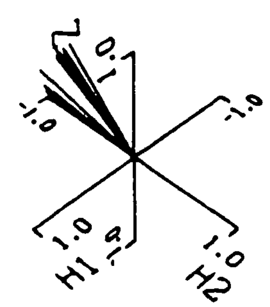

LEVEL 9

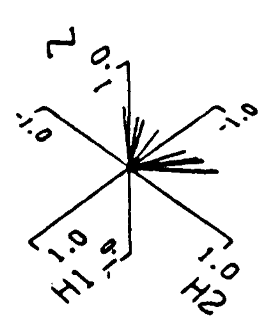

LEVEL 10

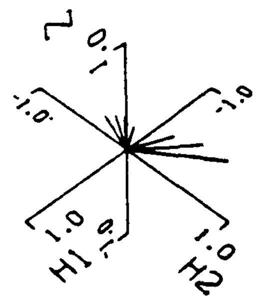

LEVEL 11

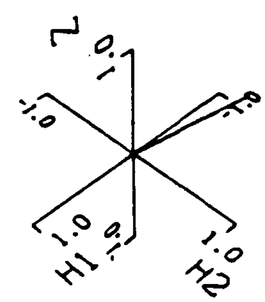

LEVEL 12

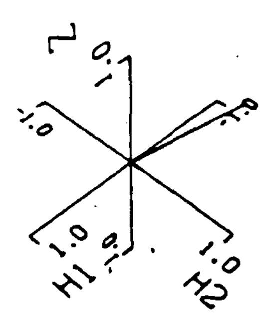

FAR OFFSET SV SOURCE

LEVEL 13

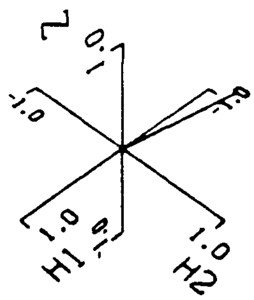

LEVEL 14

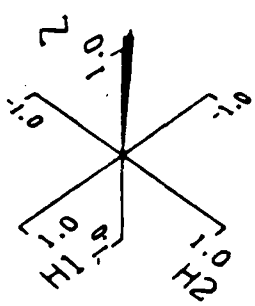

LEVEL 15

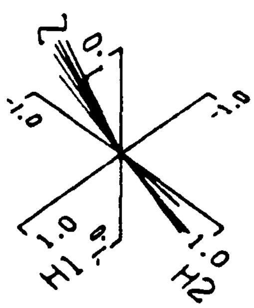

LEVEL 16

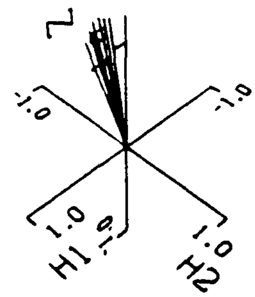

LEVEL 17

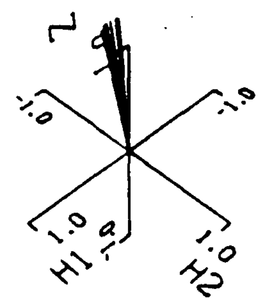

LEVEL 18

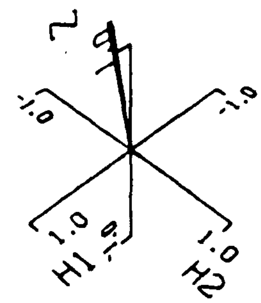

FAR OFFSET SV SOURCE

LEVEL 19

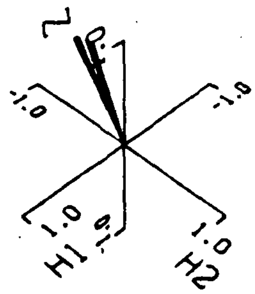

LEVEL 22

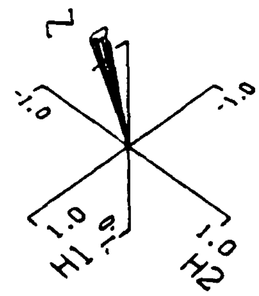

LEVEL 20

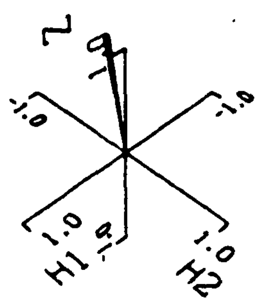

LEVEL 23

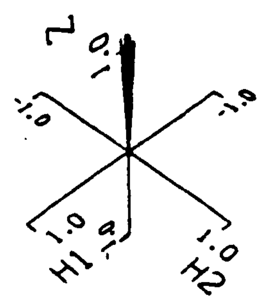

LEVEL 21

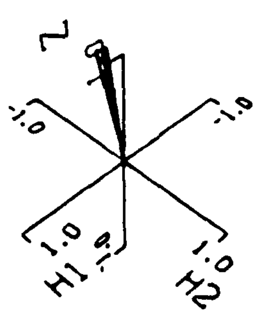

LEVEL 24

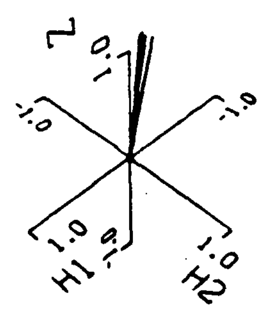

FAR OFFSET SV SOURCE

LEVEL 25

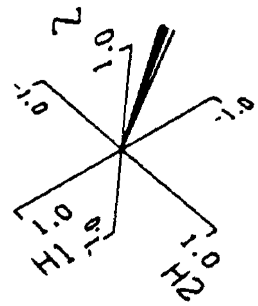

LEVEL 28

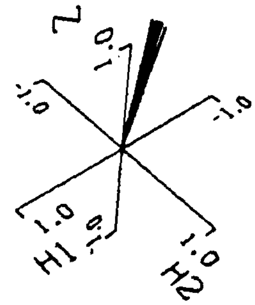

LEVEL 26

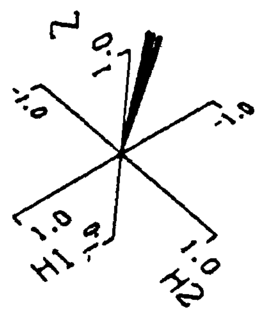

LEVEL 29

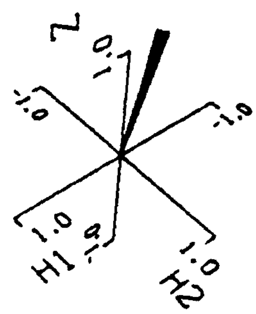

LEVEL 27

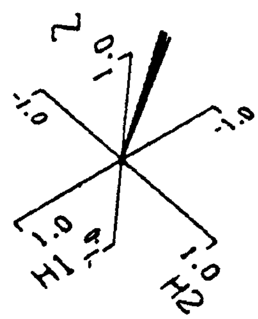

LEVEL 30

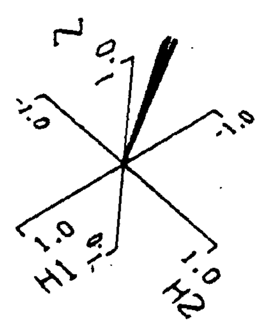

FAR OFFSET SV SOURCE

LEVEL 31

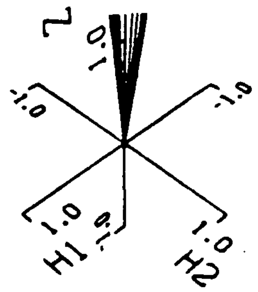

LEVEL 34

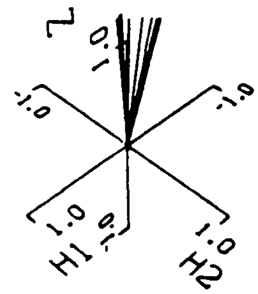

LEVEL 32

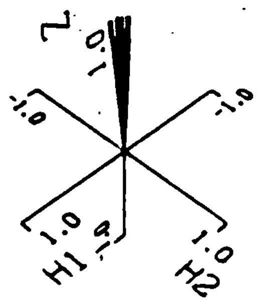

LEVEL 35

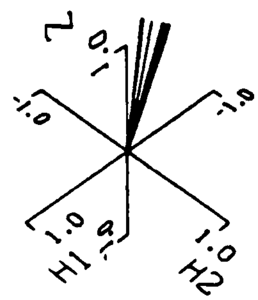

LEVEL 33

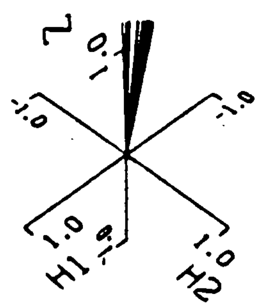

LEVEL 36

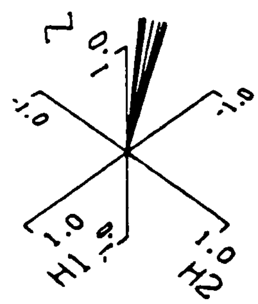

FAR OFFSET SV SOURCE

LEVEL 37

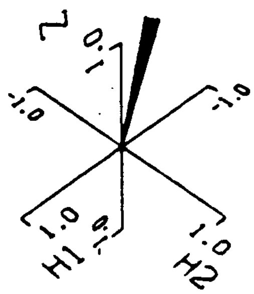

LEVEL 38

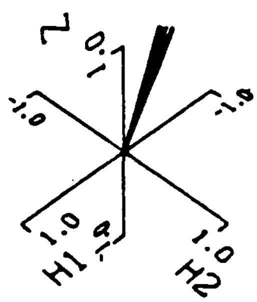

LEVEL 39

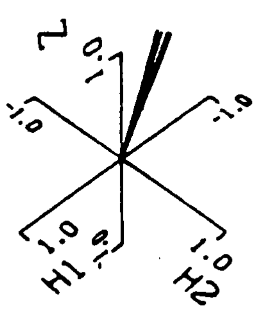

LEVEL 40

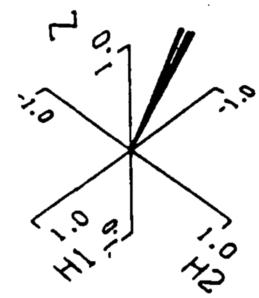

LEVEL 41

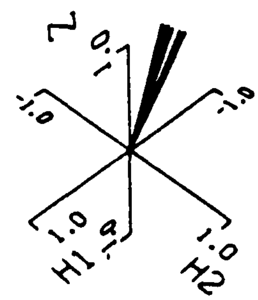

LEVEL 42

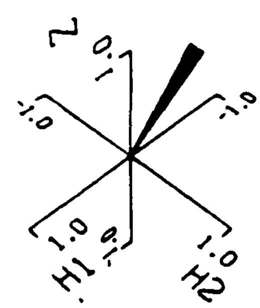

FAR OFFSET SV SOURCE

LEVEL 43

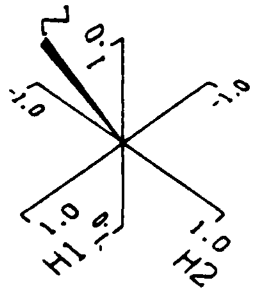

LEVEL 46

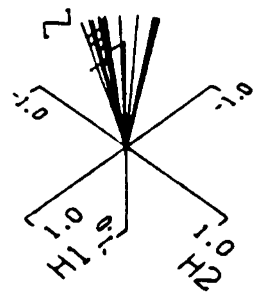

LEVEL 44

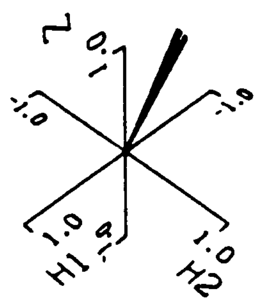

LEVEL 47

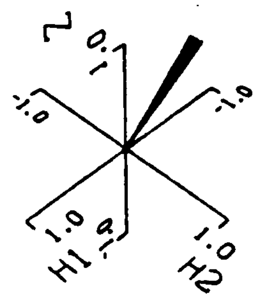

LEVEL 45

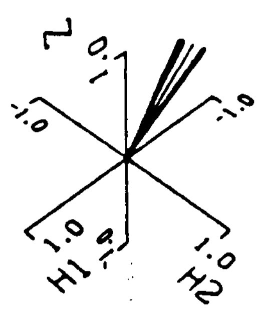

LEVEL 48

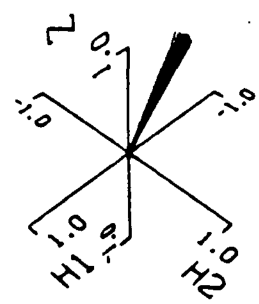

FAR OFFSET SV SOURCE

LEVEL 49

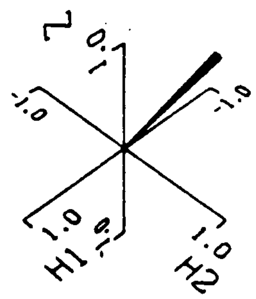

LEVEL 50

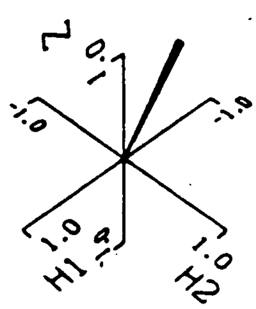

APPENDIX 4

FORTRAN 77 PROGRAM LISTINGS

HODOS.FOR
VEL.FOR
ROTBOR.FOR

```
      PROGRAM  HODOS

C WRITTEN BY TOM DALEY FROM IDEAS OF FRED EASTWOOD 12/86
C                                              CURRENT VERSION 3/4/87
C*********************************************************************
C*******  THIS PROGRAM IS DESIGNED TO PLOT HODOGRAMS FROM A DATA FILE
C*******  WRITTEN FROM THE DISCO PROGRAM  'DISCOUT.'  IT SHOULD HAVE
C*******  THE DATA FROM A 3 COMPONENT GEOPHONE FOR A WINDOW OF TIME.
C*******  THE DATA FILE SHOULD BE ORGANIZED SUCH THAT IT HAS, IN ORDER,
C*******  THE NUMBER OF TRACES, THE NUMBER OF SAMPLES IN THE FIRST
C*******  TRACE, THE DATA FOR THE FIRST TRACE, THE NUMBER OF SAMPLES
C*******  IN THE SECOND TRACE, THE DATA FOR THE SECOND TRACE, ETC.
C*******  I HAVE ASSUMED THE TRACES ARE IN THE ORDER P,SV,SH.
C*********************************************************************

      REAL   TRACE1(100),TRACE2(100),TRACE3(100),TEMP(100),ZMTR(100,100)
      REAL   TRACEA(100),TRACEB(100),TRACEC(100),PLTST,KOUNT
      DOUBLE PRECISION GSCALE
      CHARACTER*64   FILEIN,TITLE1,TITLE2
      INTEGER XTRC,YTRC,JKOUNT2

      WRITE(6,*)'WHAT FILE ARE THE TRACES IN?'
      READ(5,10)FILEIN
 10   FORMAT(A64)
C      FILEIN='SV2SROT.TRC'
      OPEN(UNIT=1,FILE=FILEIN,STATUS='OLD',FORM='UNFORMATTED')


      READ(1)NTRACE
      REWIND(1)
      NLEVEL=NTRACE/3                ! THERE ARE 3 TRACES PER LEVEL

      WRITE(6,*)'THERE ARE',NLEVEL,' LEVELS.  HOW MANY PLOTS DO YOU WANT?'
      READ(5,*)NPLOTS

      WRITE(6,*)'DO YOU WANT 2D OR 3D PLOTS?  (ANSWER 2 OR 3)'
      READ(5,*)NDIM

      IF(NDIM.EQ.3)THEN
           WRITE(6,*)'DO YOU WANT 2-D SLICES, 3-D PLOTS, OR BOTH?
     &     ANSWER 2,3 OR 4'
           READ(5,*)PLTST
C           PLTST=2
           WRITE(6,*)'WHICH LEVEL DO YOU WANT TO START AT?'
           READ(5,*)SPLT
           GO TO 300
      ENDIF

*********************************************************************
C*************  LOOP 100 IS FOR 2D PLOTS  ***************************
*********************************************************************

      DO 100 I=1,NPLOTS

      WRITE(6,*)'WHICH TRACES DO YOU WANT TO PLOT?'
      READ(5,*)XTR,YTR
      READ(1)NTRACE
      READ(1)NPOINTS

      REWIND(1)
      READ(1)NTRACE

      DO 110, ITR=1,NTRACE
      READ(1) NPOINTS
```

```
        READ(1) (TEMP(J) ,J=1,NPOINTS)        !READ A TRACE IN TEMP STORAGE

        IF(ITR.EQ.XTR) THEN                   !CHECK IF WE WANT THIS TRACE

                WRITE(6,*)'THERE ARE',NPOINTS,' SAMPLES, WHICH ONES TO PLOT?'
                READ(5,*)ISTART,ISTOP

                NPTS=ISTOP-ISTART+1
                DO 115 J=ISTART,ISTOP
                TRACE1(J-ISTART+1)=TEMP(J)     !INPUT DATA TO PLOTTING ARRAY 1
115             CONTINUE
        ENDIF

        IF(ITR.EQ.YTR)THEN
                DO 117 J=ISTART,ISTOP
                TRACE2(J-ISTART+1)=TEMP(J)     !INPUT DATA TO PLOTTING ARRAY 2
117             CONTINUE
        ENDIF

110     CONTINUE
        REWIND(1)

****************************************************************************
C*****************  USE GSCALE TO NORMALIZE THE HODOGRAMS
****************************************************************************
        GSCALE=10**-20
        XMAX=0
        YMAX=0
        DO 120 J=1,NPTS                       ! FIND THE MAXIMUM VALUE OF EITHER TRACE
        XMAX=MAX(XMAX,ABS(TRACE1(J)))
        YMAX=MAX(YMAX,ABS(TRACE2(J)))
        GSCALE=MAX(XMAX,YMAX)
120     CONTINUE
        DO 130 J=1,NPTS                       ! NORMALIZE SO THAT MAX VALUE = 1
        TRACE1(J)=TRACE1(J)/GSCALE
        TRACE2(J)=TRACE2(J)/GSCALE
130     CONTINUE

CCCCCCCCCCCCCCCCCCCCCCCCC  MAKE A TITLE FOR PLOTS   CCCCCCCCCCCCCCCCCCCCCCCCC
        ENCODE(38,141,TITLE1),YTR,XTR
141     FORMAT('PARTICLE MOTION - TRACES ',F4.0,' VS ',F4.0,'$')

****************************************************************************
C*****************       CALL   3-D   GRAPHICS  *****************************

C         CALL NOMIN3
C         CALL PVT240
        CALL TALARS
        CALL PAGE(8.0,8.0)
        CALL AREA2D(2.0,2.0)
        CALL XNAME('              $',100)
        CALL YNAME('              $',100)
        CALL XNONUM
        CALL YNONUM
        CALL CROSS
        CALL HEADIN(%REF(TITLE1),100,1.5,1)
        CALL GRAF(-1.0,'SCALE',1.0,-1.0,'SCALE',1.0)

        CALL MARKER(13)
        CALL CURVE(TRACE2,TRACE1,3,1)
        CALL MARKER(4)
        CALL CURVE(TRACE2,TRACE1,NPTS,1)
        CALL ENDPL(0)
100     CONTINUE
        CALL DONEPL
```

```
      GO TO 999
**************************************************************************
C******************    THE 300 LOOPS ARE FOR 3-D HODOGRAMS     *****************
**************************************************************************

 300  CONTINUE
      KOUNT=0
      JKOUNT2=0

      DO 399 JPLT=1,NPLOTS
C       WRITE(6,*)' WHICH LEVEL DO YOU WANT TO PLOT?'
C       READ(5,*)ILEVEL
      ILEVEL=JPLT                   ! USE THIS STATEMENT FOR MULTIPLE LEVEL PLOTS

      REWIND(1)
      READ(1) NTRACE

      DO 390 ITR=1,NTRACE
      KOUNT=FLOAT(ITR+2)/3                     ! KOUNT IS THE CURRENT LEVEL
      IF(KOUNT.LT.FLOAT(ILEVEL))THEN
              READ(1) NPOINTS
              READ(1) (TEMP(J), J=1,NPOINTS)
      ENDIF
      IF(KOUNT.EQ.FLOAT(ILEVEL))THEN
              READ(1) NPOINTS
              READ(1) (TRACE1(J), J=1,NPOINTS)
              READ(1) NPOINTS
              READ(1) (TRACE2(J), J=1,NPOINTS)
              READ(1) NPOINTS
              READ(1) (TRACE3(J), J=1,NPOINTS)
      ENDIF
 390  CONTINUE

      IF(JPLT.LT.SPLT)GO TO 399                ! LOOP UNTIL DESIRED FIRST LEVEL

C       WRITE(6,*)' THERE ARE',NPOINTS,' POINTS, WHICH ONES DO YOU WANT TO PLOT?
C    &     FIRST,LAST'
C       READ(5,*)ISTART,ISTOP
      ISTART=1
      ISTOP=NPOINTS

      NPTS=ISTOP-ISTART+1

      DO 380 J=ISTART,ISTOP
      TRACE1(J-ISTART+1)=TRACE1(J)
      TRACE2(J-ISTART+1)=TRACE2(J)
      TRACE3(J-ISTART+1)=TRACE3(J)
 380  CONTINUE

      DO 381 J=1,NPTS          ! CREATE DUMMY ARRAYS FOR 2-D PROJECTION ON
      TRACEA(J)=-1             ! SIDES OF PLOT
      TRACEB(J)=-1
      TRACEC(J)=1
 381  CONTINUE

**************************************************************************
C********************   COMPUTE SCALING FACTORS  FOR 3-D PLOTS  **************
      GSCALE=10**-20
      XMAX=0
      YMAX=0
      ZMAX=0
```

```
      DO 385 J=1,NPTS                          ! FIND THE MAXIMUM VALUE OF
      XMAX=MAX(XMAX,ABS(TRACE1(J)))            ! ALL 3 TRACES
      YMAX=MAX(YMAX,ABS(TRACE2(J)))
      ZMAX=MAX(ZMAX,ABS(TRACE3(J)))
385   CONTINUE

      GSCALE=MAX(XMAX,YMAX,ZMAX)
      IF(GSCALE.LT.10.0**-10)GSCALE=1.0
C       WRITE(5,*)' SCALING FACTOR=',GSCALE

      DO 370 J=1,NPTS                          !  NORMALIZE TO MAX =1.0
      TRACE1(J)=TRACE1(J)/GSCALE
      TRACE2(J)=TRACE2(J)/GSCALE
      TRACE3(J)=TRACE3(J)/GSCALE
370   CONTINUE

CCCCCCCCCCCCCCCCCCCCCCCCCCCCCCCCCCCCCCCCCCCCCCCCCCCCCCCCCCCCCCCCCCCCCCCCCC
CCCCCCCCCCCC  SET UP 3D GRAPHICS    CCCCCCCCCCCCCCCCCCCCCCCCCCCCCCCCCCCCCCC
C       WRITE(6,*)' DO YOU WANT A NEW VIEW POINT FOR THE 3D PLOT?  (1=YES)'
C       READ(5,*)VUTEST
      PHI=-40
      THETA=20
      RADIUS=12

      IF(VUTEST.EQ.1)THEN
              WRITE(6,*)' ENTER VIEWPOINT -  PHI,THETA,RADIUS'
              READ(5,*)PHI,THETA,RADIUS
      ENDIF

      ENCODE(28,389,TITLE2),ILEVEL               ! CREATE PLOT TITLE
389   FORMAT(' PARTICLE MOTION AT LEVEL',I3,'$')

      KOUNT2=KOUNT2+1
      JKOUNT2=JKOUNT2+1
      IF(JKOUNT2.GT.6)THEN
              JKOUNT2=1
              CALL ENDPL(0)
      ENDIF

      IF(JKOUNT2.EQ.1)THEN
C               CALL NOMIN8
C               CALL PTK41
C               CALL PVT240
              CALL TALARS
              CALL PAGE(8.5,11.0)
      ENDIF

      IF(JKOUNT2.EQ.1)CALL PHYSOR(0.1,7.0)
      IF(JKOUNT2.EQ.2)CALL PHYSOR(0.1,3.5)
      IF(JKOUNT2.EQ.3)CALL PHYSOR(0.1,0.1)
      IF(JKOUNT2.EQ.4)CALL PHYSOR(4.1,7.0)
      IF(JKOUNT2.EQ.5)CALL PHYSOR(4.1,3.5)
      IF(JKOUNT2.EQ.6)CALL PHYSOR(4.1,0.1)

C       CALL NOMIN8                              ! PICK PLOTTING DEVICE
C       CALL PTK41
C       CALL PAGE(8.5,8.5)
      CALL AREA2D(4.0,3.5)
      CALL VOLM3D(5.0,5.0,5.0)
      CALL MESSAG(%REF(TITLE2),27,0.5,3.25)
      CALL VUANGL(PHI,THETA,RADIUS)
      CALL X3NAME('SV',2)
      CALL Y3NAME('SH',2)
      CALL Z3NAME('RADIAL',1)
```

```
      CALL GRAF3D(-1,1,1,-1,1,1,-1,1,1)        ! DRAW AXIS
      CALL BOX3D

      IF(PLTST.NE.2.0)THEN
            CALL MARKER(15)
            CALL CURV3D(TRACE2,TRACE3,TRACE1,3,1)        ! MARK FIRST 3 POINTS
            CALL MARKER(16)
            CALL CURV3D(TRACE2,TRACE3,TRACE1,NPTS,1)     ! PLOT 3-D CURVE
      ENDIF

      IF(PLTST.NE.3.0)THEN
            CALL MARKER(13)
            CALL CURV3D(TRACE2,TRACE3,TRACEA,3,1)      ! MARK FIRST 3 POINTS
            CALL CURV3D(TRACE2,TRACEC,TRACE1,3,1)      !     "
            CALL CURV3D(TRACEB,TRACE3,TRACE1,3,1)      !     "
            CALL MARKER(4)
            CALL CURV3D(TRACE2,TRACE3,TRACEA,NPTS,1)     ! PLOT 3-D PROJECTIONS
            CALL CURV3D(TRACE2,TRACEC,TRACE1,NPTS,1)     !     "
            CALL CURV3D(TRACEB,TRACE3,TRACE1,NPTS,1)     !     "
      ENDIF
C      CALL BGNMAT(NPTS,NPTS)                          ! MAKE 3-D MATRIX
C      CALL GETMAT(TRACE2,TRACE3,TRACE1,NPTS,0)        !     "
C      CALL ENDMAT(ZMTR,0)                             !     "
C      CALL SURMAT(ZMTR,1,NPTS,1,NPTS,0)             ! PLOT 3-D SURFACE
C      CALL ENDPL(0)
      CALL ENDGR(0)                             ! END SUBPLOT

 399  CONTINUE

      CALL DONEPL
 999  END
```

```
      PROGRAM VELOCITY
C**         WRITTEN BY TOM DALEY 12/86              CURRENT VERSION         3/23/87
C*************************************************************************
C******** THIS PROGRAM READS IN TRAVEL TIME INION FROM BOREHOLE DATA
C******** AND COMPUTES AVERAGE VELOCITIES, INTERVAL VELOCITIES FOR ANY
C******** INTERVAL MULTIPLE. THE RATIOS OF P/SV AND P/SH WITH POISSON'S
C******** RATIO ARE COMPUTED FOR AVERAGE OR INTERVAL VELOCITIES. VELOCITIES
C******** ARE CORRECTED FOR SOURCE OFFSET WITH A STRAIGHT RAYPATH.
C*************************************************************************

      DIMENSION  DEPTH(100),PTT(100),SVTT(100),SHTT(100),DIST(100)
      DIMENSION  SVRATIO(100),SHRATIO(100),VPDEPTH(100),VSVDEPTH(100)
      REAL     VP(100),VSV(100),VSH(100),VSHDEPTH(100),SHRDEPTH(100)
      REAL     SVRDEPTH(100),SVPOIS(100),SHPOIS(100),VEL(100),VDEPTH
      CHARACTER*25 FILEIN

      WRITE(6,*)'WHAT FILE IS THE DATA IN?'
      READ(5,7)FILEIN

C       FILEIN='VEL.DAT'


C       OFFSET=2500.0
      WRITE(6,*)'WHAT IS THE SOURCE OFFSET'
      READ(5,*)OFFSET

      WRITE(6,*) 'HOW MANY DEPTHS IN DATA?'
      READ(5,*)N

      OPEN(UNIT=2,FILE='VELDAT.OUT',STATUS='NEW')

 100  WRITE(6,*)'DO YOU WANT TRAVEL TIME,  VELOCITIES  OR RATIOS?,
     &  1, 2 OR 3 ?'
      READ(6,*) TEST

      OPEN(UNIT=1,FILE=FILEIN,STATUS='OLD')

      WRITE(2,*)'   '

      IF(TEST.EQ.1)THEN

      WRITE(2,*) '        DEPTH        P TRAVEL TIME     SV TRAVEL TIME
     & SH TRAVEL TIME   '

      DO 10  I=1,N
             READ(1,5)DEPTH(I),PTT(I),SHTT(I),SVTT(I)
             WRITE(2,9)DEPTH(I),PTT(I),SVTT(I),SHTT(I)
 10   CONTINUE
      ENDIF


      IF(TEST.EQ.2.OR.TEST.EQ.3)THEN

      WRITE(6,*)'DO YOU WANT AVERAGE VELOCITY OR INTERVAL VELOCITY, 1 OR 2 ?'
      READ(5,*)TEST2

      IF(TEST2.EQ.2)WRITE(6,*)'HOW MANY INTERVALS DO YOU WANT TO AVERAGE ?'
      IF(TEST2.EQ.2)READ(5,*)INT

      IF(TEST.EQ.2)WRITE(2,*)'      DEPTH       P VELOCITY        SV VELOCITY
     &          SH VELOCITY    '
      IF(TEST.EQ.3)WRITE(2,*)'           DEPTH
     &     P/SH        SH POISSON       DEPTH
     &      P/SV       SV POISSON'
```

```
      WRITE(2,*)'
C
CCCC    LOOP 20 COMPUTES THE AVERAGE VELOCITIES
C
      IF(TEST2.EQ.1)THEN                 ! COMPUTE AVERAGE VELOCITIES

      DO 20 I=1,N
          READ(1,5)DEPTH(I),PTT(I),SHTT(I),SVTT(I)
          DIST(I)=OFFSET/(COS(ATAN(DEPTH(I)/OFFSET)))   ! COMPUTE STRAIGHT
                                                        ! LINE DISTANCE
          IF(PTT(I).NE.0)THEN
              VP(I)=DIST(I)/PTT(I)              ! P VELOCITIES AND RATIOS
              SVRATIO(I)=SVTT(I)/PTT(I)
              SHRATIO(I)=SHTT(I)/PTT(I)
              SHPOIS(I)=0.5*(SHRATIO(I)**2-2.0)/(SHRATIO(I)**2-1.0)
              SVPOIS(I)=0.5*(SVRATIO(I)**2-2.0)/(SVRATIO(I)**2-1.0)
          ENDIF
          IF(SVTT(I).NE.0)VSV(I)=DIST(I)/SVTT(I)
          IF(SHTT(I).NE.0)VSH(I)=DIST(I)/SHTT(I)
          IF(TEST.EQ.2)WRITE(2,11)DEPTH(I),VP(I),VSV(I),VSH(I)
          IF(TEST.EQ.3)WRITE(2,39)DEPTH(I),SHRATIO(I),SHPOIS(I),
     &                            DEPTH(I),SVRATIO(I),SVPOIS(I)
   20 CONTINUE
      ENDIF

      IF(TEST2.EQ.2)THEN
C
CCCC    LOOP 30 COMPUTES THE STRAIGHT RAYPATH DISTANCE
C

      DO 30 I=1,N
          READ(1,5)DEPTH(I),PTT(I),SHTT(I),SVTT(I)
          DIST(I)=OFFSET/(COS(ATAN(DEPTH(I)/OFFSET)))
   30 CONTINUE
C
CCCCC   LOOP 40 COMPUTES THE INTERVAL MEASUREMENTS
C
      DO 40 I=(INT+1),N
          CHECK=0
          CHECK2=0
          CHECK3=0
          CHECK4=0
          CHECK5=0
          VP(I)=0
          VSH(I)=0
          VSV(I)=0
          SHRATIO(I)=0
          SVRATIO(I)=0
          SHPOIS(I)=0
          SVPOIS(I)=0
C
CCCC    COMPUTE P INTERVAL MEASUREMENTS
C
          IF(PTT(I).NE.0.AND.PTT(I-INT).NE.PTT(I))THEN
              IF(PTT(I-INT).EQ.0)THEN
                DO 41 J=1,(I-INT)
                  INT2=INT+J-1
                  IF(PTT(I-INT2).EQ.0) GO TO 41
                  IF(CHECK.EQ.1)GO TO 41
                  VP(I)=(DIST(I)-DIST(I-INT2))/(PTT(I)-PTT(I-INT2))
                  VPDEPTH(I)=(DEPTH(I)-DEPTH(I-INT2))/2.0+DEPTH(I-INT2)
                  CHECK=1
   41           CONTINUE
```

```
                ELSE
                  VP(I)=(DIST(I)-DIST(I-INT))/(PTT(I)-PTT(I-INT))
                  VPDEPTH(I)=DEPTH(I-INT)+(DEPTH(I)-DEPTH(I-INT))/2.0
                ENDIF
              ENDIF
C
CCCC        COMPUTE SV INTERVAL MEASUREMENTS
C
              IF(SVTT(I).NE.0.AND.SVTT(I-INT).NE.SVTT(I))THEN
                  IF(SVTT(I-INT).EQ.0)THEN
                    DO 42 J=1,(I-INT)
                     INT2=INT+J-1
                     IF(SVTT(I-INT2).EQ.0) GO TO 42
                     IF(CHECK2.EQ.1) GO TO 42
                     VSV(I)=(DIST(I)-DIST(I-INT2))/(SVTT(I)-SVTT(I-INT2))
                     VSVDEPTH(I)=(DEPTH(I)-DEPTH(I-INT2))/2.0+DEPTH(I-INT2)
                     CHECK2=1.0
  42                CONTINUE
                  ELSE
                    VSVDEPTH(I)=DEPTH(I-INT)+(DEPTH(I)-DEPTH(I-INT))/2.0
                    VSV(I)=(DIST(I)-DIST(I-INT))/(SVTT(I)-SVTT(I-INT))
                  ENDIF
              ENDIF
C
CCCCC       COMPUTE SH INTERVAL MEASUREMENTS
C
              IF(SHTT(I).NE.0.AND.SHTT(I-INT).NE.SHTT(I))THEN
                 IF(SHTT(I-INT).EQ.0)THEN
                   DO 43 J=1,(I-INT)
                    INT2=INT+J-1
                    IF(SHTT(I-INT2).EQ.0) GO TO 43
                    IF(CHECK3.EQ.1) GO TO 43
                    VSH(I)=(DIST(I)-DIST(I-INT2))/(SHTT(I)-SHTT(I-INT2))
                    VSHDEPTH(I)=(DEPTH(I)-DEPTH(I-INT2))/2.0+DEPTH(I-INT2)
                    CHECK3=1.0
  43               CONTINUE
                 ELSE
                   VSHDEPTH(I)=DEPTH(I-INT)+(DEPTH(I)-DEPTH(I-INT))/2.0
                   VSH(I)=(DIST(I)-DIST(I-INT))/(SHTT(I)-SHTT(I-INT))
                 ENDIF
              ENDIF
C
CCC         COMPUTE INTERVAL SH RATIOS
C
              IF(PTT(I).NE.0.AND.SHTT(I).NE.0)THEN
                   IF(PTT(I-INT).EQ.0.OR.SHTT(I-INT).EQ.0)THEN
                      DO 44 J=1,(I-INT)
                        INT2=INT+J-1
                        IF(PTT(I-INT2).EQ.0.OR.SHTT(I-INT2).EQ.0)GO TO 44
                        IF(CHECK4.EQ.1)GO TO 44
                        SHRATIO(I)=(SHTT(I)-SHTT(I-INT2))/(PTT(I)-PTT(I-INT2))
                        SHPOIS(I)=0.5*(SHRATIO(I)**2-2.0)/(SHRATIO(I)**2-1.0)
                        SHRDEPTH(I)=(DEPTH(I)-DEPTH(I-INT2))/2.0+DEPTH(I-INT2)
                        CHECK4=1.0
  44                  CONTINUE
                   ELSE
                      SHRATIO(I)=(SHTT(I)-SHTT(I-INT))/(PTT(I)-PTT(I-INT))
                      IF(SHRATIO(I).NE.1.0)
     &                SHPOIS(I)=0.5*(SHRATIO(I)**2-2.0)/(SHRATIO(I)**2-1.0)
                      SHRDEPTH(I)=(DEPTH(I)-DEPTH(I-INT))/2.0+DEPTH(I-INT)
                   ENDIF
              ENDIF
```

```
C
CCCCC       COMPUTE INTERVAL SV RATIOS
C
         IF(PTT(I).NE.0.AND.SVTT(I).NE.0)THEN
              IF(PTT(I-INT).EQ.0.OR.SVTT(I-INT).EQ.0)THEN
                   DO 45  J=1,(I-INT)
                    INT2=INT+J-1
                    IF(PTT(I-INT2).EQ.0.OR.SVTT(I-INT2).EQ.0)GO TO 45
                    IF(CHECK5.EQ.1)GO TO 45
                    SVRATIO(I)=(SVTT(I)-SVTT(I-INT2))/(PTT(I)-PTT(I-INT2))
                    SVPOIS(I)=0.5*(SVRATIO(I)**2-2.0)/(SVRATIO(I)**2-1.0)
                    SVRDEPTH(I)=(DEPTH(I)-DEPTH(I-INT2))/2.0+DEPTH(I-INT2)
                    CHECK5=1.0
  45               CONTINUE
              ELSE
                   SVRATIO(I)=(SVTT(I)-SVTT(I-INT))/(PTT(I)-PTT(I-INT))
                   IF(SVRATIO(I).NE.1.0)
     &             SVPOIS(I)=0.5*(SVRATIO(I)**2-2.0)/(SVRATIO(I)**2-1.0)
                   SVRDEPTH(I)=(DEPTH(I)-DEPTH(I-INT))/2.0+DEPTH(I-INT)
              ENDIF
         ENDIF
                   IF(TEST.EQ.2)WRITE(2,3)VPDEPTH(I),VP(I),VSVDEPTH(I),
     &                 VSV(I),VSHDEPTH(I),VSH(I)
                   IF(TEST.EQ.3)WRITE(2,39)SHRDEPTH(I),SHRATIO(I),SHPOIS(I),
     &                 SVRDEPTH(I),SVRATIO(I),SVPOIS(I)

C                   IF(TEST.EQ.2)WRITE(6,3)VPDEPTH(I),VP(I),VSVDEPTH(I),
C       &                VSV(I),VSHDEPTH(I),VSH(I)
C                   IF(TEST.EQ.3)WRITE(6,39)SHRDEPTH(I),SHRATIO(I),SHPOIS(I),
C       &                SVRDEPTH(I),SVRATIO(I),SVPOIS(I)

  40     CONTINUE
         ENDIF
         ENDIF
         CLOSE(1)
         WRITE(6,*)'DO YOU WANT MORE DATA BEFORE PLOTTING?   1=YES'
         READ(5,*)MORE
         IF(MORE.EQ.1)GO TO 100
C
******************************************************************
C************  REMOVE THE ZERO VALUES FOR PLOTTING  ****************

         IP=0
         ISH=0
         ISV=0
         IRSH=0
         IRSV=0
         ISHP=0
         ISVP=0

         CALL ZERO(VP,VPDEPTH,N,INT,IP)
         CALL ZERO(VSH,VSHDEPTH,N,INT,ISH)
         CALL ZERO(VSV,VSVDEPTH,N,INT,ISV)
         CALL ZERO(SVRATIO,SVRDEPTH,N,INT,IRSV)
         CALL ZERO(SHRATIO,SHRDEPTH,N,INT,IRSH)
         CALL ONE(SHPOIS,N,INT,ISHP)
         CALL ONE(SVPOIS,N,INT,ISVP)


  3      FORMAT(3(F12.0,F8.0))
  5     FORMAT(F8.2,3F8.4)
  7      FORMAT(A64)
  9      FORMAT(F16.0,3F16.3)
  11     FORMAT(4F16.0)
```

```
39      FORMAT(2(F15.0,2F12.3))
CCCCCCCCCCCCCCCCCCCCCCCCCCCCCCCCCCCCCCCCCCCCCCCCCCCCCCCCCCCCCCCCCCCCCCC
CCCCCCCCCCCCCC   CALL GRAPHICS    CCCCCCCCCCCCCCCCCCCCCCCCCCCCCCCCCCCCCCCC
99      CONTINUE
        CALL NOMIN8
c        CALL PVT240
        CALL PAGE(11.0,8.5)

        IF(TEST.EQ.2)CALL YNAME('INTERVAL VELOCITY (FT/SEC)$',100)
        IF(TEST.EQ.3)CALL YNAME('SH POISSON RATIO$',100)

C        CALL YNAME('P/SH RATIO$',100)
        CALL XNAME('DEPTH (FEET)$',100)

        CALL AREA2D(8.0,6.0)

        IF(TEST.EQ.3)CALL GRAF(0.,1000.,6000.,0.0,0.05,.5)


        IF(TEST.EQ.2)CALL GRAF(0.,1000.,6000.,0.0,3000.0,18000.0)


        CALL MARKER(2)
        IF(TEST.EQ.3)THEN
C        CALL CURVE(SVRDEPTH,SVPOIS,ISVP,1)
        CALL CURVE(SHRDEPTH,SHPOIS,ISHP,1)
        ENDIF

C        CALL CURVE(SHRDEPTH,SHRATIO,IRSH,1)

C        CALL MARKER(4)
        IF(TEST.EQ.2)THEN
                CALL CURVE(VSHDEPTH,VSH,ISH,1)
                CALL CURVE(VPDEPTH,VP,IP,1)
        ENDIF

        CALL ENDPL(0)
c        CALL DONEPL

        WRITE(6,*)' ','DO YOU WANT ANOTHER PLOT OR MORE DATA?   1=PLOT AGAIN,
     &  2=MORE DATA,  3=THE END'
        READ(5,*)COPY
        IF(COPY.EQ.1) GO TO 99
        IF(COPY.EQ.2) GO TO 100
        CALL DONEPL
        END

        SUBROUTINE ZERO(VEL,VDEPTH,N,INT,ISTEP)                      ZERO
C
CCCCC     THIS SUBROUTINE REMOVES VALUES OF VEL EQUAL TO ZERO
CCCCC     AND REORDERS VEL AND VDEPTH WITHOUT THOSE VALUES
C
        REAL VEL(100),VDEPTH(100)
        INTEGER N,INT,ISTEP

        ISTEP=0
        DO 10 I=(INT+1),N
                IF(VEL(I).NE.0)THEN
                        ISTEP=ISTEP+1
                        VEL(ISTEP)=VEL(I)
                        VDEPTH(ISTEP)=VDEPTH(I)
                ENDIF
10      CONTINUE
        RETURN
        END
```

```
      SUBROUTINE ONE(VEL,N,INT,ISTEP)
C
CCCC    THIS SUBROUTINE REMOVES VALUES OF VEL EQUAL TO ONE OR ZERO
CCCC    AND REORDERS VEL  WITHOUT THOSE VALUES
C
      REAL VEL(100)
      INTEGER N,INT,ISTEP

      ISTEP=0
      DO 20 I=(INT+1),N
              IF(VEL(I).NE.1.AND.VEL(I).NE.0)THEN
                      ISTEP=ISTEP+1
                      VEL(ISTEP)=VEL(I)
              ENDIF
 20   CONTINUE
      RETURN
      END
```

```
          PROGRAM ROTBOR
c
c Originally written by Fred Eastwood, modifications by Tom Daley
c ****************************************************************
c this program computes the rotation of randomly
c oriented three component traces into a
c borehole coordinate system
c ****************************************************************

          character filein*64,fileout*64,EIGEN*64
          real*4 cross(3,3),traces(1000),traceh1(1000),traceh2(1000)
          real*4 temps(1000),temph1(1000),temph2(1000)
c
c open input file
c
          type 140,filein
140       format(' input filename=',a)
          accept 145,filein
145       format(a)
          open(unit=2,file=filein,status='old',form='unformatted')
c
c open output file
c
          type 240,fileout
240       format(' output filename=',a)
          accept 245,fileout
245       format(a)
          open(unit=3,file=fileout,status='new',CARRIAGECONTROL='LIST')
c
          WRITE(6,*)' EIGEN VALUE FILE NAME= '
          READ(5,145)EIGEN
          OPEN(UNIT=4,FILE=EIGEN,STATUS='NEW')

          read(2) ntrace
          type 250,ntrace
250       format(' headers say ntrace=',i)
          write(3,260) ntrace
260       format(' headers say ntrace=',i)
c
c solve system
c
          do 1000 i=1,ntrace/3                          ! read in data traces
                    read(2) nsamp
                    read(2) (traces(j),j=1,nsamp)
                    read(2) nsamp
                    read(2) (traceh1(j),j=1,nsamp)
                    read(2) nsamp
                    read(2) (traceh2(j),j=1,nsamp)


c
c calculate zero lag auto and cross correlations
c
                    call docross(traces,traces,nsamp,cross(1,1))
                    call docross(traceh1,traceh1,nsamp,cross(2,2))
                    call docross(traceh2,traceh2,nsamp,cross(3,3))
                    call [illegible](traces,traceh1[illegible]ss(1,2))
                    call [illegible](traces,traceh[illegible]ss(1,3))
                    call [illegible](traceh1,trace[illegible]ss(2,3))
                    cros[illegible]ss(1,2)
                    cros[illegible]ss(1,3)
                    cros[illegible]ss(2,3)
```

```
c
c normalize cross correlation matrix
c
                fact=cross(1,1)

                do 600 j=1,3
                        do 500 k=1,3
                                IF(FACT.EQ.0.0) THEN
                                CROSS(J,K)=0.001
                                GO TO 500
                                ENDIF
                                cross(j,k)=cross(j,k)/fact
500                     continue
600             continue
c
c calculate polarization
c

                call polar(cross,phi,theta,ellip)
c

                phi=0.0         ! SET PHI=0 FOR BOREHOLE COORDINATES

                type 800,i,phi,theta,ellip
800             format(' i=',i,' phi=',f,' theta=',f,' ellip=',f)
                write(3,900) i,phi,theta,ellip
900             format(1X,i2,5X,f8.3,f8.3,10x,f8.3)
1000    continue
        CLOSE(2)
        CLOSE(3)
        CLOSE(4)
        stop
        end

        subroutine polar(cross,phi,theta,ellip)
c
        real*4 cross(3,3),xinvar(3),cubic(3),croot(3),evect(3)
        pi = 3.1415926
c
        call calcinv(cross, xinvar)
c
        cubic(1) = -xinvar(3)
        cubic(2) = xinvar(2)
        cubic(3) = -xinvar(1)
c
        call rcubic(cubic,croot)
        call sorteigval(croot)
c
        cross(1,1) = cross(1,1) - croot(1)
        cross(2,2) = cross(2,2) - croot(1)
        cross(3,3) = cross(3,3) - croot(1)
c
        DO 30 JJ=1,3
        WRITE(4,*) CROOT(JJ)
  30    CONTINUE

        call doevect(cross, evect)
        if (evect(1).lt.0.0) then
                evect(1) = -evect(1)
                evect(2) = -evect(2)
                evect(3) = -evect(3)
        endif
```

polar

...polar

```
C
C        IF TRACES HAVE BEEN EDITED SET
C         THETA = 0
C         PHI   =0
C         ELLIP = 0

          IF (EVECT(2).EQ. 0.)GO TO 8
          GO TO 11
8         IF(EVECT(3).EQ. 0.) GO TO 10
c
11         theta = 180.0 * atan2(evect(3), evect(2)) / pi
           phi = 180.0 * acos(evect(1) / xmag(evect)) / pi
           ellip = 1.0 - croot(2) / croot(1)
c
           return
10        THETA = 0.
          PHI =0
          ELLIP = 0
          RETURN
          end
          subroutine calcinv(matrix,invar)
```

calcinv

```
c
          real*4 matrix(3,3),invar(3)
c
          invar(1) = matrix(1, 1) + matrix(2, 2) + matrix(3, 3)
c
          invar(2)=0.0
          do 200 i=1,3
                   do 100 j=1,3
                            invar(2)=invar(2)+0.5*(matrix(i, i) * matrix(j, j) -
     1                                   matrix(i, j) * matrix(i, j))
100                continue
200       continue
c
          invar(3) = det(matrix)
c
          return
          end
          function det(a)
```

det

```
c
          real*4 a(3,3)
c
          term1 = a(2, 2) * a(3, 3) - a(2, 3) * a(3, 2)
          term2 = a(2, 1) * a(3, 3) - a(3, 1) * a(2, 3)
          term3 = a(2, 1) * a(3, 2) - a(3, 1) * a(2, 2)
          det = a(1, 1) * term1 - a(1, 2) * term2 + a(1, 3) * term3
          return
          end
          subroutine rcubic (a,x)
```

rcubic

```
c
          real*4 a(3),x(3)
c
          pi=3.1415926
c
          p = a(2) - (a(3) * a(3) / 3.0)
          q = (2.0 * a(3)**3 / 27.0) - (a(2) * a(3) / 3.0) + a(1)
          delta = 27.0 * q**2 + 4.0 * p**3
          if (delta .gt. 0.0) then
                   type 100
100                format(' this cubic has two complex roots, and one real root')
          else
                   phi = atan2(-sqrt(-delta / 27.0) , q)
```

```
c
                if(phi.lt.0.0) phi=phi+pi
c
                amp = 2.0 * sqrt(-p / 3.0)
                x(1) = amp * cos(phi / 3.0) - a(3) / 3.0
                x(2) = -amp * cos((pi - phi) / 3.0) - a(3) / 3.0
                x(3) = -amp * cos((pi + phi) / 3.0) - a(3) / 3.0
        endif
c
        return
        end
```

sorteigval

```
        subroutine sorteigval (a)
c
        real*4 a(3)
c
        do 200 i=1,2
                do 100 j=1,2
                        if(a(j).lt.a(j+1)) call swapscalar(a(j),a(j+1))
100             continue
200     continue
        return
        end
```

swapscalar

```
        subroutine swapscalar (a, b)
c
        temp = a
        a = b
        b = temp
        return
        end
```

doevect

```
        subroutine doevect (a,evect)
c
        real*4 a(3,3),evect(3)
        integer*4 index(3)
c
c initialise indexes
c
        index(1)=1
        index(2)=2
        index(3)=3
c
c swap   columns and rows if needed)
c
        if (a(1,1) .eq. 0.0) call swap(1, 2, a, index)
        call calceigenvect(a, evect, iflag)
        if (iflag .gt. 0) then
                call swap(2, 3, a, index)
                call calceigenvect(a, evect, iflag)
        endif
c
c unscramble eigenvector
c
        call unscramble(evect, index)
        return
        end
```

swap

```
        subroutine swap (k, l, a, index)
c
        real*4 a(3,3)
        integer*4 index(3)
c
c swap columns
c
        do 200 i=1,3
                temp = a(i, k)
                a(i, k) = a(i, l)
```

```
                    a(i, l) = temp
200         continue
c
c swap rows
c
            do 300 i=1,3
                    temp = a(k, i)
                    a(k, i) = a(l, i)
                    a(l, i) = temp
300         continue
c
c update indexes
c
            i = index(k)
            index(k) = index(l)
            index(l) = i
c
            return
            end
            subroutine calceigenvect (a, af, iflag)
c
            real*4 a(3,3),af(3),ea(3),ainverse(3,3)
c
            iflag = 0
c
c initialize ainverse
c
            do 100 i=1,3
                    do 50 j=1,3
                            ainverse(i,j)=0.0
50                  continue
100         continue
            ainverse(1, 1) = 1.0 / a(1, 1)
c
            do 500 n=1,2
c
c calculate ea and af
c
                    eaf = 0.0
                    do 400 j=1,n
                            ea(j) = 0.0
                            af(j) = 0.0
                            fj = a(j, n + 1)
                            do 300 i=1,n
                                    ei = a(n + 1, i)
                                    fi = a(i, n + 1)
                                    ea(j) = ea(j) + ei * ainverse(i, j)
                                    af(j) = af(j) + fi * ainverse(j, i)
                                    eaf = eaf + ei * ainverse(i, j) * fj
300                         continue
400                 continue
c
                    af(n + 1) = -1.0
                    ea(n + 1) = -1.0
c
                    if (n .lt. 2) g = a(n + 1, n + 1)
c
c check for divide by zero
c
                    if (abs(g - eaf) .lt. 0.005) then
                            iflag = n
                            return
                    endif
```

calceigenvect

...calceigenvect

```
c
                z = 1.0 / (g - eal)
                ainverse(i,j)=0.0
                do 450 i=1,n+1
                        do 425 j=1,n+1
                            ainverse(i, j) = ainverse(i, j) + z * al(i) * ea(j)
425                     continue
450             continue
c
500     continue
        return
        end
```

unscramble

```
        subroutine unscramble (vect, index)
c
        real*4 vect(3),vtemp(3)
        integer*4 index(3)
        do 100 i=1,3
                vtemp(index(i)) = vect(i)
100     continue
        do 200 i=1,3
                vect(i)=vtemp(i)
200     continue
        return
        end
```

xmag

```
        function xmag (vect)
c
        real*4 vect(3)
c
        temp = 0.0
        do 100 i=1,3
                temp = temp + vect(i) * vect(i)
100     continue
        xmag = sqrt(temp)
        return
        end
```

docross

```
        subroutine docross(trace1,trace2,nsamp,cross)
c
        real*4 trace1(nsamp),trace2(nsamp)
c
        cross=0.0
        do 1000 i=1,nsamp
                cross=cross+trace1(i)*trace2(i)
1000    continue
        return
        end
```

LAWRENCE BERKELEY LABORATORY
TECHNICAL INFORMATION DEPARTMENT
UNIVERSITY OF CALIFORNIA
BERKELEY, CALIFORNIA 94720